Structural Optimisation of Permanent Magnet Direct Drive Generators for 5MW Wind Turbines

Aristeidis Zavvos

Doctor of Philosophy (PhD)

The University of Edinburgh

2013

Abstract

This thesis focuses on permanent magnet 'direct drive' electrical generators for wind turbines with large power output. A variety of such generator topologies is reviewed, tested and optimised in an attempt to increase their potential as commercial concepts for the wind industry.

Direct drive electrical generators offer a reliable alternative to gearbox drivetrains. This novel technology reduces energy loses thus allowing more energy to be yield from the wind and decreases the maintenance cost at the same time. A fundamental issue for these generators is their large size which makes them difficult to manufacture, transport and assembly. A number of structural designs have been suggested in the literature in an attempt to minimise this attribute.

A set of design tools are set out in an attempt to investigate the structural stiffness of the different permanent magnet direct drive generator topologies against a number of structural stresses that apply to such wind turbine energy converters. Optimisation techniques, both analytical and structural, are also developed for minimising the total mass of a variety of 'directly driven' machines with power output of 5MW or greater. Conventional and promising generator designs are modelled and optimised with the use of these optimisation techniques. The topologies under examination are then compared in terms of structural mass, stiffness and cost.

As the number of wind turbine manufactures who adopt the direct drive concept increases, it is important to outline the unique characteristics of the different topologies and increase their manufacturing potential. Discussions and conclusions will provide an indication of the design solutions that could help decrease the mass and cost of such machines.

Declaration

I hereby declare that this thesis has been composed by myself, that the work is my own and that the work has not been submitted for any other degree or professional qualification.

Aristeidis Zavvos, September 2013

Acknowledgements

I would like to thank my principal supervisor, Professor Markus Mueller who gave me the opportunity, support and freedom to carry out the research contained within this thesis. Without his moral and technical contributions, as well as his excellent proof-reading, this thesis would not have been possible.

I would like to thank my second supervisor, Dr John Chick for his concern and advice, especially during the first steps of this work.

My gratitude goes to my friends and colleagues at the Institute for Energy Systems at the University of Edinburgh, for their support over the last three years. Ozan Keysan, Juan Pablo Echenique and Isaac Portugal are due particular thanks for all the help and diversion they provided while “trapped” in the Powerlab.

I am also grateful to Deok-je Bang and Henk Polinder from TU Delft for providing loads of data and papers on transverse-flux machines, as well as NGenTec for allowing publication of the research made on the C-cored aircored machine. This research was fully funded by Hopwell Holdings and I would like to thank them for their generous support.

On a more personal note, I would like to express my eternal gratitude to my parents, Nikos and Roula for always being there for me no matter the distance, and for their unconditional love and patience. I cannot thank you enough for supporting me on this journey.

Finally, but most importantly, I would like to thank my partner Mary, for her understanding and love. Her patience, support and encouragement (not to mention her early wake up calls) were in the end what made this dissertation possible. Every day since I met you is the best of my life. This thesis is dedicated to you.

Table of Contents

List of Figures

List of Tables

Nomenclature

Roman letters

a	Cross area of the stator's arm, m^2
A	Cross area of the stator's cylinder, m^2
A	Blade swept area, m^2
b	Support arm's width, m
b_m	Magnet's width, m
b_t	Stator tooth width, m
b_w	Winding space width, m
B_g	Peak flux density in the airgap, T
B_r	Remanent flux density in the airgap, T
C_p	Wind turbine's power coefficient
d	Support arm's depth, m
D	Plate constant, Nm
D_g	Airgap diameter of machine, m
E	Young's modulus, Pa
f	Uniform outward radial force per unit length, N/m
F_d	Shear stress of machine, Pa
g	Acceleration due to gravity, 9.81 m/s^2
h_m	Magnet height, m
h_s	Winding space height, m
h_yr	Rotor yoke height, m
h_ys	Stator yoke height, m
I	Second moment of area of the stator's cylinder, m^4
$I_\mathrm{arm\text{-}axi}$	Second moment of the area of the stator arm, m^4
$I_\mathrm{arm\text{-}tor}$	Second moment of area of the stator arm, m^4
K_c	Carter coefficient
K_fill	Stator slot fill factor
K_rad	Aspect ratio
l	Axial length of machine, m

l_{g}	Airgap length, m
l_{ge}	Effective airgap length, m
l_{m}	Magnet length, m
l_{s}	Winding space length, m
l_{sp}	Stator pole length, m
m	Number of phases
$mass_{\mathrm{copper}}$	Mass of copper, kg
$mass_{\mathrm{PM}}$	Mass of permanent magnet material, kg
$mass_{\mathrm{steel}}$	Mass of steel, kg
M_{o}	Moment applied at shaft, Nm
M_{rb}	Unit radial bending moment at shaft, N
n	Number of support arms
N_{arms}	Number of stator support arms
p	Number of pole pairs
P	Power rating, W
q	Normal component of Maxwell stress, Pa
R	Rotor blade radius, m
R	Radius of machine, m
R_{a}	Rotor's outer radius of machine, m
R_{o}	Radius of the generator's shaft, m
s	Number of stator slots
t_{d}	Support disc thickness, m
t_{wr}	Rotor support arm's thickness, m
t_{ws}	Stator support arm's thickness, m
T	Torque, Nm
T_{sc}	Short cirquit torque, Nm
T_{n}	Nominal torque, Nm
u_{A}	Radial deflection in the airgap, m
u_{G}	Axial deflection due to gravity, m
u_{T}	Tangemtial deflection, m
v_{t}	Blade's tip speed, m/s
v_{w}	Wind speed, m/s

W	Uniform annular line load, N/m

Greek letters

δ_1	Axial deflection due to moment M_o, m
δ_2	Axial deflection due to stress q, m
$\delta_{\text{TFPM-2}}$	Total axial deflection of TF machine, m
θ	Blade pitch angle, deg
θ	Half angle between support arms, rad
λ	Tip speed ratio
μ_o	Permeability of free space, $4\pi\times10^{-7}$ Wb/Am
μ_r	Relative permeability of permanent magnet material. 1.06
ρ_{air}	Air mass density, kg/m³
ρ_{copper}	Copper density, kg/m³
ρ_{PM}	Permanent magnet density, kg/m³
ρ_{steel}	Steel density, kg/m³
σ	Airgap shear stress, Pa
τ_p	Pole pitch, m
τ_t	Armature slot pitch, m
ψ_1	Meridional slope, deg
ω	Angular velocity, rad/s

Abbreviations

AC	Alternating Current
AEP	Annual Energy Production
AF	Axial Flux
DC	Direct Current
DD	Directly Driven
DFIG	Doubly Fed Induction Generator
EEDD	Electrically Excited Directly Driven
EU	European Union
EWEA	European Wind Energy Association
FEA	Finite Element Analysis

GA	Genetic Algorithm
GHGs	Greenhouse Gases
ICC	Initial Capital Cost
IEA	International Energy Agency
IGBT	Insulated Gate Bipolar Transistors
MMF	Magnetomotive Force
PM	Permanent Magnet
PMDD	Permanent Magnet Directly Driven
RF	Radial Flux
SCIG	Squirrel Cage Induction Generator
SRG	Switched Reluctance Generator
TF	Transverse Flux
WEC	Wind Energy Converter

Chapter 1

Introduction

1.1 Introduction

Electric power is conventionally generated by the exploitation of fossil fuels such as coal, oil and gas. Almost 80% of electricity production worldwide is made by conventional power stations that produce electrical power through the combustion of fossil fuels (Figure 1.1) [1].

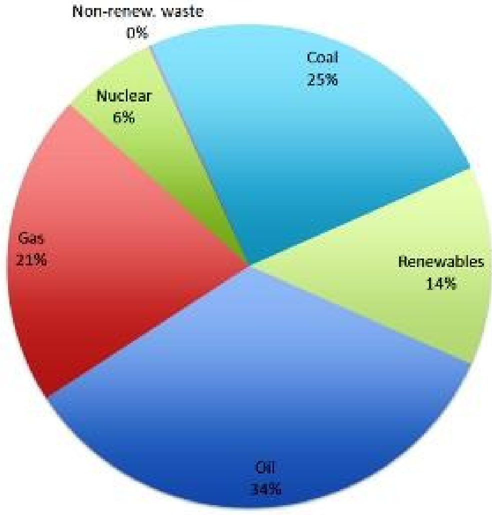

Figure 1.1 - Shares of energy sources in total global primary energy supply in 2011 [2]

The fact that Earth’s supplies of fossil fuels are not replenished, along with their continuous exploitation, will eventually lead to their depletion [3]. Furthermore, through a series of publications over the last decade ([4]-[12]), the scientific community has come to the conclusion that fossil fuels have a direct impact on our planet’s climate and various ecosystems (Figure 1.2).

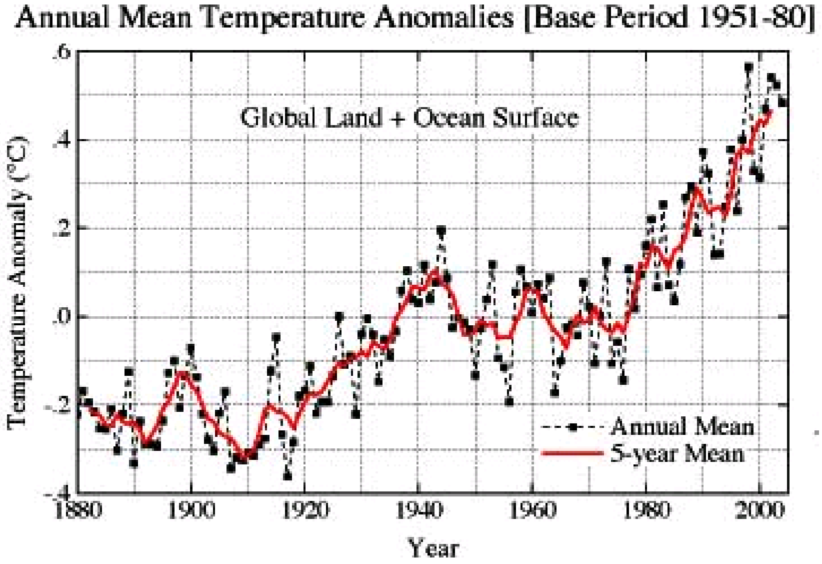

Figure 1.2 - Global mean temperature from 1880 to 2000 [13]

This is primarily due to the release of greenhouse gases (GHGs) into the atmosphere such as carbon dioxide (CO_2), sulphur dioxide (SO_2), nitrous oxide (N_2O), methane (CH_4) and other gasses that are produced during fossil fuel combustion [3].

The diminishing fossil fuels along with the environmental concerns of their exploitation have made the need for renewable energy more demanding during the past years. Renewable energy as defined by Johansson is the energy derived from sources which cannot perish as a result of extraction [14]. Such energy sources are solar, hydro, wind, wave, tidal and geothermal. The origin of these sources can be attributed to the Sun which is the main cause of Earth's weather effects and the gravitational effects between the Earth, the Sun and the Moon. These sources are essentially inexhaustible and their exploitation creates zero greenhouse emissions during the procedure of energy production [1].

Among the renewable energy sources, wind energy seems to have the highest potential as the wind exists everywhere on the earth and can be exploited both onshore and offshore. Wind energy technology has achieved the fastest growth since the 1980s and has reached an average of 30% annual increase of energy penetration over the last ten years (Figure 1.3) [15]. By the end of 2020, the global installed energy capacity of wind turbines is expected to rise over 1,260GW, almost 12% of the world’s electricity consumption [16]. A large amount of that capacity is expected to be installed offshore [17].

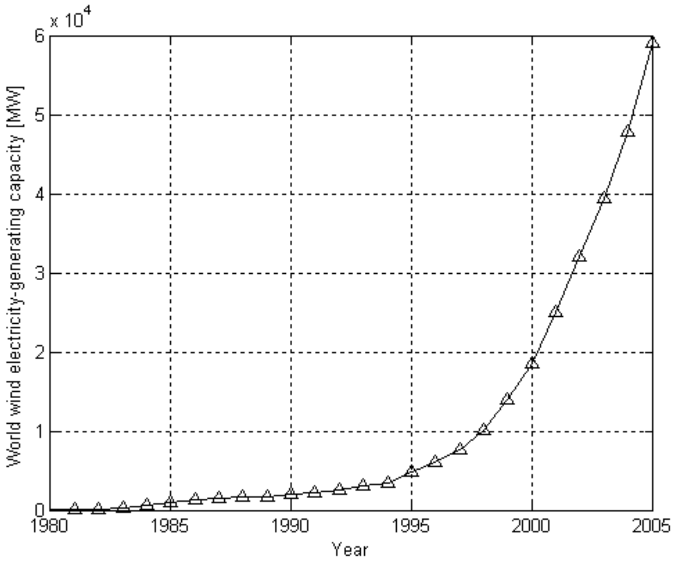

Figure 1.3 - World wind electricity generating capacity during 1980-2005 [15]

Wind turbines are energy converters that turn the kinetic energy that is engulfed in the wind’s movement into electrical power. Through constant research and development on all the parts of a wind turbine (structural materials, blade profile and construction, new generator technologies, advanced gearboxes, pitch control), their size keeps growing annually by approximately 7%, and their power rating by 20% [18]. Wind turbines with rated power more than 2MW usually require wind blades with a rotor diameter of 80m or larger [19][20].

The basic generator technology for modern wind turbines (since late 1990s) is that of variable speed generators. These offer higher efficiency, lower noise levels and a better output power quality for the grid than first generation wind turbines [21]. The two main technologies used for variable speed wind turbine generators are that of the gearbox driven Doubly Fed Induction Generator (DFIG) and the directly driven (DD) synchronous machine.

DFIG machines use a 3-stage gearbox to drive the generator. Although the gearbox is not the most unreliable component, it does cause the greatest downtime resulting in lost revenue [22]. Maintaining or replacing the gearbox can be costly, especially for offshore developments. Twenty-seven intermediate speed and twelve high speed gearbox bearings of the Vestas V-80 wind turbines had to be replaced at Scroby Sands, one of the UK's first offshore wind farms resulting substantial unplanned work in the final three months of 2005 [23]. Another example is that of the Horns Rev offshore wind farm where Vestas had to remove and replace 80 of its V-90 gearboxes [24].

In a DD system the gearbox is eliminated, and the slowly rotating turbine rotor is coupled directly to the electrical generator which rotates at the same speed [25]. This configuration employs the minimum number of rotating parts, making them more reliable compared to their geared counterparts and ideal for offshore applications. The synchronous direct drive machine with permanent magnet excitation (PMDD) is highly efficient compared to the electrically excited alternative since the excitation losses are eliminated, allowing smaller pole pitches to be used [26]. A fundamental issue for DD generators is their large mass and the large diameters required to create a high power output, which in turn increases the overall manufacturing and installation costs [27][28].

A variety of structural topologies have been suggested in the literature in an attempt to minimise the structural mass of PMDD generators such as transverse flux and aircored machines [27][29]. A number of optimisation tools have also been developed in attempts to reduce their mass [30][31]. None of the suggested tools however managed to optimise simultaneously the structural and the electromagnetic material of the DD generator or expand the optimisation techniques for other DD machine topologies.

1.2 Thesis statement

"If there are ways to efficiently decrease both the active and inactive mass of multi-MW permanent magnet direct drive generator systems to a minimum, then their resulting total mass could be comparable to commercial DFIG or geared brushless machines".

1.3 Aims of the thesis

The main aim of this thesis is to investigate the various low speed PMDD generator topologies, focusing on machines with large power outputs such as 5MW or greater. A comparison among the suggested technologies is made in order to provide valuable conclusions regarding the most suitable one for onshore or offshore wind generation. The objectives of the thesis include;

- the production of design tools for the various PMDD technologies that can model the different machine structures under operation.
- outlining the characteristics and potential of each tested permanent magnet topology.
- the comparison of the suggested machine topologies in terms of stiffness, mass or cost.
- the creation of optimisation tools for the various PMDD technologies that would minimise their mass, both active and inactive.
- the production of guidelines that can be taken under consideration in the early design stages of a PMDD generator in order to decrease its total mass.
- the exploration of the potential of a low speed, directly driven generator being as lightweight or as demanding in terms of cost as a gearbox driven DFIG.

1.4 Thesis layout

The following chapter will introduce the reader to renewable energy and mainly focus on wind energy and wind energy converters. The basic parts that compose a wind turbine system will be reviewed.

In chapter 3 the various direct drive topologies that have been suggested for wind power generation are presented. A representative of each topology will be chosen for further testing and comparison during the rest of the thesis.

The structures that were chosen for testing and comparison in this thesis are presented in chapter 4. The structural models that were created with the help of a selected FEA tool are presented to the reader.

In chapter 5, the analytical models for calculating the forces acting on the different structures are presented. A mechanical finite element analysis is then used to predict deflections in simple structures of radial-flux, transverse-flux and aircored axial-flux permanent magnet machines. These results are then used for comparison purposes.

Chapter 6 will use a similar finite element analysis tool to optimise the structure of the same low speed generators that were tested in chapter 5. The resulting lightweight structures are compared for their total structural mass.

An analytical optimisation tool is presented in chapter 7 that can optimise both active and inactive material on a permanent magnet direct drive machine simultaneously. The optimisation tool is used to minimise the total mass or the total cost of different radial-flux and transverse-flux machines. The resulting lightweight structures are compared for drawing valuable conclusions regarding their mass and cost.

Chapter 8 will draw the final conclusions that this research provided, further discuss the work in this thesis and highlight the design solutions that can be applied for minimising the mass of a direct drive generator.

Chapter 2

Wind Turbine Systems

2.1 Introduction

It is essential for any thriving economy to be able to satisfy its energy demands. Brown *et al*. [32] and Warr *et al*. [33] outlined the proportionate relationship between economic growth and energy demand. Fossil fuels, namely oil, coal and gas, have the lion's share on global energy supply. The oil crisis in the 1970s [34] made it clear that there is an extensive need for alternative energy sources if energy supply is to be assured. In addition, the recent Deepwater Horizon incident [35] demonstrated the environmental impacts that the extraction of offshore fossil fuels can have on the environment. The above arguments were reinforced by a report of the International Energy Agency (IEA) in 2011 which declared that liquid fuel production reached its peak in 2005 (Figure 2.1) [2]. Although conventional fuel production has remained at the same levels for the last years, it is expected to eventually start to decline, leading to so-called depletion [3].

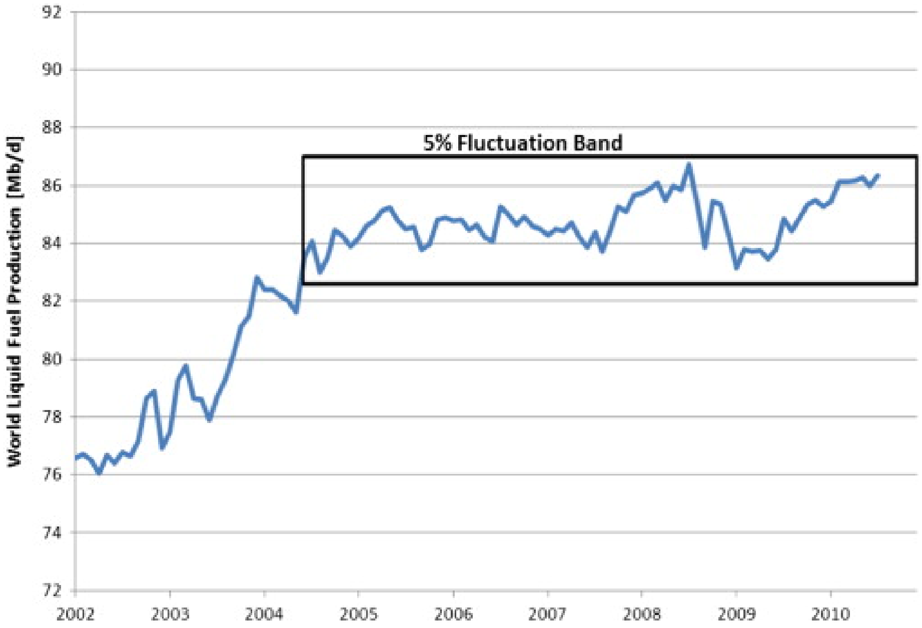

Figure 2.1 - World liquid fuel production over the last decade [2]

As a result of the increasing energy demand and fossil fuel extraction becoming more expensive and difficult, most of the world's major economies have turned to renewable energy sources in order to ensure power generation. Renewable energy sources are those "flows of energy" that are constantly replenished [36], thus they cannot perish through their exploitation.

In 2008, the EU agreed to set a binding target that 20% of the total electricity produced would be generated by renewable energy for 2020 [37]. From the previously mentioned energy sources, wind energy has achieved the fastest technological growth, which makes it the one with the highest potential to be used for reaching that target.

Wind energy is a source available in every part of the world. This attribute, in addition with the great technological leaps over the last two decades, has contributed into making wind energy the fastest growing renewable energy source with an installed capacity that almost doubles every three years [16][38] (Figure 2.2). According to the Global Wind Energy Council, the total installed capacity of wind turbines worldwide reached 194GWs, which is equal to 4% of the world's power generation [38].

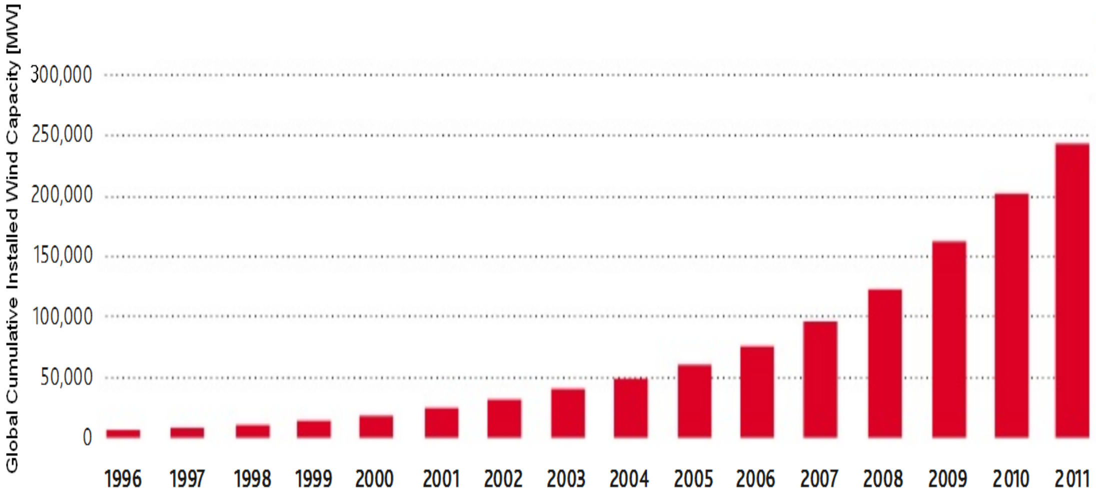

Figure 2.2 - Global cumulative installed wind capacity 1996-2010 [38]

Wind turbines are energy converters that turn the kinetic energy that is engulfed in the wind's movement into electrical power. Figure 2.3 demonstrates the growth in wind turbines' size over the years, while Figure 2.4 depicts the rising trend of wind turbines with power capacity greater than 5MW for offshore development.

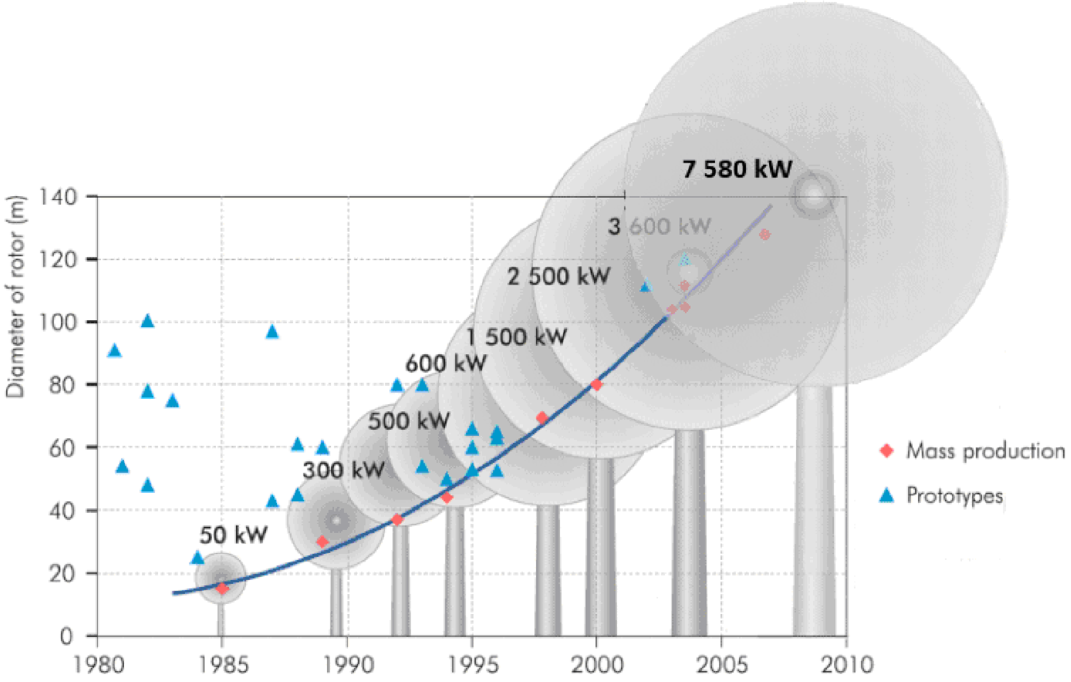

Figure 2.3 - Growth in scale of commercial wind turbines [39]

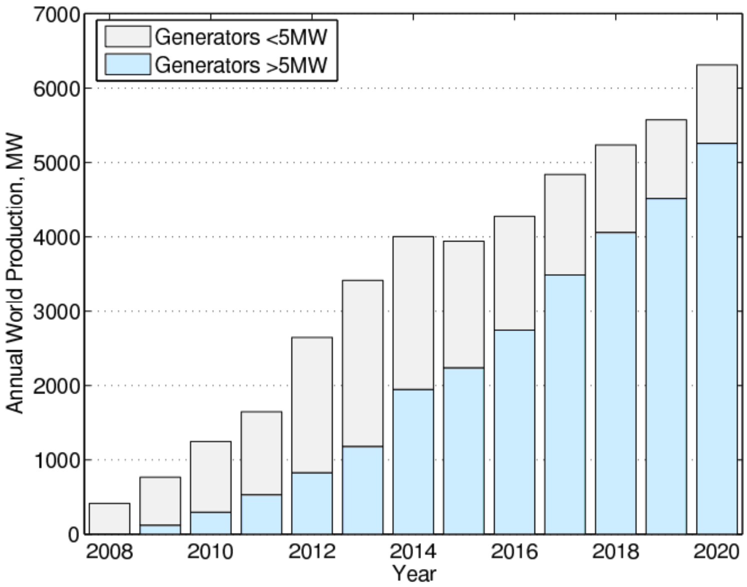

Figure 2.4 - Expected installed power capacity for offshore wind energy converters [40]

Wind turbines can be placed to harness wind both onshore and offshore. Onshore wind farms account for more than 99% of the installed wind capacity worldwide. This can be attributed to the lower cost of investment compared to that of offshore. Nevertheless, more and more investments are starting to favour offshore development due to the higher and more constant wind speed characteristics that can be provided. Average wind speeds can be much greater offshore compared to those onshore, hence more energy can be contributed to the grid. In addition, the lower turbulence of the wind results in less fatigue for the turbine. There are no space restrictions offshore and the visual and audio impact is also negligible compared to onshore sites. The environmental impact of an offshore wind farm is also less compared to an onshore one since there is no need for new infrastructure on the countryside for the transportation of the turbines.

In order to reach the 2020 renewable energy target that is set by the European Union, the European Wind Energy Association (EWEA) suggested that more than 55GW of wind power capacity should be installed offshore [17]. Such a venture would require new technologies together with a great upscale in the wind turbine generator power output. Before explaining how an upscale in power generation can be achieved, the fundamentals of wind energy must be understood and the individual parts that compose a wind turbine should be analysed.

The power P (W) extracted from a stream of wind that flows through an area A(m²) covered by a wind turbine's blades can be calculated according to (2.1) [41]

$$P = \tfrac{1}{2}\rho_{\mathrm{air}} C_{\mathrm{p}} A v_{\mathrm{w}}^{3} \tag{2.1}$$

where ρ_{air} is the air mass density (kg/m³), v_{w} is the wind speed (m/s) and C_{p} is the turbine's power coefficient which depends on the specific design of the wind converter and its orientation to the wind direction. Its theoretical maximum value is 16/27 = 59.3% (Betz limit). For a wind turbine with given blade diameter it can be shown that the power coefficient C_{p} is a function of the blade pitch angle θ (deg) and the tip speed ratio λ. Pitch angle θ is defined as the angle between the cord of the blade and the plane of the wind rotor, whereas λ can be calculated according to (2.2)

$$\lambda = v_t / v_w \tag{2.2}$$

where v_t the blade's tip speed (m/s) and v_w the given wind speed (m/s). For a wind rotor with radius R(m), (2.1) can be rewritten as:

$$P = \tfrac{1}{2} \rho_{air} C_p(\lambda, \theta) \pi R^2 v_w^3 \tag{2.3}$$

Figure 2.5 shows a typical $C_p - \lambda$ curve [42]

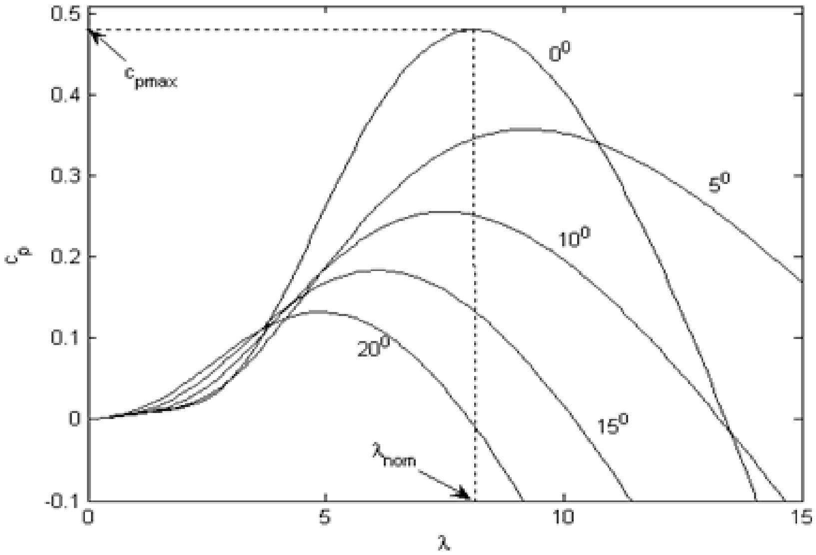

Figure 2.5 - Power coefficient C_p as a function of tip speed ratio λ and pitch angle θ for a given blade [42]

There are two basic types of modern wind turbine alignments: horizontal-axis and vertical-axis wind turbines. The name of each turbine type demonstrates the axis on which the turbine rotates. Horizontal-axis turbines have dominated the market, as they are more efficient compared to vertical axis [43]. Figure 2.6 shows the parts that compose a conventional horizontal-axis wind turbine, which consists of the blades and the hub, the main shaft, the gearbox (for conventional geared topologies), the generator and the transformer.

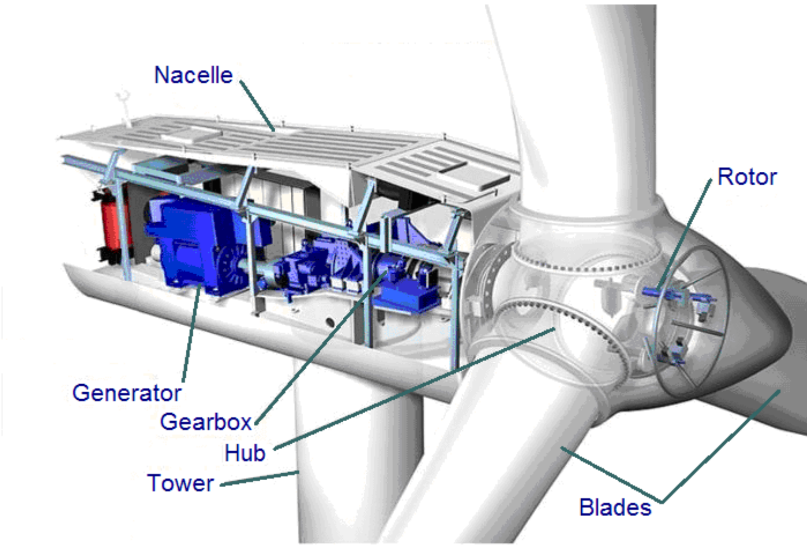

Figure 2.6 - Basic components of a conventional wind turbine [44]

2.2 Rotor

2.2.1 Rotor blades

Wind turbines capture the energy that is engulfed in the wind's movement and convert it into mechanical power with the use of blades. Modern wind turbines have three such blades that are set into motion by the wind according to the principle of aerodynamic lift. When the wind hits a rotor blade, the air is guided downstream from above and below the blade (Figure 2.7).

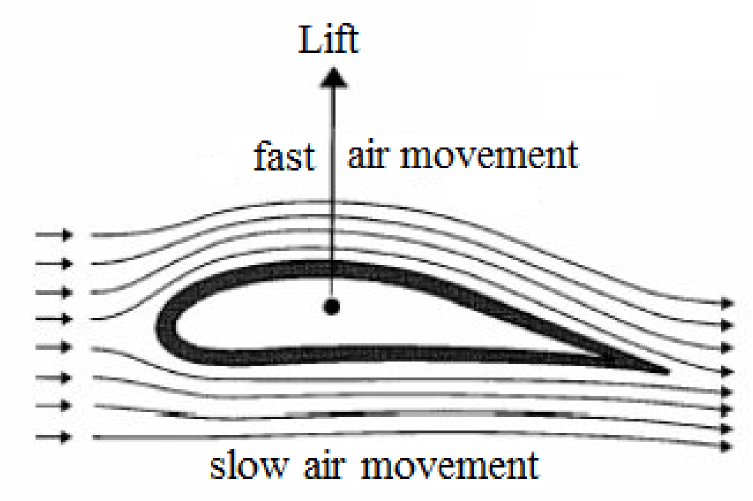

Figure 2.7 - Air movement around the blade profile [45]

The rotor blade profile forces the air on the upper side to travel a longer distance than the air on the lower side and makes it move with a higher velocity in order to reach the wind travelling below. This creates a negative pressure above the blade and a positive underneath (Figure 2.8). Due to this pressure difference, a force perpendicular to the flow is generated, which drives the rotor blade and sets the rotor in motion. Blades are always oriented perpendicular to the wind flow.

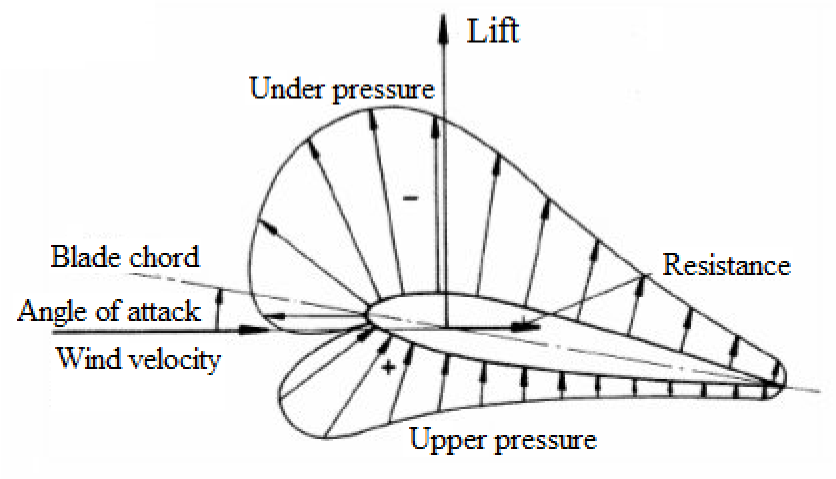

Figure 2.8 - The aerodynamic lift principle on a wind turbine blade [45]

Aerodynamic losses occur on the rotor blade by friction at the surface as well as by pressure imbalance. More aerodynamic losses arise due to the flow through the air column as the blades rotate. Thus, while the theoretical maximum rotor efficiency is approximately 59% according to the Betz limit, an efficiency of 50% or less is actually achieved [43].

Equation (2.2) showed that the generated power is proportional to the cube of the wind speed. Modern wind turbines typically reach their nominal power output for wind speeds from 8 to 12m/s. For wind speeds greater than that, performance limitation measures are installed to ensure production of a constant rate of power and prevent overheating and material damage. This is achieved by pitch or stall control. In this way the C_p curve is adjusted to the weather conditions in order to protect the rotor blades against excessive wind loads or overspeed and to ensure that the wind turbine will operate with a constant power output.

Modern rotor blades are typically made of glass-fibre reinforcements. E-glass epoxy materials, carbon fibre and hybrids are commonly used by manufacturers, especially in the production of longer blades [46]. The blades of a typical wind turbine vary from 30 to 80m long and are non-sectional (Figure 2.9).

Figure 2.9 - Conventional wind blades [46]

As wind turbines grow in power, they would require even larger blades that would make their transportation and assembly even more demanding, especially for offshore development. Gamesa, a Spain-based wind turbine manufacturer, recently developed a sectional blade called INNOBLADE® [46][47]. INNOBLADE® (Figure 2.10) was designed for the benefit of offshore development, offering a way to reduce transportation and installation costs since it can be divided into sections and assembled on-site, using the same transportation equipment as the rest of the turbine.

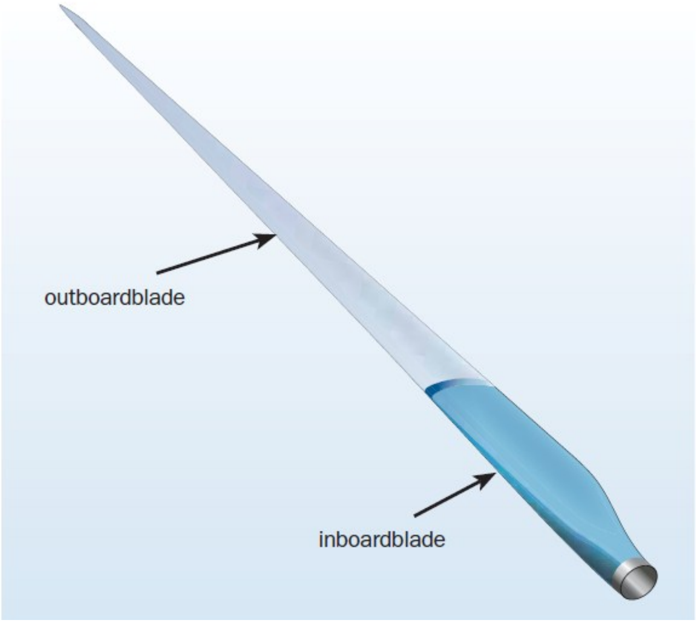

Figure 2.10 - Sectional blade (INNOBLADE®) with bolted joints [48]

2.2.2 Rotor hub

The hub connects the rotor blades with the rest of the machine (Figure 2.11). For pitch regulated machines, the pitching mechanism is contained within the hub.

Figure 2.11 - Rotor hub of Enercon's E82 [49]

The vast majority of hub systems for wind turbines use active torque regulation through pitch control. This system type enables the blades to rotate on the longitudinal axis and adjust the pitch angle θ based on the wind's measured parameters. Thus, the performance of the system can be controlled according to the $C_p(\lambda,\theta)$ curve which was presented in Figure 2.5. Each of the blades can be rotated individually using hydraulic actuators, acting as an aerodynamic brake for the rotor (Figure 2.12). Pitch control is achieved through electric controls [43][50].

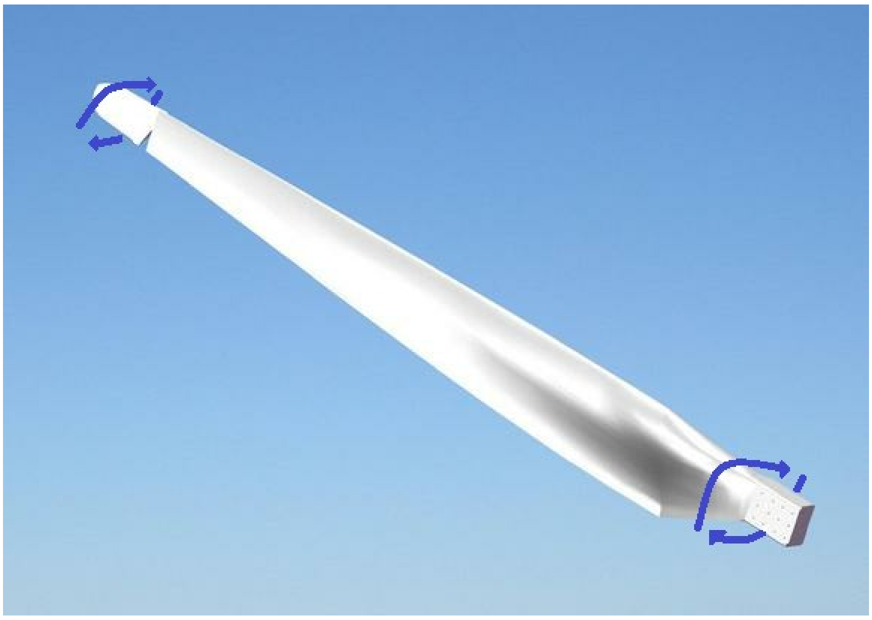

Figure 2.12 - The direction of a blade's rotation [51]

The rotor hub system is not only responsible for stalling or bringing the blades to the right angular position, but also for stopping the rotation of the rotor in case of an emergency, for example extreme weather conditions with wind speeds more than 25m/s or an electrical problem.

2.3 Main shaft

The main shaft connects the hub with the rest of wind turbine's drive train. This could be either the gearbox for conventional geared topologies or the generator for direct drive power take offs. Main shaft configurations can be distinguished according to the bearing configuration that is employed to support the main shaft and connect it to the drive train. Common bearing configurations are the three point suspension, the double bearings outside the gearbox and the integrated main bearing [52].

The three point suspension configuration (1 main bearing, 2 torque arms) is the most common support type for wind turbines with power output less than 2 MW. In this suspension system, a single self-aligning roller bearing supports the rotor shaft. Two torque arms are used on the gearbox side to fix the gearbox with the main-frame (Figure 2.13).

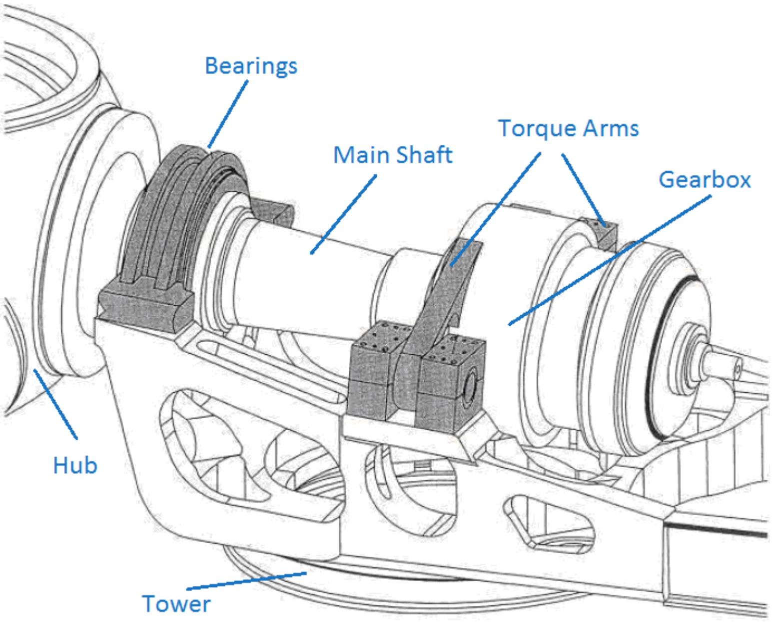

Figure 2.13 - Three point suspension configuration [53]

As the rotor blades move, they create axial loads and bending moments that are transmitted from the main shaft to the gearbox. Loads generated from the main shaft side are transmitted through the gearbox's torque arms to the wind turbine structure, turning the gearbox into part of the whole structure [52]. Problems with this configuration often occur due to the highly variable load conditions that are generated in all directions on the main bearing side and can cause a displacement and trigger a gearbox failure [54].

For the double bearing configuration, as its name implies, two main bearings are used to support the main shaft (Figure 2.14). This configuration is more common for larger wind turbines with nominal power greater than 2MW. Although the second bearing increases the cost, it also increases the system's stiffness against the high internal loads generated in such wind turbines. This configuration can be more successful in isolating the gearbox from loads and bending moments coming from the rotor side, leading to a lighter, cheaper and more reliable gearbox. A high degree of mounting accuracy is expected in such configurations to avoid a drive train misalignment that might lead to harmful non-toroidal forces reaching the gearbox [52] [54].

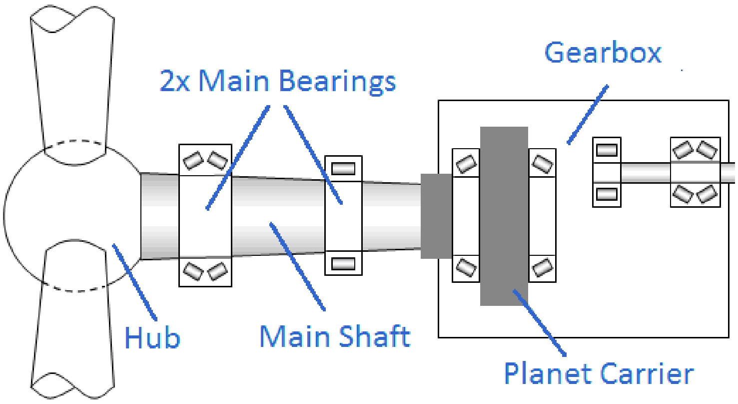

Figure 2.14 - The double bearing configuration [56]

An alternative bearing configuration is suggested by Alstom [57]. Alstom's PURE TORQUE® drive system, which was included in the company's Eco100 wind turbine, utilizes a pair of bearings that connect the rotor to a cast iron frame. The main shaft is then coupled to the gearbox through an elastic coupler which allows a certain degree of misalignment. Thus, torque transmission and load support are separated, and all the gravitational or bending loads are transferred to the tower structure as demonstrated in Figure 2.15 [58][59]. This way the main shaft and the gearbox are protected by hazardous loads and only the torque component is transferred to the gearbox, increasing reliability and extending gearbox life.

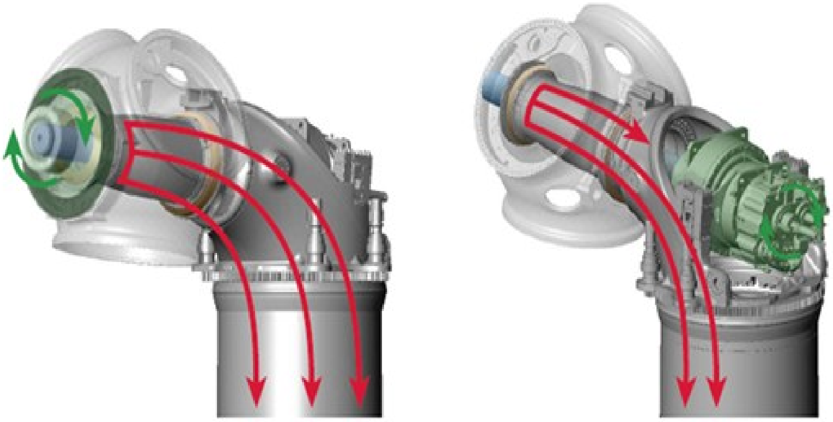

Figure 2.15 - Alstom Pure Torque® System directs bending loads to the tower structure [59]

In recent years a more compact, integrated bearing configuration that eliminates the main shaft has been developed for wind turbines [52]. Such configuration can be used for geared or direct drive systems, with the gearbox or the generator directly mounted on the outer side of the bearing, thus rotating at the same speed with the hub.

The elimination of the main shaft reduces the total mass of the nacelle and simplifies the design but increases concern regarding transmitted bending moments. To avoid loads being transmitted towards the drive train, SKF suggested a double row tapered bearing. In the Nautilus integrated design [60], dynamic loads are absorbed by the bearing and only the torque component is transmitted to the gearbox. The Nautilus bearing design was specifically designed for multi-megawatt offshore wind turbines. Figure 2.16 illustrates how the Nautilus design can be adjusted for geared or direct drive systems.

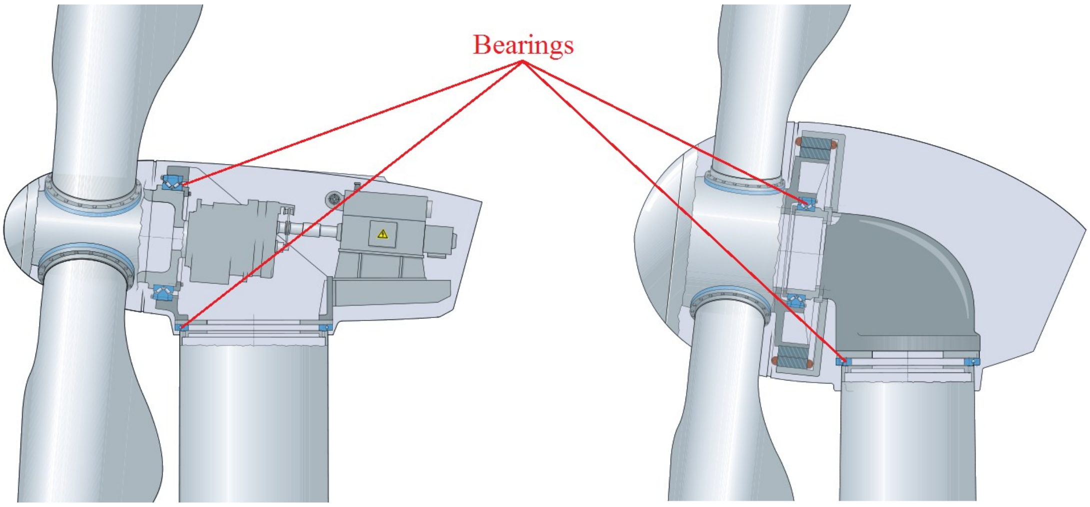

Figure 2.16 - Nautilus bearing: single bearing design for geared (left) and direct-drive (right) topologies for wind turbines [60]

2.4 Gearbox

The dominant drive train configuration among wind turbine manufacturers is that of a gearbox coupled with a high speed generator [43]. The gearbox is driven by the low speed main shaft and increases the rotational speed on its output through a set of gears. Typical modern gearboxes run at speeds of 1200 to 1800rpm. Gearboxes can be classified according to the number of stages they employ for increasing the rotational speed. The type and design of the gearbox has a significant effect on the generator's size and efficiency and on the reliability of the drive train [61].

Single-stage gearboxes usually consist of a planetary stage, with various numbers of outer gears, planets, which revolve around a centre gear, sun. An outer ring is required for the speed change (Figure 2.17). This enables them to obtain speed ratios up to 15:1 and average rotational speeds of 150 rpm [62]. Single stage gearboxes have fewer gears and bearings than multi-stage alternatives, an attribute that increases their reliability and efficiency.

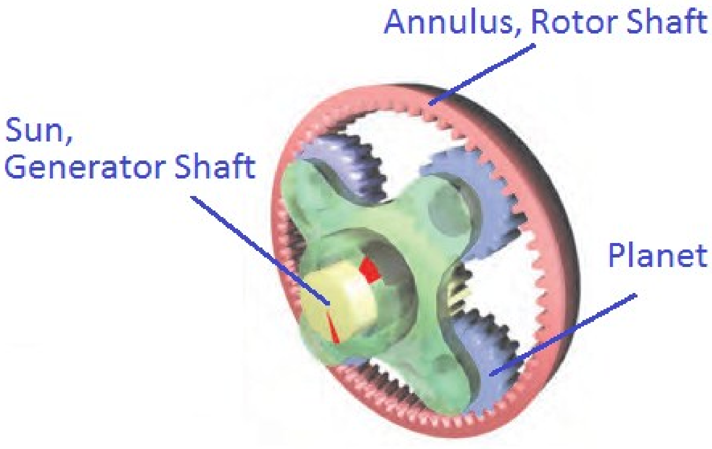

Figure 2.17 - Planetary gearing system [61]

Multi-stage gearboxes are the most common type of gearboxes for wind turbines. They are usually coupled to high speed generators such as the doubly-fed induction generator. Multi-stage gearboxes consist of a combination of planetary gear stages and additional high-speed parallel shaft helical stages. Speed ratios more than 100:1 can be achieved and average rotational speeds of 1500 rpm. Their designs are highly complex as manufacturers try to maximise the rotational speed output within the minimum volume. A typical three-stage gearbox with two planetary stages coupled with a single stage parallel shaft is shown in Figure 2.18.

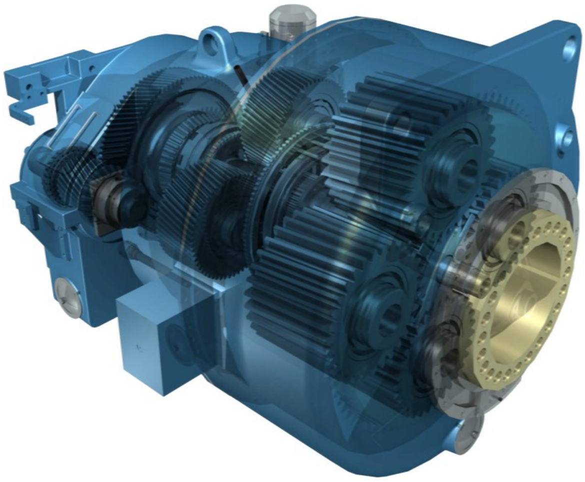

Figure 2.18 - Typical three-stage gearbox [63]

Gearboxes have proven to be the weakest link in modern wind turbines. According to the data presented in [64], gearbox breakdowns represent more than 20% of a typical wind turbine's downtime and are expected to experience a severe breakdown once every five to ten years. Furthermore, gearboxes require the longest downtime period in case of a failure compared to all other wind turbine components (Figure 2.19) [65].

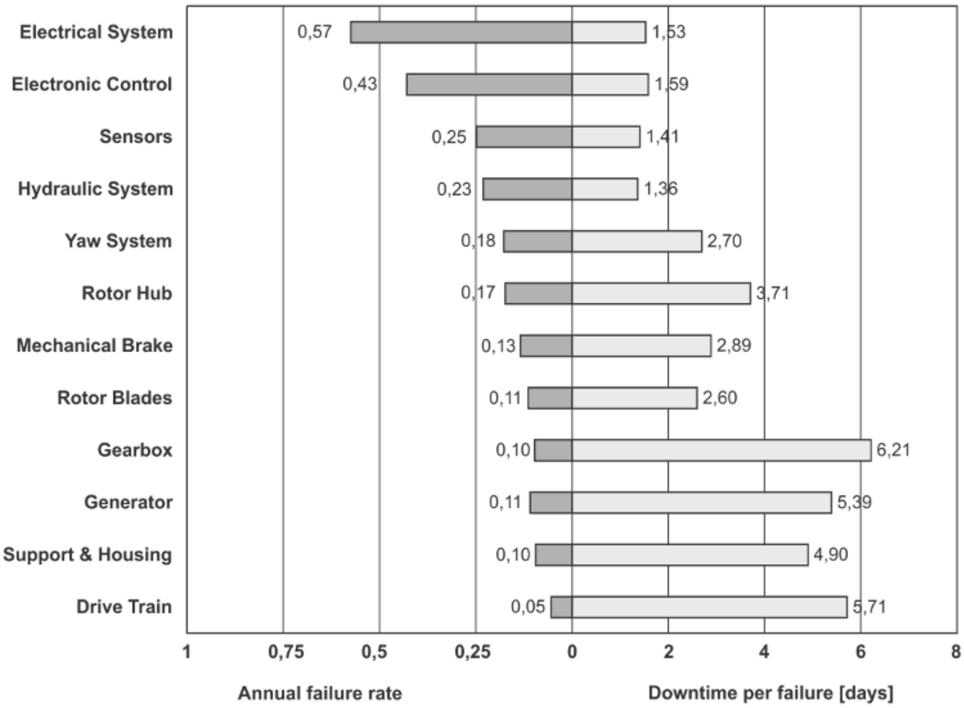

Figure 2.19 - Failure frequency and downtime period for wind turbine components [65]

These failure rates can be attributed to the random gusts of wind that create uneven loading on the rotor blades. As discussed in section 2.4, the bending moments created on the rotor side will generate axial loads on the rotor shaft that if transmitted to the gearbox can misalign the teeth of the gears. This misalignment burdens the teeth and can trigger a chain reaction of further misalignments and wear of the gearbox teeth that may eventually break down the gearbox [43]. To reduce the risk of a failure, condition monitoring of the gearbox is required [66]. Early detection of faults can prevent gear tooth breakage or bearing misplacement.

As wind turbines with power output greater than 2MW are developed for offshore applications, health monitoring of the gearbox becomes more significant. The increased rotor size and the stronger winds increase the criticality of the gearboxes due to the increased load conditions. In order to increase reliability, manufacturers are now turning to alternative drive train solutions for power take off, such as medium-speed geared and direct drive.

2.5 Generator

The generator of a wind turbine is the key component responsible for converting the mechanical power of the rotating shaft into electrical. Various generator concepts have been developed over the years in the wind turbine industry in an attempt to create a reliable machine and increase the energy captured, improve the produced power quality, while minimizing the total cost of the machine. The generator systems that are more commonly used for wind power generation are discussed in [18, 26, 41, 52, 64, 65, 66].

The constant speed squirrel cage induction generator (SCIG) was the first machine to dominate the wind energy market (Figure 2.20). The rotor of a SCIG is made of a ring of conducting bars, short-circuited at both ends by rings forming a “squirrel cage”. The “squirrel cage” is driven by a multi-stage gearbox. This generator type is cheap to build and robust against power swings caused by turbulent wind variation. On the downside they produce power of low quality with much ‘flicker’ and are passive systems that cannot offer ancillary services to the grid.

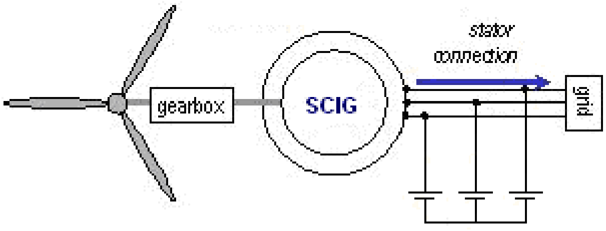

Figure 2.20 - The SCIG system

As the power output of wind turbines reached the MW scale and their penetration to the grid increased, manufacturers started to look into different power take off systems. Constant speed generators were dropped by many manufacturers after the late 1990's for variable speed generators (Figure 2.21). Variable speed generators offer higher efficiency since they can reach peak energy production at a wider range of wind speeds, leading up to 5% more energy capture, lower noise levels and a better output power quality with less 'flicker' for the grid [21]. The main technologies used for variable speed wind turbine generators are that of the Doubly Fed Induction Generator (DFIG), the Geared Brushless Generator and the Direct Drive (DD) system.

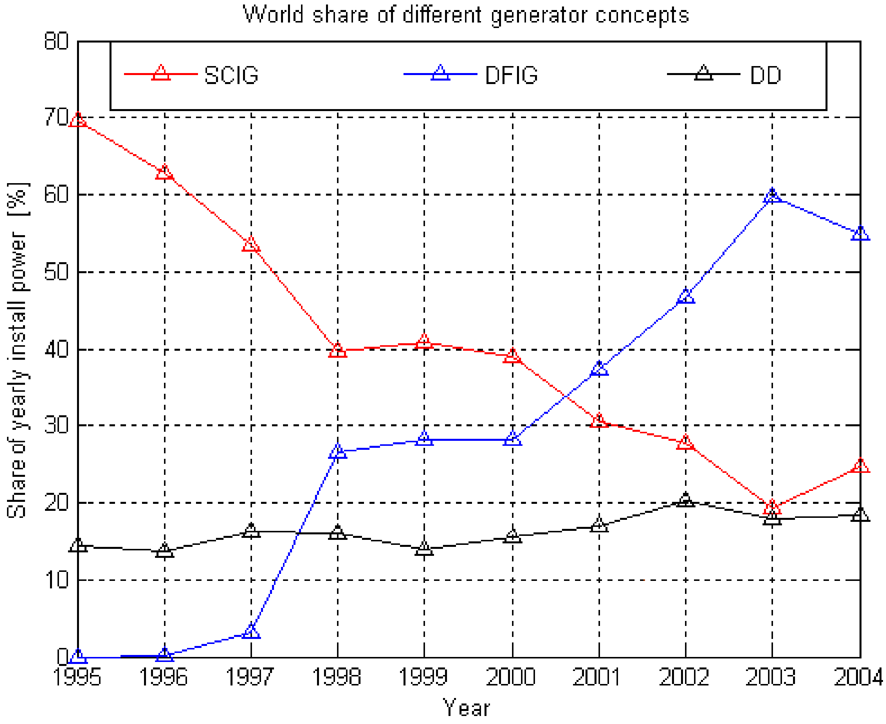

Figure 2.21 - World market share for different wind turbine generator types [18]

Variable speed DFIGs, driven by a multi-stage gearbox, quickly became the work horse of the wind industry for the last decade, getting more than 50% of the total market [16][18]. In a DFIG system, the stator is directly connected to the grid while the rotor is decoupled from the mechanical rotor frequency through the use of power converters and slip rings (Figure 2.22). This configuration enables the rotor to have a different electrical frequency from the mechanical one, thus making variable speed operation possible. Vestas Wind Systems [19] has risen as the world's largest manufacturer of installed DFIG turbines driven by a multi-stage gearbox.

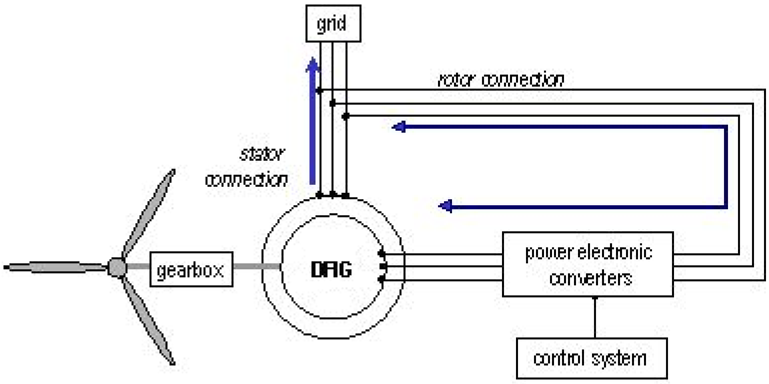

Figure 2.22 - The DFIG system

An alternative geared topology is that of the Geared Brushless Generator (Figure 2.23). The gearbox can be single or multi-stage and the brushless generator with permanent magnets (PM) mounted on the rotor or with an induction “squirrel cage”. This generator type is more efficient compared to the DFIG system and more flexible to grid faults. On the other hand the required converter can be bigger in terms of ratings and therefore more expensive.

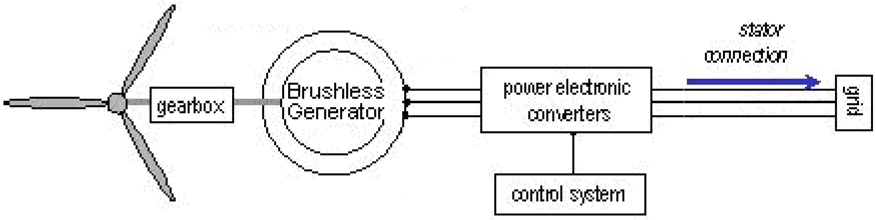

Figure 2.23 - The Geared Brushless Generator system

Unlike geared topologies, direct drive machines operate at low rotational speed, moving together with the hub. The gearbox is omitted from the drive train of such a machine along with the losses and maintenance issues related to it. Since this generator operates at low rotational speed, noise from this system is reduced. The generator of the DD system is completely decoupled from the grid, offering better energy yield and advanced control against wind fluctuations and grid faults (Figure 2.24). Excitation on the rotor can be provided either electrically (EEDD) or with permanent magnets (PMDD). The main drawback of DD generators is their increased size that makes them more difficult to manufacture and install compared to geared systems and this increases their overall cost.

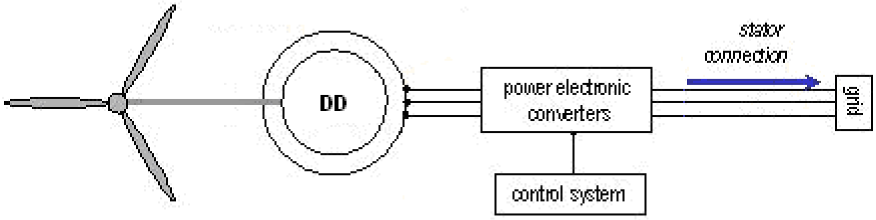

Figure 2.24 - The DD system

Despite their large size and cost, direct drive configurations gained a large percentage of the market since 2001 due to their advanced reliability and energy yielding characteristics [18]. The commercial success of the DD system that Enercon [20] developed proved the viability of such a drive train and attracted other major industry companies to exploit the possibilities of such a configuration. GE recently acquired Scanwind in order to expand on the PMDD generator market [71]. The 4.0MW proposed design was specifically built for offshore purposes (Figure 2.25) [63]. Siemens (3.0 MW) has also turned to PM excitation for their direct drive wind turbine systems [70]. Goldwind (1.5-2.5 MW), STX Windpower (1.5-2.0 MW), Emergya Wind Technologies (0.5-2.0 MW), Vensys (1.5-2.5 MW), Leitwind (1.5-3.0 MW) and XEMC Darwind (5.0 MW) are some of the wind turbine companies that manufacture PMDD generators in the MW scale [68, 71-75].

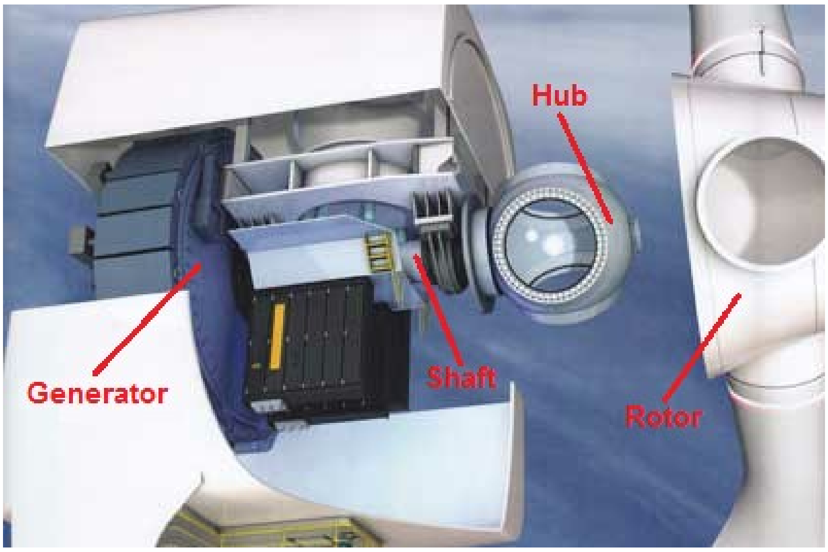

Figure 2.25 - The interior parts of the 4MW GE (former Scandwind) wind turbine [63]

Four out of ten top wind turbine manufacturers worldwide are now producing direct drive generators according to Table 2.1 [67].

Manufacturer	**Concept**	**Power Range**
Vestas (Denmark)	DFIG PM Geared Brushless	850 kW - 3.0 MW 3.0 MW
General Electric (US)	DFIG PM Geared Brushless PMDD*	1.5 MW 2.5 MW 4.0 MW
Sinovel (China)	DFIG	1.5 MW - 3.0 MW
Enercon (Germany)	EEDD*	300 kW - 7.5 MW
Goldwind (China)	PMDD*	1.5 MW - 2.5 MW
Gamesa (Spain)	DFIG PM Geared Brushless	850 kW - 2 MW 4.5 MW
Dongfang (China)	DFIG	1 - 2.5 MW
Suzlon (India)	SCIG	600 kW - 2.1 MW
Siemens (Germany)	SC Geared Brushless PMDD*	2.3 MW - 3.6 MW 3.0 MW
Repower (Germany)	DFIG	2.0 MW - 6.0 MW

Table 2.1 - Top 10 turbine manufacturers of 2009, employed generator concepts and power outputs [67]

2.6 Grid connection

Wind farms include a large number of wind turbines installed in arrays to create a wind power plant. In most cases, each individual wind turbine can have different power output and power take off system from the rest. Nevertheless, all outputs are collected at the collector bus of the wind power plant and the accumulated power is then fed into the grid (Figure 2.26) [77].

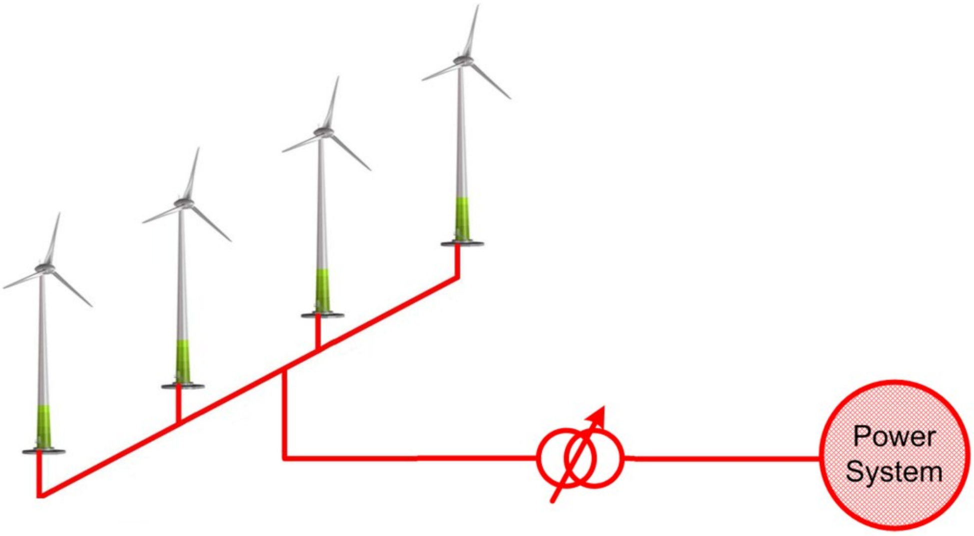

Figure 2.26 - Wind turbines connected to the grid via a collector bus

Before the 1990s when wind power penetration was relatively small, wind plants were treated as a negative load and were not expected to provide support for the grid. In case of a grid disturbance, wind farms were simply disconnected from the grid [78]. As wind turbine units increase in power output and the number of installed wind turbines increases significantly over Europe, grid operators have imposed grid code requirements that wind farms must comply with in order to get connected to the grid [79]. Wind power plants are now required to provide ancillary services to the grid that include frequency and voltage regulation and deliver active or reactive power to the grid during fault conditions [78][80].

Multi-MW coal, gas or nuclear power plants employ large synchronous generators for the production of energy that are directly connected to the grid. Such plants have a very controllable active and reactive power output that can be adjusted according to the demands of the grid. Wind power plants on the other hand are not that easy to control, since the energy produced depends on the wind characteristics and cannot be predicted or programmed. Furthermore, harmonics that should not be fed to the grid are often created due to wind fluctuations.

The first generation of induction machines could not offer quality ancillary services to the grid since they are completely passive systems that draw reactive power from the grid instead of controlling it [78]. Variable speed DFIGs on the other hand allowed active and reactive power control through the use of advanced power electronics and converters [81]. The converter includes two three-phase ac-dc converters linked by a dc capacitor line, allowing vector control of the active and reactive powers of the machine [82]. Geared Brushless Generators offer a less complex grid-fault control but the converter rating is larger compared to that of the DFIG system, thus more expensive, and the losses of the system increase since all the generated power is processed by the converter [67].

While DFIGs have their stator's winding directly connected to the grid, synchronous direct drive generators are completely decoupled from it. An ac-dc-ac link is used to achieve that. The ac-dc link creates a constant dc current that is then fed to the dc-ac link to create a fixed frequency output that can be provided to the grid. The generator link also acts as energy storage with the help of capacitors, while the grid side controls the amount of active and reactive power that is delivered to the grid, preventing penetration of harmonics at the same time [82][83]. Direct drive machines can therefore provide better power quality with a flexible control method and quick response to wind or load variation [67][83].

The wind power plant in Estinnes of Belgium is proof of the advanced grid characteristics that direct drive generators can provide. Eleven units equipped with Enercon's 7MW prototype generators have been connected to the grid during the European 7-MW-WEC-by-11 project [84]. The wind farm can operate as any other conventional power plant and provide high level ancillary services to the grid through the use of completely controllable links. The specific wind power plant can successfully deliver reserve active or reactive power for voltage control even at still air or provide a highly dynamic reactive current while riding through a voltage dip [85].

Modern power converters are based on the technology of insulated gate bipolar transistors (IGBT). Such power converters were too expensive to manufacture when wind turbine systems started to develop over two decades ago, but their price has dropped as their technology matured [83].

2.7 Conclusions

As the penetration of wind energy into the grid increases, so does the debate about the more suitable drive train. In this chapter the parts that compose a wind turbine system were presented. The main two drive trains currently competing in the market are geared and direct drive. Direct drive generators seem to offer a number of advantages in terms of simplicity of the drive train, reduced maintenance issues, annual energy yield compared to their geared counterparts. These characteristics are essential for the development of offshore wind farms where large power outputs are required and maintenance is difficult to provide. Their large size though is the main issue holding back this generator system. It would be therefore worthwhile to investigate the proposed direct drive technologies and try to find out which one offers the greatest potential in terms of mass and cost reduction, while providing the maximum energy yield. The following chapter will focus on the direct drive generator concept and guide the reader through the various technologies that have been suggested in the literature.

Chapter 3

Direct Drive Generators

3.1 Introduction

Large scale direct drive generators have attracted the attention of wind turbine manufacturers over the last few years as an alternative to geared systems. In a direct drive system the gearbox is removed from the drive train and the generator is directly coupled to the hub of the wind turbine (Figure 3.1). They both rotate at the same speed which typically varies between 8-15 rpm.

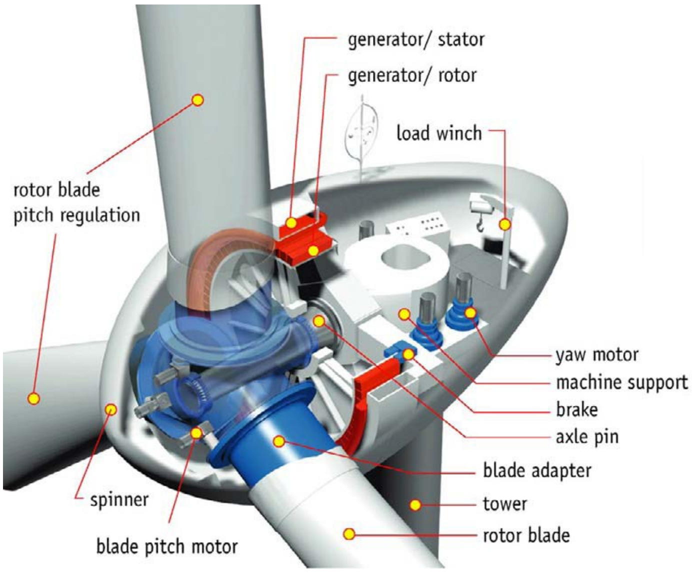

Figure 3.1 - The direct drive system [67]

Elimination of the gearbox has several benefits such as reduced noise levels, simplification of the drive train that increases reliability, reduced losses due to the reduced steps in energy conversion and lower maintenance cost [55][64]. Costly gearbox maintenance issues that can cause long downtime periods like oil replacement, gearbox failures or gearbox replacement are avoided [62, 64, 65]. Furthermore, the decreased number of bearings required for direct drive systems and the fewer moving parts gives a more robust machine with increased lifetime [26].

These advanced characteristics draw a number of manufacturers towards this system which now represents 20% of the sold wind turbines worldwide [18].

In order to compete with the high speed geared generators, direct drive machines need to attain high torque levels. (3.1) describes the relationship between the power output of a rotating machine with given speed and the required torque.

$$P = \omega T \tag{3.1}$$

where P is the power output (W), ω the angular velocity (rad/s) and T the rated torque of the machine. When ω is low, T needs to increase to create the same power output. (3.2) gives the torque of a rotating machine.

$$T = 2\pi R^2 l F_d \tag{3.2}$$

where R the radius of the machine (m), l the axial length (m) and F_d (Pa) the shear stress applied on the machine's structure due to the interaction of the machine's magnetic field and the generated currents (Figure 3.2).

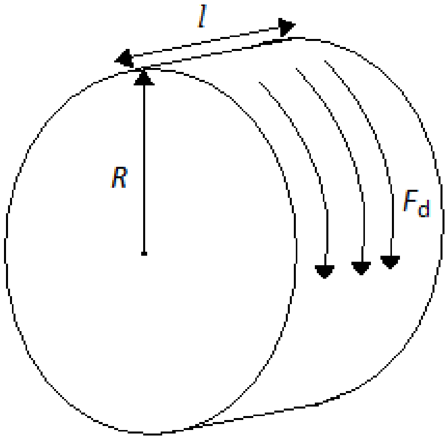

Figure 3.2 - The dimensions of a rotating machine and the acting shear stress

The combination of (3.1) and (3.2) leads to the conclusion that since direct drive machines operate at a low rotational speed, given a fixed axial length and shear stress, it would be necessary to increase the machine's diameter in order to achieve the required torque levels. Thus, direct drive machines need large diameters for achieving high power outputs. This attribute makes them very demanding in raw materials and expensive. Their very large size makes them also heavy and difficult to build, transport and install.

Although the structural loads applied to these machines do not differ from conventional wind turbine generators, it is their size that increases the magnitude of these forces and makes them so structurally demanding. A direct drive generator's structure has to be stiff and robust in order to maintain the small airgap clearance between the rotor and the stator against the various structural forces and hold the electromagnetically active materials in place against the attraction forces and gravity at the same time [86]. McDonald outlined that the structural mass for a direct drive generator with nominal output of 5MW can reach up to 80% of its total mass [87].

Different direct drive configurations have been suggested in the literature in an attempt to produce a highly efficient machine with reduced structural mass. The aim of this chapter is to present the proposed direct drive generator topologies for wind turbines and outline the ones with the highest potential to produce large power outputs at the least possible mass.

3.2 Excitation methods

An AC synchronous machine can be electrically excited or permanent magnet excited. A switched reluctance generator (SRG) has single electrical excitation on the stator without any excitation on its rotor.

3.2.1 Electrically Excited Direct Drive generators (EEDD)

Magnetisation of the rotor poles of an EEDD generator is provided by a DC source. DC excitation is usually provided via slip rings and brushes. Brushless DC excitation is also possible by employing a rotary AC exciter connected to the rotor through a bridge rectifier, but this arrangement is less common for wind turbine generators [88].

The rotor poles of an EEDD machine can be salient or cylindrical with the former being most commonly used. In any case, the rotor poles of the EEDD generator should be large enough to provide adequate space for the excitation windings. The stator of an EEDD is similar to that of the induction generator with 3-phase coil windings wrapped around its iron core [90].

A power converter is utilised to process the generated power and connect the EEDD generator to the grid. The amplitude and frequency of the voltage, as well as the active and reactive power of the machine can be fully controlled even at fault grid conditions. Furthermore, the generator speed can be fully controllable for a wide range of wind speeds [27][85].

Electrically excited synchronous machines are robust and simple to construct. Furthermore, for large power outputs, EEDD machines have a better power factor and efficiency compared to that of an induction machine. However, the need for constant DC current supply to the main field winding leads to additional losses through the form of generated heat, reducing overall efficiency [90]. On the other hand, the external electrical excitation can be adjusted according to the occurring wind conditions and keep the voltage at rated values for low or high wind speeds.

The EEDD technology has matured over the last decade and is now the dominant technology for low speed direct drive applications in the wind turbine market [90]. Enercon is the main supplier of this generator type, representing more than 15% of the total market and 75% of the installed direct drive applications [18]. Enercon's prototype direct drive system E-126 [20] (Figure 3.3) with a blade diameter of 127m and generator diameter in the order of 12m can reach a power output up to 7.5MW. MTorres also produces EEDD systems with a power output up to 2.5MW [91].

Figure 3.3 - Enercon E-126 7MW WEC [84]

3.2.2 Permanent Magnet Direct Drive generators (PMDD)

Electrical excitation of the rotor poles of a direct drive machine, brushless or not, can lead to resistive heat losses in the system. These losses decrease the system's efficiency and may cause maintenance issues. To avoid the heat transfer in the direct drive system and the complicated cooling schemes that are required, a number of manufacturers have turned to systems with permanent magnets for their characteristics, such as the reduction of the required active material for the same airgap diameter and the increased energy yield [30].

In a PMDD machine, the rotor poles are made of permanent magnet material, therefore no external power supply is needed. This attribute releases the generator from excitation losses and decreases the heat developed in the system. The energy yield and the overall efficiency are thus increased while the absence of slip rings increases the reliability of the machine. Smaller pole pitches can also be used, reducing the size of the generator [92]. On the downside, PM materials are expensive and difficult to handle in manufacture [67]. The stator of a PMDD is usually identical to that of an EEDD generator, but alternative stator topologies have been proposed as well [89][93]. A full-scale power converter is required for their connection to the grid. Advances in power electronics have decreased the cost of such power converters and allow PMDD generators to produce a clean power output [82][83].

The rotor poles of a PMDD machine are made of rare earth materials such as Samarium-Cobalt (SmCo) or Neodymium-Iron- Boron (NdFeB) that exhibit high magnetic energy densities within a small volume and geometry. SmCo magnets are mainly used in high temperature applications. Vilsboll *et al.* concluded in favour of the NdFeB magnets as they produce a greater remanent flux density - 1.2T instead of 1.0T - and can reduce the overall mass and price of the PMDD generator even further [94].

The originally high cost of PM materials prevented many manufacturers from employing such excitation for their machines. Nevertheless, magnet prices decreased between 1995 and 2005 almost by a factor of 10, increasing their use in a number of commercial or military applications [95]. However, 95% of the mined rare earth magnets come from China. The current monopoly that China holds, in addition with today's increased demand, has raised the prices once more and created a generalised uncertainty regarding their extended use. Nevertheless, the future of PMDD generators seems to be promising as the number of sites mining the rare earth materials used in permanent magnets increases [95].

Permanent magnet excitation produces a robust and simple machine with superior efficiency and torque density and decreased maintenance and life cost. The drop in prices of PM materials and power converters during the last decade encouraged a number of developers to turn to this excitation type for direct drive machines [60, 67-73].

Due to the rapid commercial and military interest that PM technology has experienced over the last decade, the industrial base for high power PM machines has also increased. This can be also verified by the increasing number of PMDD manufacturers who have established the PM synchronous generator as a prime candidate for direct drive wind turbine applications [88].

3.2.3 Switched reluctance direct drive generator

The operating principle of the switched reluctance generator (SRG) is based on the tendency of a magnetic field to follow the path of least reluctance. In a SRG, the rotor of the machine “tries” to align with the stators rotating magnetic field to obtain the lowest magnetic resistance, and therefore the lowest reluctance [88][98][99].The rotor of the SRG is made of ferrous material that carries the flux from the stator with salient poles on its circumference. There are no coils on the rotor and hence there is no need for brushes or PM poles, resulting in lower manufacturing costs. The stator has wound-up salient poles which are energised with the help of a power electronic converter when the salient poles of the rotor are away from their aligned position due to rotation (Figure 3.4). The switched nature of this machine makes it suitable for variable speed operation since it can lessen the stress within the system due to variations in the load thanks to its low inertia.

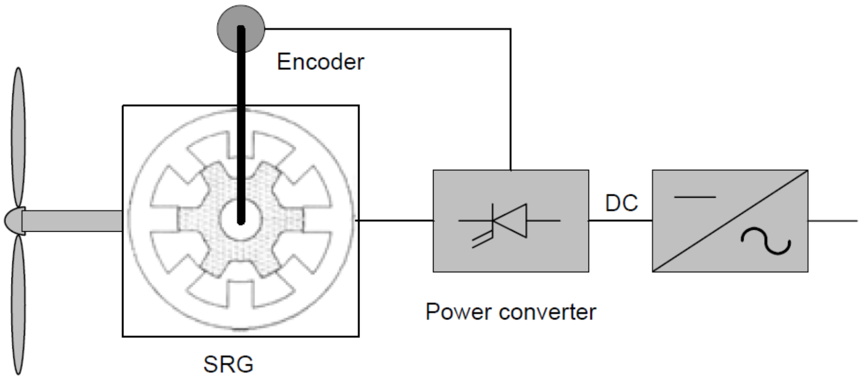

Figure 3.4 - Switched reluctance generator in a wind turbine [99]

SRGs have been considered for direct drive wind turbine generation because it is simple and cheap to manufacture, highly robust and easier to cool [100]-[102]. On the downside, they have a sophisticated control for their phase currents and a relatively low torque density. Therefore, in order to reach the same torque and power output with that of EE and PM direct drive machines, SRGs have to be significantly larger in size and much heavier. This major disadvantage has prevented manufacturers from considering the reluctance machine as an option for direct drive power take off systems for wind turbine applications [88].

3.3 PMDD generator topologies

PMDD generators seem to have the largest potential for onshore and offshore direct drive wind development for their advanced characteristics compared to EEDD and SRG machines. Nevertheless, their large size and heavy structures remain the fundamental issue. A vast number of different PMDD topologies have been proposed in the literature in an attempt to produce machines with high torque/mass or power/cost ratio. The easiest way to categorise them is according to the orientation of the magnetic flux as it crosses the airgap within the machine, leading to radial flux (RF), axial flux (AF) and transverse flux (TF) topologies. Depending on the stator's core design, the machine can be slotted or stottless [93]. Another way to categorise PMDD generators is by the existence of iron in the stator's core or not, leading this way to iron-cored or "aircored" machines accordingly [29][103].

3.3.1 RF PMDD machines

In a RF machine a magnetic flux flows radially across the airgap. The iron-cored RF machine with surface mounted permanent magnet poles rotating inside the stationary armature windings is the most common topology for PMDD generators for its structural stability and robust design (Figure 3.5). The slotted RF PMDD machine is the most conventional one, as it combines the structural characteristics of an EEDD machine with the advanced magnetic characteristics of the permanent magnets. The reduced mass for high torque ratings has established RF machines as the most common option for industrial PMDD generators for wind applications in the MW scale [18, 29, 64, 82, 83]. However, alternative topologies have been suggested with non-conventional permanent magnet placement, rotor position or stator core design.

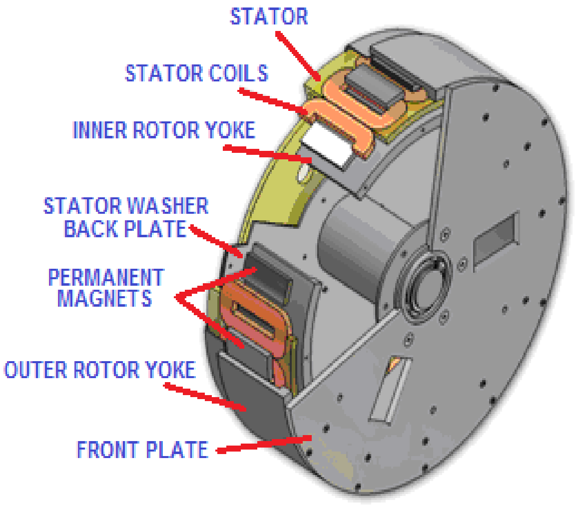

Figure 3.5 - The RF PMDD machine [104]

Spooner *et al*. suggested flux concentration methods for decreasing the required active material and total cost of RF PMDD machines [105]-[107]. Flux concentrators are active substructures that allow a higher flux density in the airgap than the remanent flux density of the permanent magnets. Steel concentrators also house the permanent magnets on the rotor and transfer the torque and thermal energy to the support structure (Figure 3.6). This topology allows ferrite magnets to be used which are much cheaper than NdFeB magnets [108][109]. However, burying the magnets together with the flux concentrators is difficult to handle and creates a complex structure with manufacturing issues.

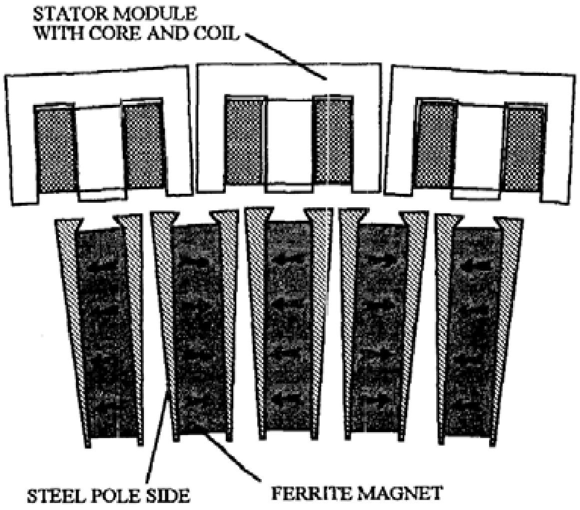

Figure 3.6 - The RF PMDD machine with flux concentrators housing the PM material [106][107]

The rotor and the stator of a RF PMDD can be alternatively positioned with the rotor on the outer side of the machine (Figure 3.7). Outer rotor RF PMDD generators permit a larger airgap diameter at the same dimensions of a conventional inner rotor RF PMDD machine [110]-[113]. This attribute is of benefit to the machine's efficiency as it allows a larger number of magnetic poles to be used. On the downside, they require stiffer structures that increase the total mass and complexity. Furthermore, complex cooling systems such as liquid cooling is necessary for their operation as they do not allow the natural cooling of the stator, an attribute that introduces additional reliability issues and maintenance cost [67].

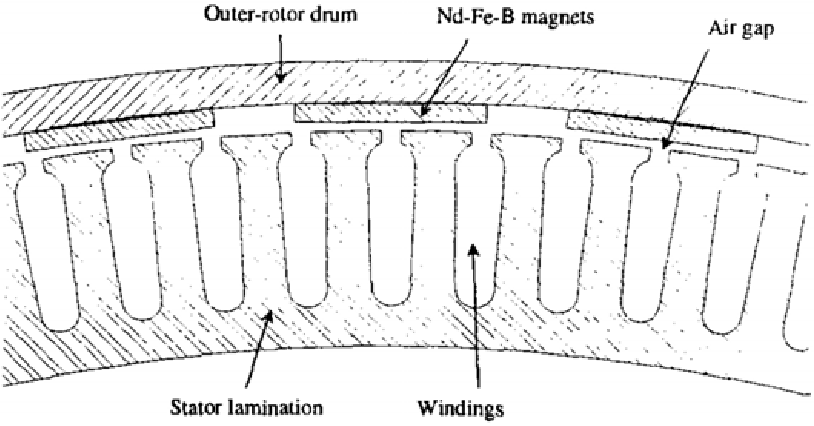

Figure 3.7 - Outer rotor RF PMDD machine [113]

In a conventional machine, the copper windings of the stator are placed in the stator's vertical slots. In a slotless machine however, the windings have a toroidal shape and are placed in a flat recess. A slotless stator topology with a double rotor was suggested by Korouji in [114]. This topology is characterised by short end windings that reduce the overall mass and cost of the active material. The absence of teeth reduces the iron losses in the machine and increases the overall efficiency [115]. However, the eddy current losses in the coil are increased because they are situated in the main airgap field.

Another suggested way to reduce the cost of RF PMDD generators is to use fractional pitch windings as illustrated in Figure 3.8 [116]. This topology is expected to reduce cost due to the lower number of simpler coils around the stator's teeth compared to conventional complicated end windings. On the downside, more eddy current losses in the magnets and the back iron are generated in this machine type due to an increase in the number of sub harmonics.

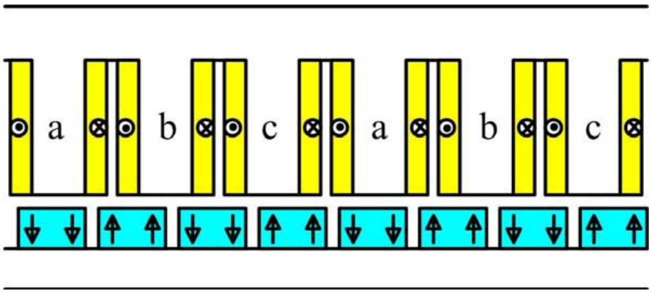

Figure 3.8 - Sketch of a cross-section of eight poles of a permanent-magnet synchronous machine with a cheap fractional pitch winding [67]

Spooner *et al*. proposed an outer rotor topology for large direct drive wind turbines with an ironless stator and a pair of spoked wheels that carry the structure [117]. The machine's cross section is depicted in Figure 3.9. The elimination of iron from the stator releases the structure from the large attractive forces and effectively reduces the required stiffness of the machine, bringing down the mass to that of a geared generator. Manufacture is also simplified and cogging torque is reduced to zero. On the downside, without a stator core the magnetic flux cannot easily cross the airgap, thus larger volumes of permanent magnet are required. Eddy current losses in the windings are also likely to be higher for such machine. Furthermore, the suggested spokes can be aerodynamically inefficient for large diameters.

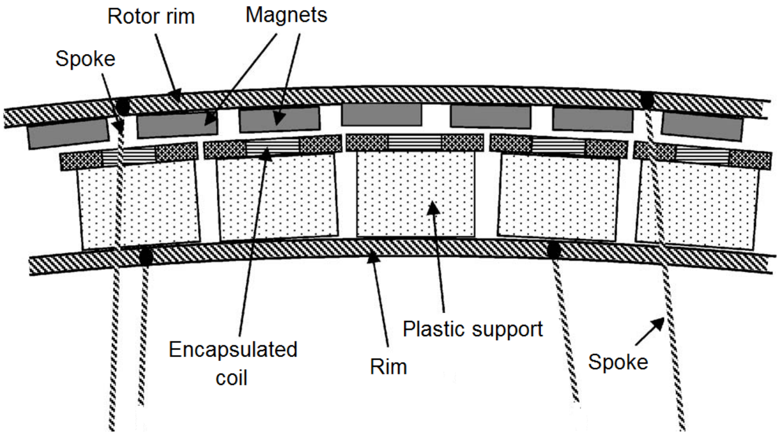

Figure 3.9 - Cross section of suggested ironless RF PMDD machine [117]

Mechanical support that takes the loading path from the generator structure and reduces the required stiffness of the machine has been reported in the literature for RF PMDD machines [118]-[122]. In these concepts, bearings are placed near the airgap, increasing the load capacity of the structure and contribute to airgap management. Thus the required structural mass of the rotor and stator can be reduced. Versteegh suggested using large diameter bearings near the airgap for the STX 72 machine (former Harakosan Z72) [118]. Although these bearings would reduce the total mass of the direct drive generator, the required stiffness for large diameters would make them heavy and expensive [120]. Engstrom and Lindgren suggested wheels at the airgap that are supported on a rail which is embedded in the stator structure (Figure 3.10) [119]. The NewGen design resulted in a significant reduction of the mass and the stiffness of the direct drive generator. However, the large number of wheels running at high speeds would raise the bearings' temperature and create maintenance and reliability issues due to vibration.

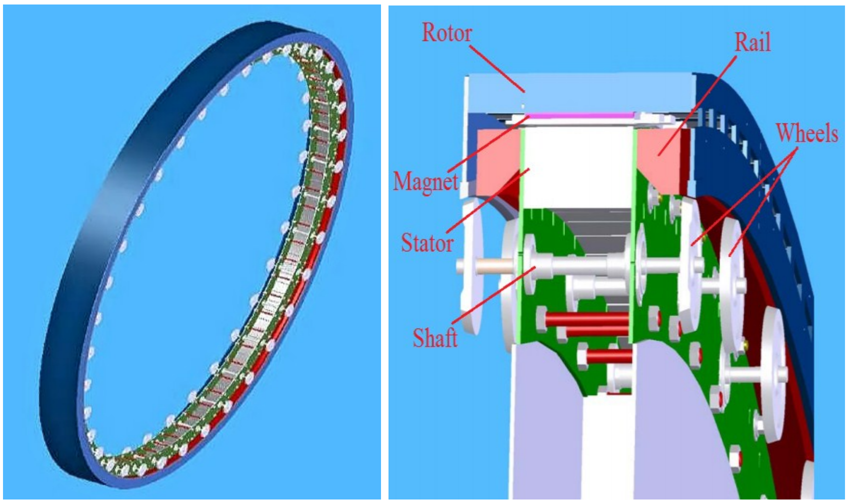

Figure 3.10 - The NewGen generator concept [119]

Shrestha *et al.* suggested replacing the bearing wheels with non-contact magnetic bearings that levitate the machine, eliminating the unreliable gear wheels at the airgap (Figure 3.11) [121]. Torque carriers and a mechanical bearing are also employed. This assembly is expected to reduce the structural mass of a 5MW RF PMDD generator by more than 40%. Since magnetic bearings require active control, this concept would introduce unnecessary control issues and increase the total cost of the direct drive machine due to the expensive magnetic bearings [122].

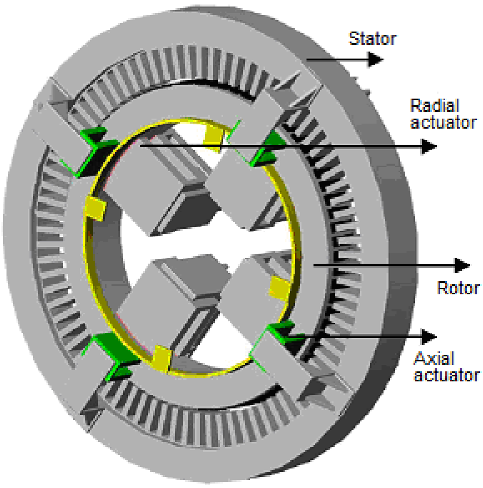

Figure 3.11 - View of the magnetic bearing setup for an iron-cored RF PMDD generator [120]

Despite the novelty in all the alternative concepts, a number of researchers who have compared the various RF designs conclude in favour of the conventional RF PMDD machine with mounted permanent magnets on the surface of the rotor for its structural simplicity, the high energy yield, torque density and reliability and the reduced manufacture or maintenance costs [25, 29, 82, 83, 104, 118].

3.3.2 AF PMDD machines

In an AF machine the magnetic flux flows in the axial direction across the airgap. Disc structures are most commonly employed. The slotted AF PMDD machine with the PM material mounted on the rotor and the stator facing the rotor is the basic structural design for this generator type (Figure 3.12). Their characteristics and technological evolution, from the early 80s until now, is described in [123]-[128].

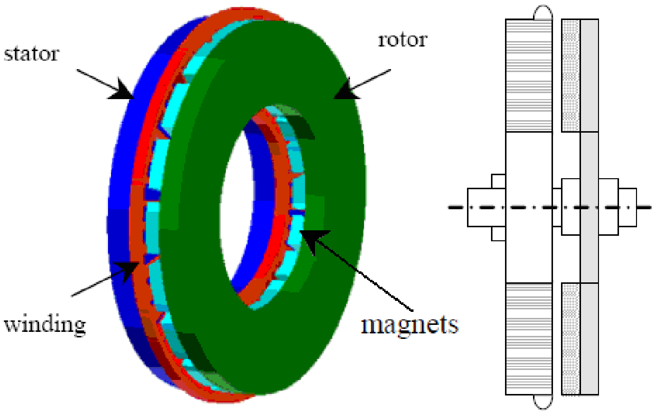

Figure 3.12 - Single-sided slotted AF PMDD machine [129]

Slotted AF PMDD machines offer a compact design with relatively low cogging torque and noise, short axial length and a high torque density [130]-[134]. In his extended comparison among different PMDD generator technologies, Dubois *et al.* concludes that slotted AF PMDD machines have a lower cost/torque ratio compared to conventional RF machines [108].

A fundamental issue about single-sided AF machines is the large magnetic attraction force between the PM disc and the iron stator which increases the stiffness requirements for this machine type. An additional rotor or stator is commonly used to form a double sided machine in which the forces are balanced, preventing the rotor from moving towards the stator and vice versa (Figure 3.13). This leads to machines heavier than their RF counterparts [135].

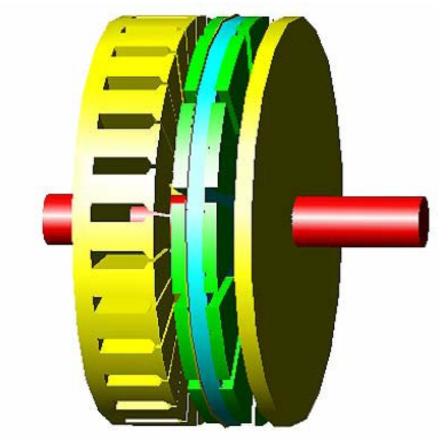

Figure 3.13 - Single-sided slotted AF PMDD machine with stator balance [135]

Alternative double-sided topologies with a double stator or a double rotor structure have been proposed in the literature for slotted AF PMDD machines. Bang made a structural comparison among the slotted AF designs for large power outputs and concluded that the double-stator design with permanent magnets mounted on both sides of the rotor seems to be a lighter slotted topology compared to single-sided or double-rotor topologies [89] (Figure 3.14).

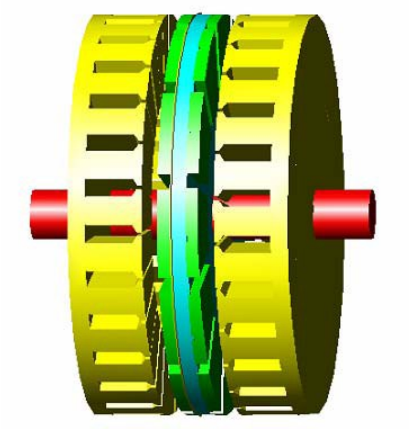

Figure 3.14 - Double-sided slotted AF PMDD machine with double-stator [135]

However, the complicated core designs make slotted AF machines difficult to manufacture compared to RF PMDD machines. In addition, a second magnetic flux path that moves along with the main axial flux and is both radially and axially oriented is created in such topologies due to magnetic flux leakage [129]. The resulting complex three-dimensional electromagnetic design is hard to calculate and makes it difficult to accurately predict the performance of such machines. These attributes in addition to the difficulty to maintain the airgap in large diameters and the complicated cooling systems that are required make slotted AF PMDD machines even less favourable [88]. An efficient way to minimise these characteristics is the removal of the stator's teeth from the structure.

The slotless AF PMDD generator with toroidal windings (TORUS) is described Spooner and Chalmers in [93] and [136]-[139]. The stator of TORUS consists of a stack of laminated steel with the windings wrapped around its core in a toroidal manner. A double-sided structure with a single stator between two rotors with permanent magnets mounted on them is the preferred topology for such a machine (Figure 3.15).

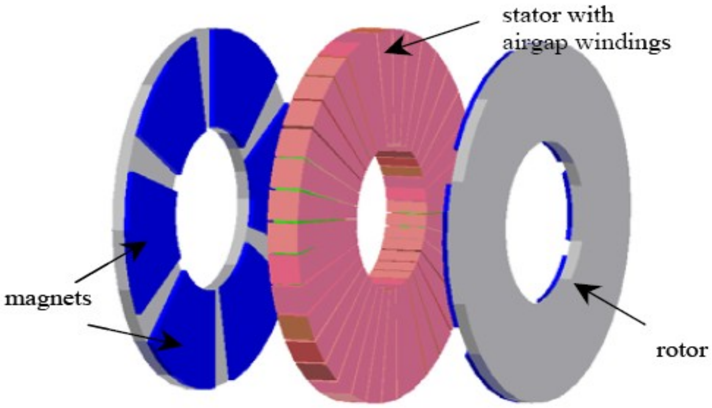

Figure 3.15 - The double-sided AF PMDD TORUS machine [129]

The slotless stator design offers short end windings, which reduce copper losses, increases the overall efficiency and creates a more compact design with a shorter axial length that is easier and cheaper to manufacture [129][135][136]. Effects due to the presence of the slots like cogging torque, flux ripple and high frequency rotor loss are eliminated. In addition, the TORUS concept has twice the torque/mass ratio of a conventional RF PMDD machine due to the reduced structural mass. However, this design is embedded with a small power density, making necessary the use of large outer diameters and thicker magnets for compensation [135]. TORUS has therefore a high cost/torque ratio which can be twice as large as that of a common RF machine for any given diameter [108]. Thus this configuration would not be cost effective for high power rated wind turbines with large diameters.

Ironless - or “aircored” as they are more commonly referred to - AF PMDD machines have also been suggested for wind applications [29]. The double-sided topology with two rotors and a stator is also favoured for this generator design. The stator structure is eliminated in this case and the conducting material is embedded in a pocket made of non-magnetic material such as glass fiber reinforced epoxy [122]. An ordinary rotor is employed with the permanent magnets mounted on its disc. The rotor and stator structures are relieved from maintaining the airgap clearance against strong attraction forces in such configuration, leading to a more compact and lightweight design that is easy to manufacture and assembly. The efficiency of the generator is also increased since the cogging torque and possible iron losses are reduced to zero [140]. An aircored arrangement leads to very low machine inductances and negligible armature reaction compared to TORUS machines [141]. On the downside, without an iron core to aid the movement of the flux across the airgap, larger outer diameters and greater volumes of permanent magnets are required to establish the necessary flux density in the airgap [89].

TORUS and aircored machines can be constructed with multiple stages for application with small diameter and high torque requirements. Multistage AF PMDD topologies are reviewed in [129] and [142]-[146]. To create '*n*' stages in a machine, *n* stators are placed between *n*+1 rotors that are mounted on the same shaft.

A three stage TORUS design is illustrated in Figure 3.16. However multistage configurations would have to compensate for the large attraction forces in the case of an imbalance in the airgaps on either side of the stator. Even for aircored multistage machines, there will be a force imbalance between the outer rotors and the stators. In addition, the small flux density in the airgap should be significantly improved for large power output applications and the structure should have the adequate stiffness to withstand possible unbalanced load sharing among the stages [147].

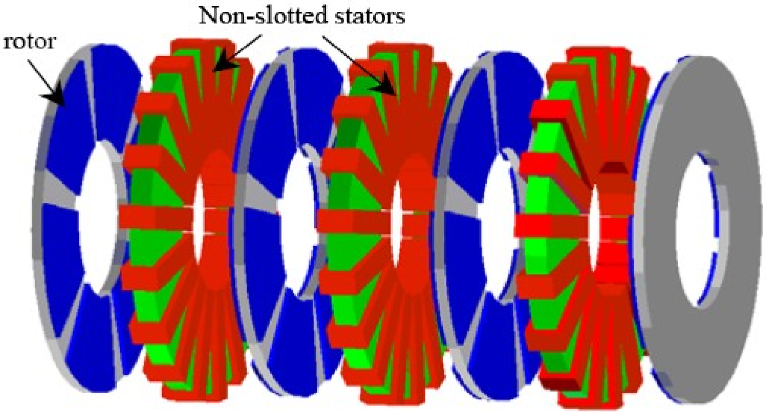

Figure 3.16 - A three stage TORUS machine [129]

Mueller et al. suggested in [86] a C-core design for an aircored AF PMDD machine with the C-cores mounted on the rotor structure while the stator winding is held independently between them (Figure 3.17). The C-core orientation could be radially or axially oriented. The AF orientation has been chosen as it offers extra structural simplicity and can be more easily extended to multistage machines.

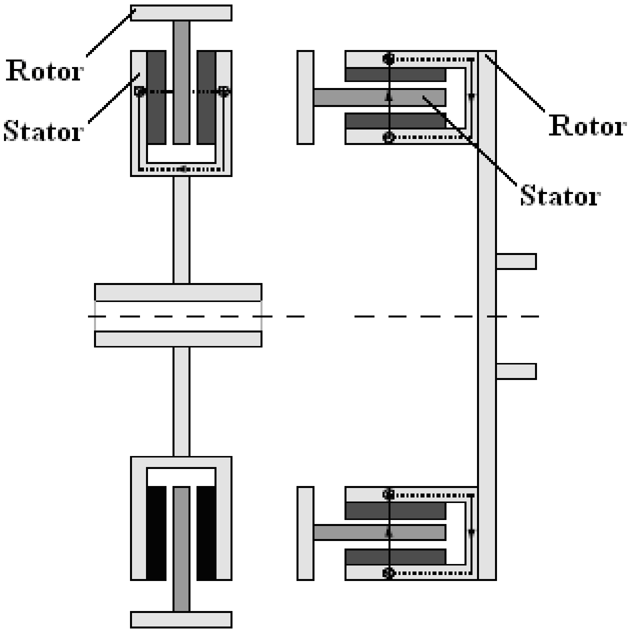

Figure 3.17 - The aircored PMDD generator topology suggested by Mueller *et al.* AF orientation (left) and RF orientation (right) [86]

A significant mass reduction of up to 55% on the inactive mass of the generator is suggested for this concept without compromising the structure's stiffness [148]. Relieved from the electromagnetic attraction forces the structure has only to support its mass relieved from large bending moments. Multistage is also benefited by the C-core structure as all unbalanced loading are successfully transmitted to the main structure's body. The finite magnetic gap of this design, unlike that in [29] and [103], proves to be beneficial in terms of the magnetic circuit that enables the maximum airgap flux density with the minimum permanent magnet material. Also the resulting magnetic loading is minimised without having to resort to large diameters like conventional double-sided AF topologies. In addition, the high degree of modularity is beneficial in terms of manufacture, operation and maintenance as the machine can be kept on the grid when a fault occurs in one of the machine's modules or stages without having to stop the rest of the stages and the generator's continuous operation. A 1MW prototype of such a C-core aircored AF PMDD generator has been developed and commercialized by NGenTec Ltd, a spin out company from the

University of Edinburgh [149][150]. A multi-MW machine would be possible by increasing the stages of such a machine.

3.3.3 TF PMDD machines

In a TF machine the path of the magnetic flux in the core is perpendicular to the direction of the rotor rotation (Figure 3.18).

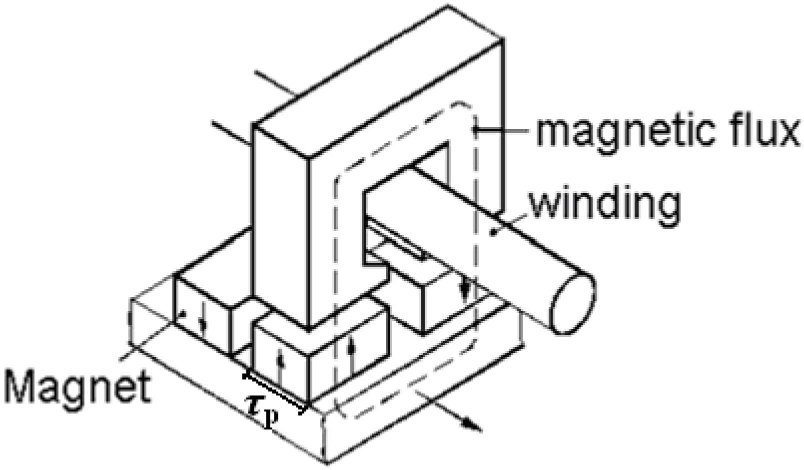

Figure 3.18 - A single-sided surface-mounted TFPM machine [151]

TF PMDD topologies allow very small pole pitches (τ_p) to be utilised leading to higher current loadings and force density compared to other PMDD machine types. Furthermore, they allow an increase in the winding space without decreasing the available space for the main flux. The winding reduces the total amount of copper that is used for these machines, reducing copper losses and allowing lower values of mass/torque ratios to be achieved and minimizing the required active mass [89]. In their extended comparison among a number of suggested direct drive technologies Dubois *et al*. came to the conclusion that the iron-cored TF PMDD topology offered the greatest potential in terms of power density and cost/torque ratio [108].

A fundamental issue for TF PMDD generators is their low power factor (typical between 0.35 for surface and 0.55 for buried magnets) due to large armature leakage fields [152]. This can be overcome by using an appropriately rated power converter and active control. Schuttler et al. used a DSP controller board for each phase converter to optimise the power factor of a C-core TF PMDD generator with flux concentration using a normalized open-circuit voltage as a current reference signal, giving a power factor of one [153]. Other optimisation methods for the power factor include magnetostatic and transient three-dimensional finite element analysis (FEA) for obtaining the best magnetic circuit to minimise the leakage paths of the machine [153][154].

Despite their many advantages, TF PMDD machines have complicated structures with complex core designs that are difficult to manufacture and assembly compared to RF and AF PMDD ones. Slotless or aircored TF PMDD machines that would simplify the manufacturing procedure are not possible since a sophisticated core design is required to create a flux path perpendicular to the rotor's movement. A very small airgap is also required for such machines [155]. The small airgap combined with the specialised core designs produce a fluctuation in the normal force applied on the structure and result in noise and vibration. Modification of the geometry of the magnetic path can be applied though to reduce these torque ripples and force fluctuations [156]. Various TF PMDD topologies have been proposed in an attempt to decrease complexity and ease manufacturing and assembly.

A straightforward way to distinguish the large number of TF PMDD designs suggested from the late 1990s' until today is whether or not flux-concentrating PM poles are mounted on the rotor disc. Outer rotor topologies have been described by [157]-[159] but they prove to create a heavier and more expensive machine according to [26]. Thus, inner-rotor topologies seem to be the best choice for TF PMDD machines, with or without flux concentration. Other suggested topologies of TF PMDD machines without flux concentration include single or double-sided winding [151][160] and different core designs such as U-core [151][161], U-core with stator bridges [162]-[164], and claw pole core [165] (Figure 3.19). However, all surface mounted TF PMDD machines that lack flux concentration are plagued by a low power factor that makes them unsuitable for large wind power applications [25, 148, 151, 162].

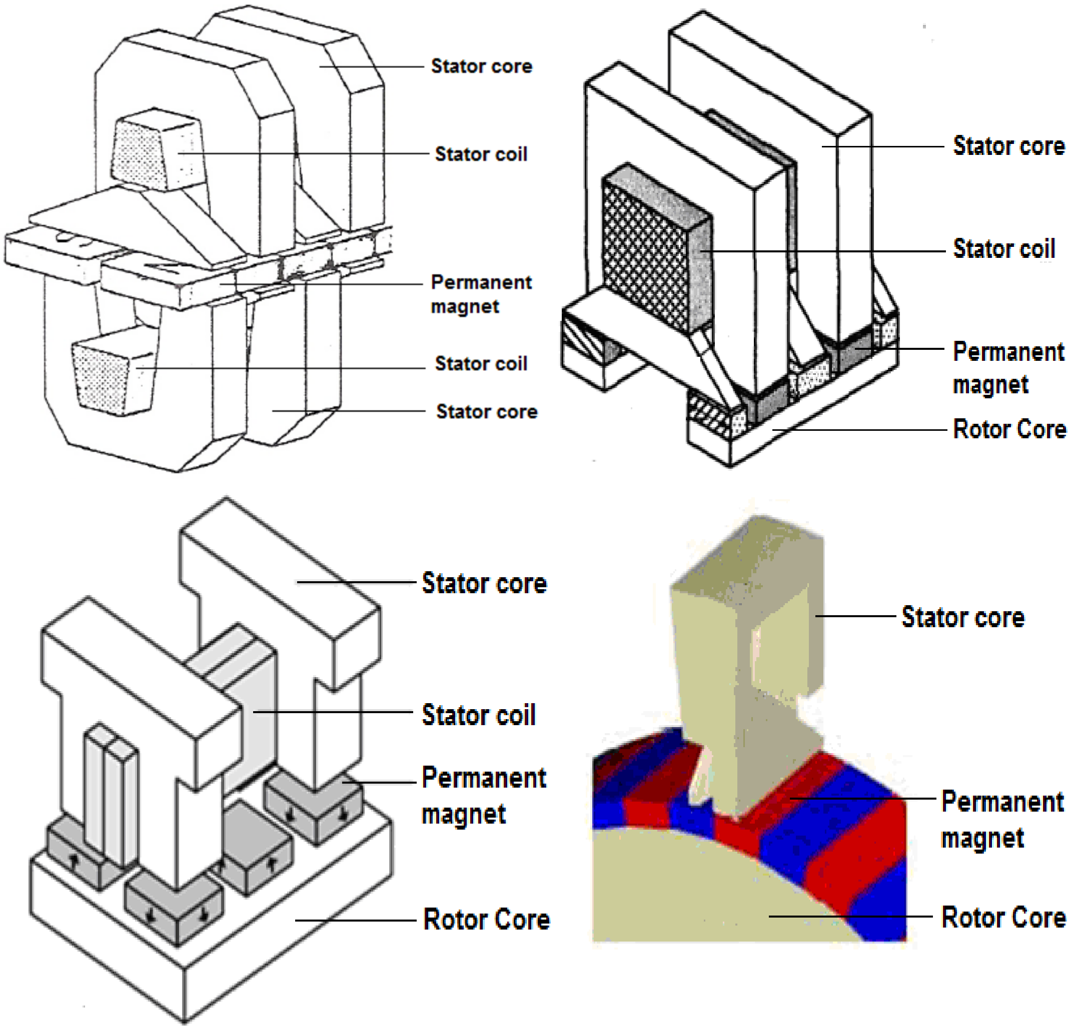

Figure 3.19 - Suggested TF PMDD topologies found in literature (without flux concentrators) [151][161][162][165]

TF PMDD machines with flux concentration are superior to their surface mounted counterparts in terms of force density and power factor. Suggested stator core topologies are similar to the surface mounted ones, but with more complicated core designs. A single or double winding has been proposed [167]-[174], with the former topology advancing as more efficient and lightweight since the second winding increases outer diameter and structural complexity and leads to larger airgaps that reduce torque density [26][155]. The numerous suggested structures can be distinguished by the shape of their stator core, leading to U-core [167]-[169], C-core [163, 166, 167, 168], E-core [167][169] and claw-pole designs [170][173][174]. Figure 3.20 illustrates an example of each core design that can be found in the literature.

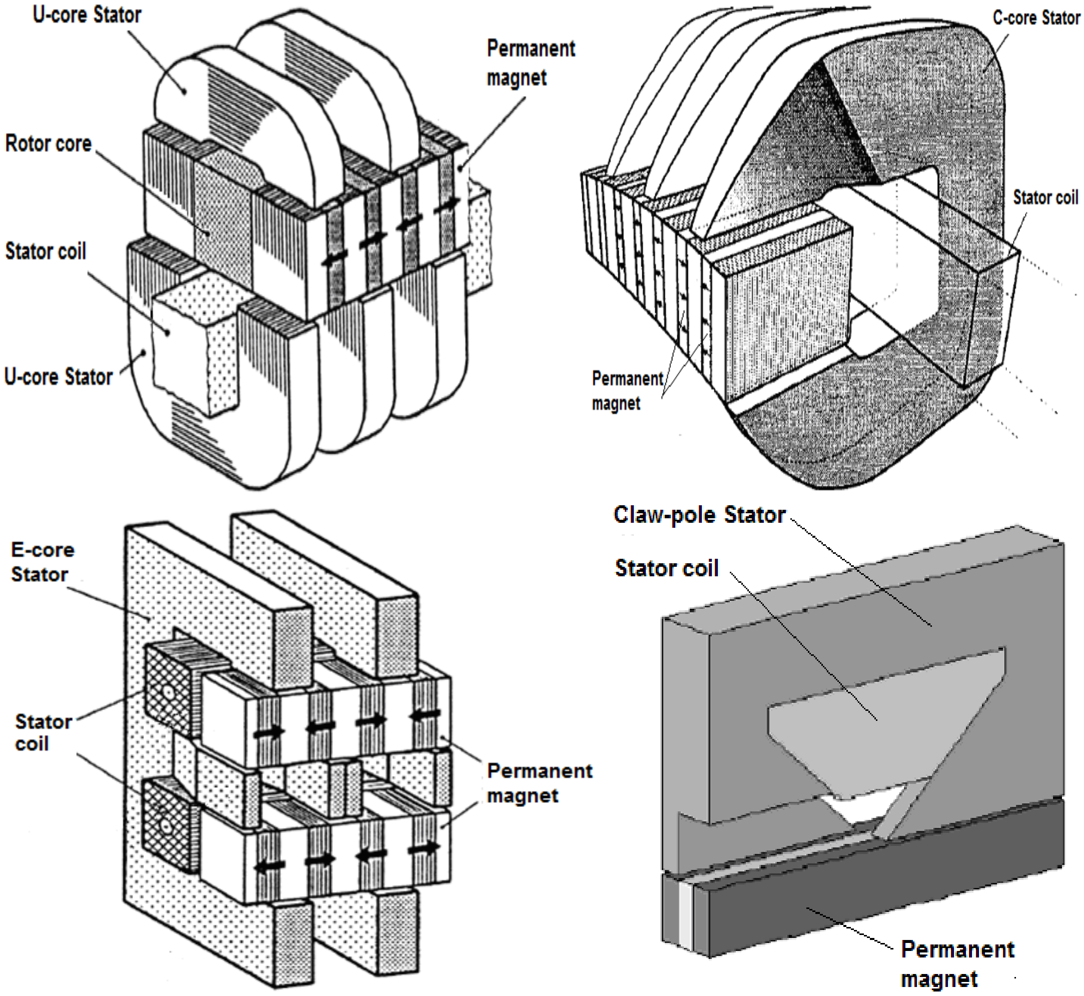

Figure 3.20 - Suggested TF PMDD topologies found in literature (with flux concentration) [167][170][171]

The claw-pole TF PMDD machine with toothed rotor and flux concentrators proposed by Dubois in [174] simplifies manufacturing while providing the same characteristics as conventional RF PMDD machines regarding mass/torque and cost/torque ratios (Figure 3.21).

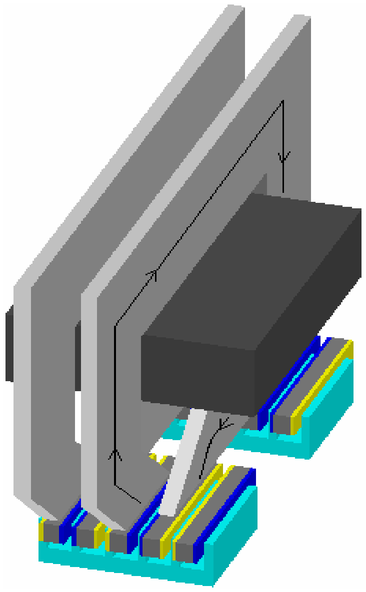

Figure 3.21 - TF PMDD machine with toothed rotor and flux concentrators [174]

However, the value of these ratios increase for diameters larger than 1m and for torque ratings higher than 10kNm according to [89], therefore such a topology would not be applicable for large offshore wind development.

Bang compared the different surface mounted and flux concentrating TF PMDD designs in terms of active mass/torque ratio and distinguished the C-core flux concentrating arrangement as the one with the highest torque density for the lightest mass [89].

3.4 Conclusions

PMDD machines have several advantages, which make them superior to both EEDD and SRG machines, such as increased reliability and higher energy yield. Additionally, the performance of power electronics has been improving and the cost of PM materials is expected to drop once more in the near future. Therefore, PMDD machines can be more attractive for offshore wind turbine applications.

Slotted RF PMDD machines with an inner rotor and surface mounted PMs are the lightest and more reliable among RF machines.

The C-cored AF PMDD machine suggested in [86][148][149] provides a structural topology with all the positive attributes of an aircored AF machine - such as structural simplicity, zero cogging torque and increased efficiency - and can effectively maintain the airgap clearance against electromagnetic and structural bending forces, reducing the required structural and active mass requirements compared to other AF or RF PMDD designs at the same time.

The C-core TF PMDD generator with an inner rotor and flux concentration was defined as the topology that combines successfully all the beneficial attributes of a TF machine - high force density, high current loadings and reduced copper losses - with the highest torque/mass ratio compared to RF and AF machines or other TF PMDD designs [89]. The same topology was also chosen as the one with the highest potential of taking advantage of the novel power factor and structural optimisation techniques [153][154].

These three PMDD machines were selected from the overview of the suggested topologies to be tested and compared for their structural stiffness and to be structurally optimised in the next chapters of this thesis.

Chapter 4

PMDD Generator Structural Modelling

4.1 Introduction

From the various PMDD generator topologies suggested in the literature, the following three were chosen for the highest potential for offshore wind development:

- The conventional iron-cored RF machine with an inner rotor topology and a slotted stator.
- The iron-cored TF machine with an inner rotor and a C-cored shaped stator.
- The aircored AF machine with a C-cored shaped rotor.

All suggested machines have the permanent magnet material mounted on the rotor surface.

In this chapter, structural models that correspond to a 5MW direct drive machine were created for each generator concept. The work presented in this chapter could be part of the early design steps taken in the manufacturing process of a direct drive generator. All models were designed with the help of the ANSYS finite element analysis (FEA) tool [175]. ANSYS is recognised as an industrial standard software for structural design and stress analysis. All models were simplified in terms of detail due to hardware limitations and to decrease the time the modeller would require to come to a solution. The stator core of the iron-cored structures was assumed to be a solid piece of steel instead of a series of laminations. All components of the structures were considered to be perfectly fitted to each other without bolts or bearings. Although such hypothesis results in adding extra stiffness to the models, valuable conclusions can still be drawn regarding the mass and response of the different machines to the applied loads.

Structural steel was used for the body of each support structure, NdFeB permanent magnet material for the surface magnets and glass epoxy for the stator modules of the AF aircored machine. Their physical properties are described in Table 4.1.

	Structural Steel	**Permanent Magnet**	**Glass Epoxy**
Young's Modulus (MPa)	20000	16000	24000
Poisson's Ratio	0.3	0.24	0.24
Density (kg/m³)	7850	7500	1850
Thermal expansion (1/ºC)	1.2×10^{-5}	3.4×10^{-6}	1.5×10^{-5}
Tensile Yield Strength (MPa)	250	800	375
Compressive Yield Strength (MPa)	250	780	300
Thermal Conductivity (W/mm ºC)	6.05×10^{-2}	9×10^{-3}	2.5×10^{-4}
Specific heat (J/kg ºC)	434	502	1000
Relative Permeability	100	1.05	4.9

Table 4.1 - Physical properties of elements [176]

McDonald in [177] tried to minimise the mass of a conventional iron-cored RF PMDD generator structure with a disc rotor and an armed stator, with power output of 2, 3 and 5 MW (Figure 4.1). The total structural mass of the generator was optimised by acquiring the best aspect ratio (K_{rad}) of the structure's axial length l to the airgap diameter D_g.

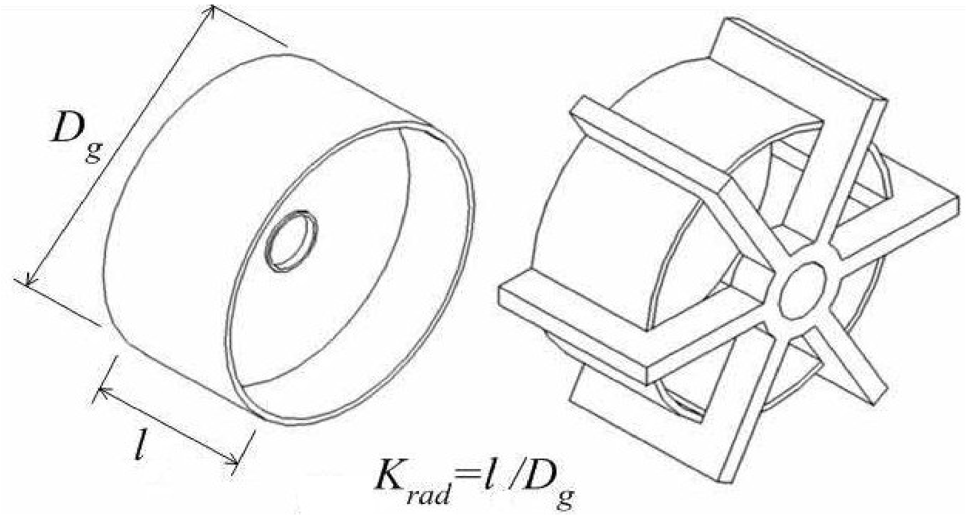

Figure 4.1 - A RF PMDD structure with disc rotor and armed stator [177]

Figure 4.2 depicts the resulting total structural mass of the generator as a function of K_{rad} for different power ratings. The minimum structural mass for a 5MW PMDD machine was acquired for a K_{rad} of ≈0.3. Thus, the models created in this thesis also had a 0.3 aspect ratio to minimise their structural mass.

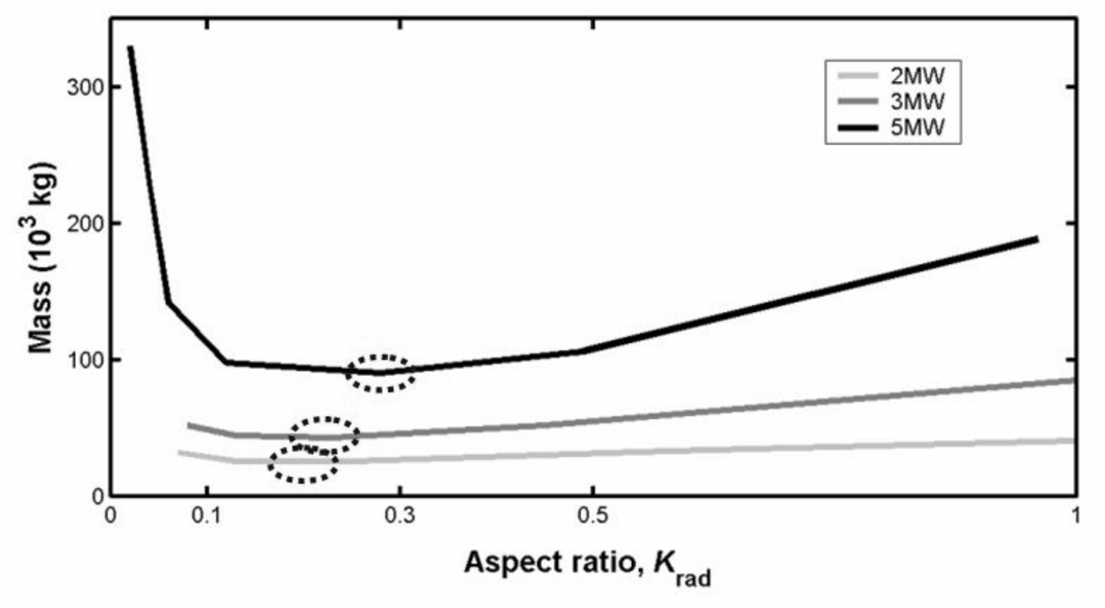

Figure 4.2 - Total mass of a RF PMDD generator for varying aspect ratios [177]

4.2 The RF PMDD structural model

The external shape of a RF PMDD structure is shown in Figure 4.3. Figure 4.4 depicts the dimensional parameters of the machine.

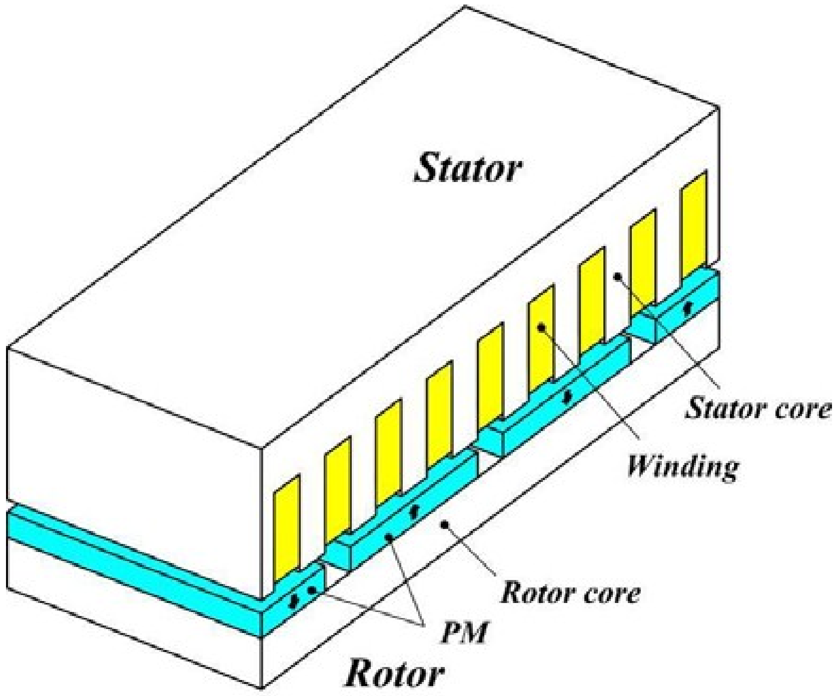

Figure 4.3 - Iron-cored RF PMDD generator with mounted magnets on its surface [89]

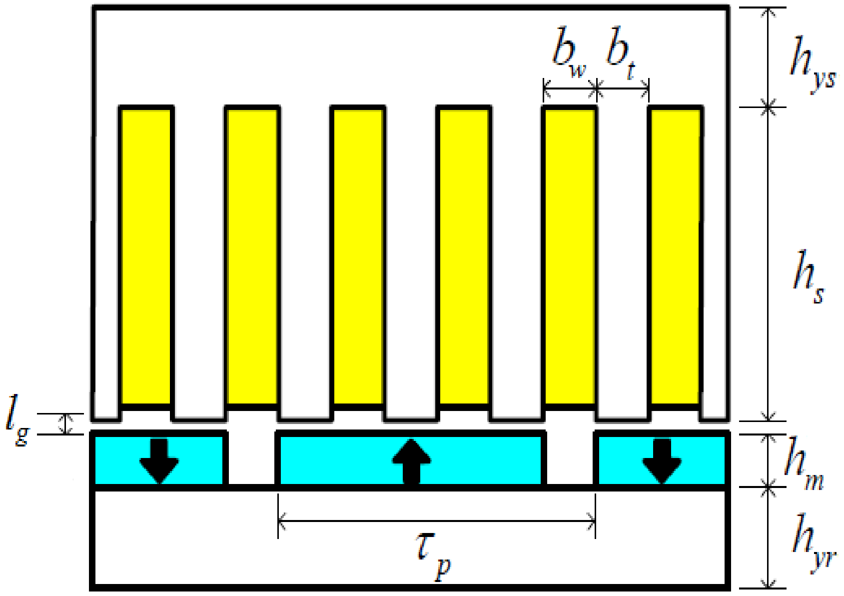

Figure 4.4 - Dimensional parameters used for the description of a RF PMDD generator

The electromagnetic parameters and the structural dimensions of a 5MW RF PMDD generator were calculated by Bang in [89] and are included in Table 4.2 [21]. All dimensions were calculated so that the required nominal power output P (W) would be produced for a blade tip speed of 80m/s and an average wind speed of 12m/s.

	5 MW RF PMDD
Airgap diameter, D_g (mm)	6360
Axial length, l (mm)	1720
Number of phase, m	3
Airgap length, l_g (mm)	6.36
Magnet height, h_m (mm)	15.9
Pole pitch, τ_p (mm)	100
Number of pole pair, p	100
Rotor yoke height, h_{yr} (mm)	40
Stator yoke height, h_{ys} (mm)	40
Winding space height, h_s (mm)	80
Winding space width, b_w (mm)	15
Stator tooth width, b_t (mm)	18
Peak flux density in the airgap, B_g (T)	1.1

Table 4.2 - Parameters and dimensions of a 5MW RF PMDD generator

The generator structure described above was modelled with the help of the FEA tool. The surface magnets were modelled as a single long piece of magnet, even though in reality they would consist of a number of smaller sections. Suggested support structures for the RF topology are with discs or with arms for both the rotor and the stator of the PMDD machine.

4.2.1 RF PMDD Disc Structures

The FEA model of the RF rotor structure with disc is depicted in Figure 4.5.

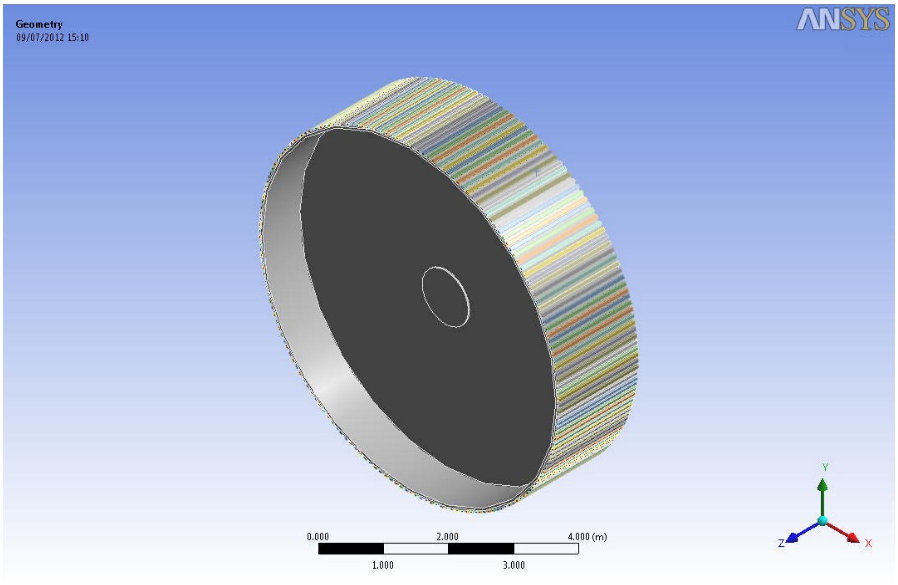

Figure 4.5 - RF rotor structure with disc

The structure is made of structural steel, while the poles from permanent magnet material. All the poles are perfectly bonded with the rotor’s body. A random value was set for the thickness of the supporting disc, t_d = 100mm. The total mass of the structure was 41 tons. The dimensions that describe the rotor structure are illustrated in detail in Figure 4.6 and Figure 4.7.

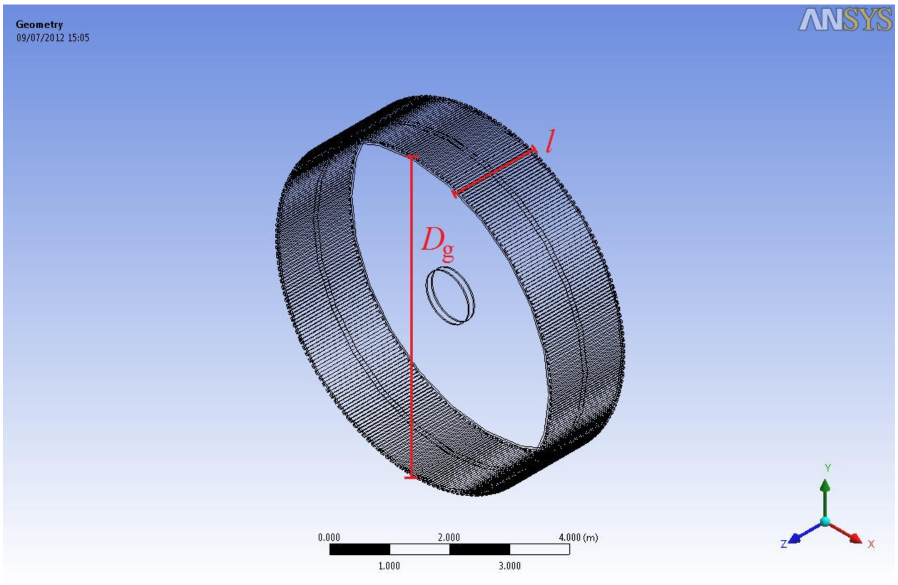

Figure 4.6 - The airgap diameter (D_g) and the axial length (l) of the RF rotor with disc

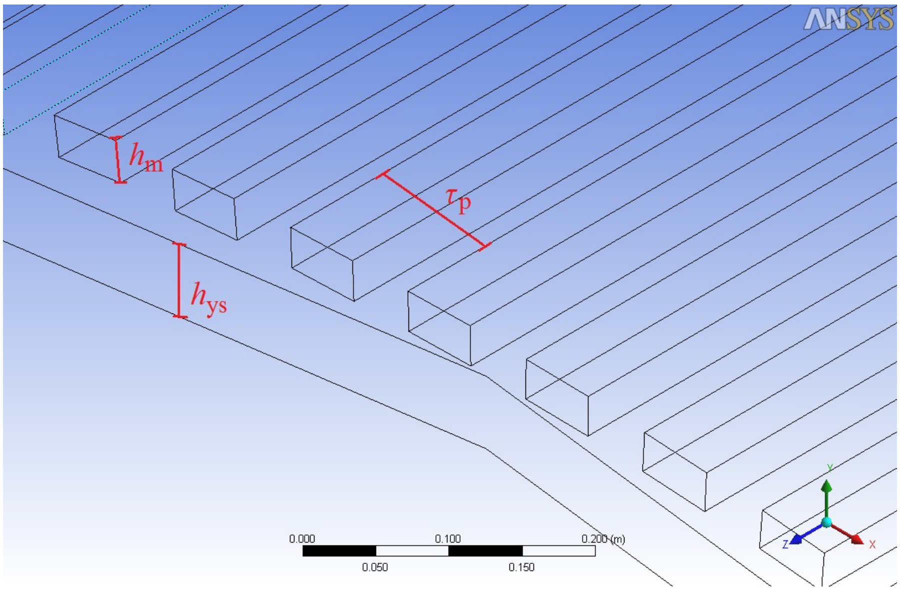

Figure 4.7 - The magnet height (h_m), the pole pitch (τ_p) and the yoke height (h_{yr}) of the RF rotor with disc

The FEA model of the stator with discs on both sides is illustrated in Figure 4.8. The structure is modelled as a solid (non-laminated) structure made of steel. The copper windings were not included in the structural modelling of the stator for simplicity.

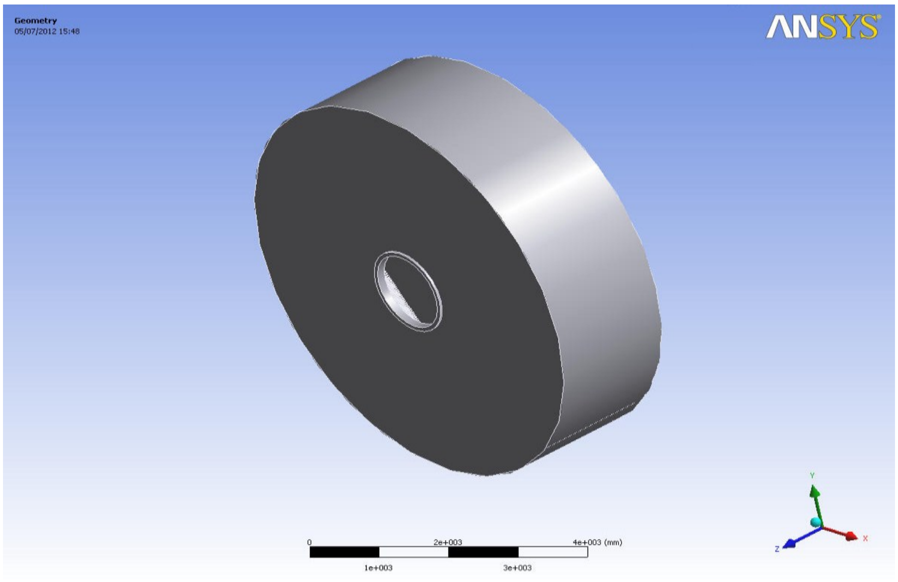

Figure 4.8 - The RF stator structure with discs

Introduction of windings to the stator model would increase its complexity and the system requirements for the structural analysis to follow. However, apart from the structural response is expected be in pair with a model that includes the copper windings, since the simulation assumptions and the magnitude of the applying forces would remain the same. A random value was set for the thickness of the supporting discs, t_d = 100mm. The total mass of the structure was 70 tons. The dimensions that describe the rotor structure are illustrated in detail in Figure 4.9 and Figure 4.10.

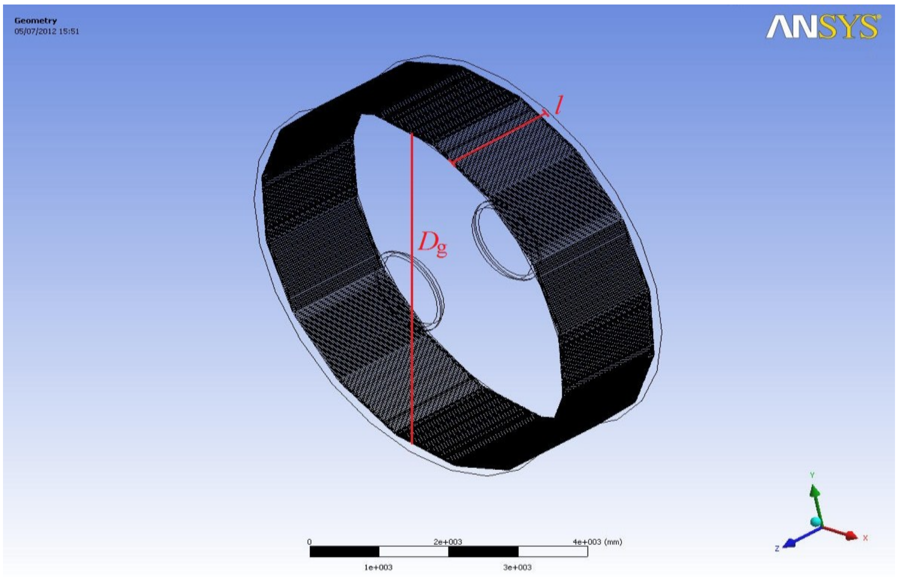

Figure 4.9 - The airgap diameter (D_g) and the axial length (l) of the RF stator with discs

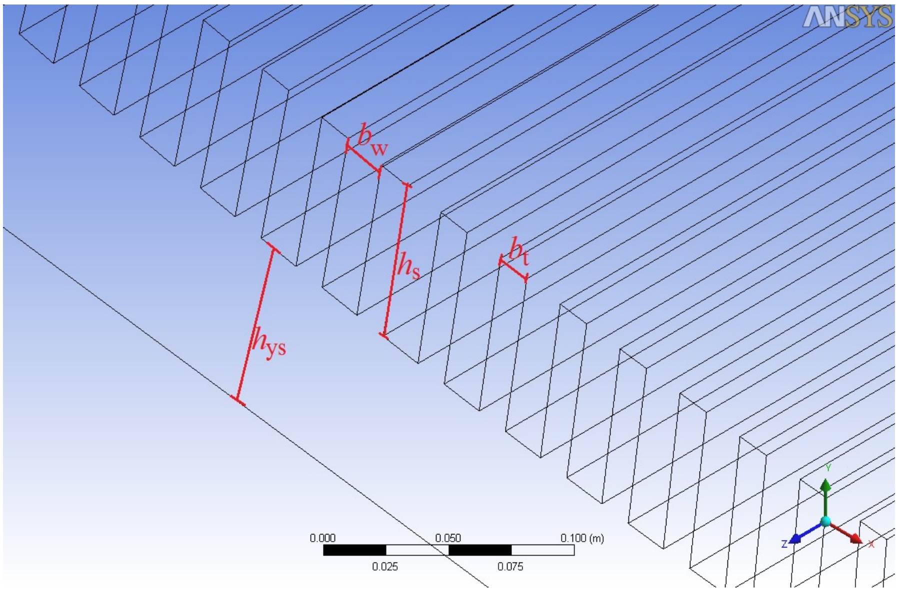

Figure 4.10 - The winding space width (b_w), the winding space height height (h_s), the tooth width (b_t) and the yoke height (h_{ys}) of the RF stator with discs

4.2.2 RF PMDD Armed Structures

The FEA model of the RF rotor structure with arms is depicted in Figure 4.11. The number of arms was set to $n = 5$.

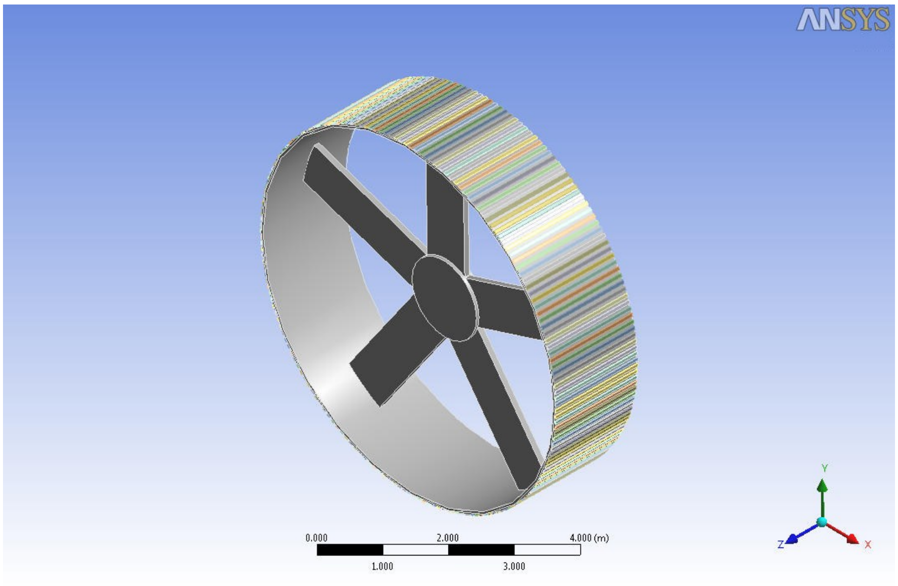

Figure 4.11 - RF rotor structure with arms

The structure is made of structural steel with solid arms. Its poles consist of permanent magnet material and are considered to be perfectly bonded with the rotor's yoke. A random value was set for the arms' depth, d = 100mm, while their width was calculated according to $b = 2\pi(D_g/10)/n$. The total mass of the structure was 23 tons. The dimensions that describe the rotor structure are illustrated in detail in Figure 4.12 and Figure 4.13.

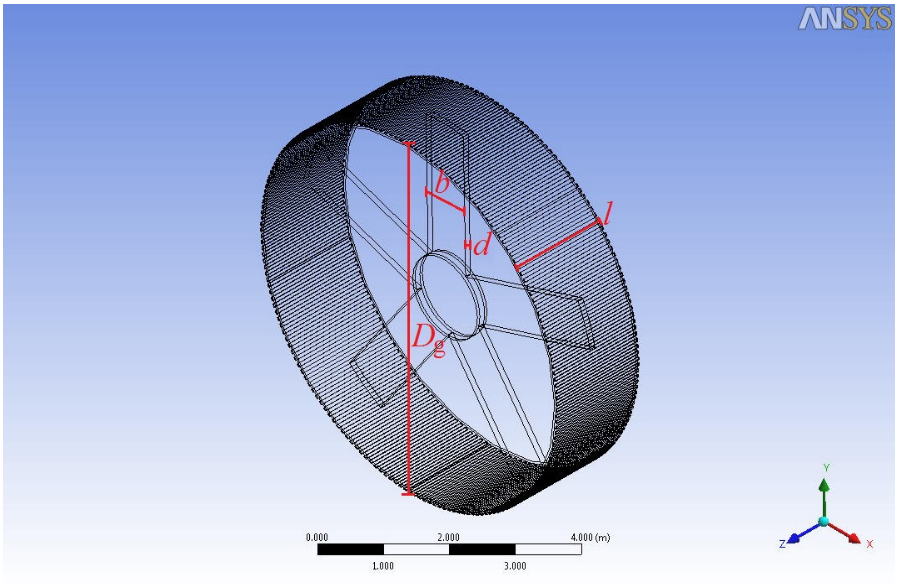

Figure 4.12 - The airgap diameter (D_g), the axial length (l), the arm's depth (d) and the arm's width (b) of the RF rotor with arms

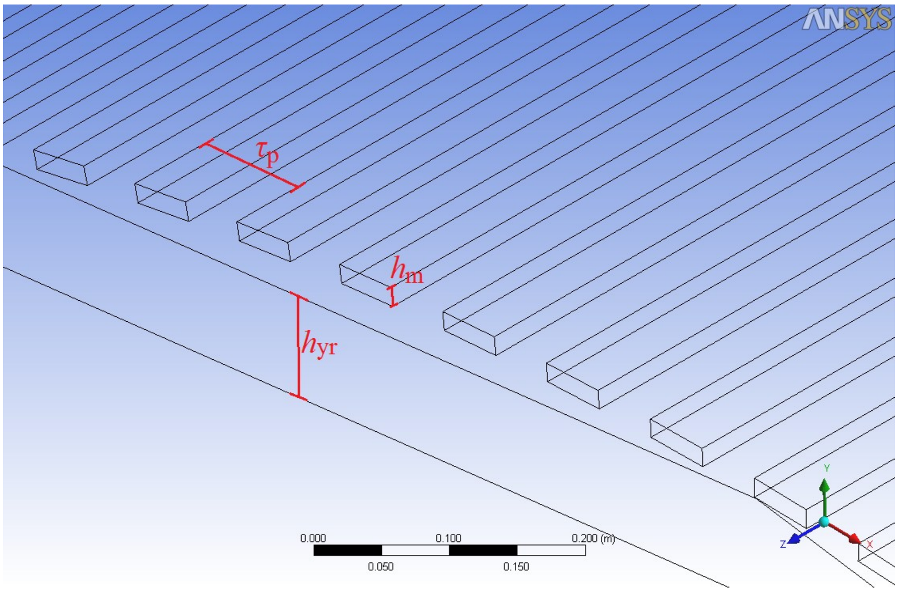

Figure 4.13 - The magnet height (h_m), the pole pitch (τ_p) and the yoke height (h_{yr}) of the RF rotor with arms

The FEA model of the stator with arms on both sides is illustrated in Figure 4.14.

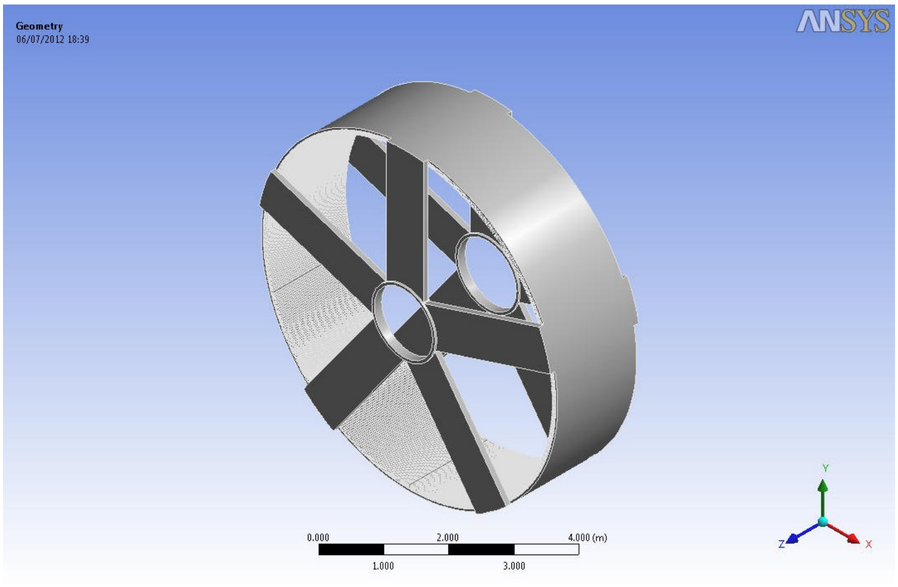

Figure 4.14 - The RF stator structure with arms

The structure is made of structural steel. The copper coils were not included in the structural modelling of the stator for simplicity. All arms are solid with structural dimensions d = 100mm and $b = 2\pi(D_g/10)/n$. The total mass of the structure was 37 tons. The dimensions that describe the rotor structure are illustrated in detail in Figure 4.15 and Figure 4.16.

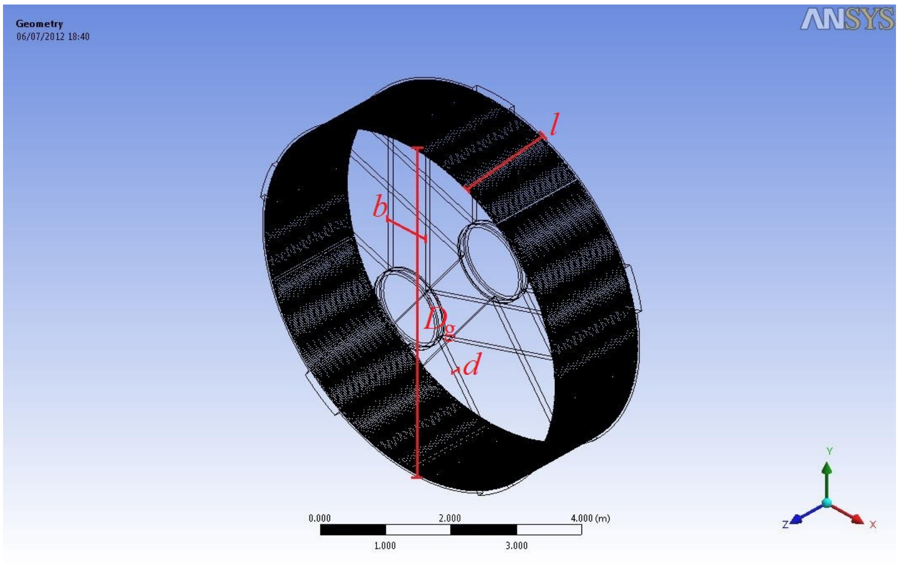

Figure 4.15 - The airgap diameter (D_g), the axial length (l), the arm's depth (d) and the arm's width (b) of the RF stator with arms

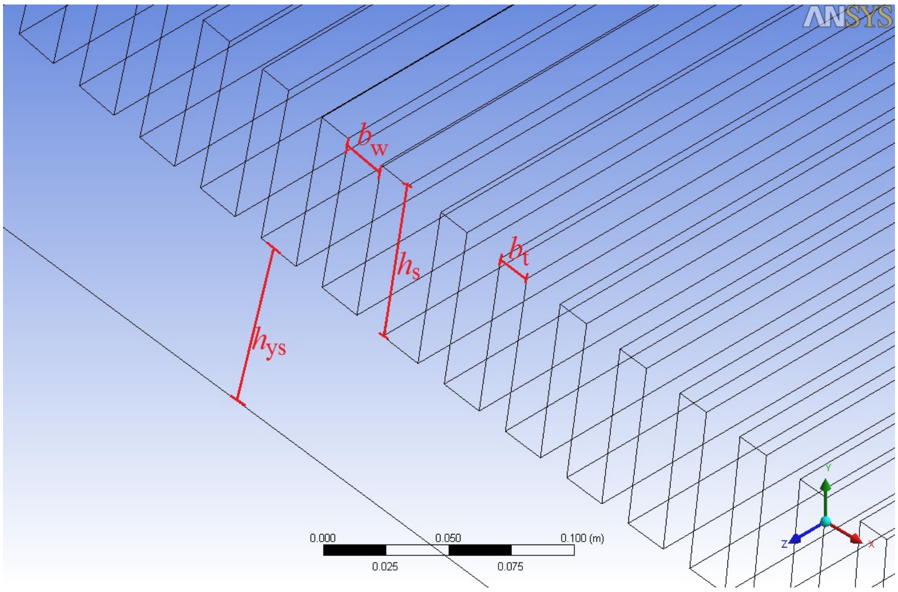

Figure 4.16 - The winding space width (b_w), the winding space height height (h_s), the tooth width (b_t) and the yoke height (h_{ys}) of the RF stator with arms

4.3 The TF PMDD structural model

Two different topologies were modelled for the single-winding C-cored TF PMDD machine: one with the stator core facing the permanent magnet poles similar to the conventional RF machine and one with the stator C-cores engulfing the rotor poles. Both machines employ a disc rotor and an armed stator structure. For the rest of this thesis the first TF topology will be referred to as the TF-1 PMDD machine (Figure 4.17) and the second as the TF-2 PMDD machine (Figure 4.18).

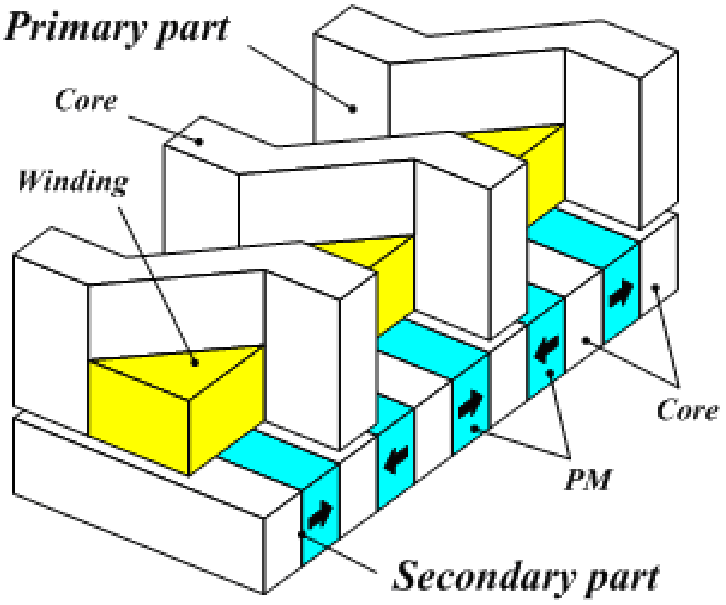

Figure 4.17 - Single-sided iron-cored flux concentrating TF-1 PMDD generator [89]

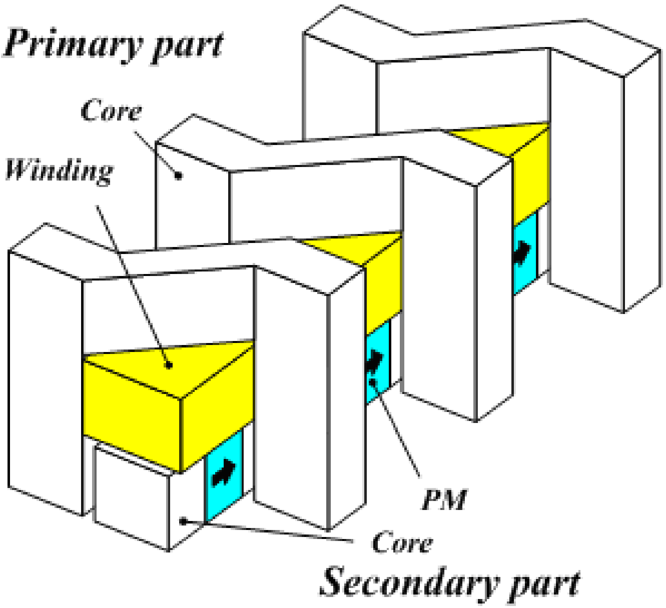

Figure 4.18 - Double-sided iron-cored flux concentrating TF-2 PMDD generator [89]

Figure 4.19 depicts the dimensional parameters of the TF-1 machine while Figure 4.20 the same parameters but for the TF-2 machine.

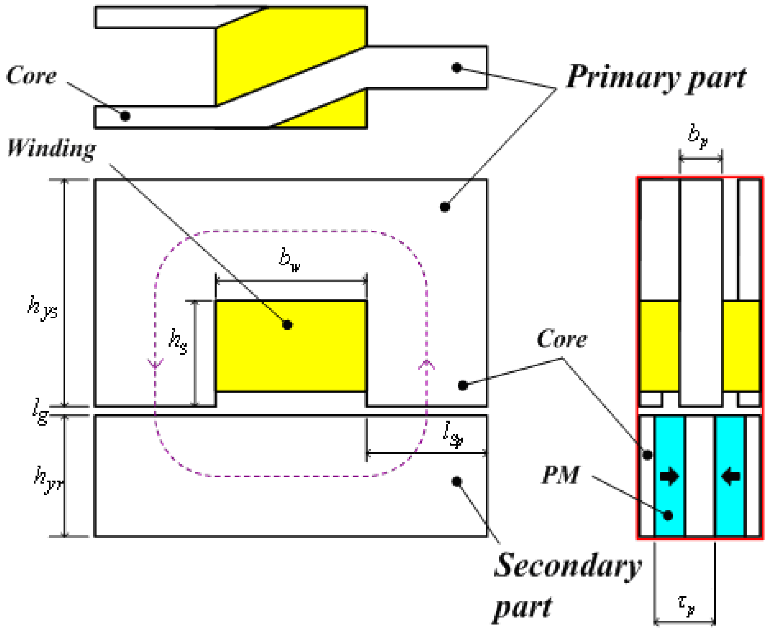

Figure 4.19 - Dimensional parameters used for the description of a TF-1 PMDD generator

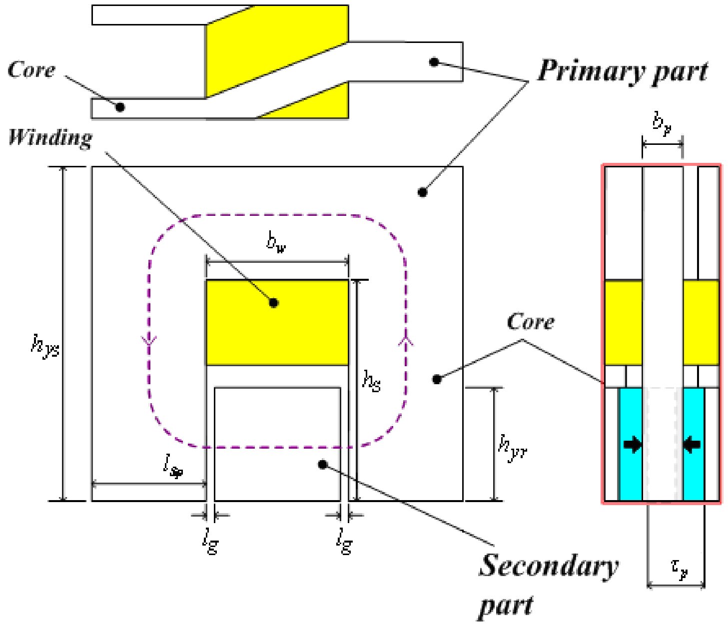

Figure 4.20 - Dimensional parameters used for the description of a TF-2 PMDD generator

The electromagnetic parameters and the structural dimensions that describe the two different 5MW TF PMDD generator topologies were calculated by Bang in [89] and can be seen in Table 4.3. All dimensions were calculated so that the required nominal power output P (W) would be produced for an average wind speed of 12m/s and a blade tip speed of 80m/s.

	5 MW TF-1 PMDD	5 MW TF-2 PMDD
Airgap diameter, D_g (mm)	6360	6360
Axial length, l (mm)	1030	1030
Number of phase, m	3	3
Airgap length, l_g (mm)	6.36	6.36
Magnet height, h_m (mm)	25.4	25.4
Pole pitch, τ_p (mm)	63.6	63.6
Number of pole pair, p	157	157
Rotor yoke height, h_{yr} (mm)	130.4	130.4
Stator yoke height, h_{ys} (mm)	130.4	211.2
Winding space height, h_s (mm)	80.8	80.8
Winding space width, b_w (mm)	80.8	80.8
Stator tooth width, b_t (mm)	50.9	50.9
Stator pole length, l_{sp} (mm)	474.6	474.6
Peak flux density in the airgap, B_g (T)	1.59	0.76

Table 4.3 - Parameters and dimensions of a 5MW flux concentrating TF PMDD generator with C-cores [89]

The generator structures described above were modelled with the help of the FEA tool.

4.3.1 TF-1 PMDD Structures

The FEA model of the TF-1 rotor structure is similar to that of the RF rotor with disc but with shorter axial length (Figure 4.21).

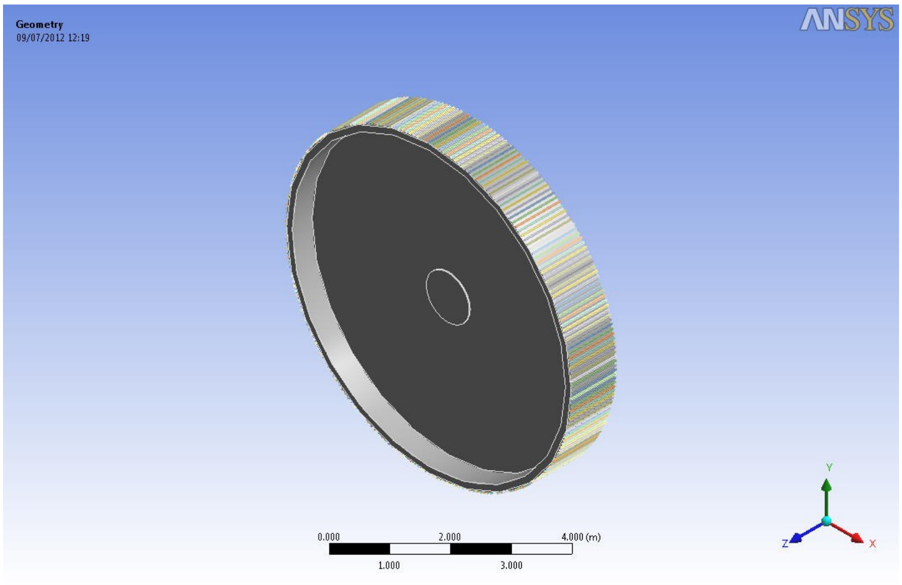

Figure 4.21 - TF-1 rotor structure

All the magnetic poles are assumed to be perfectly bonded with the rotor's yoke. A random value was set for the thickness of the supporting disc, t_d = 100mm. The total mass of the structure was 48 tons. The dimensions that describe the rotor structure are illustrated in detail in Figure 4.22 and Figure 4.23.

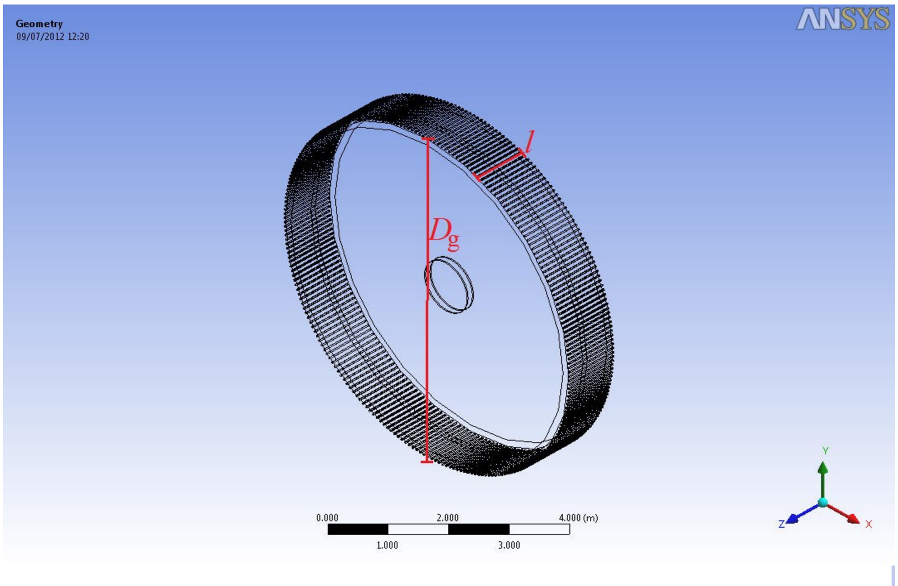

Figure 4.22 - The airgap diameter (D_g) and the axial length (l) of the TF-1 rotor

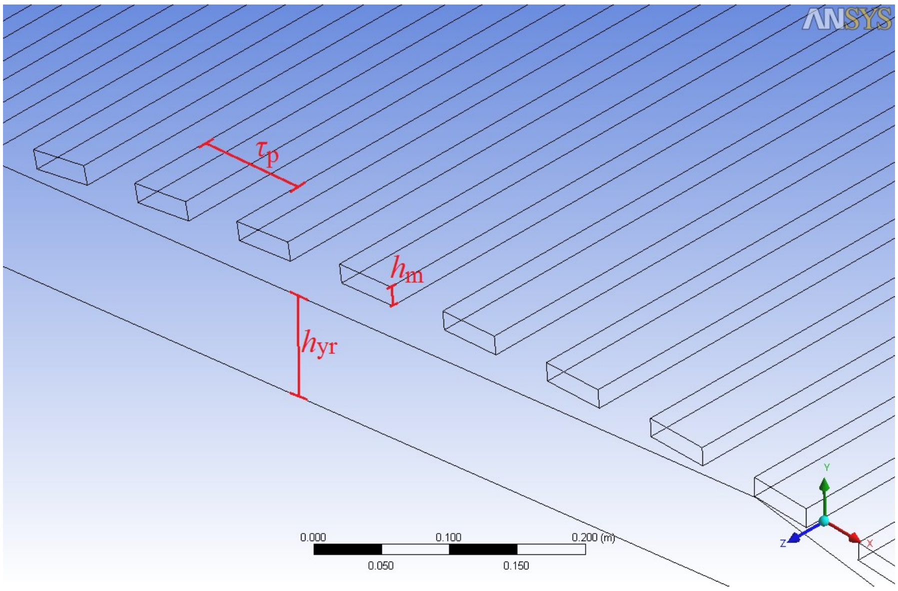

Figure 4.23 - The magnet height (h_m), the pole pitch (τ_p) and the yoke height (h_{yr}) of the TF-1 rotor

The FEA model of the TF-1 stator with arms on both sides is illustrated in Figure 4.24. The model was made of structural steel without the winding for simplicity. The arms were solid and their dimensions were the same as those of the RF armed stator, so that $d = 100$mm and $b = 2\pi(D_g/10)/n$. The total mass of the structure was 30 tons.

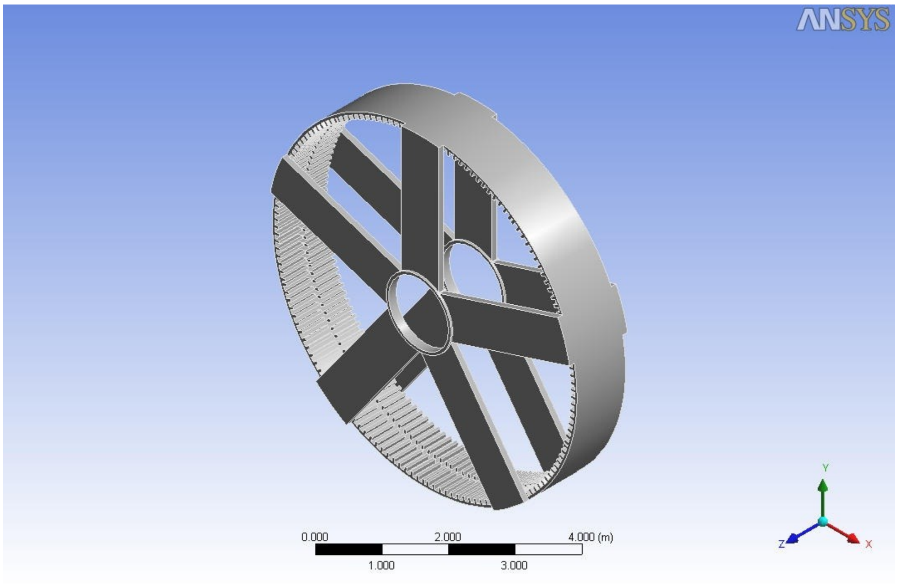

Figure 4.24 - The TF-1 stator structure

The dimensions that describe the rotor structure are illustrated in detail in Figure 4.25 and Figure 4.26.

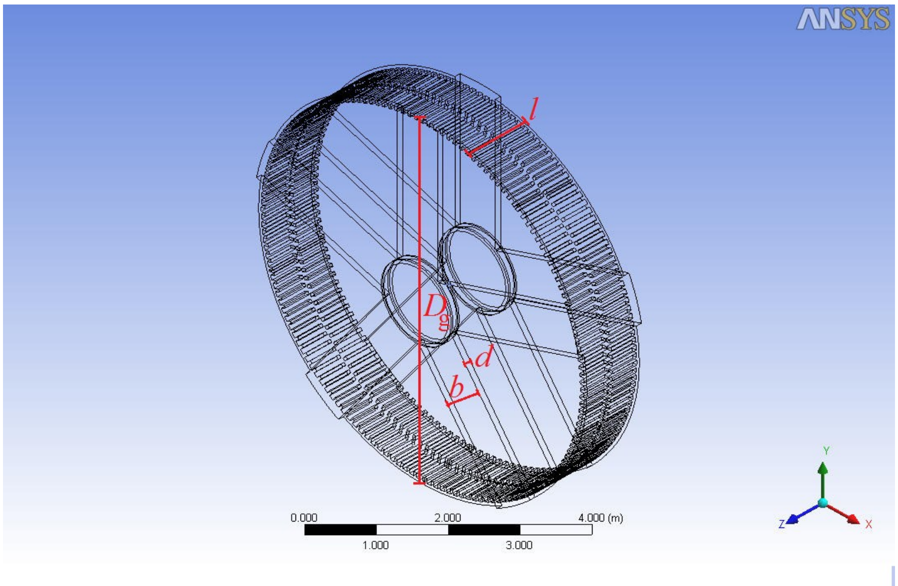

Figure 4.25 - The airgap diameter (D_g), the axial length (l), the arm's depth (d) and the arm's width (b) of the TF-1 stator

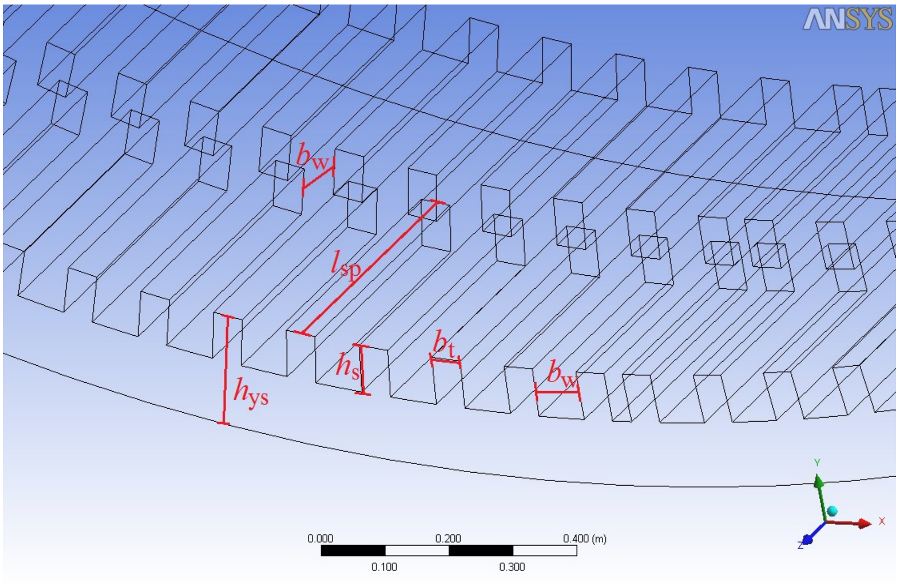

Figure 4.26 - The winding space width (b_w), the winding space height (h_s), the tooth width (b_t), the pole length (l_{sp}) and the yoke height (h_{ys}) of the TF-1 stator

4.3.2 TF-2 PMDD Structures

The FEA model of the TF-2 rotor structure is similar to the TF-1 rotor with a shorter axial length (Figure 4.27). In fact the rotor's axial length is equal to the stator's winding space b_w.

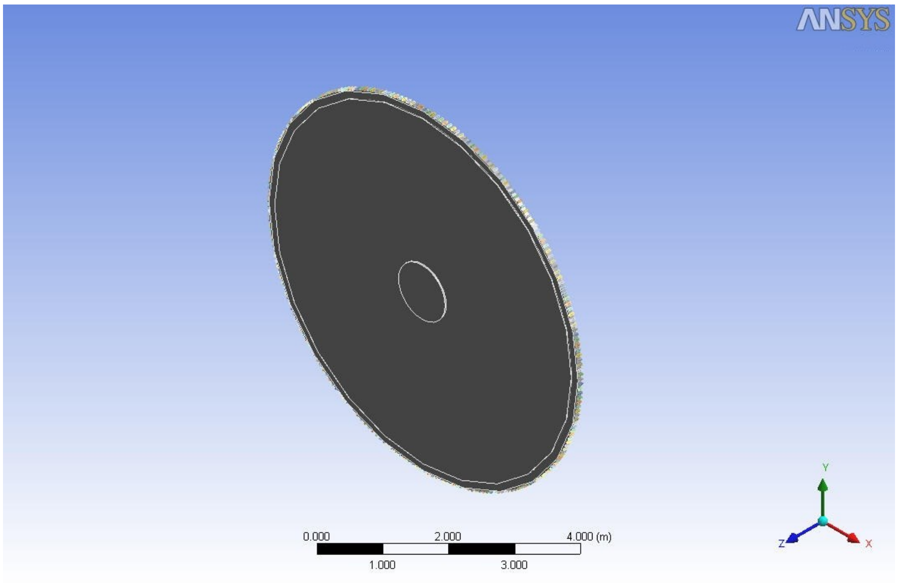

Figure 4.27 - TF-2 rotor structure

All the magnetic poles are assumed to be perfectly bonded with the rotor's yoke. A random value was set for the thickness of the supporting disc, t_d = 100mm. The total mass of the structure was 27 tons. The dimensions that describe the rotor structure are illustrated in detail in Figure 4.28 and Figure 4.29.

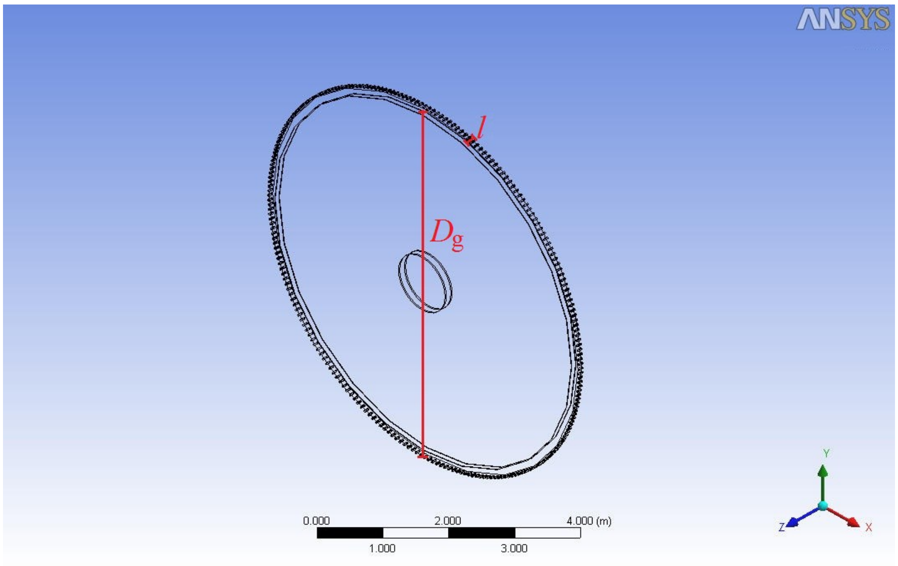

Figure 4.28 - The airgap diameter (D_g) and the axial length (l) of the TF-2 rotor

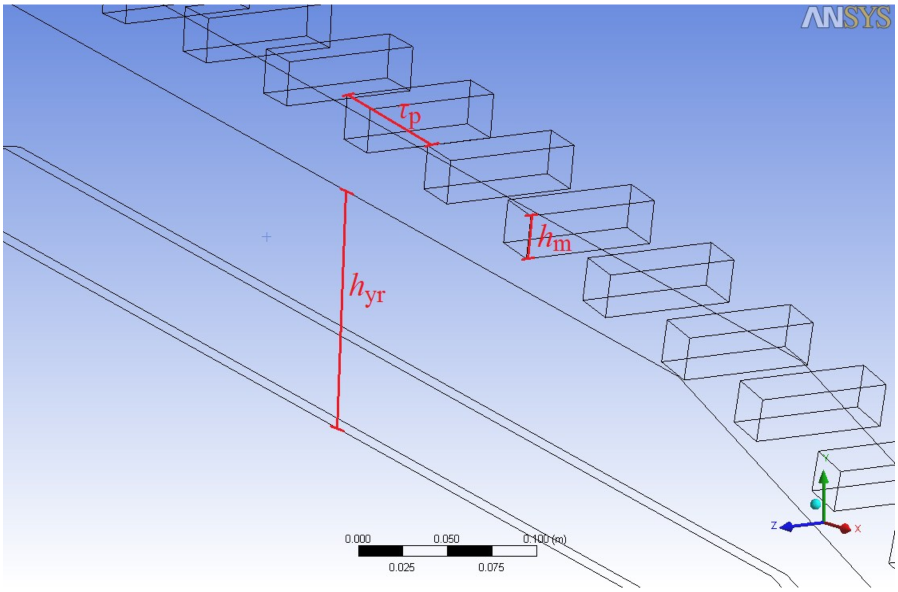

Figure 4.29 - The magnet height (h_m), the pole pitch (τ_p) and the yoke height (h_{yr}) of the TF-2 rotor

The FEA model of the TF-2 stator with arms on both sides is illustrated in Figure 4.30. The model was made of structural steel without the winding for simplicity. The arms were solid and their dimensions were the same with the previously presented armed stators, so that d = 100mm and $b = 2\pi(D_g/10)/n$. The total mass of the structure was 35 tons.

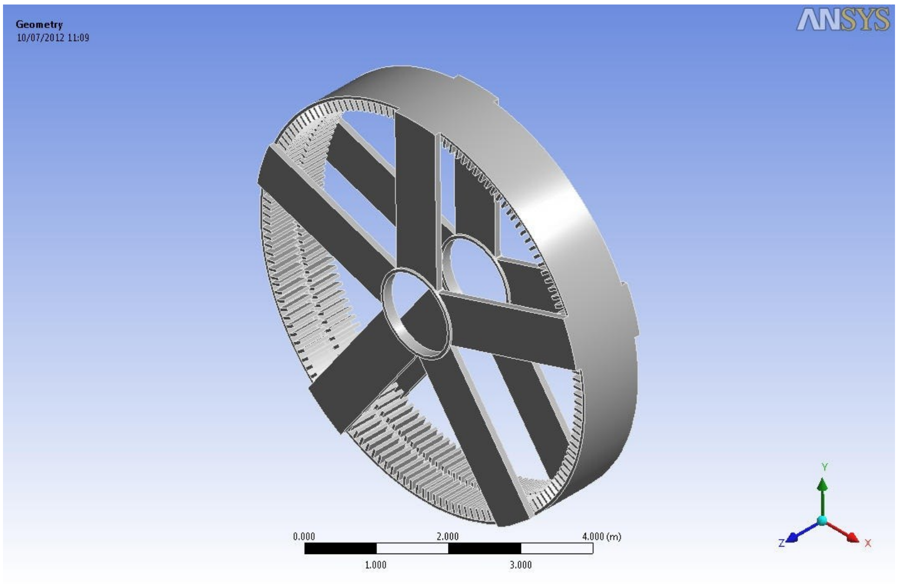

Figure 4.30 - The TF-2 stator structure

The dimensions that describe the stator structure are illustrated in detail in Figure 4.31 and Figure 4.32.

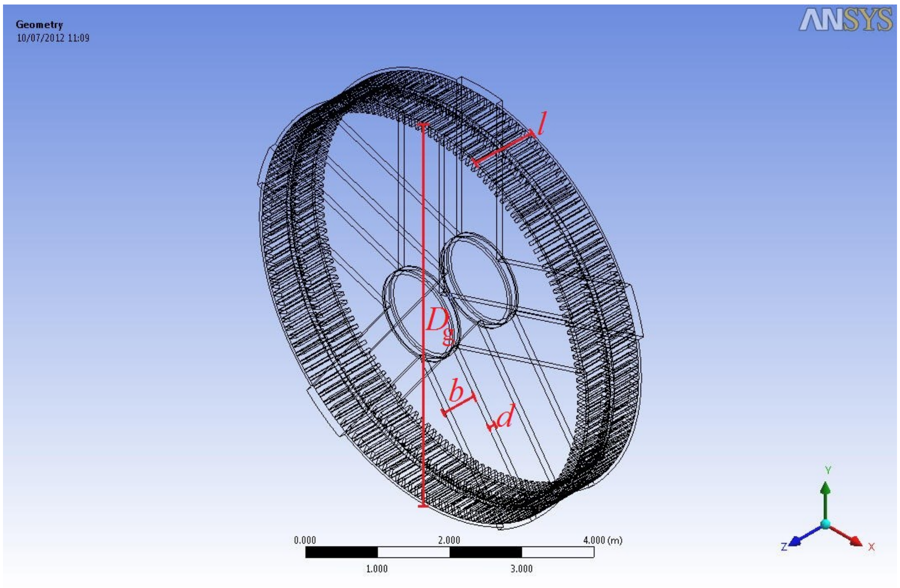

Figure 4.31 - The airgap diameter (D_g), the axial length (l), the arm's depth (d) and the arm's width (b) of the TF-2 stator

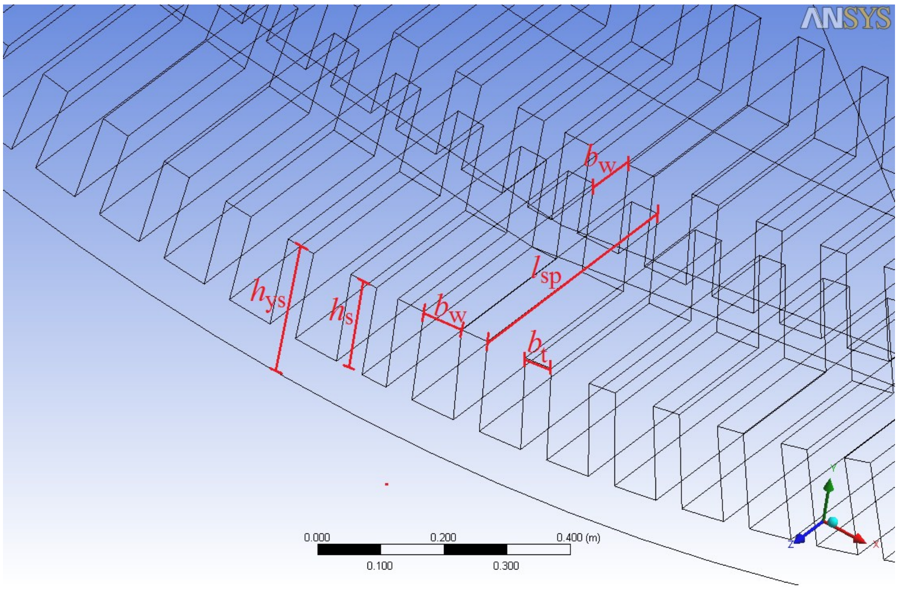

Figure 4.32 - The winding space width (b_w), the winding space height (h_s), the tooth width (b_t), the pole length (l_{sp}) and the yoke height (h_{ys}) of the TF-2 stator

4.4 The AF PMDD structural model

The aircored AF machine with a C-cored shaped rotor described in [86][149] was the final machine that was modelled for the purposes of this research. Five stages of C-Core modules were used in this design in order to reach the 5MW nominal output and were oriented as illustrated in Figure 4.33 to create the machine's axial flux.

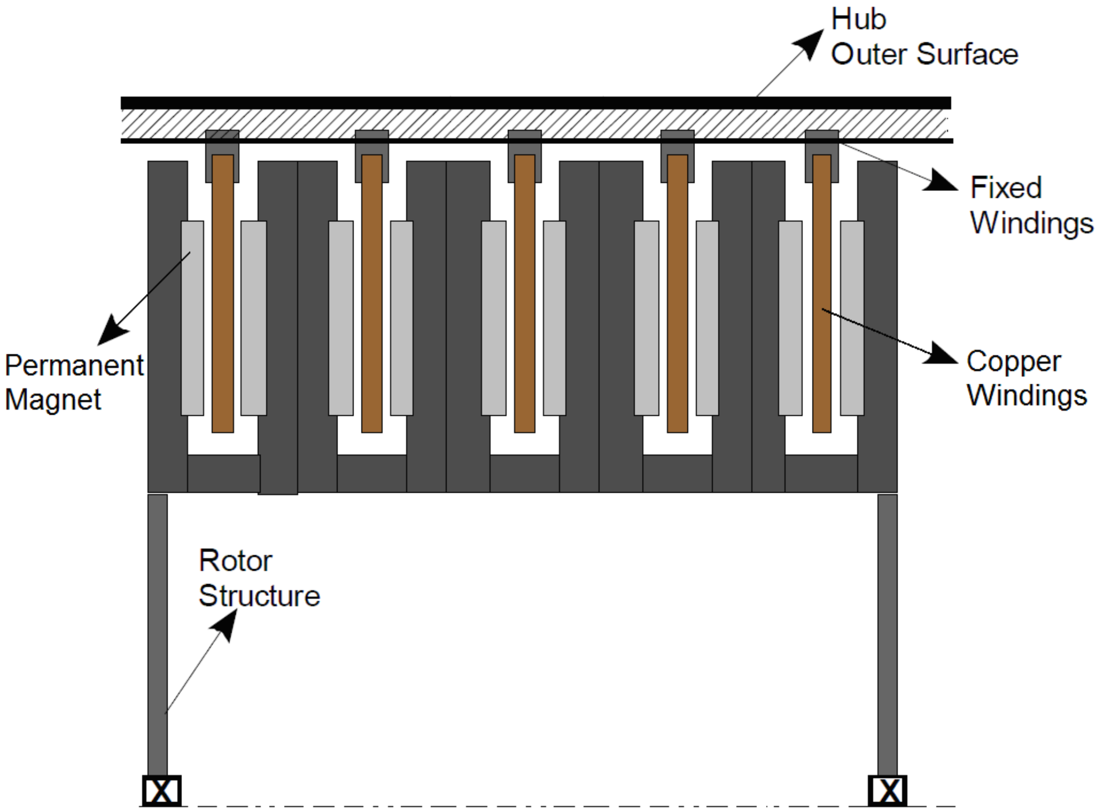

Figure 4.33 - Aircored AF machine with five stages of C-cores

The electromagnetic parameters and the structural dimensions that describe a 5MW aircored AF PMDD generator topology with C-cores were calculated by NGenTec [150] and can be seen in Table 4.4. All dimensions were calculated so that the required nominal power output P (W) would be produced for a blade tip speed of 80m/s and an average wind speed of 12m/s.

	5MW AF PMDD
Airgap diameter, D_g (mm)	7800
Axial length, l (mm)	570
Number of phase, m	3
Airgap length, l_g (mm)	5
Magnet length, l_m (mm)	576
Magnet height, h_m (mm)	27
Pole pitch, τ_p (mm)	103
Number of poles per stage, p	192
Rotor yoke height, h_{yr} (mm)	20
Stator yoke height, h_{ys} (mm)	20
Winding space length, l_s (mm)	629
Winding space width, b_w (mm)	31
Peak flux density in the airgap, B_g (T)	0.57

Table 4.4 - Parameters and dimensions of a 5MW aircored AF PMDD generator with C-cored modules

The structural models of this machine are slightly different from the previously presented rotor and stator structures as they combine arms and disc for their support. Minor changes from the original NGenTec design were necessary though for copyright reasons. The rotor of the machine is comprised of twenty four modules, each one of which consists of five stages of permanent poles. The FEA model of such AF rotor is illustrated in Figure 4.34.

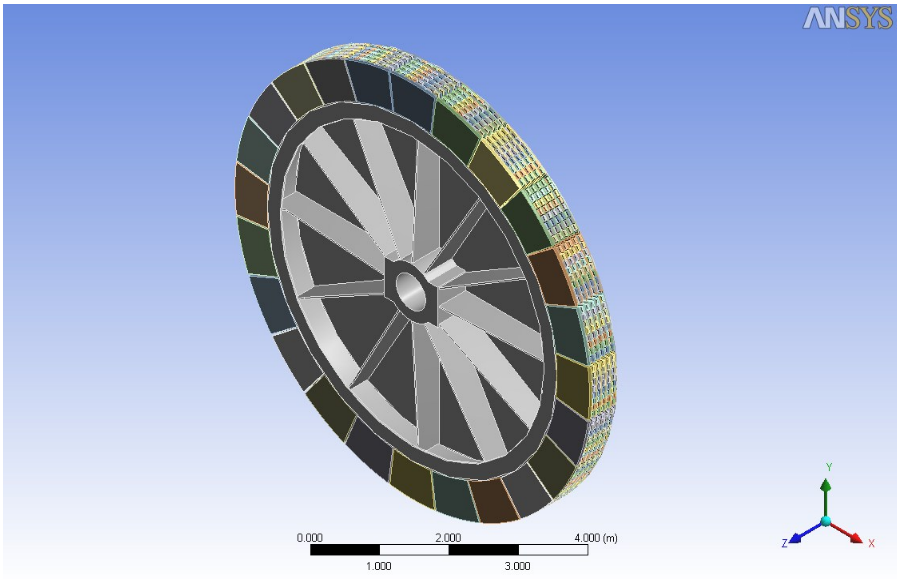

Figure 4.34 - The AF rotor structure

All the magnetic poles are assumed to be perfectly bonded with the steel C-cores. The C-core modules are also assumed to be bonded with the rotor support structure (Figure 4.35).

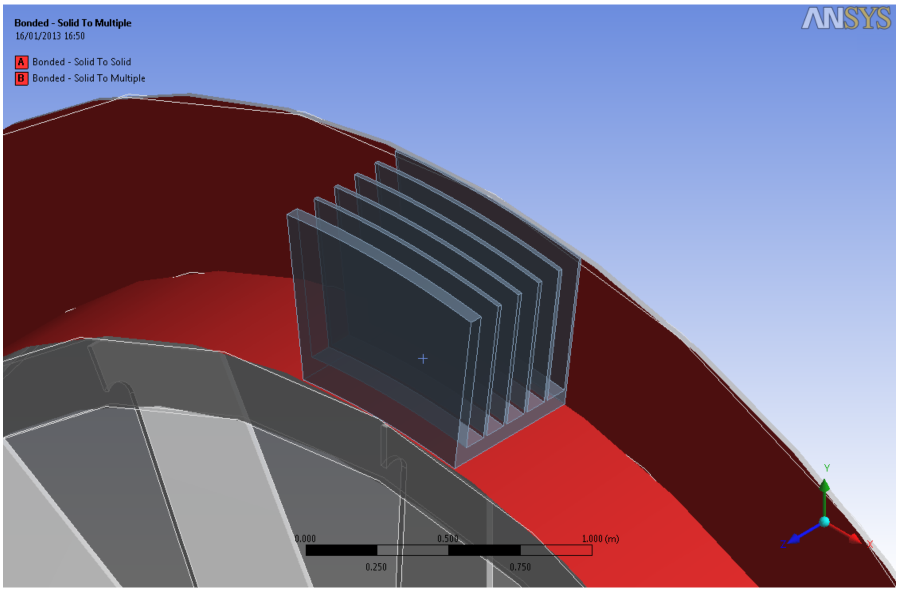

Figure 4.35 - Bonded surfaces of C-cored modules

The total mass of the structure was 48 tons. The dimensions that describe the rotor structure are illustrated in detail in Figure 4.36 and Figure 4.37.

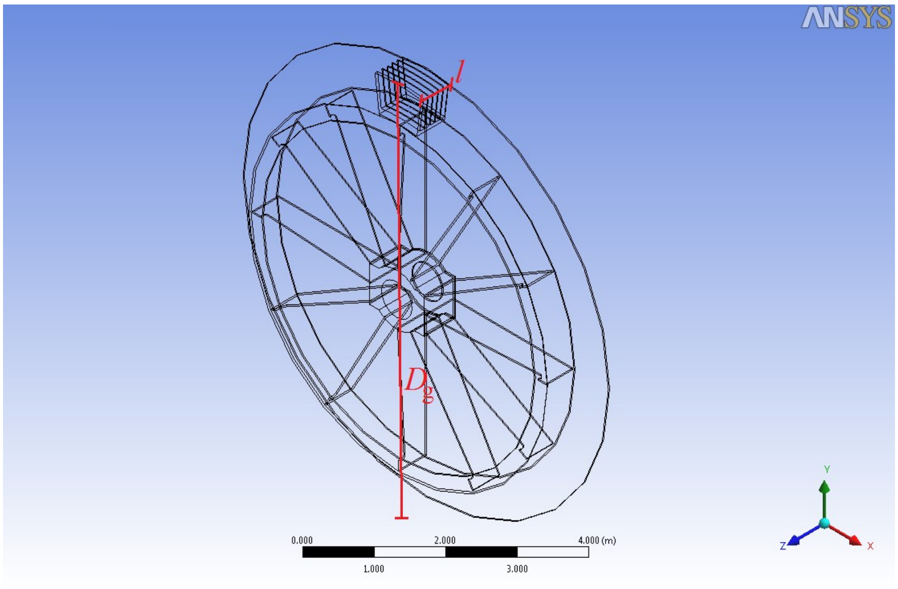

Figure 4.36 - The airgap diameter (D_g) and the axial length (l) of the AF rotor

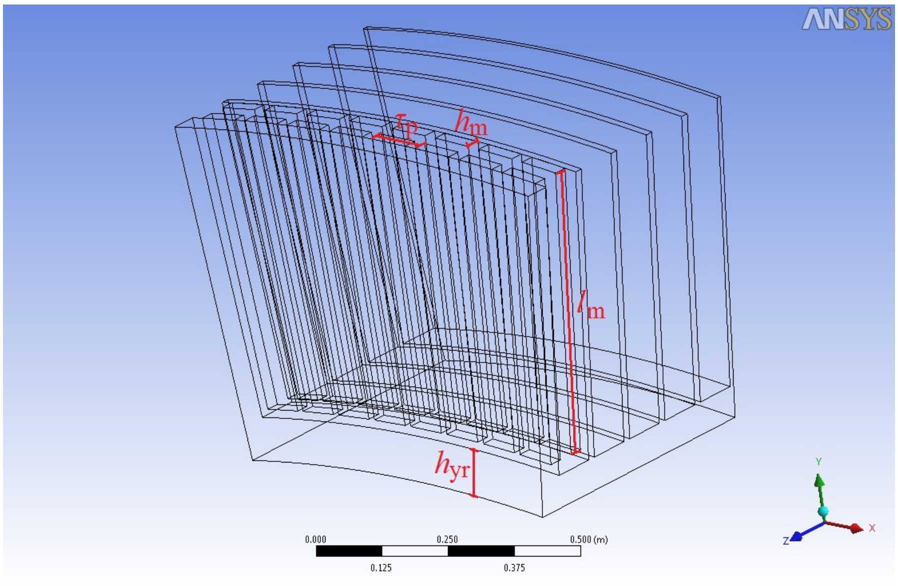

Figure 4.37 - The magnet height (h_m), the magnet length (l_m), the pole pitch (τ_p) and the yoke height (h_{yr}) of the AF rotor

The stator of the AF aircored machine is comprised of twenty four modules, each one of which consists of five stages of epoxy pockets that enclose the copper windings. The support structure of the stator is the same as that of the AF rotor with its back iron holding the epoxy pockets in position within the rotor's C-cores. The support structure is made of structural steel while the stator's plates from epoxy resin material. The copper windings were not included in this model for simplicity. The FEA model of the AF aircored stator is illustrated in Figure 4.38.

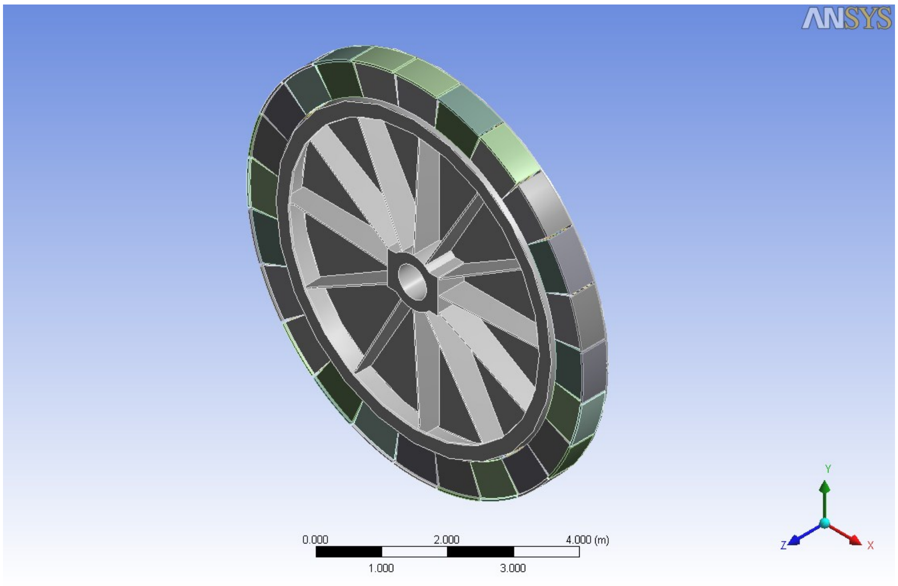

Figure 4.38 - The AF stator structure

All the stator modules are assumed to be perfectly bonded with the stator's back iron (Figure 4.39).

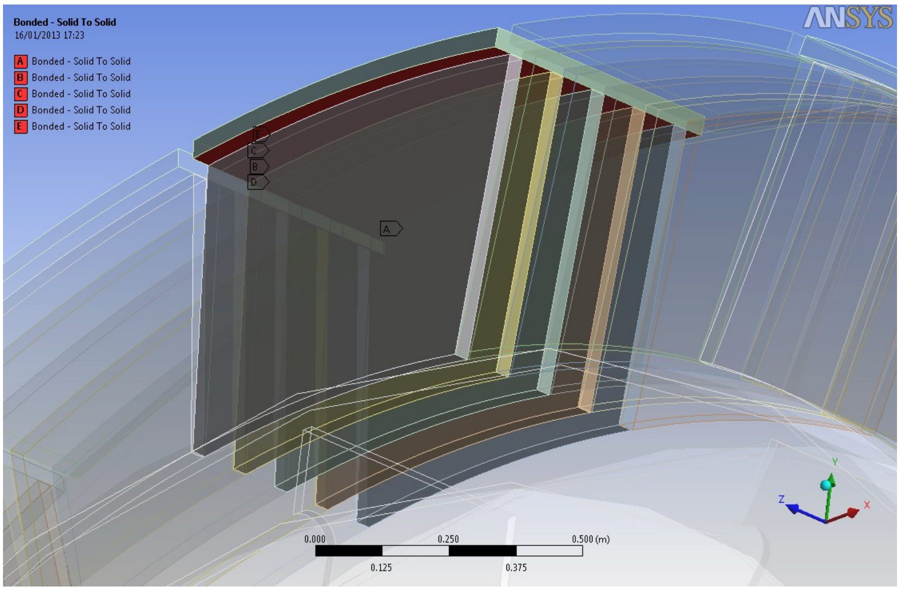

Figure 4.39 - Bonded surfaces of stator modules

The total mass of the structure was 25 tons. The dimensions that describe the stator structure are illustrated in detail in Figure 4.40 and Figure 4.41.

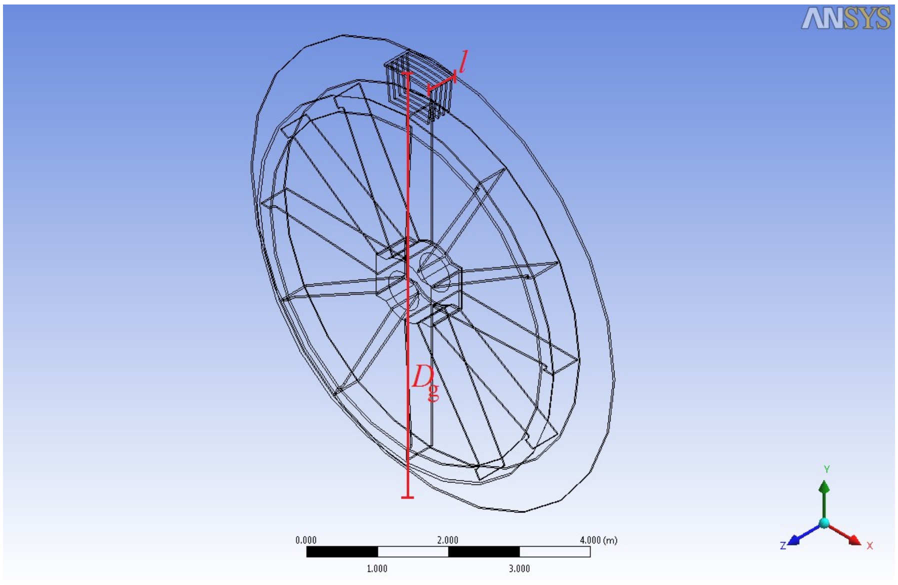

Figure 4.40 - The airgap diameter (D_g) and the axial length (l) of the AF stator

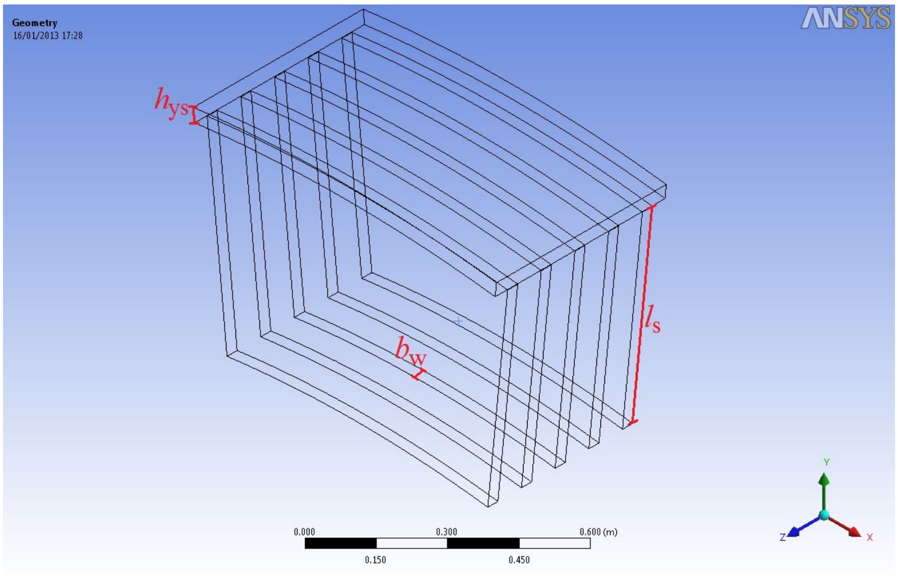

Figure 4.41 - The winding space lenght (l_s), the winding space width (b_w) and the yoke height (h_{ys}) of the AF stator

4.5 Conclusions

The potential lightweight topologies that were chosen from literature were modelled in this chapter with the help of an FEA tool. All support structures are made of structural steel while the magnet poles are made of NdFeB material. All models were simulated without the necessary copper windings in an attempt to simplify the models and reduce hardware requirements.

The provided structural dimensions correspond to a 5MW PMDD machine and the resulting masses are summarized in Table 4.5.

Generator Structure	**Mass (tons)**
RF Disc Rotor	41
RF Disc Stator	70
RF Armed Rotor	23
RF Armed Stator	37
TF-1 Rotor	48
TF-1 Stator	30
TF-2 Rotor	27
TF-2 Stator	35
AF Rotor	48
AF Stator	25

Table 4.5 - Resulting masses of the PMDD generator structural models

From these results it can be derived that the RF machine with discs is heavier compared to the RF machine with arms. TF-2 topology is also lighter than the TF-1 alternative. In general comparison, the RF machine with discs is the heaviest among the tested ones with total mass 122 tons while the AF aircored machine is the lightest with only 73 tons total mass. However the AF machine has more requirements in PM material as it has the largest number of pole pairs compared to the other topologies.

The models presented in this chapter will be tested against the static and dynamic forces that apply to such wind turbine generators in the following chapter. Results from the structural analysis will be used to draw valuable conclusions regarding the stiffness of each suggested topology according to the resulting deflections, stresses and natural frequencies. Attempt to minimise the mass of the suggested machines will be also made according to these results.

Chapter 5

Structural Comparison of PMDD Topologies

5.1 Introduction

In this chapter, the structural models of the 5MW direct drive machines that were created in chapter 4 will be tested for their structural stiffness with the help of the suggested FEA tool [175]. The structures are tested against static or dynamic forces that apply to such wind turbine generators.

The first step towards this analysis would be the description of the structural forces that apply on large PMDD generators for wind turbines. Once the loads are described and calculated they are applied on the structural models. Deflection limitation criteria are necessary to be set at this point in order to attain a structure stiff enough to maintain the airgap clearance against these forces during operation. The original structural dimensions of the PMDD generator topologies will be increased or decreased according to the resulting deflection in order to achieve the required stiffness. The original aspect ratio and the electromagnetic parameters of the machines were predefined in chapter 4, thus the parameters that are allowed to vary are the yoke height (h_{yr}, h_{ys}), the disc thickness (t_{d}) or the arms' width (d) of each support structure. Once the final structural parameters are acquired, a dynamic and a modal analysis are performed.

The final results from the structural analysis will be used to draw valuable conclusions regarding the stiffness of each suggested topology according to the resulting deflections, stresses and natural frequencies.

5.2 The structural forces

The main forces that apply on a PMDD generator are similar to those of any wind turbine generator. It is their large size though that increases the magnitude of those loads and makes their structures more demanding in terms of stiffness and resistance to fatigue. The most common loads, as described in [177], are listed in this section.

The shear stress (σ). This is the useful airgap force that gives rise to torque. Because the shear stress is perpendicular to the airgap it does not serve to close the airgap. A typical value of $\sigma = 45$ kN/m² was used for this research.

The normal component of Maxwell stress (q). q (N/m²) is the attraction force directed across the gap trying to close it. The normal component of Maxwell stress is proportional to the square of the peak flux density in the airgap as shown in (4.1).

$$q = B_g^2/(2\mu_o) \tag{4.1}$$

where B_g is the peak flux density in the airgap and μ_o is the permeability of free space with $\mu_o = 1.2566 \times 10^{-6}$ H/m.

The gravitational force. Gravity acts in the vertical direction during operation. The acceleration due to gravity was set $g = 9.81$ m/s².

The thermal expansion due to heat. The heat generated in the windings during operation leads to a temperature rise in the machine parts. The temperature difference can lead to deflections that can alter the airgap clearance. However, adequate cooling was assumed for the given generator models, thus thermal expansion was not included in the structural analysis.

The forces and moments from the rotor blades: These forces and moments can pose a threat to the airgap clearance as they include the mass of the rotor blades, the horizontal and vertical wind shear, the yaw error and the inertial effects. The Alstom Pure Torque® System was assumed for supporting the generator structures, thus these forces will not be modelled as they will be directed to the tower of the wind turbine and not into the airgap.

The torsional deflection due to the centripetal force: The rotational velocity leads to a centripetal force that is a radially outward and into the airgap and a moment that acts on the rotor's arms or disc. This force can cause a torsional deflection on the arms or the discs of the machine. The same moment acts on the stator structure as the magnets pass by the stator and interact with the copper winding. The torque T for each generator structure was calculated according to equation (3.2) for a rotational speed of ω = 12 rpm.

For the structural modelling and testing in this research, only the loads that could be a threat to reduce the airgap clearance were included. The main deflection forces that were taken into consideration were the radial deflection that is caused due to the normal component of the Maxwell stress q, the horizontal/axial deflection due to gravity and the torsional deflection due to the centripetal force. Figure 5.1 depicts the three major forces acting on the structure of a disc rotor.

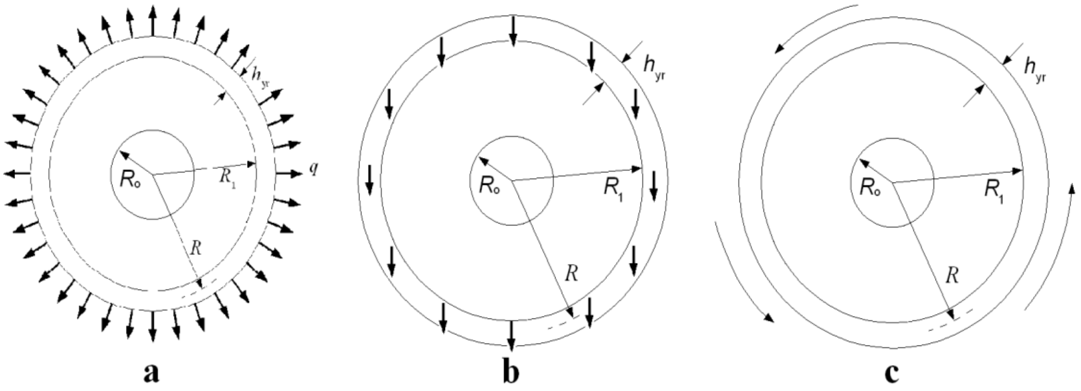

Figure 5.1 - (a) Normal component of Maxwell stress q (b) Gravity acting on the vertical direction (c) Centripetal force

5.3 Static structural analysis

Before an analysis can be made within the environment of the FEA tool, the tested geometry has to be turned into a mesh of geometrical elements. There are two basic considerations when creating such a mesh; the shape of the elements and their size.

The shape of the elements can be either free with no restrictions or mapped which contains hexahedrical elements only. A free mesh was created for all the models described in this thesis as it can be automatically generated in ANSYS and can better describe geometries that have irregular volumes and multiple elements in them [175]. The size of the elements is also critical for any FEA analysis as it has a direct effect on the presented results. Coarse meshes (large element size) are easier for the system to create and reduce the run time of the analysis to a minimum. However they might not give accurate enough results for critical areas such sharp corners, cracks, and areas with varying thickness or surfaces where different materials interact. On the other hand, finer meshes (small element size) require extra resources from the system, increase the run time of the analysis and might not converge on a solution. The size can be free for the created elements, with a minimum or maximum limit, or constant. A constant element size was chosen as it gives a better and more intuitive control over the results.

A simple way to identify an appropriate mesh size for a FEA simulation is to start with a coarse size and gradually decrease the element size in order to determine the size at which the system converges on a solution that will not be significantly altered by decreasing the mesh size any further.

Figure 5.2 shows how the maximum total deflection in the airgap of a RF rotor with disc changes for a range of element sizes. As the size decreases, the maximum deflection converges on a specific value. A finer mesh than 50mm could not be achieved due to hardware and software limitations. The element size that was chosen for the purposes of this research was 100mm as this was the value on which the total deflection would converge. Any further reduction to the size of the mesh would unnecessarily slow down the performance of the system only to give similar results. The same mesh size was used for all other topologies tested in this thesis.

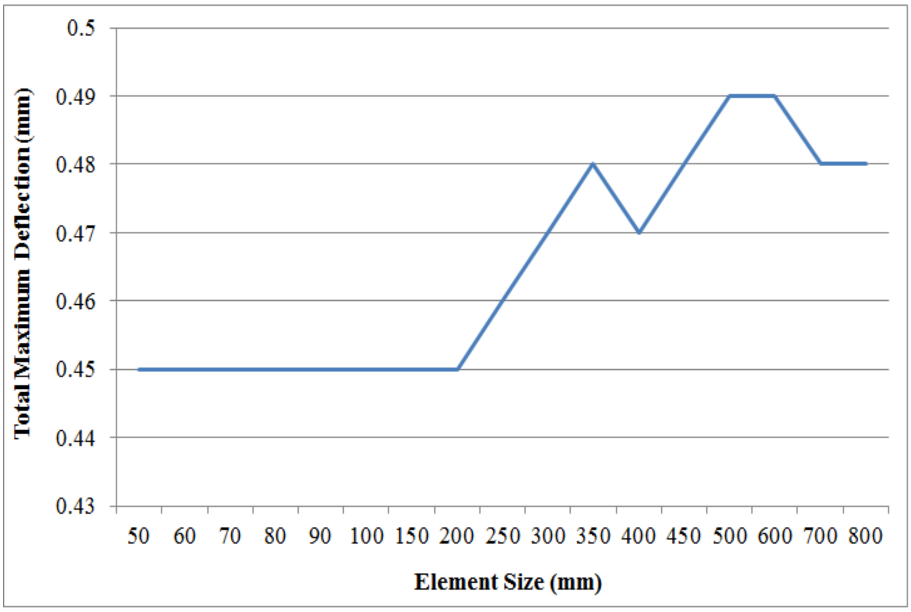

Figure 5.2 - The total deflection in the airgap of a RF rotor calculated with for a range of element sizes

Deflections calculated from the FEA tool were used as criteria for each structure to ensure a robust design. The allowable values were 10% of the airgap clearance for the deflection in the airgap due to Maxwell stress, 2% of the axial length for the gravitational deflection and a relative twist of 0.01° for torsional deflection (≈0.55 mm for each structure). When the deflection in the airgap exceeded the maximum allowed value, the yoke thickness was increased. In case the deflection due to gravity or the deflection due to torque exceeded limitations, the disc thickness or the arms' depth was increased.

Figure 5.3 shows the loads that apply on the designed model of the RF rotor with disc. The normal component of the Maxwell stress applied on the surface of the permanent magnet poles of the rotor and was calculated at q = 480 kPa. The torque was applied on the same faces as q and was calculated at T = 3.95 MNm.

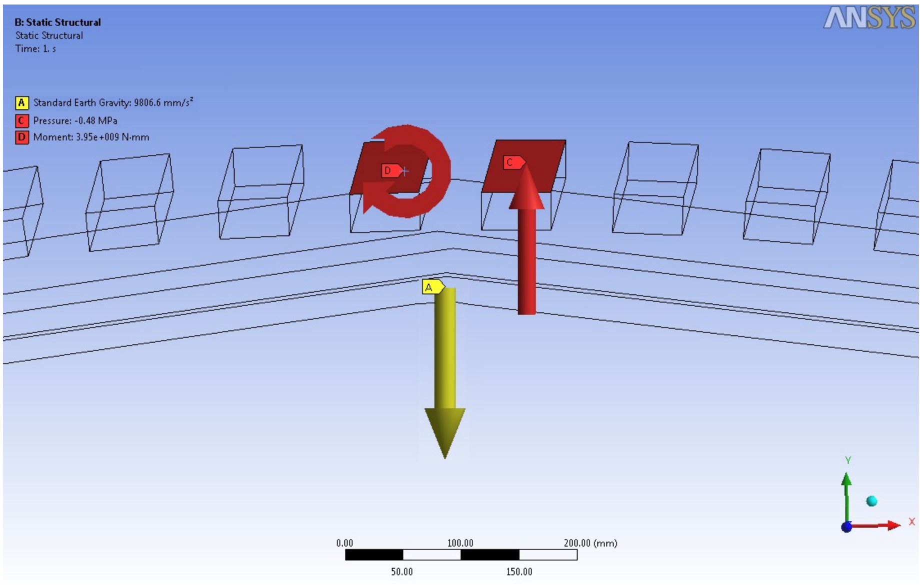

Figure 5.3 - The structural loads acting on the magnet surface of a RF rotor with disc

The total deflection in the airgap was $u_A = 0.45$ mm (Figure 5.4).

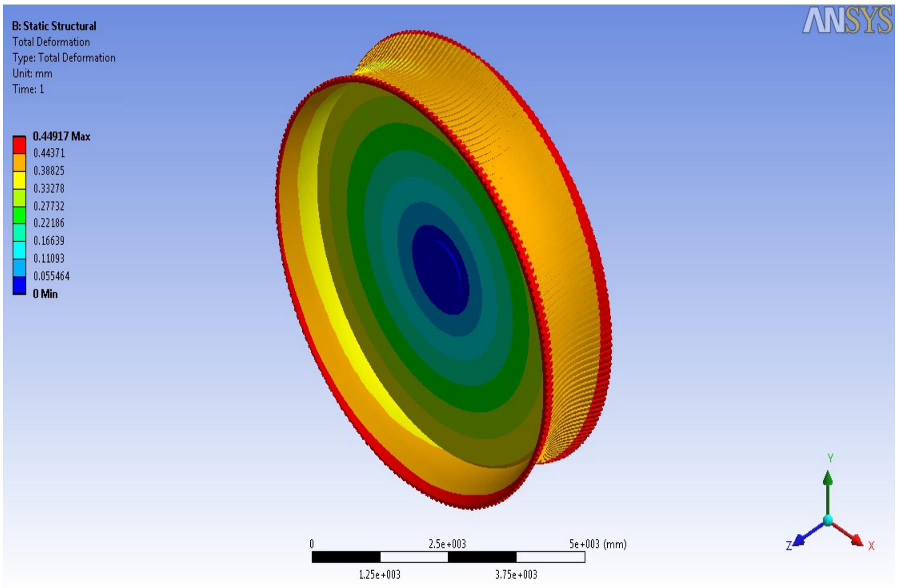

Figure 5.4 - Total deflection in the airgap of the RF rotor with disc

h_{yr} was increased from 40 mm to 60 mm while t_d was increased from 100 mm to 120 mm. The total mass of the structure increased compared to the original design from 41 to 51 tons. The resulting deflection was eventually less than the defined limit as illustrated in Figure 5.5.

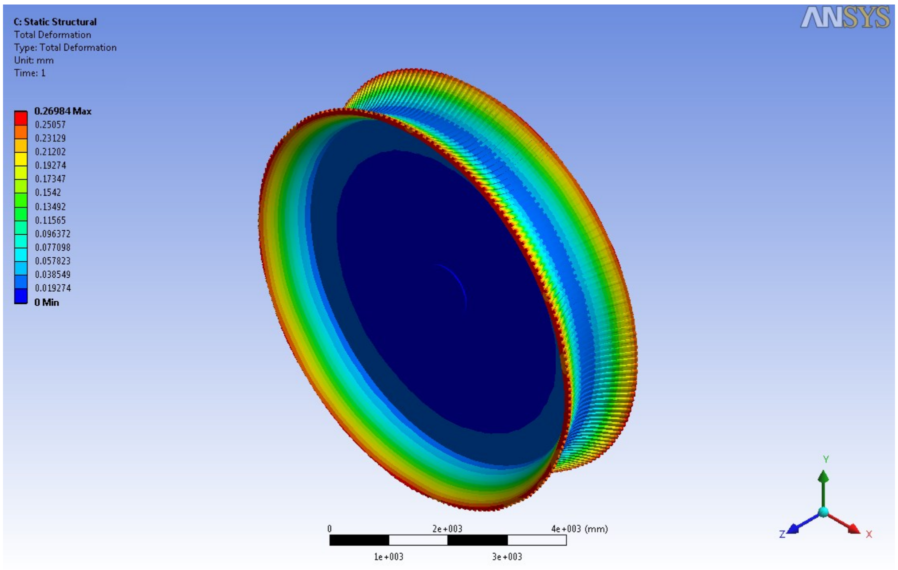

Figure 5.5 - Resulting deflection in the airgap of the RF rotor with disc

The same analysis was followed for the RF stator structure with discs. Both the normal component of the Maxwell stress and the torque were applied on the surface of the stator teeth. The forces acting on the stator with discs FEA model are illustrated in Figure 5.6.

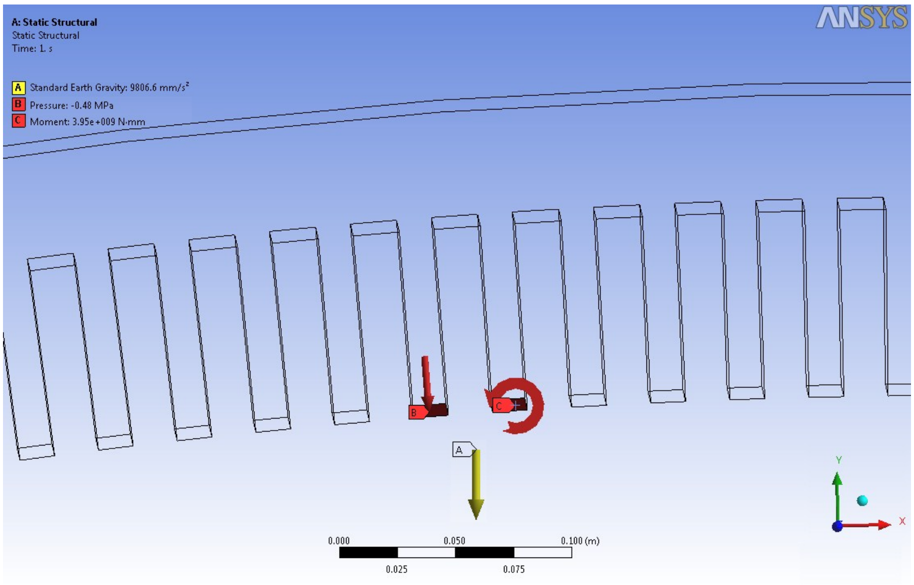

Figure 5.6 - The structural loads acting on the tooth surface of the RF stator with discs

The total deflection in the airgap was $u_A = 0.21$ mm (Figure 5.7).

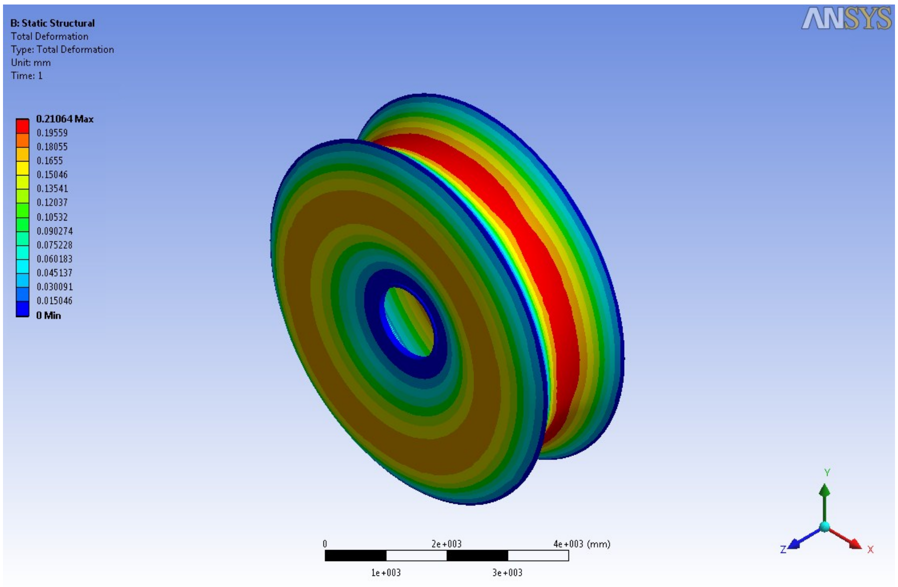

Figure 5.7 - Total deflection in the airgap of the RF stator with discs

The results indicated that structural mass could be removed from the structure without compromising its stiffness. h_{ys} was kept at 40 mm while t_d was decreased from 100 mm to 64 mm. The total mass of the structure decreased compared to the original design from 70 to 52 tons. The resulting deflections were kept within the defined limit as illustrated in Figure 5.8.

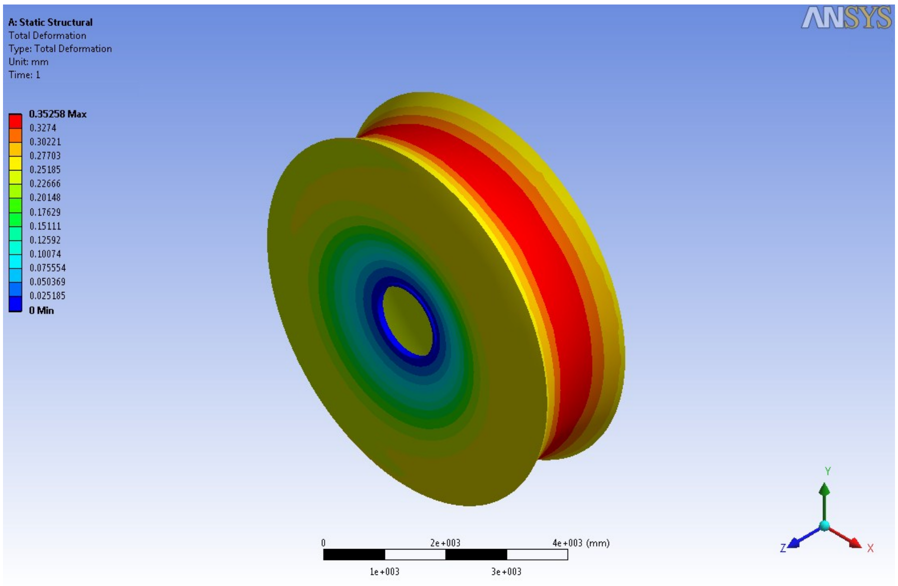

Figure 5.8 - Resulting deflection in the airgap of the RF stator with disc

The same structural analysis was made for the RF structures with arms. Both radial and tangential deflections were above the defined limit for both structures, thus the yoke height and the arms' depth had to be increased. The variations in the structural parameters of all RF structures and their masses are summarized in Table 5.1.

	h_{yr} (mm)	h_{ys} (mm)	t_d (mm)	d (mm)	mass (tons)
RF Disc Rotor	40 → 60	-	100 → 120	-	41 → 51
RF Disc Stator	-	40 → 40	100 → 64	-	70 → 50
RF Armed Rotor	40 → 90	-	-	100 → 350	23 → 60
RF Armed Stator	-	40 → 50	-	100 → 250	37 → 64

Table 5.1 - Structural parameters and masses of the RF structures

Figure 5.9 shows the loads that apply on the TF-1 rotor. The normal component of the Maxwell stress applied on the surface of the permanent magnet poles of the rotor and was calculated at q = 807 kPa. The torque applied on the same faces as q and was calculated at T = 3.95 MNm.

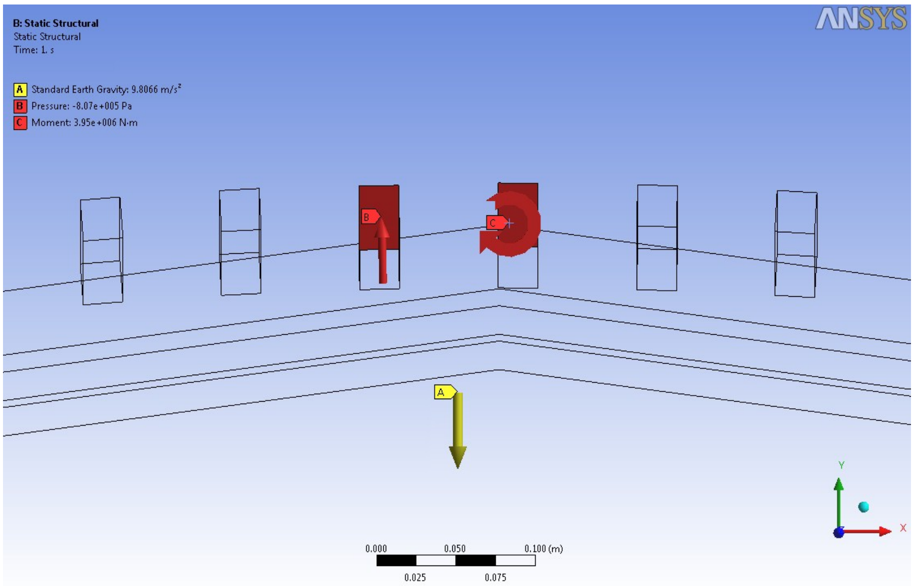

Figure 5.9 - The structural loads acting on the magnet surface of the TF-1 rotor

The total deflection in the airgap was u_A = 0.04 mm (Figure 5.10).

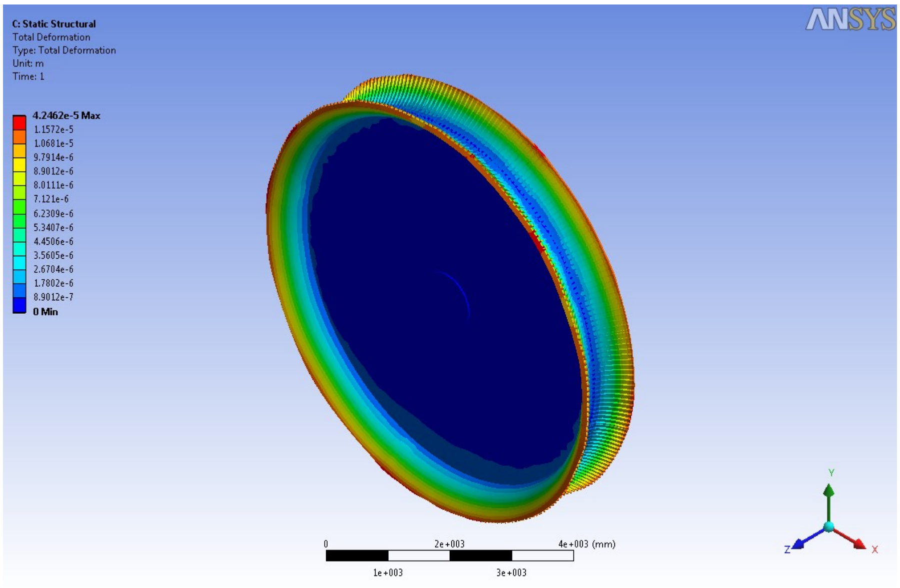

Figure 5.10 - Total deflection in the airgap of the TF-1 rotor

Since the deflection in the airgap was significantly lower than the defined limit, h_{yr} could be decreased from 130.4 mm to 50 mm while t_d was increased from 100 mm to 120 mm to decrease the deflection due to torque. The total mass of the structure decreased compared to the original design from 48 to 40 tons. The resulting deflections were eventually within the defined limit as illustrated in Figure 5.11.

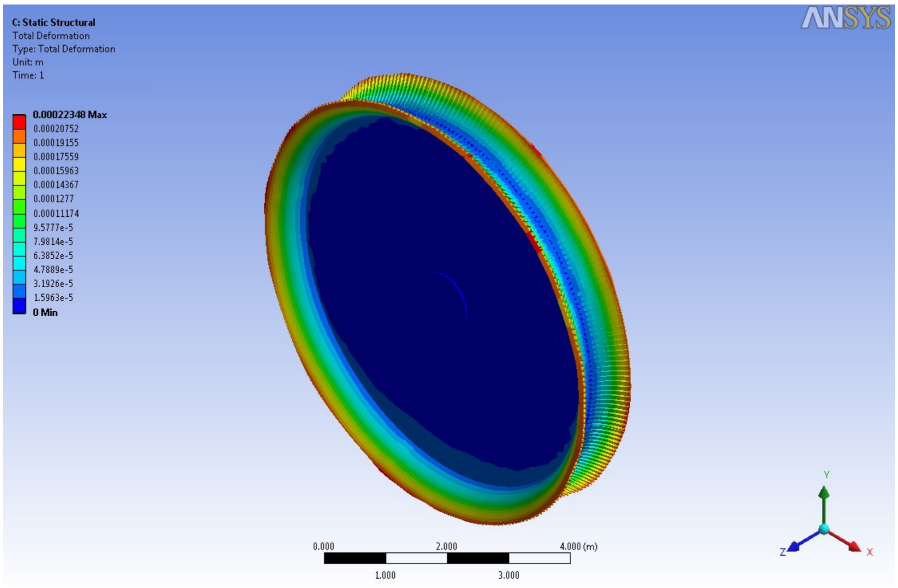

Figure 5.11 - Resulting deflection in the airgap of the TF-1 rotor

The same analysis was followed for the TF-1 stator structure. The normal component of the Maxwell stress and the torque applied on the stator's teeth as illustrated in Figure 5.12.

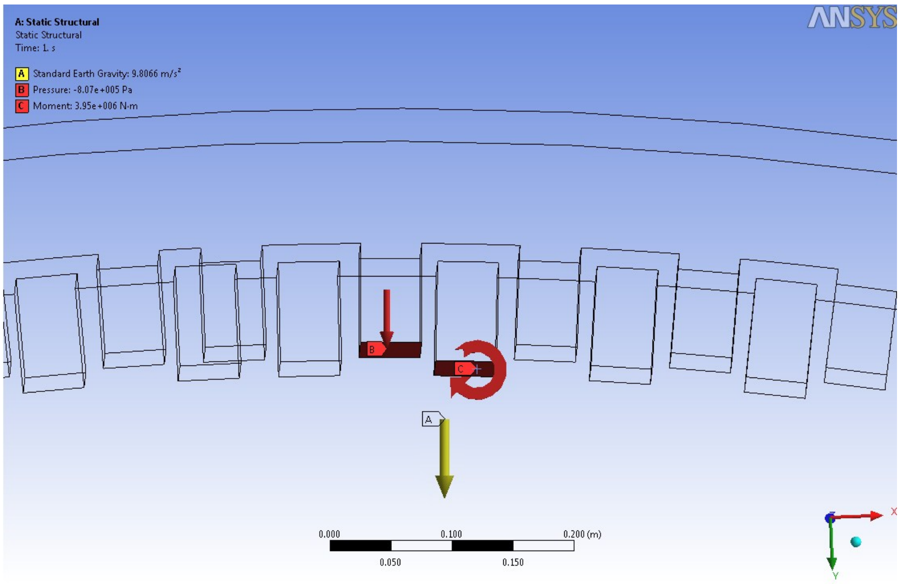

Figure 5.12 - The structural loads acting on the tooth surface of the TF-1 stator

The total deflection in the airgap was u_A = 0.73 mm (Figure 5.13).

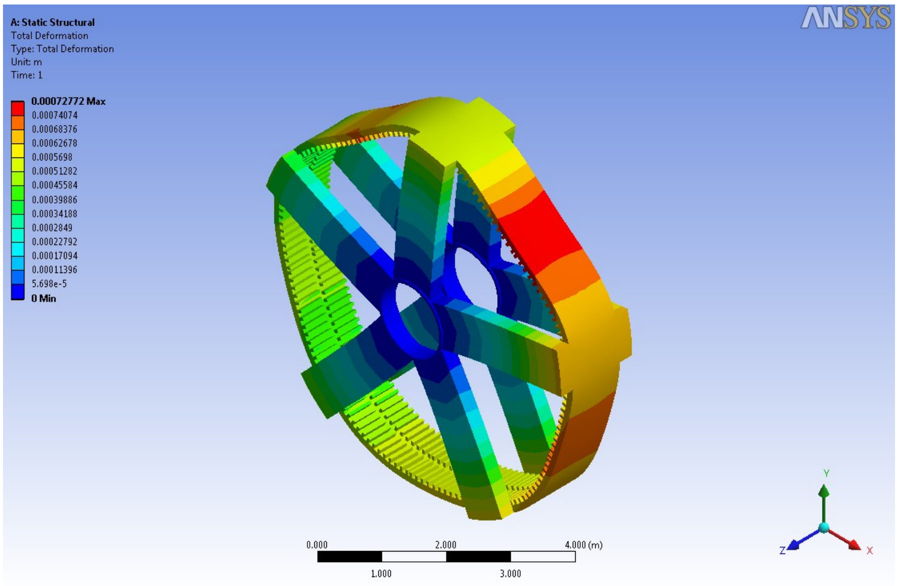

Figure 5.13 - Total deflection in the airgap of the TF-1 stator

h_{ys} had to be increased from 130.4 mm to 191 mm and d from 100 mm to 250 mm to bring both deflections within the defined limit. The total mass of the structure increased compared to the original design from 30 to 65 tons. The resulting deflections can be seen in Figure 5.14.

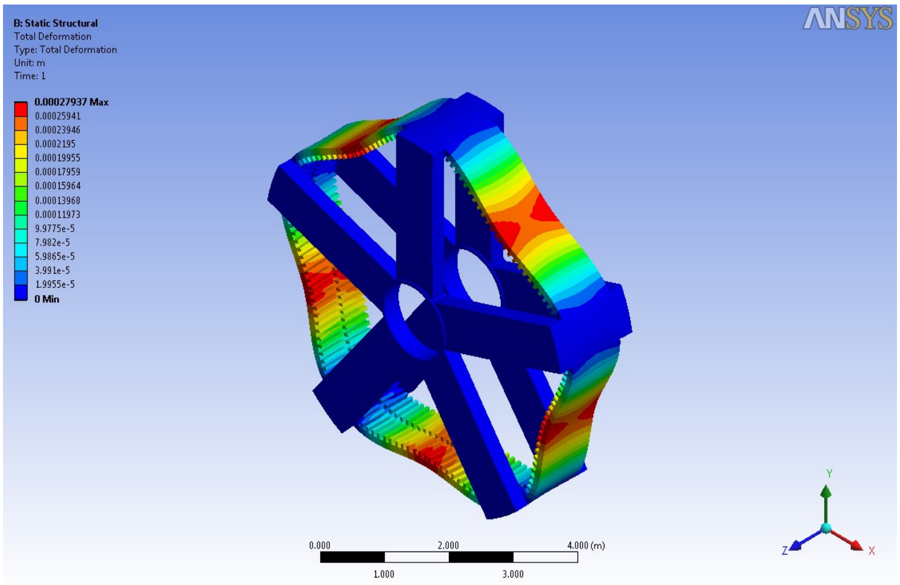

Figure 5.14 - Resulting deflection in the airgap of the TF-1 stator

Figure 5.15 shows the structural loads that apply on the FEA model of the TF-2 rotor. Unlike previous cases which have a radially oriented airgap, TF-2 has its airgap oriented in the axial direction. The normal component of the Maxwell stress was applied on both sides of the rotor poles and was calculated at q = 230 kPa. The torque was applied on the same faces as q and was calculated at T = 3.95 MNm.

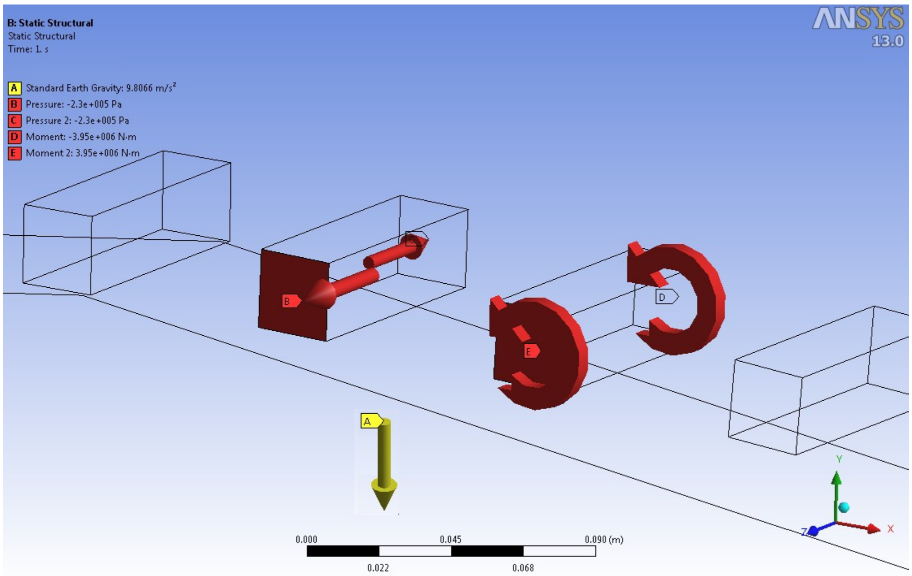

Figure 5.15 - The structural loads acting on the magnet surface of the TF-2 rotor

The total deflection in the airgap was $u_A = 0.00006$ mm (Figure 5.16).

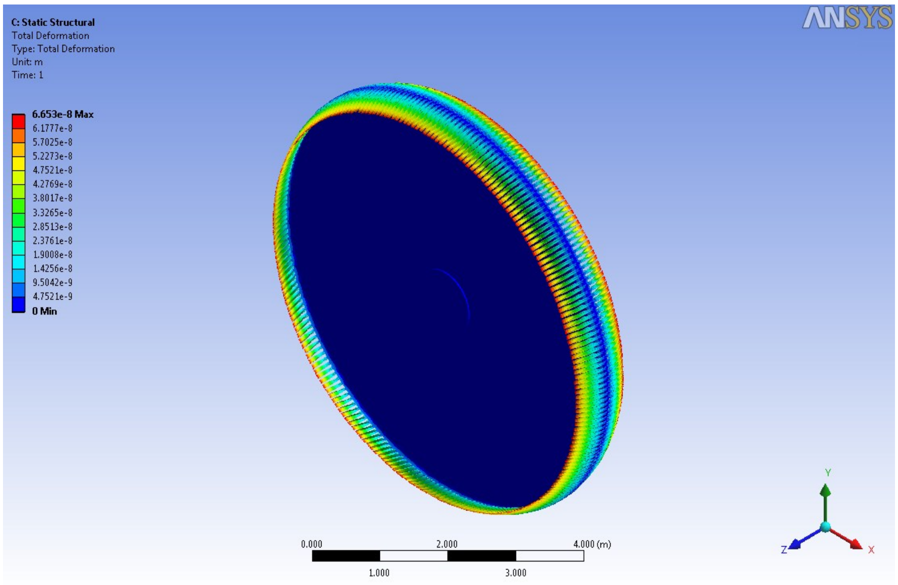

Figure 5.16 - Total deflection in the airgap of the TF-2 rotor

Despite the fact that the total deflection in the airgap was below the limit, the dimensions of the TF-2 rotor were kept intact due to the specifications of this design which set the rotor's axial length to be less than the stator's winding space.

Figure 5.17 shows the loads that apply on the teeth of the TF-2 stator. The normal component of the Maxwell stress q and the torque T both were applied on the inner sides of the stator teeth.

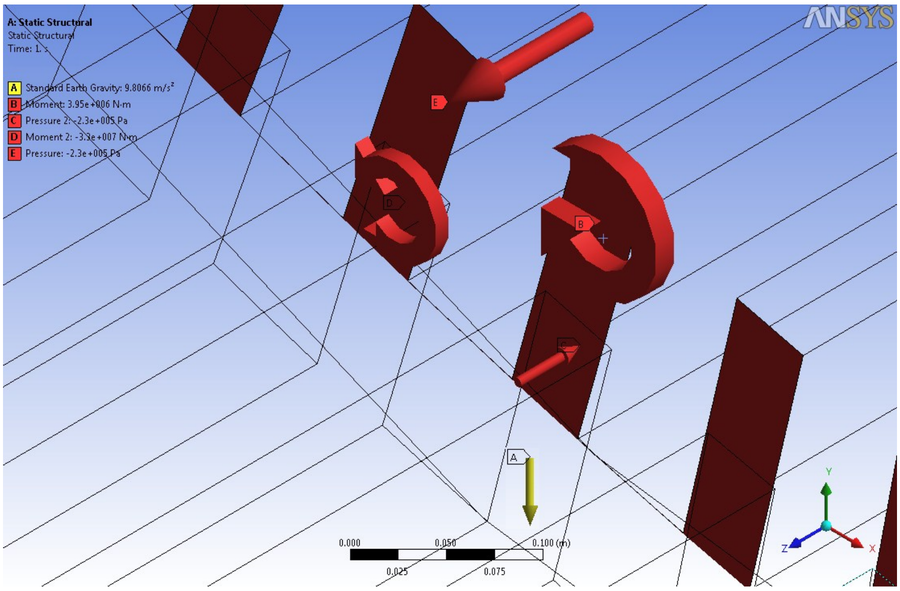

Figure 5.17 - The structural loads acting on the tooth surface of the TF-2 stator

The total deflection in the airgap was $u_A = 0.8$ mm (Figure 5.18).

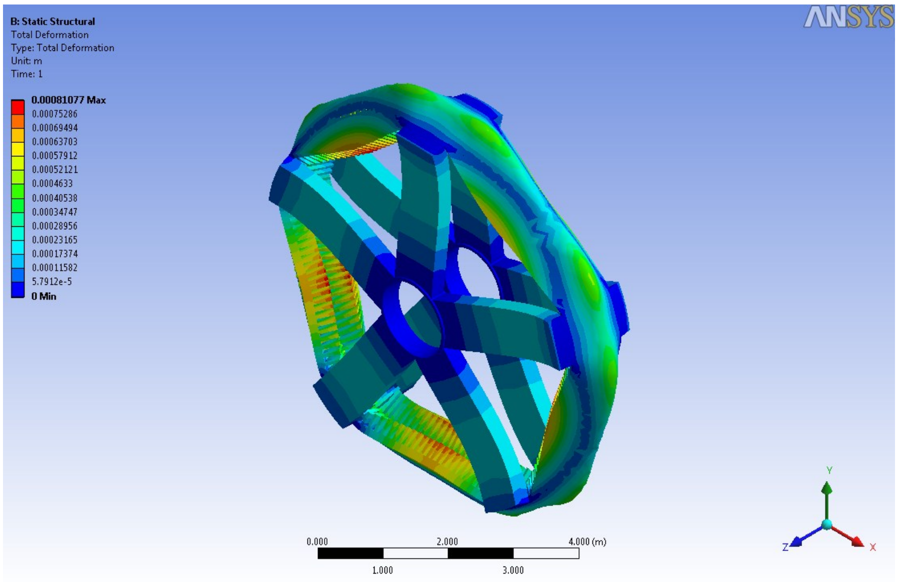

Figure 5.18 - Total deflection in the airgap of the TF-2 stator

h_{ys} had to be increased from 211.2 mm to 241.2 mm and d from 100 mm to 260 mm to bring the total deflection within the limit. The total mass of the structure increased compared to the original design from 35 to 68 tons. The resulting deflections can be seen in Figure 5.19.

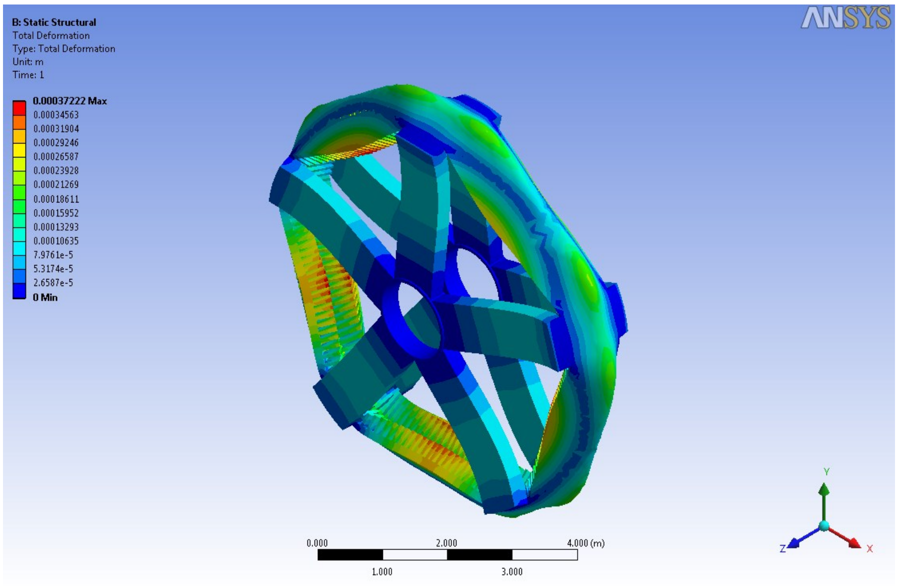

Figure 5.19 - Resulting deflection in the airgap of the TF-2 stator

The variations in the structural parameters of all TF structures and their masses are summarized in Table 5.2.

	h_{yr} (mm)	h_{ys} (mm)	t_d (mm)	d (mm)	mass (tons)
TF-1 Rotor	130 → 50	-	100 → 120	-	48 → 40
TF-1 Stator	-	130 → 191	-	100 → 250	30 → 65
TF-2 Rotor	130 → 130	-	100 → 100	-	27 → 27
TF-2 Stator	-	211 → 241	-	100 → 260	35 → 68

Table 5.2 - Structural parameters and masses of the TF structures

Figure 5.20 shows the FEA model of the AF aircored rotor and the loads that apply on it. The normal component of the Maxwell stress was applied on the magnet surfaces and was calculated at q = 112 kPa. The torque was applied on the same faces as q and was calculated at T = 1.14 MNm.

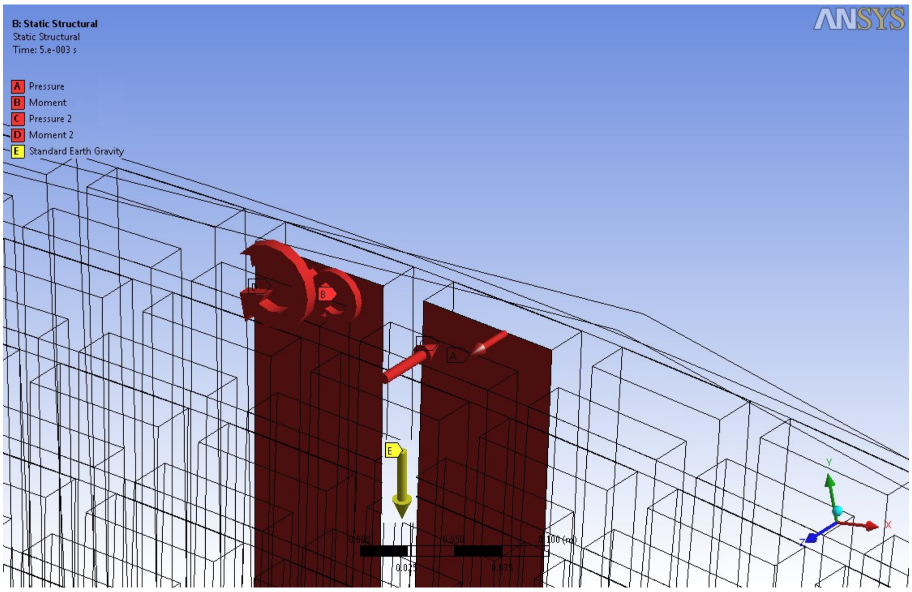

Figure 5.20 - The structural loads acting on the magnet surface of the AF rotor

The total deflection in the airgap was $u_A = 0.47$ mm as illustrated in Figure 5.21. The deflection criteria were within the limit, thus all structural parameters were kept intact.

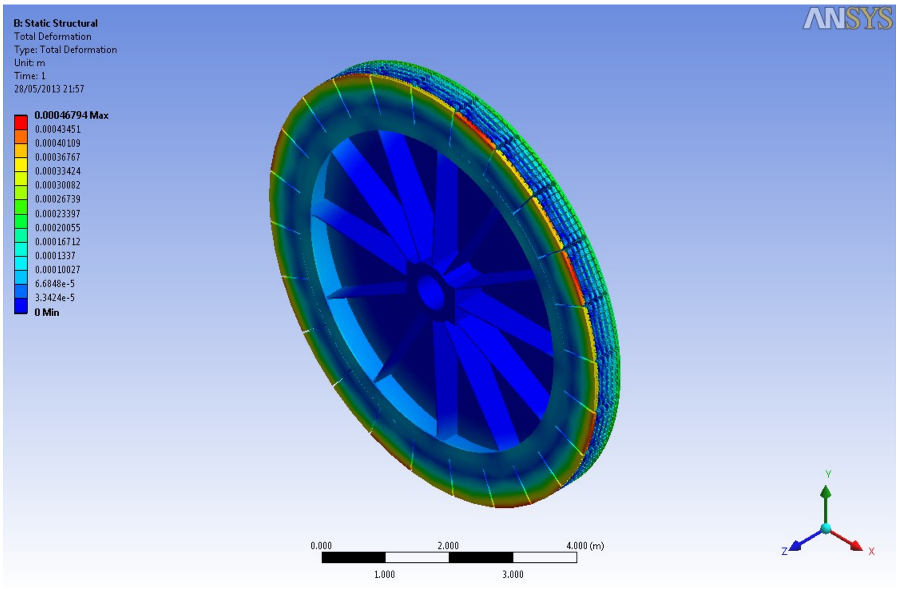

Figure 5.21 - Total deflection in the airgap of the AF rotor

Figure 5.22 shows the FEA model of the AF stator and the loads that apply on it. No attraction forces apply on this structure. The torque T was applied on both sides of the stator epoxy pockets.

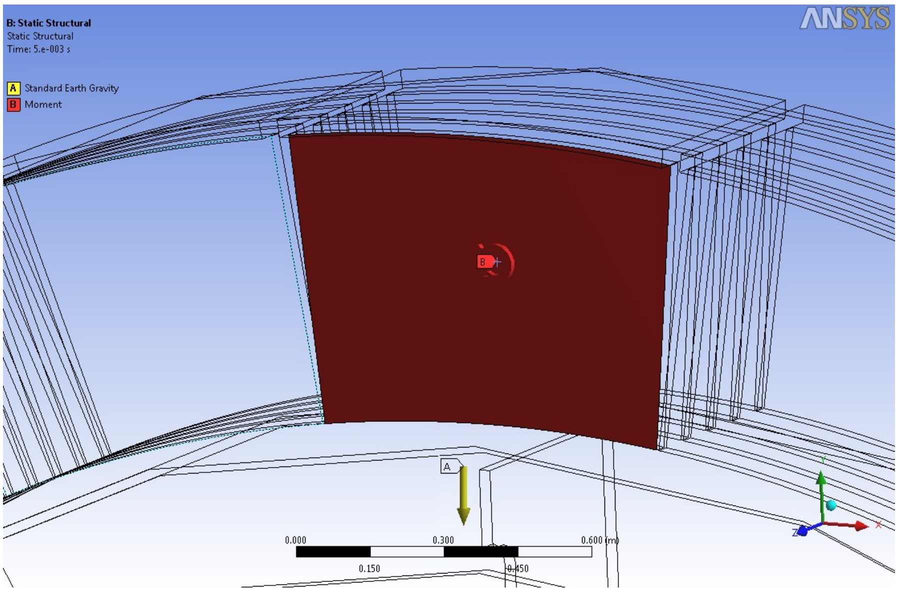

Figure 5.22 - The structural loads acting on the epoxy pockets of the AF stator

The total deflection in the airgap was u_A = 0.08 mm (Figure 5.23).

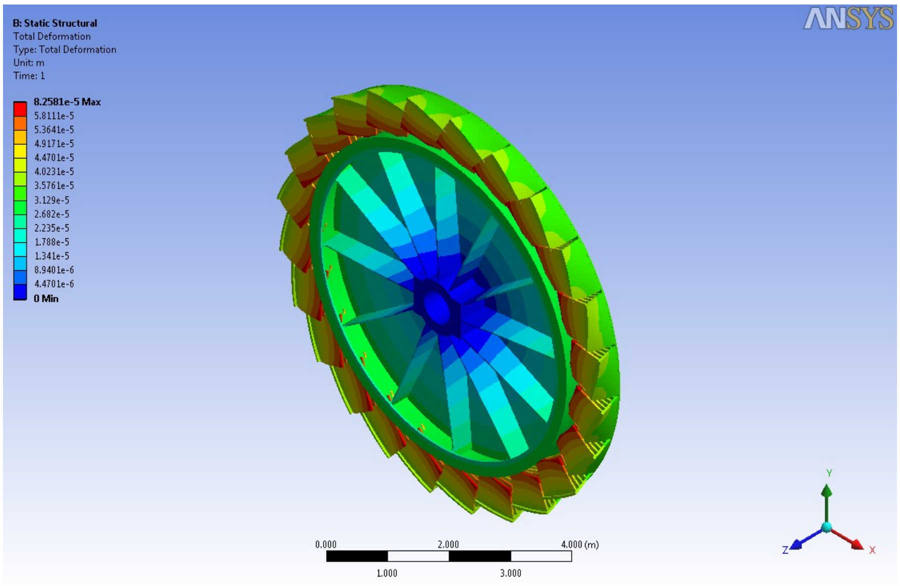

Figure 5.23 - Total deflection in the airgap of the AF stator

Both deflections were within limitations for the AF stator structure, thus all structural parameters were kept intact. Table 5.3 shows the maximum principal stresses on the rotor and stator back for all the modelled generator structures. The stress that applies on these surfaces was chosen as a criterion for potential creep on the support structures since this is where the active material is placed. The comparison to the yield stress of the materials in Table 4.1 indicates that none of the structures would be permanently deformed or broken during operation. The AF topology experiences the most stress compared to the rest topologies.

	Maximum stress (kPa)
RF Disc Rotor	16500
RF Disc Stator	14500
RF Armed Rotor	17700
RF Armed Stator	13100
TF-1 Rotor	15300
TF-1 Stator	19300
TF-2 Rotor	22400
TF-2 Stator	17500
AF Rotor	29300
AF Stator	18000

Table 5.3 - Resulting stresses of the PMDD generator models

The resulting masses of the generator models that occurred after the structural analysis in this section are summarised in Table 5.4.

	Mass (tons)
RF Disc Rotor	51
RF Disc Stator	52
RF Armed Rotor	60
RF Armed Stator	64
TF-1 Rotor	40
TF-1 Stator	65
TF-2 Rotor	27
TF-2 Stator	68
AF Rotor	48
AF Stator	25

Table 5.4 - Resulting masses of the PMDD generator models

The conventional RF topology with arms was the heaviest while the AF aircored topology was the most lightweight followed by the TF-2 machine.

Although all topologies were adjusted to have a maximum 10% total deflection in the airgap direction, TF-2 had a deflection of less than 0.001% of its airgap clearance. The structural mass of TF-2 was reduced in an attempt to determine how much of it could be deducted before reaching the same deflection in the airgap as the AF machine.

To reduce the mass of TF-2, the axial length and the depth of the arms were decreased. Since the torque requirements should remain the same as before, the diameter of the machine had to increase accordingly. The final dimensions of the machine are listed in Table 5.5.

	5 MW TF-2 PMDD
Airgap diameter, D_g (mm)	9500
Axial length, l (mm)	410
Number of phase, m	3
Airgap length, l_g (mm)	6.36
Magnet height, h_m (mm)	25.4
Pole pitch, τ_p (mm)	63.6
Number of pole pair, p	174
Rotor yoke height, h_{yr} (mm)	80
Stator yoke height, h_{ys} (mm)	200
Winding space height, h_s (mm)	80.8
Winding space width, b_w (mm)	80.8
Stator tooth width, b_t (mm)	50.9
Stator pole length, l_{sp} (mm)	164.6
Peak flux density in the airgap, B_g (T)	0.8

Table 5.5 - Dimensions of lightweight 5MW TF generator

The total mass of the generator was reduced from 95 to 83 tons. As expected, the deflection in the airgap and the tangential deflection increased. The airgap deflection increased to 0.28 mm which is 4.2% of the total airgap clearance (Figure 5.24). Although the deflection in the airgap did not reach the 10% limitation, the deduction of structural mass had to stop at this point since the deflection in the tangential direction started to exceed the limit. The AF topology remained the most lightweight of the suggested ones.

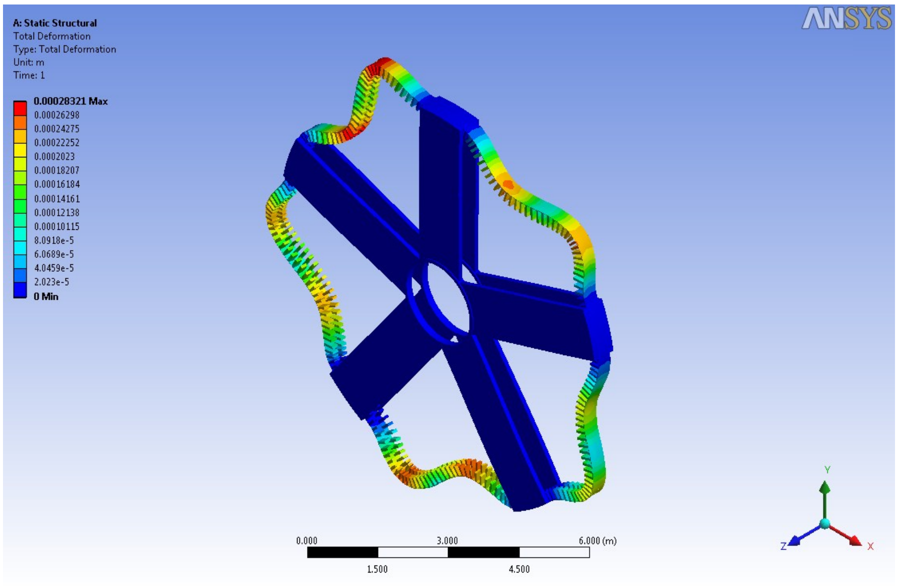

Figure 5.24 - Resulting deflection in the airgap for the lightweight TF-2 stator

5.4 Modal analysis

When natural frequencies of a rotating machine are excited, the machine inherently vibrates producing large amplitude oscillations to the forces acting on it. Such force imbalances should be avoided during operation as they can lead to increased fatigue in the generator structure and early failure.

Campbell diagrams can be used to determine the natural frequencies of a machine and evaluate whether they will be excited at regular intervals during nominal operation speeds.

The structural models generated from the structural analysis described in the last section (5.3) were tested for their natural frequencies. The results of modal analysis are detailed in Table 5.6 with all results in Hz.

	Mode 1 (Hz)	Mode 2 (Hz)	Mode 3 (Hz)	Mode 4 (Hz)	Mode 5 (Hz)	Mode 6 (Hz)	Mode 7 (Hz)
RF Disc Rotor	7	8	12	21	21	41	53
RF Disc Stator	14	46	47	60	98	103	108
RF Armed Rotor	25	25	28	35	36	41	47
RF Armed Stator	23	28	28	31	32	36	36
TF-1 Rotor	9	9	14	24	25	50	71
TF-1 Stator	24	27	28	41	42	42	43
TF-2 Rotor	11	11	12	14	14	31	31
TF-2 Stator	27	30	30	33	33	36	37
AF Rotor	15	16	19	19	20	22	39
AF Stator	13	13	13	13	13	13	13

Table 5.6 - Resulting natural frequencies of the PMDD generator models

Possible excitation frequencies that could trigger the natural frequencies of the tested generator structures are:

- The frequency of the machine’s rotation (1 Pu).
- The blade passing frequency that occurs as the blades of the rotor pass in front of the turbine’s tower (3 Pu)
- The fundamental electrical frequencies (p Pu, where p is the number of pole pairs per stage)

The Campbell diagrams presented in Figures 5.24 - 5.28 depict the natural and excitation frequencies of each structure as a function of the machine’s rotational speed ω (rpm). The average rotational speed for a PMDD wind turbine generating more than 3MW of power is between 5 and 15 rpm [20][26][63][88].

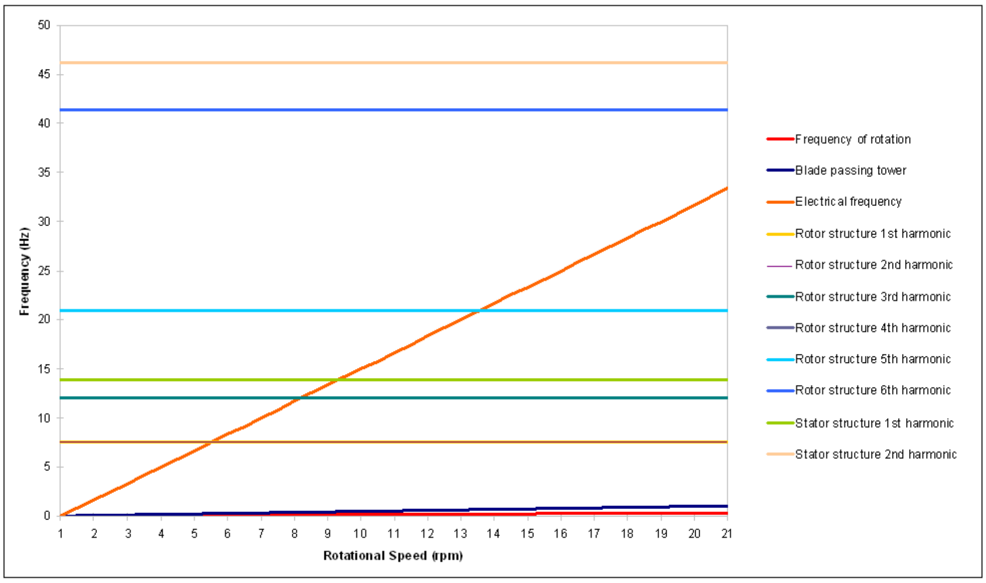

Figure 5.25 - Campbell diagram for natural frequencies matching the excitation frequencies of the RF generator with discs

Modes of the 1st up to the 5th may appear in the rotor of the RF generator with disc along with the 1st harmonic for the stator structure.

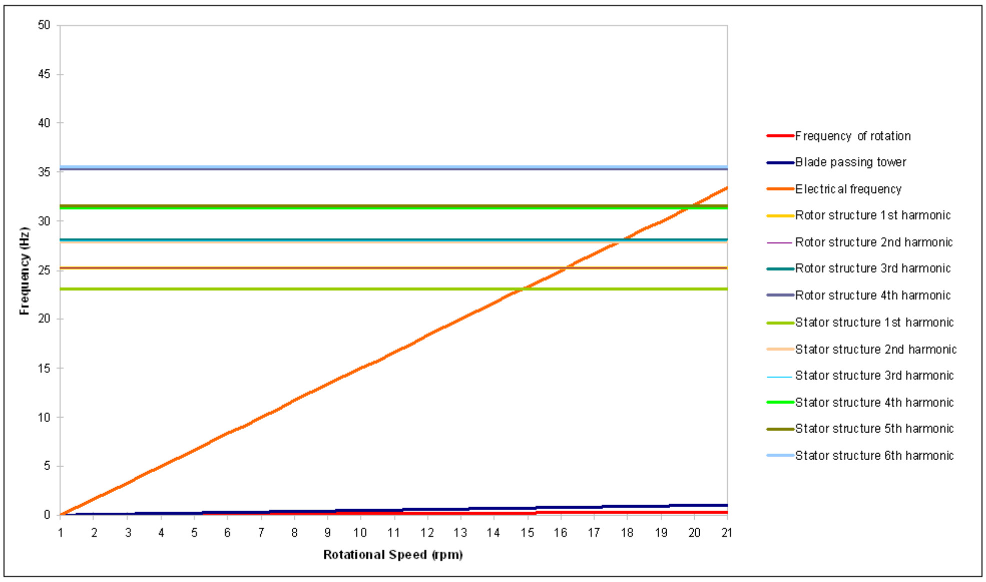

Figure 5.26 - Campbell diagram for natural frequencies matching the excitation frequencies of the RF generator with arms

Only the stator 1st harmonic may appear for the RF generator with arms during operation.

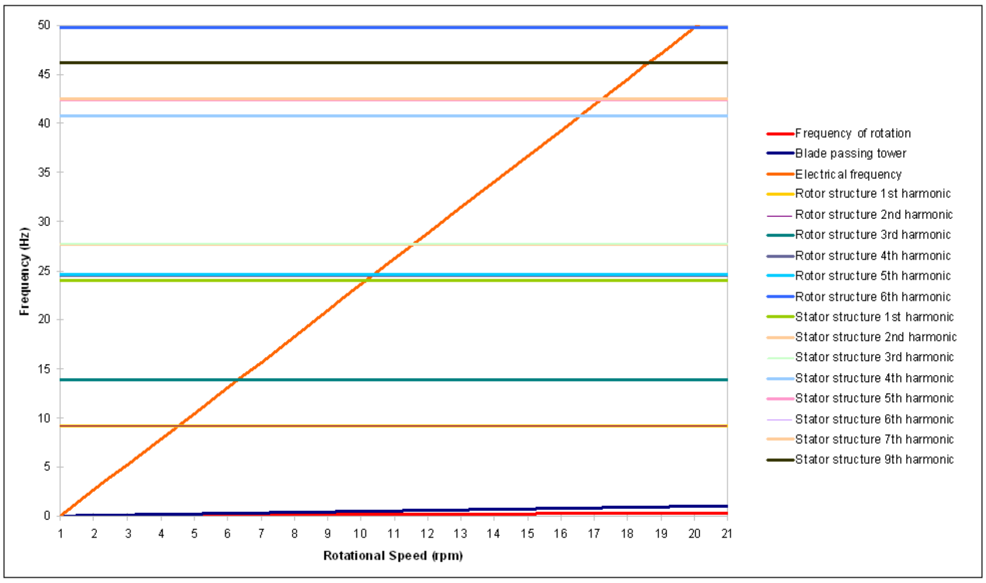

Figure 5.27 - Campbell diagram for natural frequencies matching the excitation frequencies of the TF-1 generator

Modal analysis showed that harmonics of the 3rd, 4th and 5th rate may appear in the rotor and lower harmonics of the 1st, 2nd and 3rd rate in the stator of the TF-1 machine.

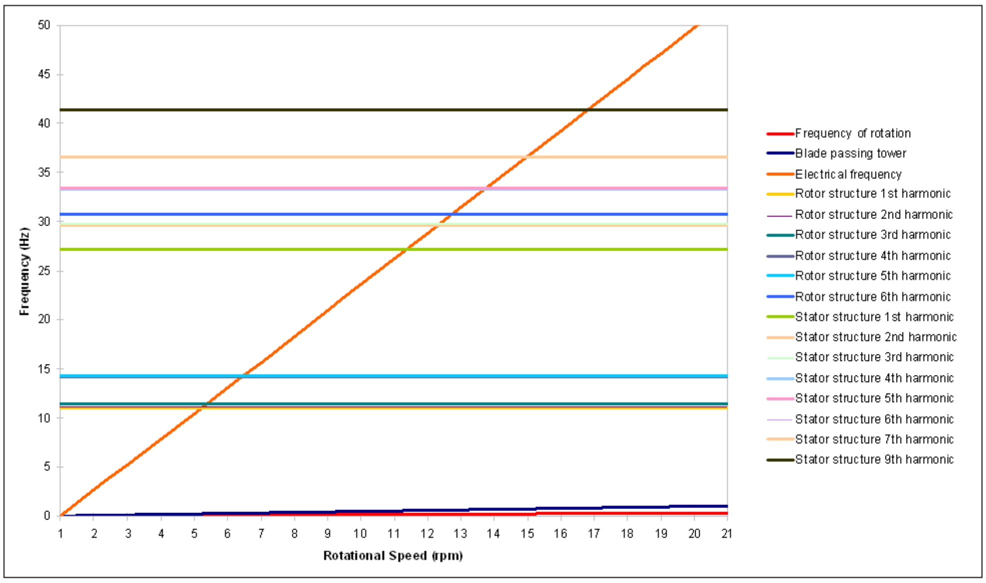

Figure 5.28 - Campbell diagram for natural frequencies matching the excitation frequencies of the TF-2 generator

Modes of the 1st up to the 7th may appear in both the rotor and the stator of the TF-2 machine.

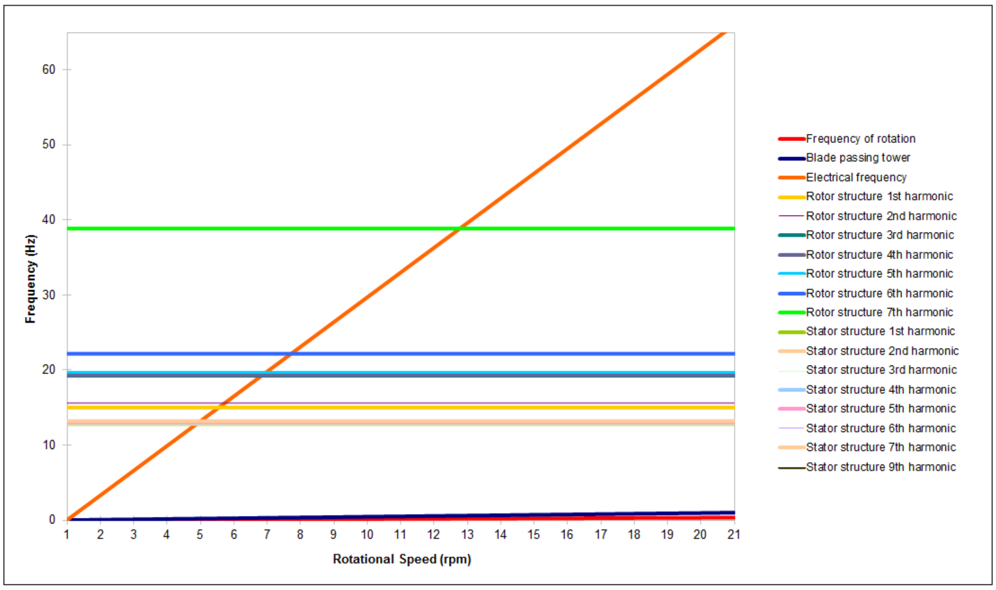

Figure 5.29 - Campbell diagram for natural frequencies matching the excitation frequencies of the AF generator

Harmonics of the 1st up to the 6th may appear in both the rotor and the stator of the AF machine during operation in low rotational speed (5 – 8rpm).

5.5 Dynamic response analysis

The ‘Dynamic Response’ of a structure is considered to be its reaction against loads that change over time. A common example of loading with non-constant amplitude is the torque of a PMDD wind turbine generator that may vary from the nominal one due to torque fluctuation. Torque fluctuation can be caused by torque ripple due to an unbalanced field distribution and fluctuations of the armature magnetomotive force (MMF) or cogging torque due to the interaction between the permanent magnets and the stator core.

In the FEA models a torque fluctuation was simulated by a small step change in the nominal torque as illustrated in Figure 5.30. The machine’s torque increases from zero to the nominal value in 1ms and remains constant for another ms. During the two following ms the torque fluctuation occurs and the torque increases by 700kNm and drops back to its original nominal value. During the final ms of the simulation the machine torque remains constant.

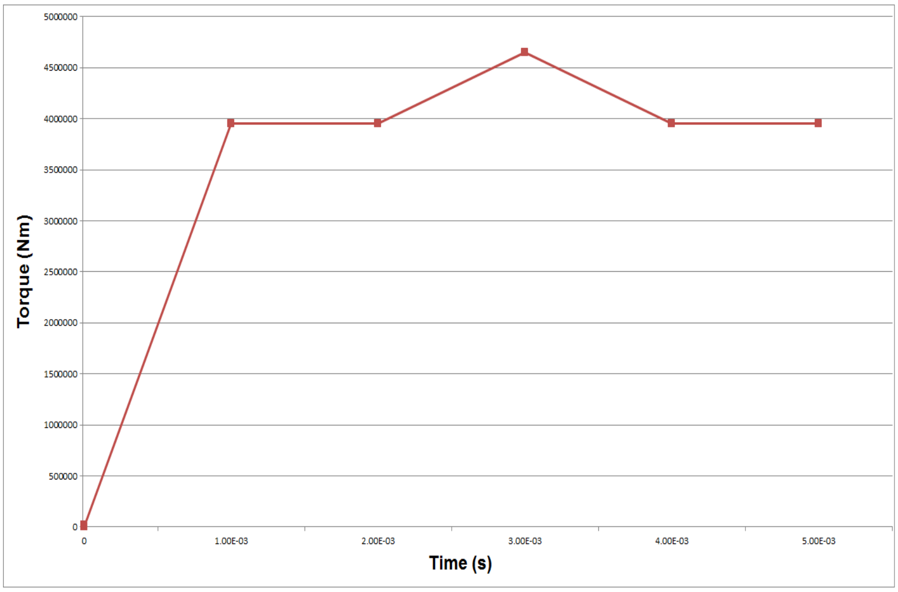

Figure 5.30 - The step change in torque as simulated for a RF PMDD machine

The gravitational pull and the Maxwell stress between rotor and stator remain the same as in the static structural analysis for all 5ms of this simulation. Figures 5.31 - 5.35 depict the resulting tangential deflection for the different generator structures due to the sum of loads that applied.

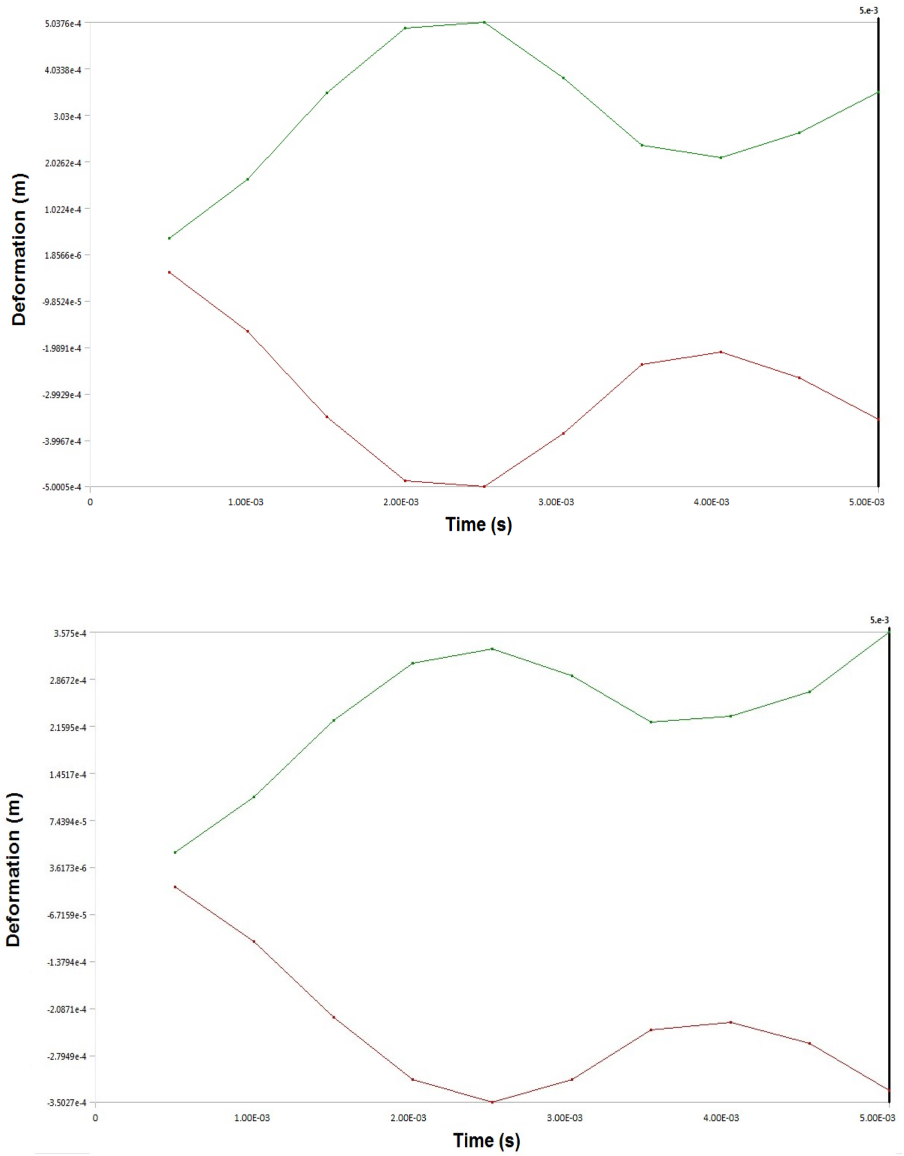

Figure 5.31 - Deflection in the tangential direction of the RF rotor (top) and stator (bottom) with discs

The maximum tangential deflection during the short circuit was 0.5 mm for the rotor and 0.36 mm for the stator structure.

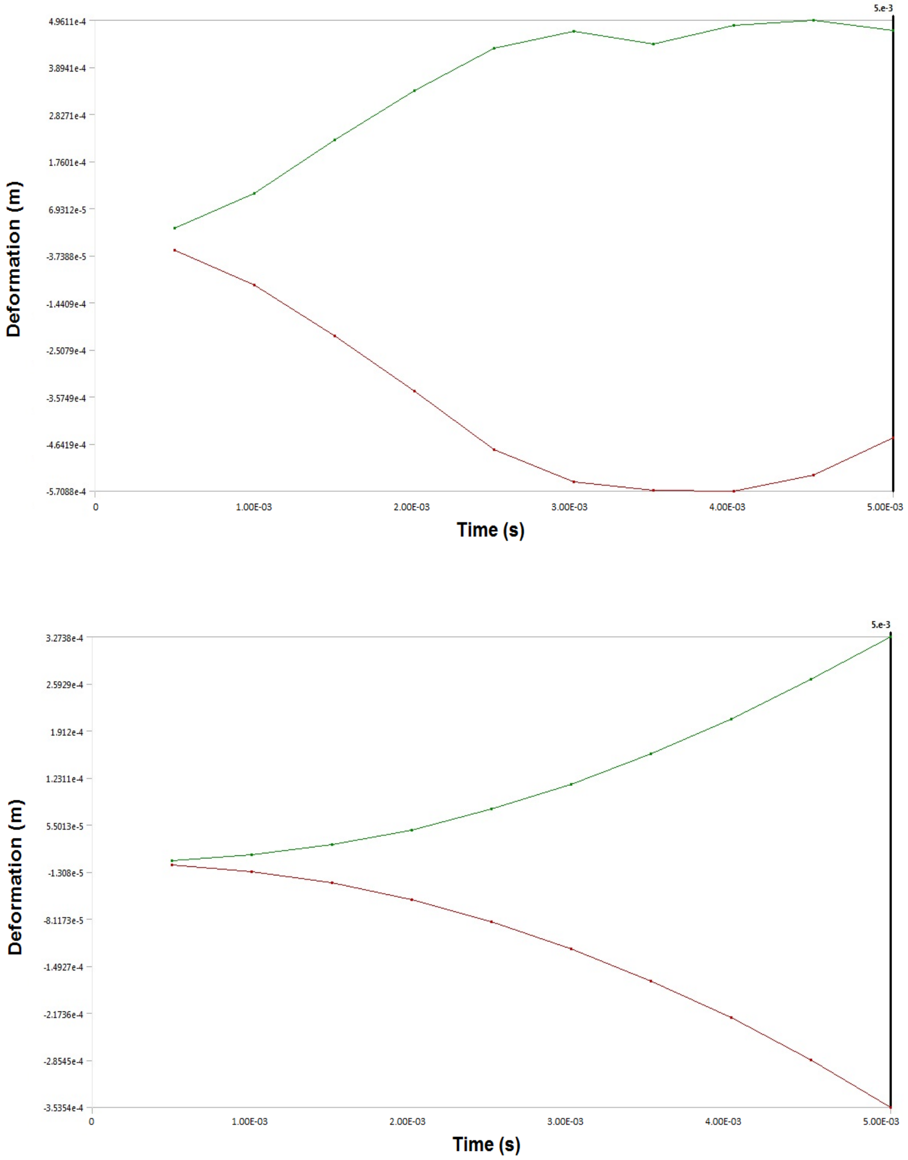

Figure 5.32 - Deflection in the tangential direction of the RF rotor (top) and stator (bottom) with arms

The maximum tangential deflection during the short circuit was 0.57 mm for the rotor and 0.35 mm for the stator structure.

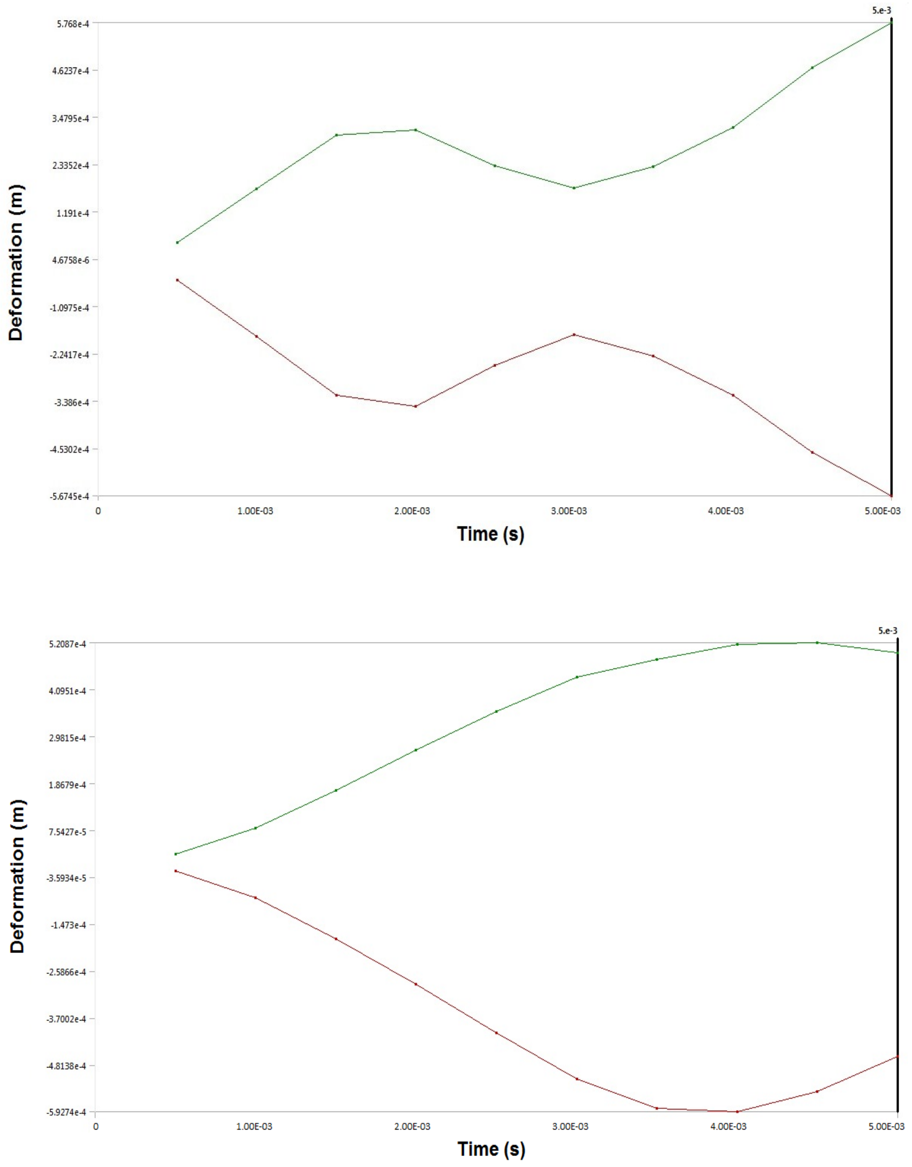

Figure 5.33 - Deflection in the tangential direction of the TF-1 rotor (top) and stator (bottom)

The maximum tangential deflection when the short circuit occurred was 0.58 mm for the rotor and 0.59 mm for the stator structure.

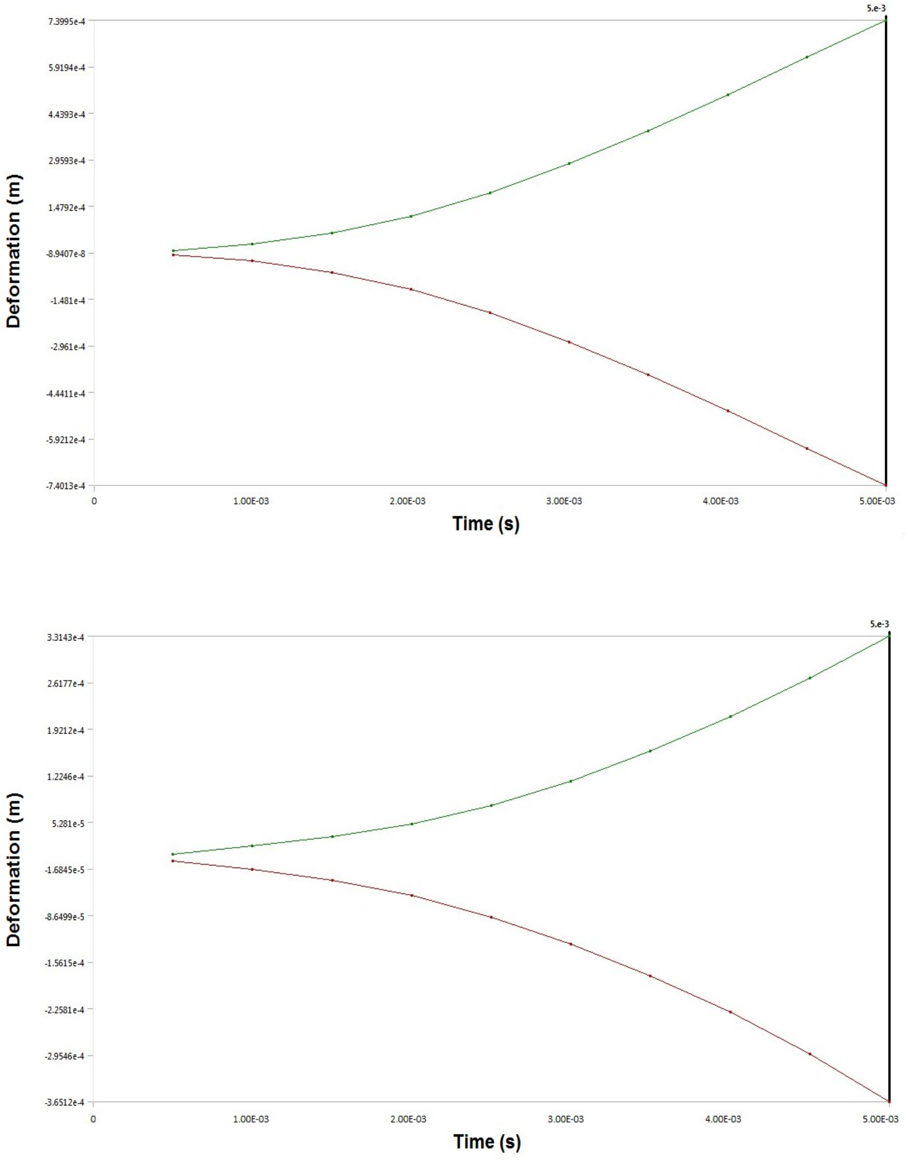

Figure 5.34 - Deflection in the tangential direction of the TF-2 rotor (top) and stator (bottom)

The maximum tangential deflection when the short circuit occurred was 0.74 mm for the rotor and 0.36 mm for the stator structure.

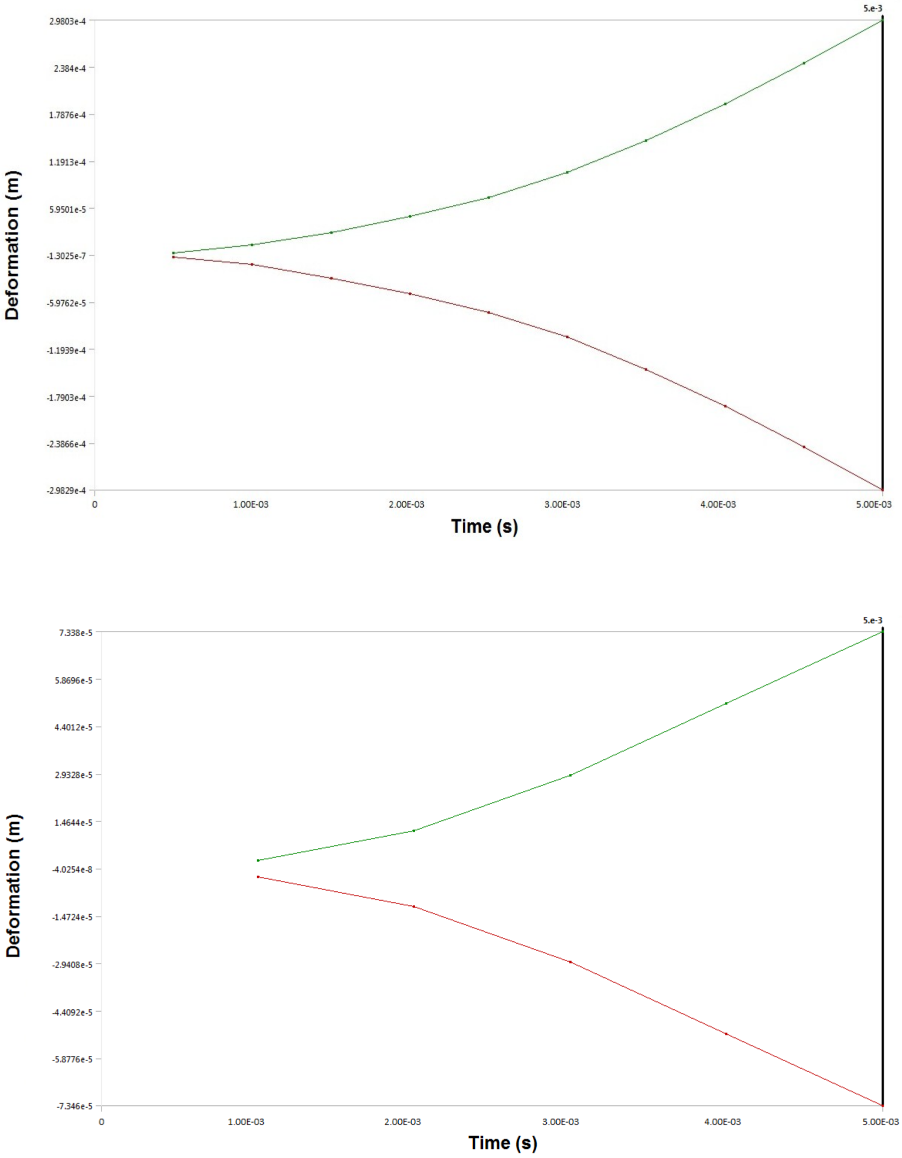

Figure 5.35 - Deflection in the tangential direction of the AF rotor (top) and stator (bottom)

The maximum tangential deflection when the short circuit occurred for one of the three stages of the AF machine was 0.3 mm for the rotor and 0.07 mm for the stator structure.

In all tested cases the deflection maximises during the last milliseconds of the simulation due to the cumulative stress. In the cases of the RF armed machine and the two different TF machines the tangential deflection was close or above the defined limit.

5.6 Conclusions

In this chapter a structural comparison among the suggested direct drive generator topologies for 5MW wind turbines was performed. The structural analysis included static, modal and dynamic analysis.

Table 5.7 summarises the original masses of the generator structures from chapter 4 and the resulting masses generated by the structural analysis in chapter 5. It is clear that there is a large difference in the masses of the structures. In almost all cases the mass increases to provide stiffer structures to react the applied loads. TF-2 rotor and the AF rotor and stator were the only structures that did not need any adjustments to their dimensions. The RF stator with discs and TF-1 rotor were the only structures whose mass decreased. The above results prove the necessity of applying structural criteria when modelling large PMDD generators. Analytic models should also be verified with the corresponding FEA models for more accurate results.

Generator Structure	**Original Mass (tons)**	**Final Mass (tons)**
RF Disc Rotor	41	51
RF Disc Stator	70	52
RF Armed Rotor	23	60
RF Armed Stator	37	64
TF-1 Rotor	48	40
TF-1 Stator	30	65
TF-2 Rotor	27	27
TF-2 Stator	35	68
AF Rotor	48	48
AF Stator	25	25

Table 5.7 - Comparison of the resulting masses of the PMDD generator structural models

From the static structural analysis, the conventional iron-cored RF generator with arms proved to be the most vulnerable against Maxwell stress and as a result the heaviest of the three topologies. The alternative RF topology with discs was much more resistive against the applied loads and as a result much lighter. The TF topology showed great potential with the best reaction against the Maxwell stress but it was vulnerable to torque. Both TF topologies were lighter compared to their RF counterparts. In addition, the TF-2 topology had the smallest deflection in the airgap compared to all other topologies, less than 0.001% of its total clearance but it was not the lightest option. When decreasing the structural mass of the TF machine, the total deflection increases. The AF generator with C-cored modules proved to be the most lightweight topology. This attribute makes this generator design the most cost effective option as far as raw materials, manufacture, transportation and assembly costs are concerned.

Modal analysis showed that the TF-2 machine has the highest risk of experiencing vibrations in operation. This attribute combined with the high levels of stress that apply on the machine makes it most susceptible to fatigue than the rest of the tested topologies. RF with discs, TF-1 and AF topologies have a moderate risk of experiencing vibrations while operating, with the AF machine being more vulnerable to fatigue due to the large stress it experiences. The conventional RF generator with arms is the least susceptible to fatigue according to the stress and frequency analysis.

The deflections that occurred during static and dynamic structural analysis have been collected in Table 5.8.

	Static loading deflections (mm)		Dynamic loading deflections (mm)	
	Rotor	Stator	Rotor	Stator
RF machine (discs)	0.53	0.29	0.5	0.36
RF machine (arms)	0.55	0.57	0.57	0.35
TF-1 machine	0.52	0.57	0.58	0.59
TF-2 machine	0.63	0.57	0.74	0.36
AF machine	0.47	0.47	0.30	0.07

Table 5.8 - Collective deflections in the tangential direction for static and dynamic loading

The RF and TF machines were more vulnerable against the dynamic loading as the resulting deflections in the tangential direction were very close to the set limit. The tangential deflection of the TF-2 rotor structure was above the defined limit. The AF aircored machine had the best dynamic response as its total tangential deformation at the end of the simulation was much less than that occurring under nominal loading.

In summary the AF aircored machine with C-cored modules seems to have the highest potential for wind development as it is the most lightweight of the suggested topologies, with the best structural response against static and dynamic loading.

In the following chapters, optimisation techniques will be used to reduce the mass of the RF and TF generators without compromising their stiffness, in an attempt to bring them as close to the AF topology as possible.

Chapter 6

Structural Optimisation Using FEA Tools

6.1 Introduction

The shape optimisation tool of ANSYS [175] is a structural analysis that seeks to find the best use of material for a body. This involves optimising the distribution of material so that the given structure will have the maximum stiffness for a set of loads. The structural forces applied on all the FEA models presented in this chapter were the normal component of Maxwel stress (*q*), the gravitational pull and the moment that gives rise to tangential stress. The output of this tool is a plot that outlines with red colour the portions of the geometry that contribute the least to the structure's stiffness for the given set of loads (Figure 6.1).

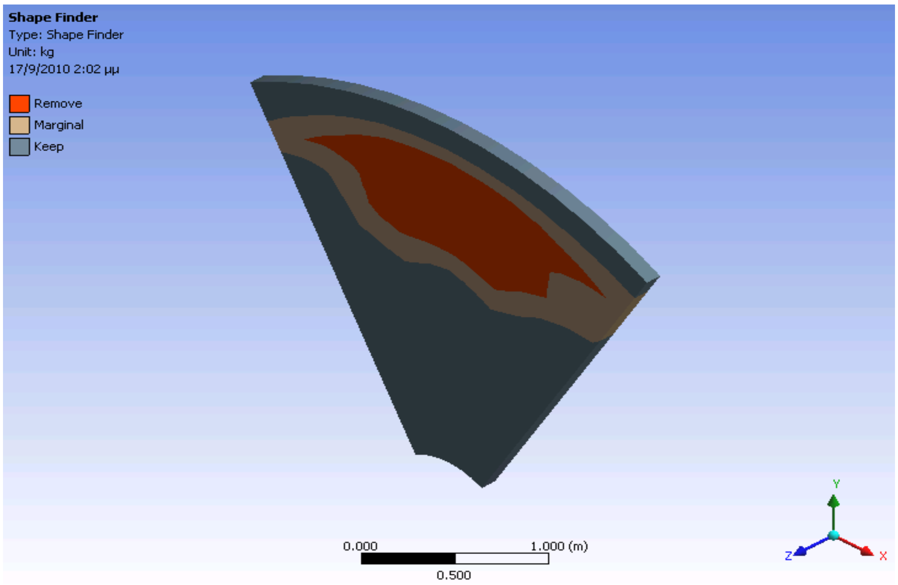

Figure 6.1 - Sample output plot of the shape optimisation tool

In this chapter, the structural models of the 5MW PMDD machines that were created in chapter 5 will be structurally optimised with the help of the suggested FEA shape optimisation tool.

Original attempts to optimise the complete structure required a large amount of time and computer resources. Furthermore, the results were inconclusive for the purposes of this research as can be seen in Figure 6.2.

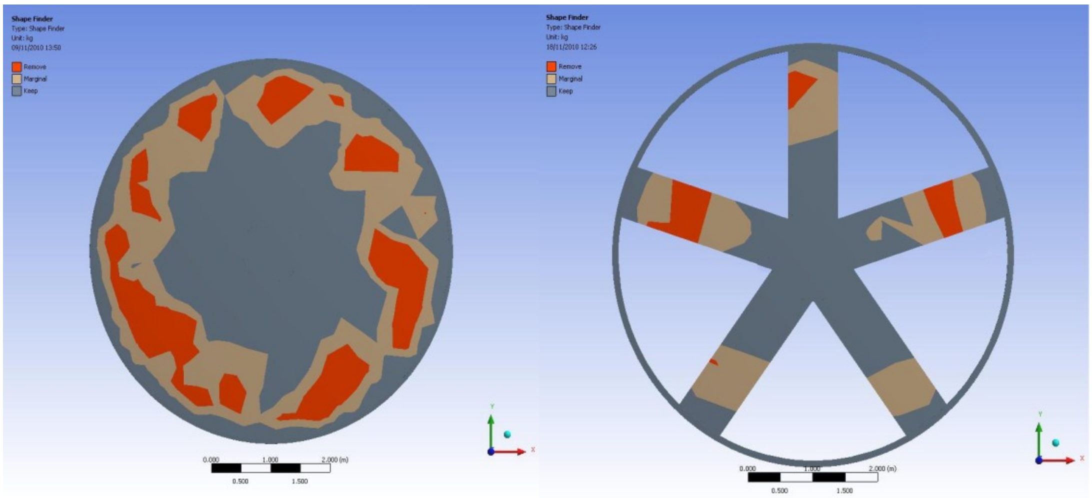

Figure 6.2 - Shape optimisation output for RF rotor structures with disc (left) and arms (right)

In order to produce more accurate results and reduce hardware requirements, symmetry in the structure was used to only model part of the complete structure. The models included part of the structures' back thickness, part of the structures' disc or one of the arms and part of the main shaft. The permanent magnets and the stator teeth were not included in the models as they cannot be part of the optimisation process and increased the complexity. Boundary conditions of symmetry were added on both sides of the structural models so that the tool would assume they are part of a complete structure (Figure 6.3).

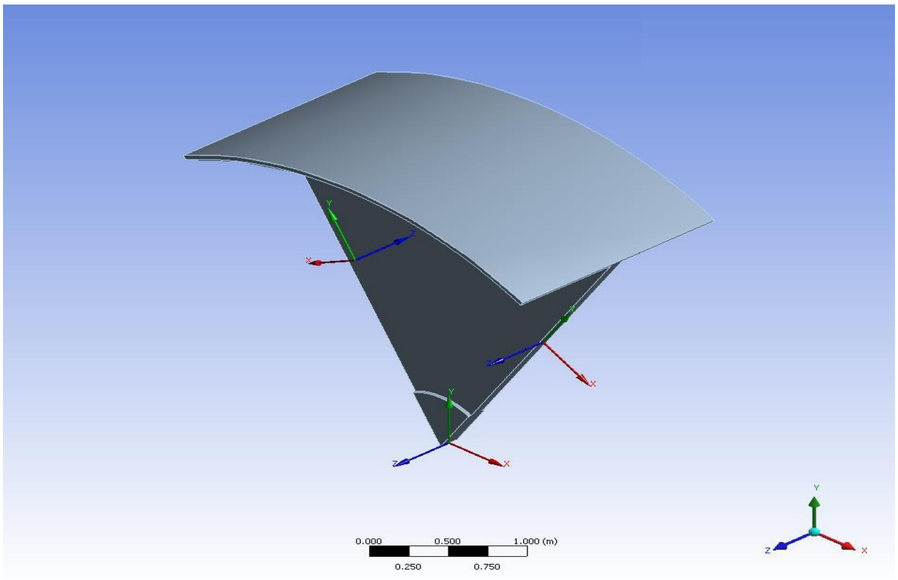

Figure 6.3 - Sample model of an RF rotor with disc and the applied symmetry regions

Using the tool's output as guideline, the unnecessary parts were removed, leading to a new geometry for the PMDD generator structures. An example of the optimisation process for a disc rotor is depicted in Figure 6.4.

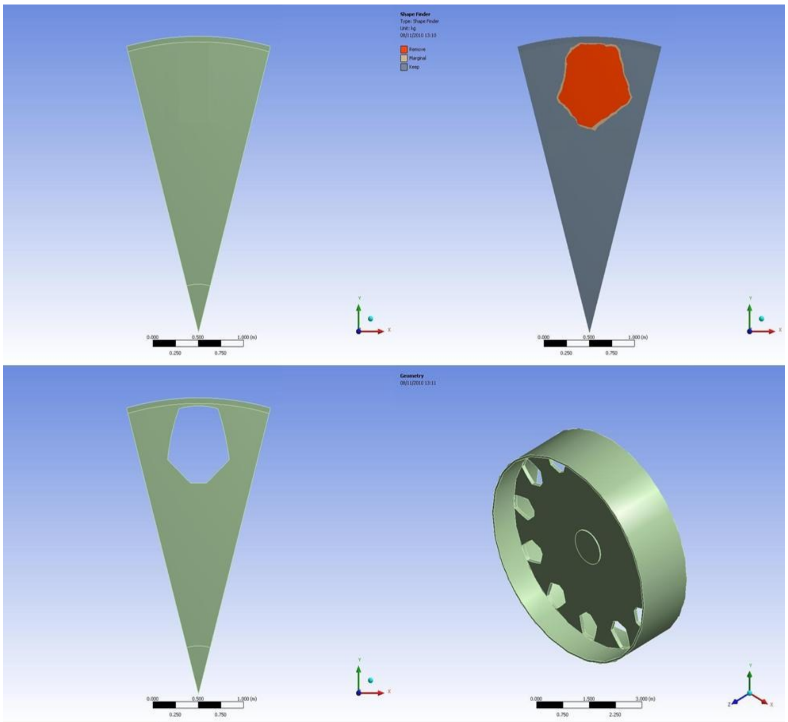

Figure 6.4 - The shape optimisation process for a RF disc rotor. The original 30º rotor part (top left), the FEA optimisation output (top right), the resulting lightweight part (bottom left) and the resulting full rotor structure (bottom right)

This optimisation process was repeated for the rotor and the stator of all the tested topologies. The arc angle of the partial structures with discs varied from 20° up to 180°, representing the number of pattern repeats that could be used in order to create a full circle (from 2 to 18). The width of the arm for the armed structures varied in each case in order to represent topologies with five to ten arms, leading to a vast number of optimised structures for each PMDD generator type. The target mass reduction for the given bodies was set to 25% in all cases.

The load conditions considered in chapter 5 were applied to the new lightweight structures and tested against the same deflection criteria: 10% of the air gap clearance for the deflection due to Maxwell stress, 2% of the axial length for the gravitational deflection and a relative twist of 0.01° for the torsional deflection. The final structures are compared to the original ones to draw valuable conclusions.

6.2 RF structural FEA optimisation

6.2.1 Optimised structures with discs

6.2.1.1 Rotor

Following the methodology described in section 6.1, a number of optimised rotor and stator parts with discs were created. In both cases the arc angle of the partial structures varied from 20° to 180°. The resulting topologies were then tested in each case against the suggested structural loads to confirm the resulting deflections were within limitations. Figure 6.5 depicts the resulting shapes (patterns) that came as a result of the optimisation process, while Figure 6.6 the final lightweight rotor structures.

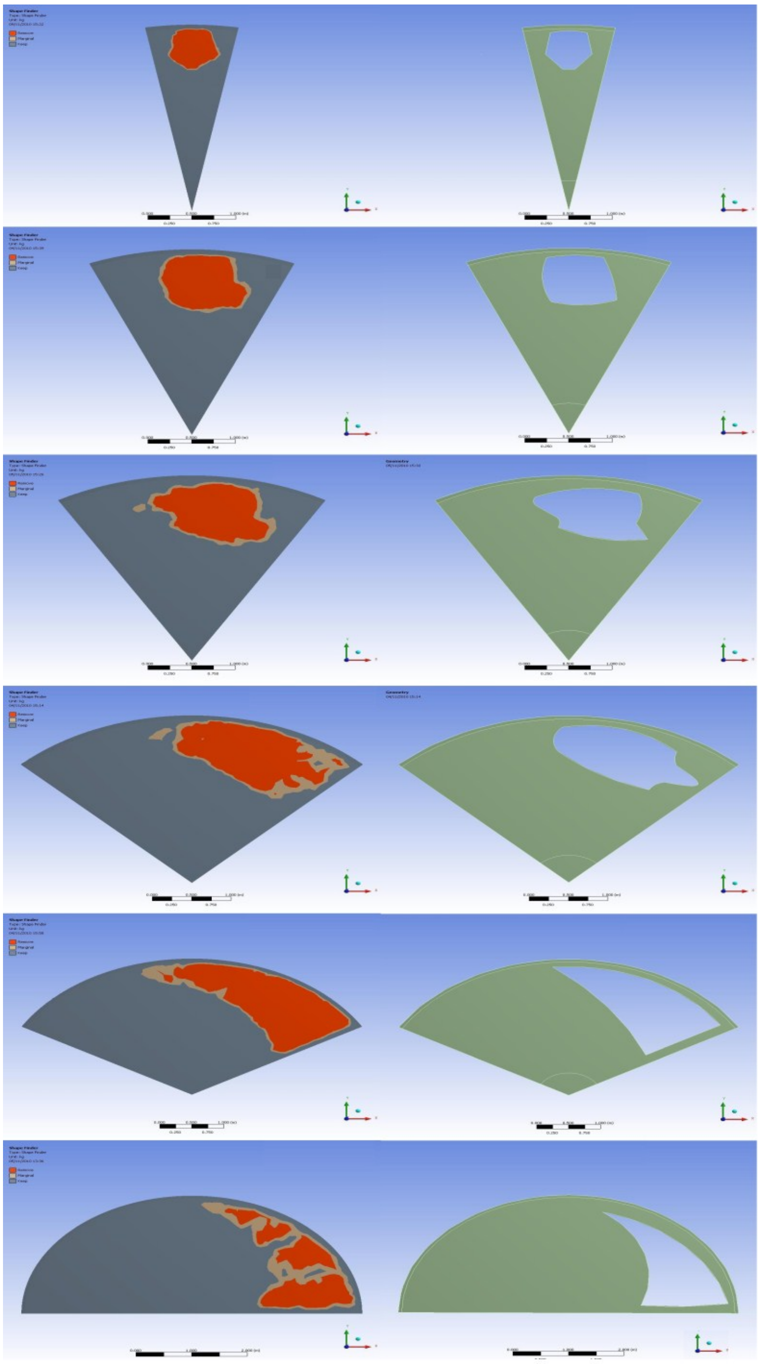

Figure 6.5 - The shape finder outputs (left) along with the shape optimised rotor parts (right).
From top: 20º, 45º, 60º, 90º, 120º and 180º.

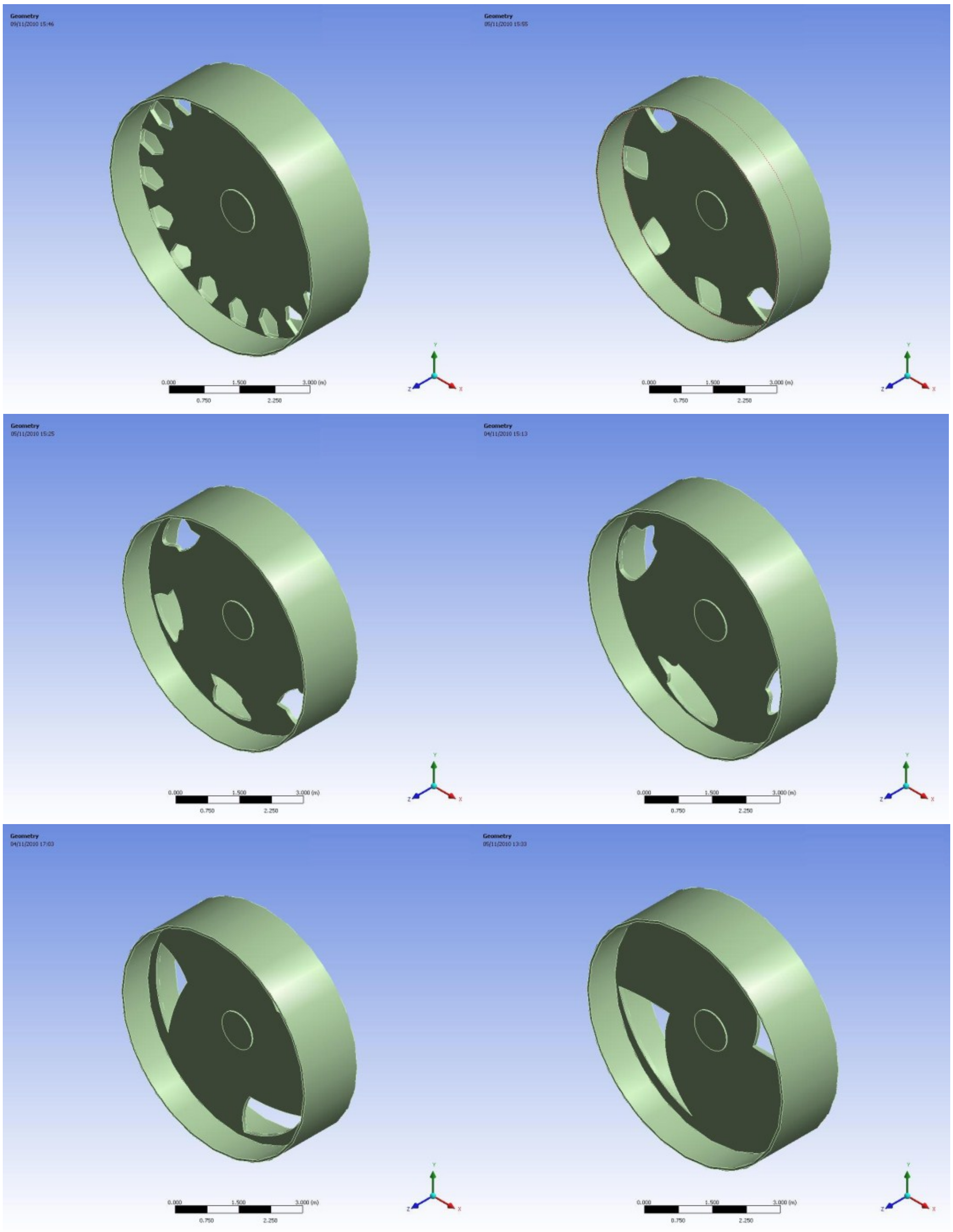

Figure 6.6 - Lightweight RF rotor structures with disc. From top to bottom and from left to right: 18, 8, 6, 4, 3 and 2 pattern repetitions.

Once the structural optimisation process was completed, the permanent magnet material was added on the RF rotor structures. The resulting masses are gathered in Table 6.1 and are illustrated in Figure 6.7.

Pattern Repetitions	Mass (tons)
0	51.0
2	47.6
3	47.4
4	47.2
6	47.0
8	46.7
12	46.6
18	46.4

Table 6.1 - Resulting masses of FEA optimised RF rotor structures with disc

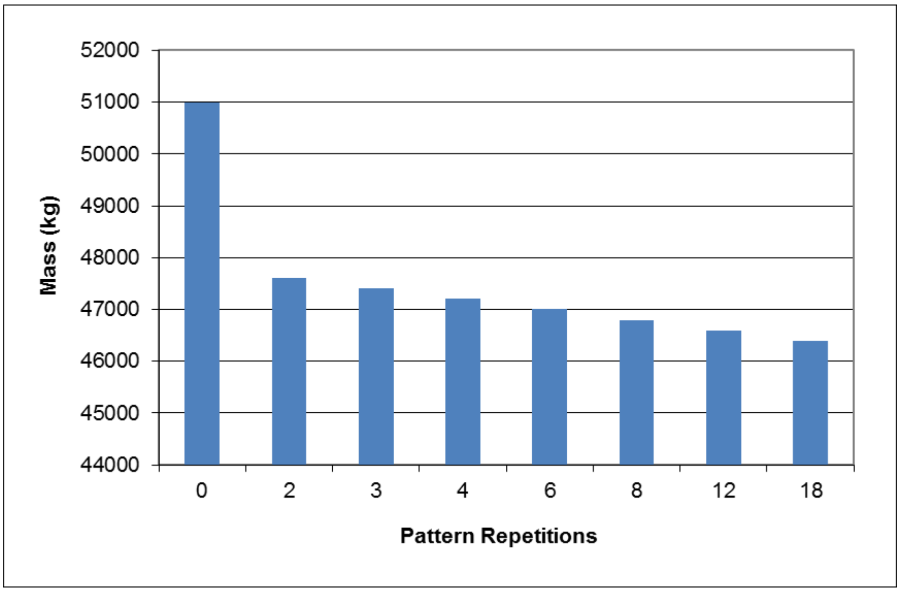

Figure 6.7 - Mass comparison of FEA optimised RF rotor structures with disc

From the results of this research it can be deducted that the mass of the RF rotor with disc can be effectively reduced by removing many small parts from the area near its circumference. Removing these parts does not compromise the rotor's stiffness against the structural loads. The most lightweight structure was achieved for eighteen pattern repetitions, with a final mass of 46.4 tons.

6.2.1.2 Stator

The same optimisation process was followed for the RF stator with discs. Figure 6.8 depicts the resulting patent shapes that came as a result of the optimisation process, while Figure 6.9 the final lightweight stator structures.

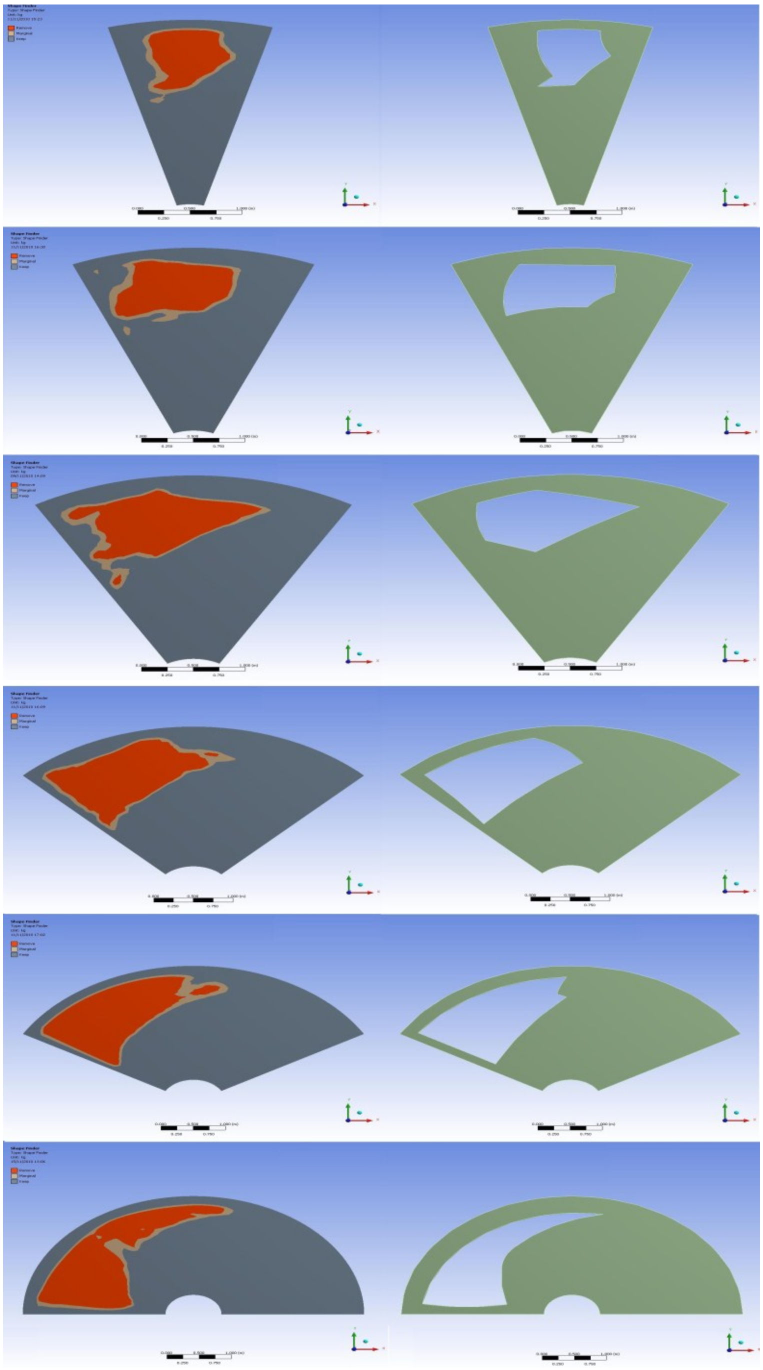

Figure 6.8 - The shape finder outputs (left) along with the shape optimised stator parts (right). From top: 30º, 45º, 60º, 90º, 120º and 180º.

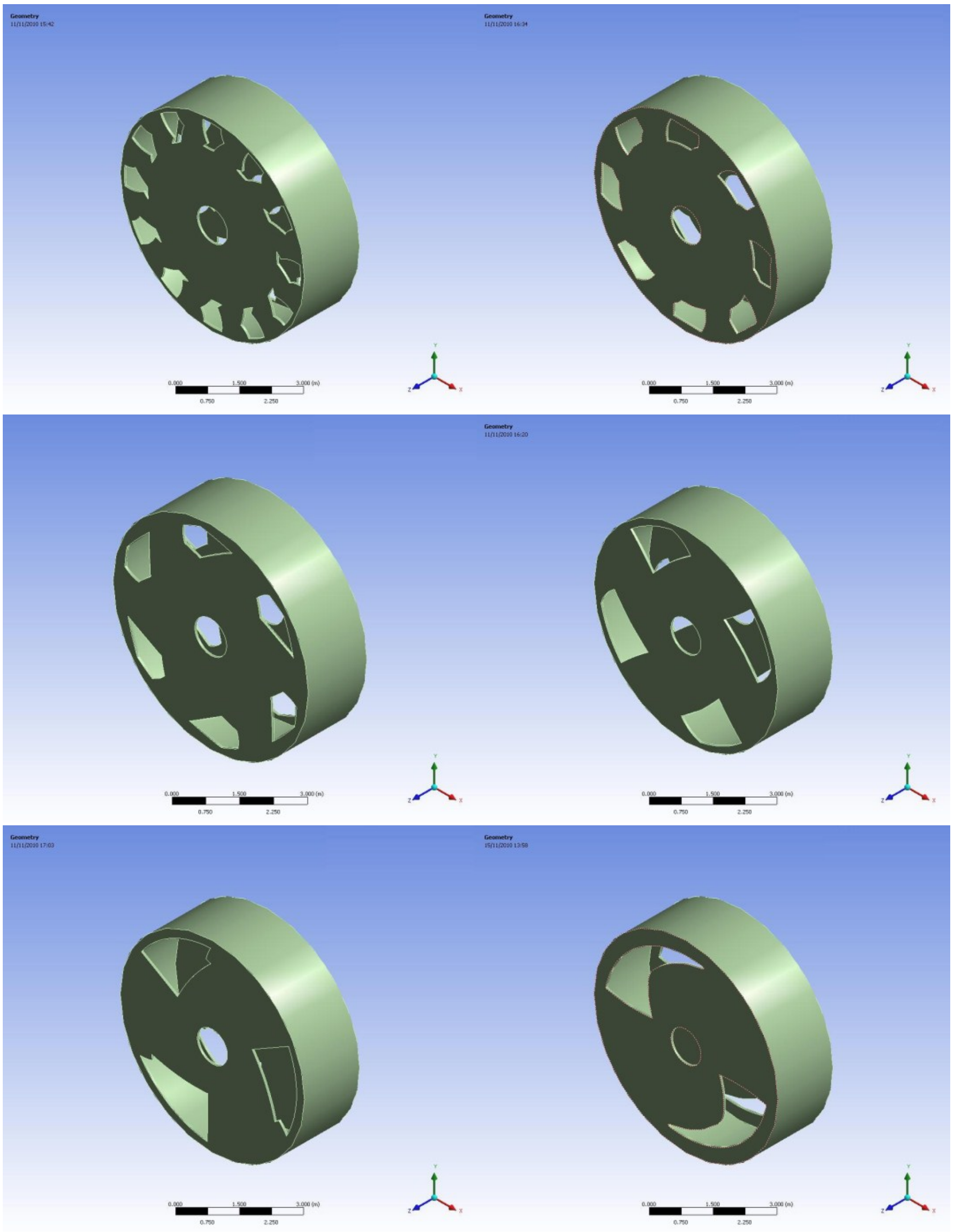

Figure 6.9 - Lightweight RF stator structures with discs. From top to bottom and from left to right: 12, 8, 6, 4, 3 and 2 pattern repetitions.

Once the structural optimisation process was completed, the stator’s teeth were added on the RF stator structures. The resulting masses are gathered in Table 6.2 and are illustrated in Figure 6.10.

Pattern Repetitions	Mass (tons)
0	51.7
2	47.0
3	46.1
4	46.3
6	46.5
8	46.7
12	46.8

Table 6.2 - Resulting masses of FEA optimised RF stator structures with discs

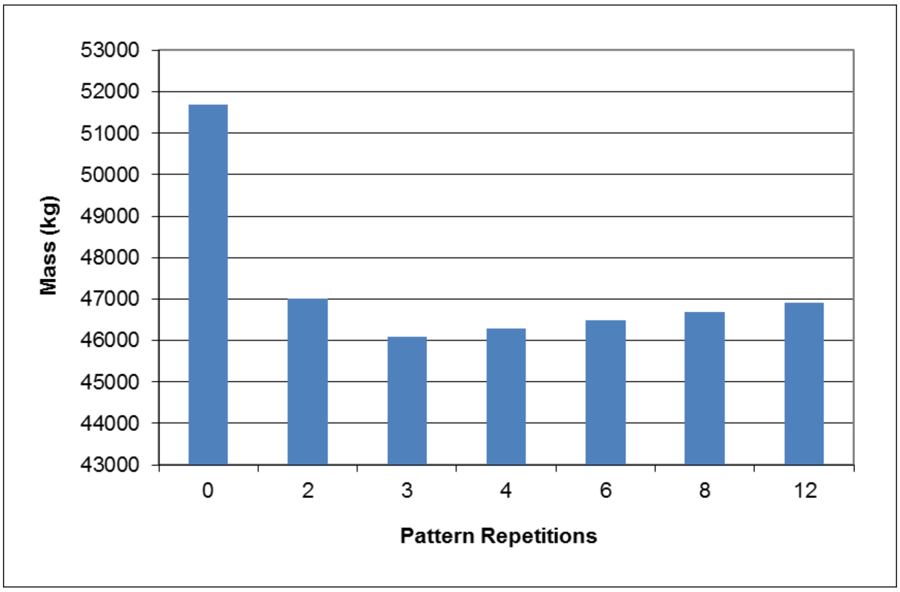

Figure 6.10 - Mass comparison of FEA optimised RF stator structures with discs

From the results of this research it can be deducted that the mass of the RF stator with discs can be effectively reduced by removing large parts from the area near its circumference. Removing these parts does not compromise the rotor's stiffness against the structural loads. The most lightweight structure was achieved for three pattern repetitions, with a final mass of 46.1 tons.

The most lightweight combination of optimised RF structures with discs was a rotor with eighteen pattern repetitions and a stator with three pattern repetitions on the discs. The total generator mass was reduced to 92.5 tons from 103 tons the original RF generator with discs used to mass, offering a total mass reduction of 10.2%.

6.2.2 Optimised structures with arms

6.2.2.1 Rotor

Following the methodology described in section 6.1, a number of optimised rotor and stator parts with arms were created. In both cases the width of the arms of the partial structures varied so that it would correspond to structures with 5 up to 10 arms. The mathematical expression that connects the width of a generator's arm (b) with the number of the structure's arms (n) was described in chapter 4 as $b = 2\pi(D_g/10)/n$, where D_g the diameter of the final RF structure. Symmetry regions were added on both sides of the structural model so that the FEA tool would "think" that it is part of a complete rotor with arms (Figure 6.11).

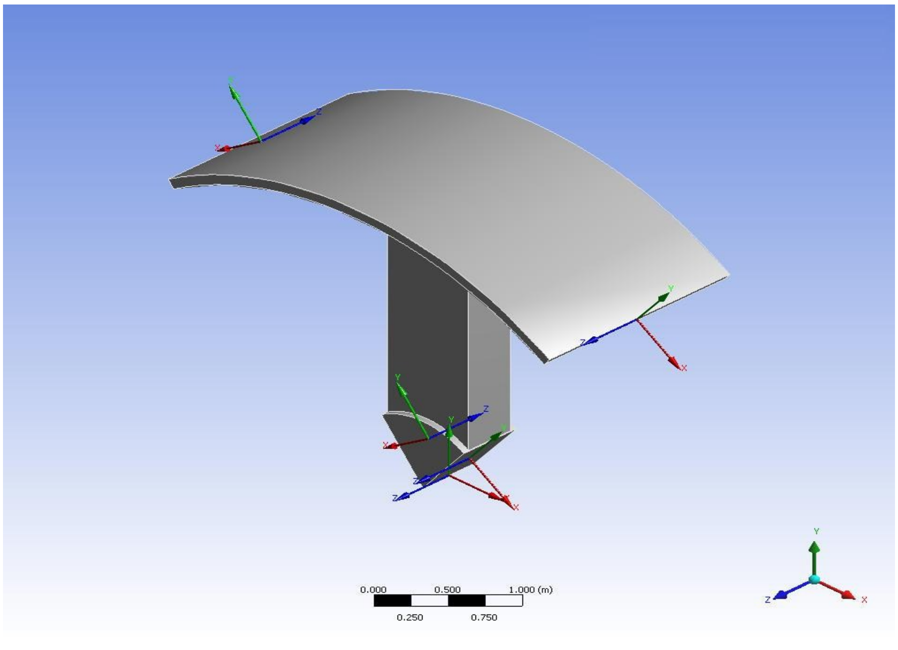

Figure 6.11 - 5-armed RF rotor model with symmetry regions

The resulting topologies were then tested in each case against the suggested structural loads to confirm the resulting deflections were within limitations. Figure 6.12 depicts the resulting patent shapes that came as a result of the optimisation process, while Figure 6.13 the final lightweight rotor structures.

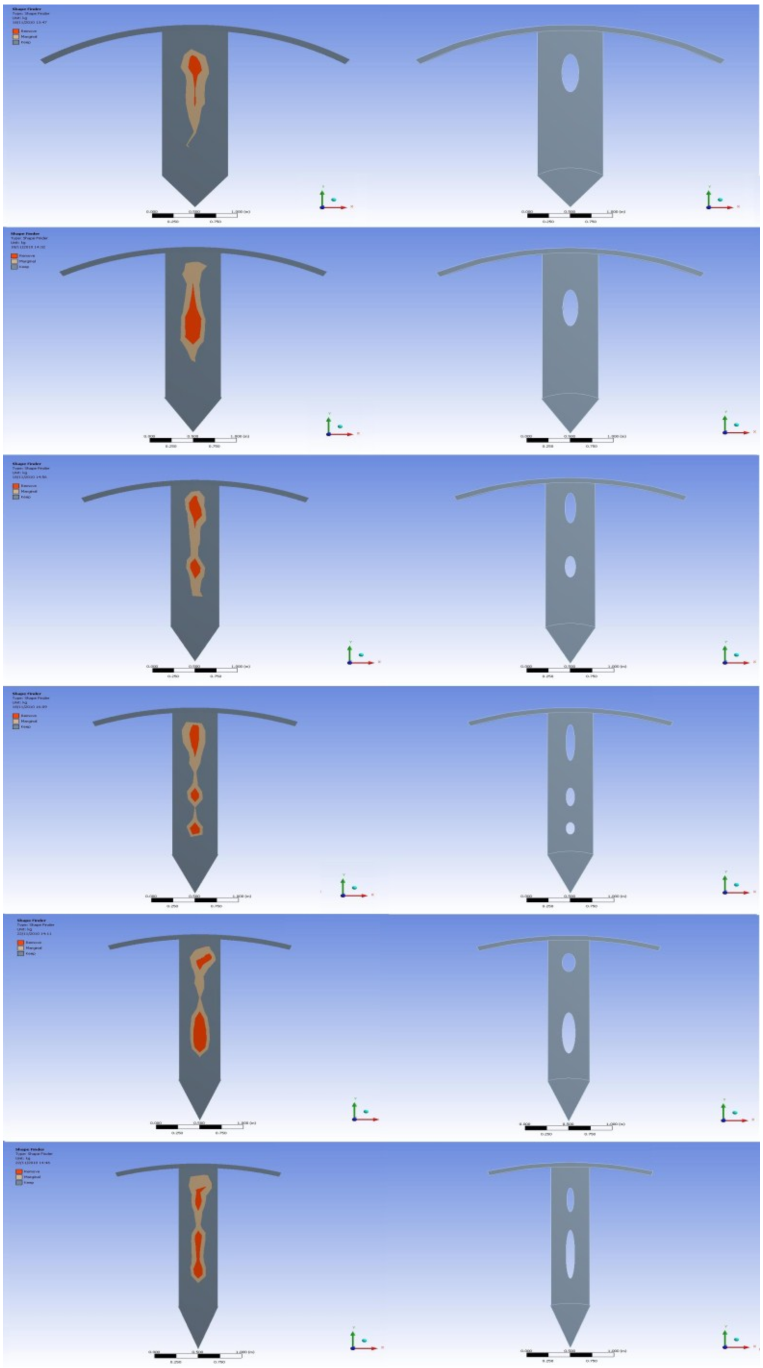

Figure 6.12 - The shape finder outputs (left) along with the shape optimised rotor parts (right). From top: 5-armed, 6-armed, 7-armed, 8-armed, 9-armed and 10-armed rotor part.

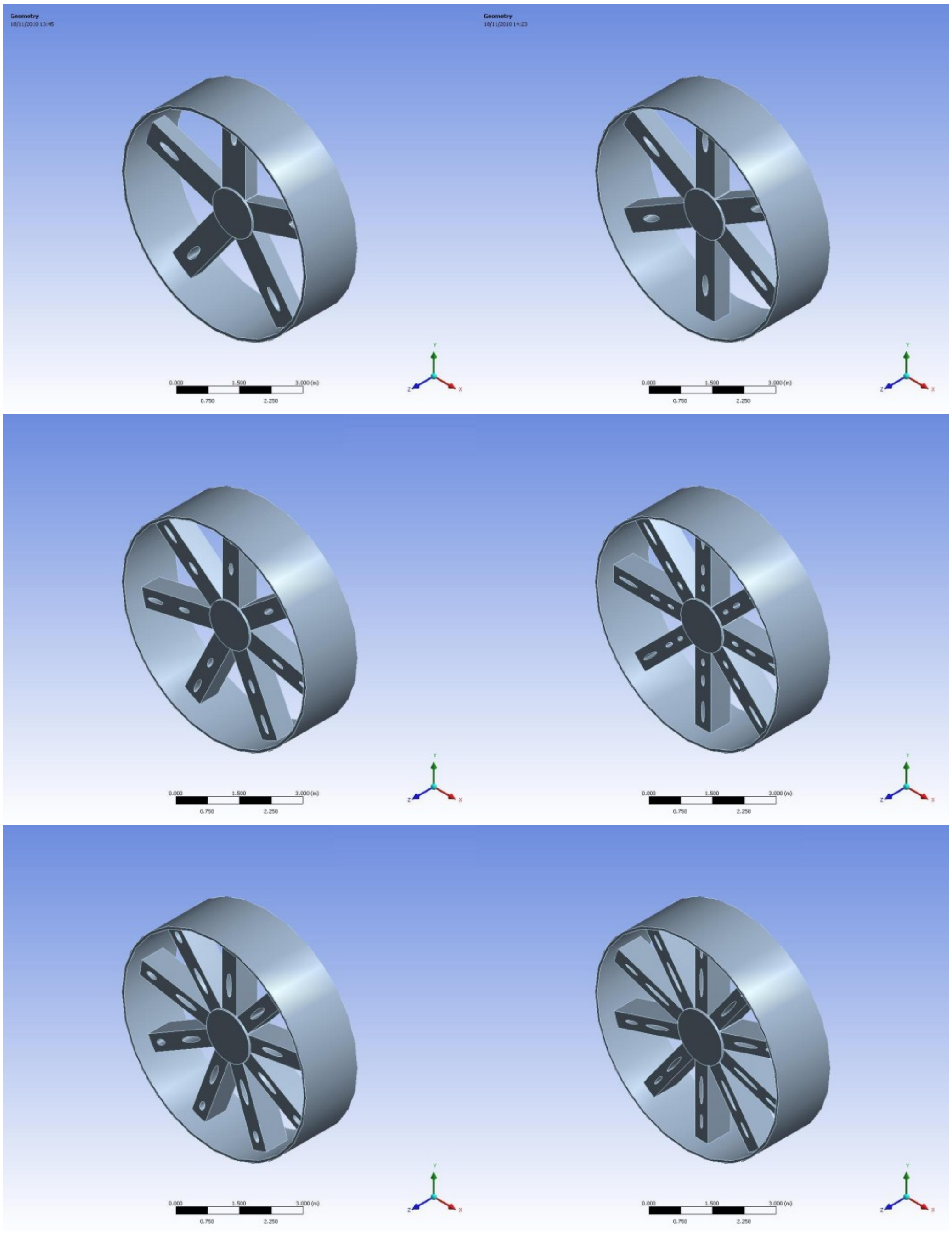

Figure 6.13 - Lightweight RF rotor structures with arms. From top to bottom and from left to right: 5-armed, 6-armed, 7-armed, 8-armed, 9-armed and 10-armed rotors.

Once the structural optimisation process was completed, the permanent magnets were added on the RF rotor structures. The resulting masses are gathered in Table 6.3 and are illustrated in Figure 6.14.

Number of arms	Original Mass (tons)	Final Mass (tons)
4	70.3	69.0
5	60.0	58.4
6	66.2	63.6
7	74.2	69.5
8	81.0	76.3
9	85.4	79.0
10	90.8	84.1

Table 6.3 - Resulting masses of FEA optimised RF rotor structures with arms

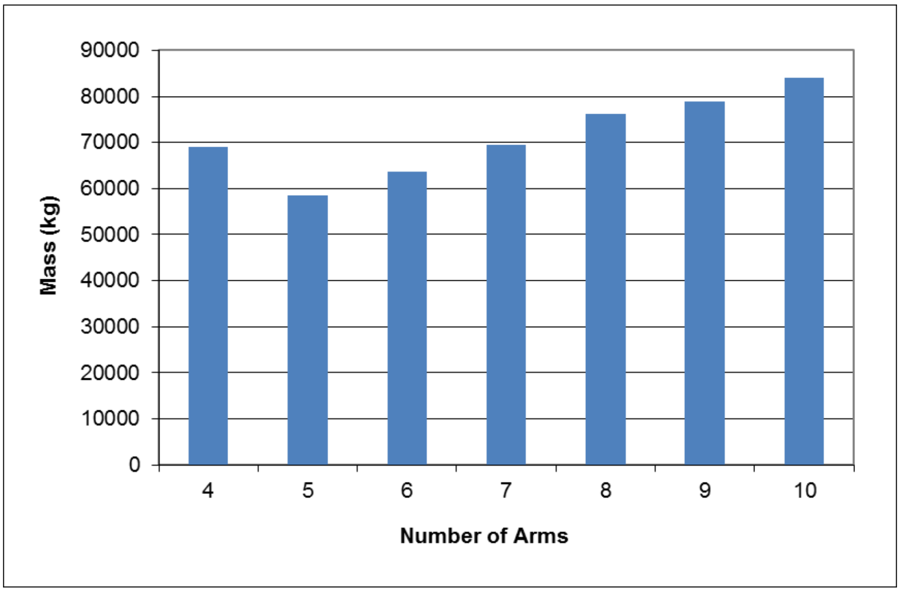

Figure 6.14 - Mass comparison of FEA optimised RF rotor structures with arms

From the results of this research it can be deducted that the mass of the RF rotor with arms increases along with the number of arms that are employed. Although the portion of mass that is removed increases for structures with more than five arms, it is not adequate to compensate for the extra mass that is put on the structure by each extra arm. This structural behaviour can be attributed to the fact that as the number of arms increases, the arms' width (*b*) decreases accordingly making the structure more vulnerable against the tangential deflection. The arms' depth (*d*) had to be increased in compensation, making the structure heavier with each arm that is added.

Therefore, the most lightweight structure achieved was the optimised 5-armed rotor, with a final mass of 56.4 tons.

Another way to create lightweight armed generator structures is to employ hollow arms (Figure 6.15). The arm's thickness is described as t_{wr} and it was the same for each side of the arm.

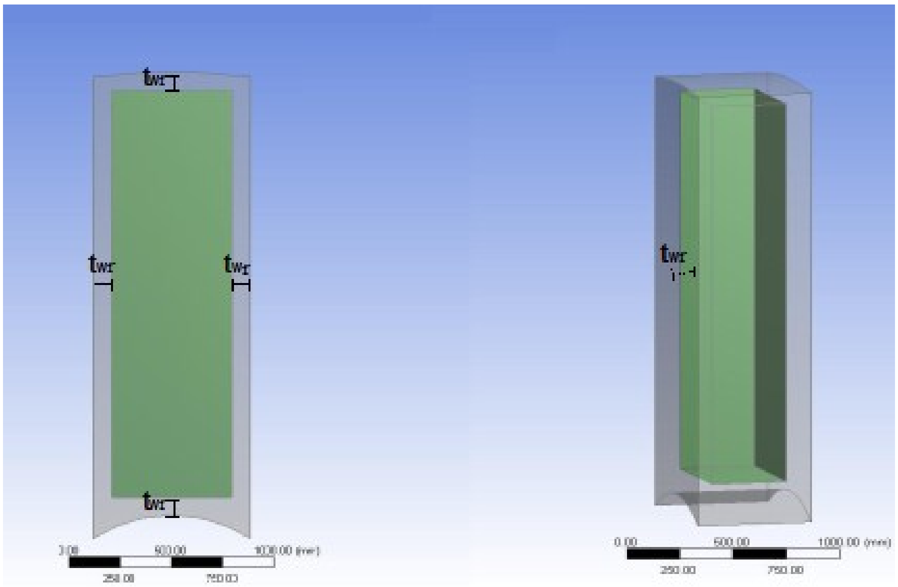

Figure 6.15 - Transparent view of a hollow arm. The arm's thickness t_{wr} is outlined.

The new structure was much lighter compared to the original 5-armed structure with solid arms and the structurally optimised one. On the downside it was more vulnerable to the tangential deflection due to the centripetal force. In order to make the new design more robust the depth of the arms (d) was increased, while the rest of the dimensions remained the same. The final dimensions of the rotor's arms were d=500 mm and t_{wr}=85 mm (Figure 6.16). The structure's final mass was 51.4 tons.

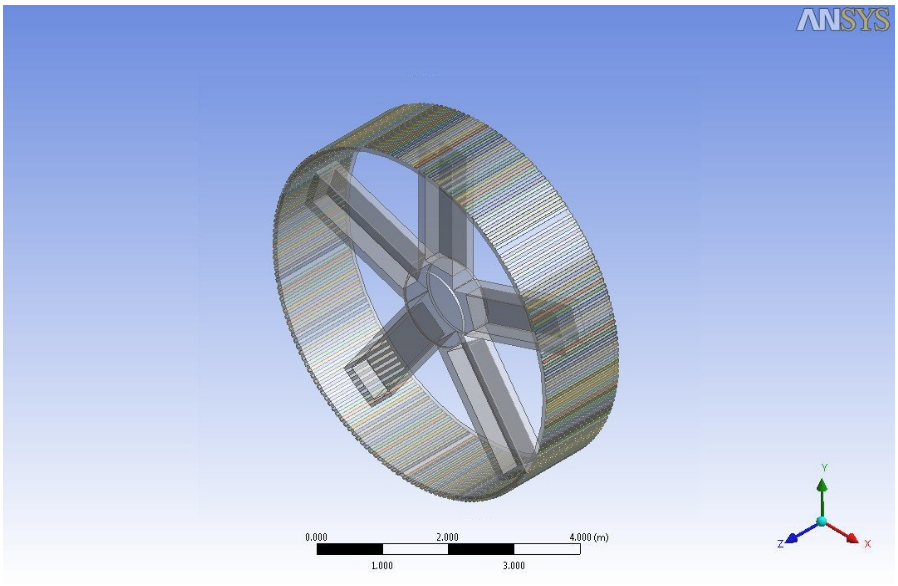

Figure 6.16 - Lightweight 5-armed RF rotor with hollow arms

6.2.2.2 Stator

The same optimisation process was followed for the RF stator with arms. Figure 6.17 depicts the resulting patent shapes that came as a result of the optimisation process, while Figure 6.18 the final lightweight stator structures.

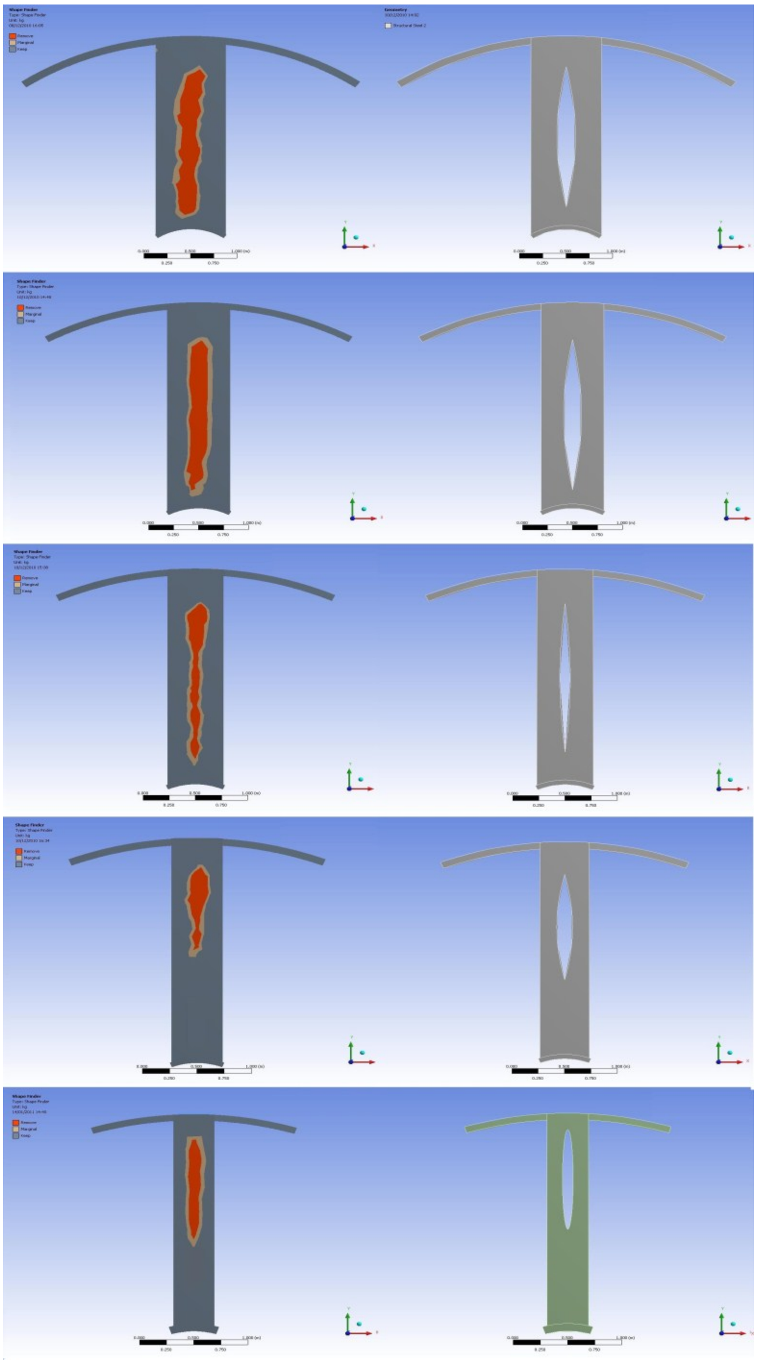

Figure 6.17 - The shape finder outputs (left) along with the shape optimised stator parts (right). From top: 5-armed, 6-armed, 7-armed, 8-armed and 10-armed stator part.

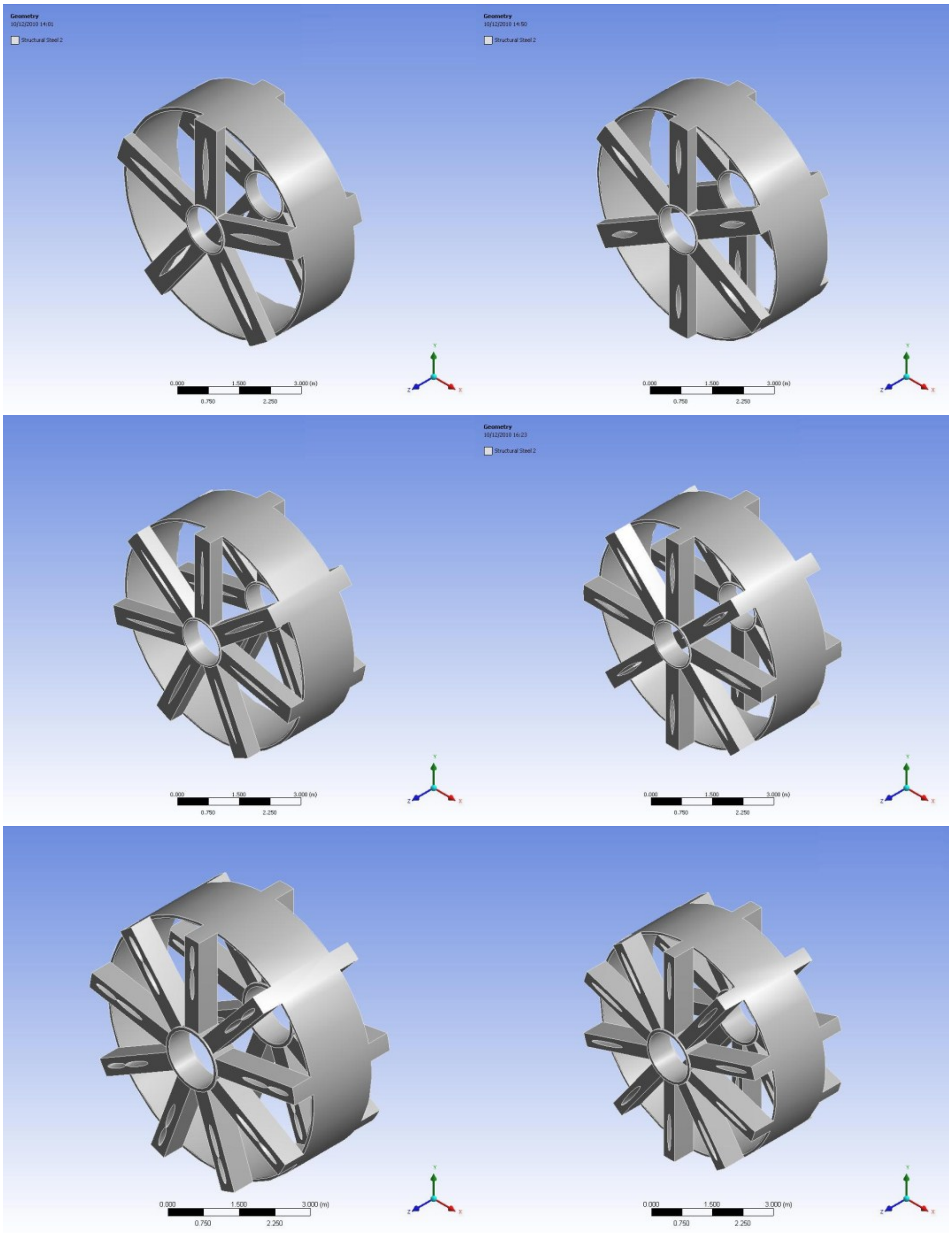

Figure 6.18 - Lightweight RF stator structures with arms. From top to bottom and from left to right: 5-armed, 6-armed, 7-armed, 8-armed, 9-armed and 10-armed stators.

Once the structural optimisation process was completed, the stator's teeth were added on the RF stator structures. The resulting masses are gathered in Table 6.4 and are illustrated in Figure 6.19.

Number of arms	Original Mass (tons)	Final Mass (tons)
4	72.6	71.5
5	64.2	60.0
6	66.8	63.4
7	84.4	80.4
8	97.5	91.0
9	100.0	94.5
10	115.0	105.0

Table 6.4 - Resulting masses of FEA optimised RF stator structures with arms

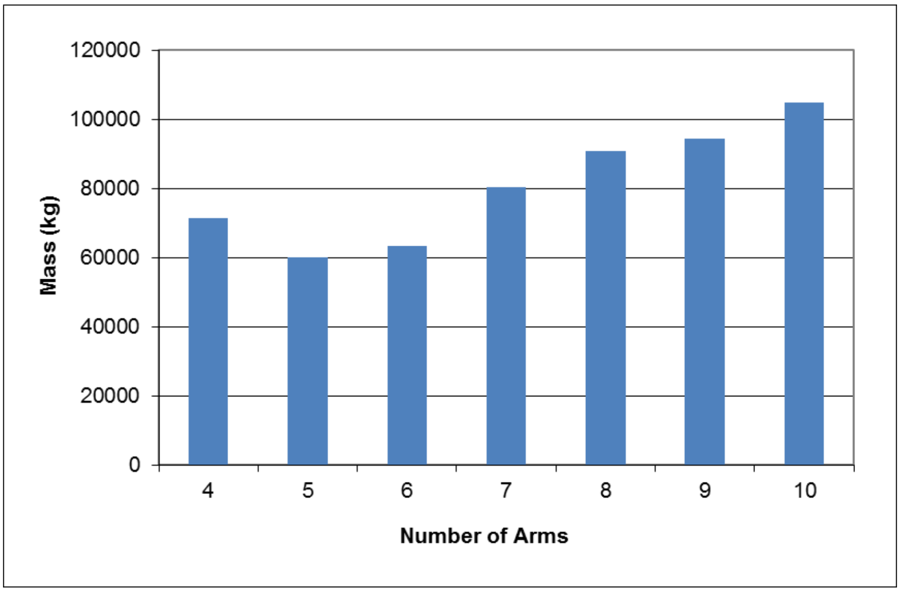

Figure 6.19 - Mass comparison of FEA optimised RF stator structures with arms

The results retrieved from this research indicate a similar structural behaviour with the RF rotor structures with arms. The mass of the RF stator with arms increases along with the number of arms that are employed for the same reasons explained in the structural analysis of the RF rotor with arms. Thus, the most lightweight structure was the optimised 5-armed stator, with a final mass of 60 tons.

An armed stator with hollow arms was also created. The arm's thickness is described as t_{ws} and it was the same for each side of the arm. The stator was checked for its stiffness against the given structural loads. The final dimensions of the stator's arms were d=300 mm and t_{ws}=30 mm (Figure 6.20). The mass of the structure was 48.3 tons, almost sixteen tons lighter than the original stator with arms.

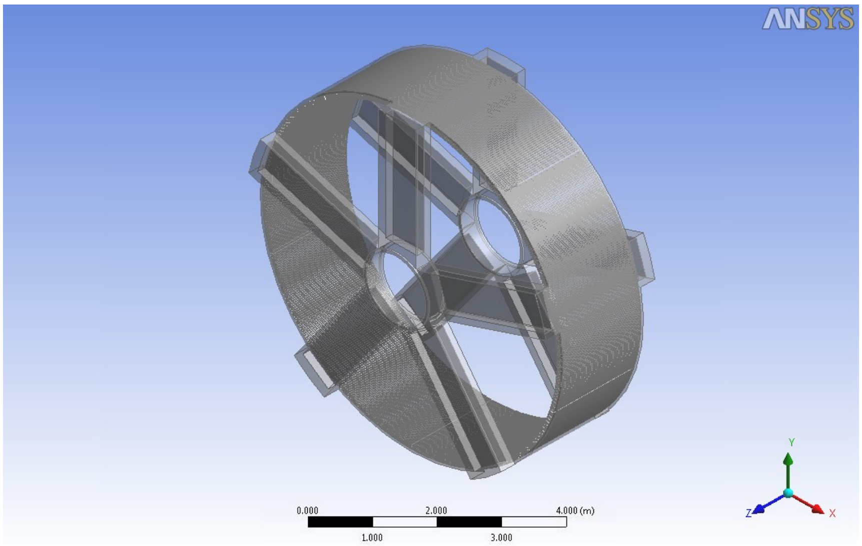

Figure 6.20 - Lightweight 5-armed RF stator with hollow arms

The most lightweight combination of optimised RF structures with arms was a rotor and stator with hollow arms. The total generator mass was reduced from 124.2 to 99.7 tons, offering a total mass reduction of 19.7%.

6.3 TF structural FEA optimisation

6.3.1 Optimised TF-1 structures

6.3.1.1 Rotor

For the rotor of the TF-1 machine, the same optimisation procedure described in section 6.2.1 was applied. Figure 6.21 depicts the output of the FEA optimisation tool along with the resulting lightweight rotor structures. The resulting structures were tested in each case to confirm their stiffness against the structural loads and to make sure that the resulting deflections were within the required limitations.

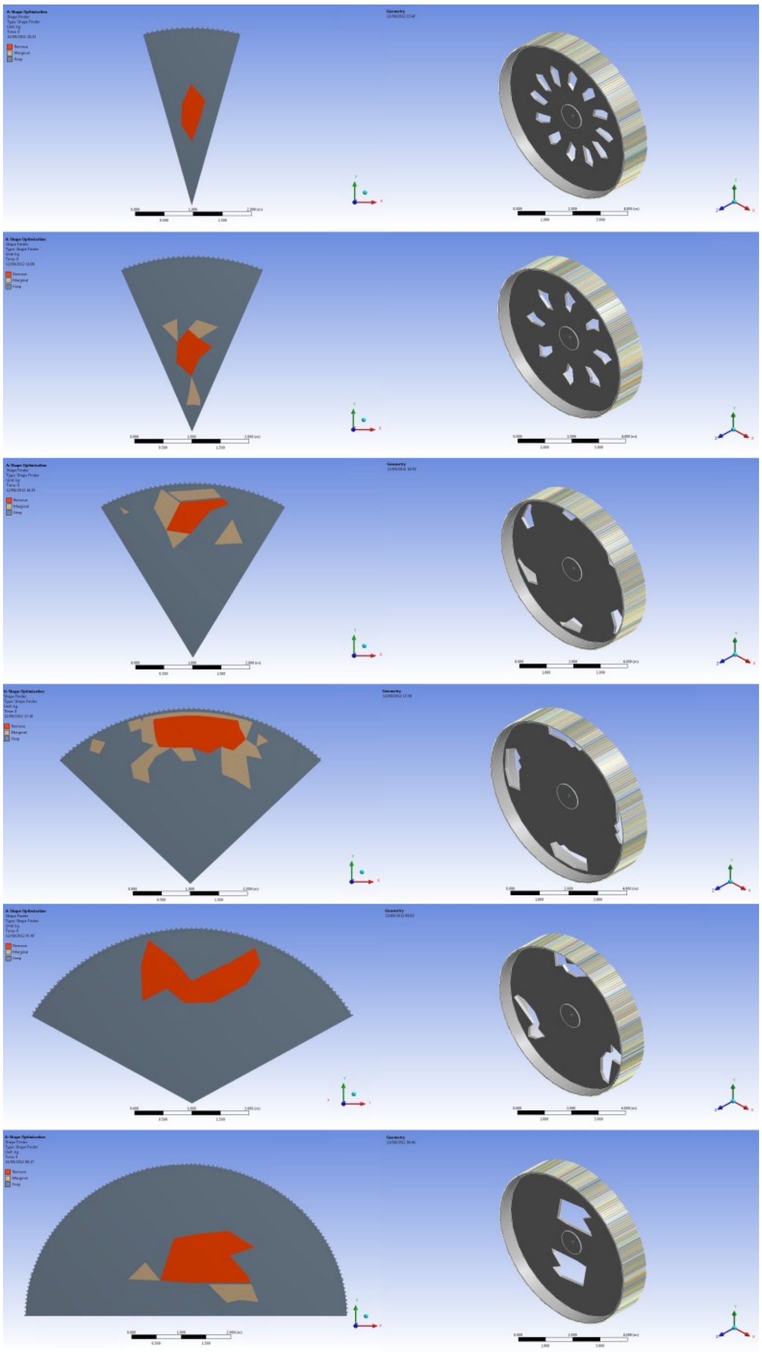

Figure 6.21 - The shape finder outputs (left) along with the resulting lightweight TF-1 rotor structures (right). From top: 12, 8, 6, 4, 3 and 2 pattern repetitions.

Once the structural optimisation process was completed, the permanent magnet material was added on the TF-1 rotor structures. The resulting masses are gathered in Table 6.5 and are illustrated in Figure 6.22.

Pattern Repetitions	Mass (tons)
0	40.0
2	37.6
3	37.1
4	36.0
6	37.6
8	38.1
12	39.2

Table 6.5 - Resulting masses of FEA optimised TF-1 rotor structures

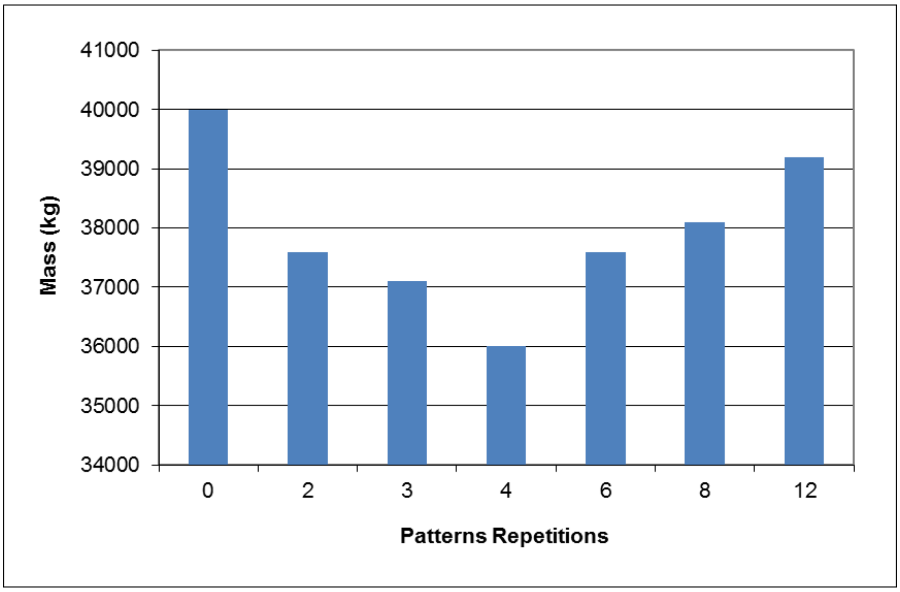

Figure 6.22 - Mass comparison of FEA optimised TF-1 rotor structures

From the results of this research it can be deducted that the mass of the TF-1 rotor can be effectively reduced by removing the indicated portions of mass from its disc. The most lightweight structure was achieved for four pattern repetitions, with a final mass of 36.0 tons.

6.3.1.2 Stator

For the stator of the TF-1 machine, the same optimisation process described in section 6.2.2 was applied. Figure 6.23 depicts the output of the FEA optimisation tool along with the resulting lightweight stator structures. The model of a TF-1 stator with hollow arms was also created. The resulting structures were tested in each case to confirm their stiffness against the structural loads and to make sure that the resulting deflections were within the required limitations.

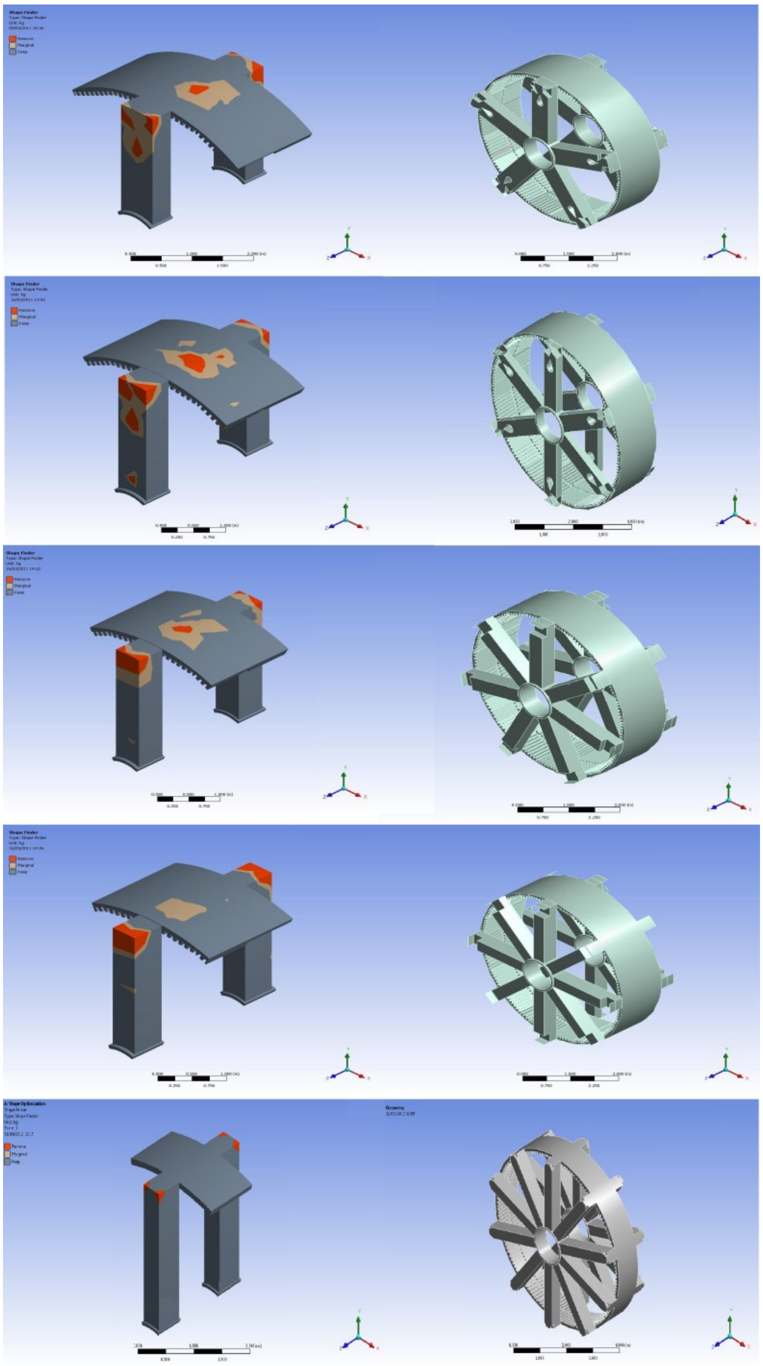

Figure 6.23 - The shape finder outputs (left) along with the resulting lightweight TF-1 stator structures (right). From top: 5-armed, 6-armed, 7-armed, 8-armed and 10-armed stators.

The resulting masses are gathered in Table 6.6 and are illustrated in Figure 6.24.

Number of arms	Original Mass (tons)	Final Mass (tons)
4	74.8	72.6
5	65.0	62.0
6	72.3	66.4
7	83.5	80.0
8	99.0	91.2
9	103.0	94.5
10	108.0	103.4

Table 6.6 - Resulting masses of FEA optimised TF-1 stator structures

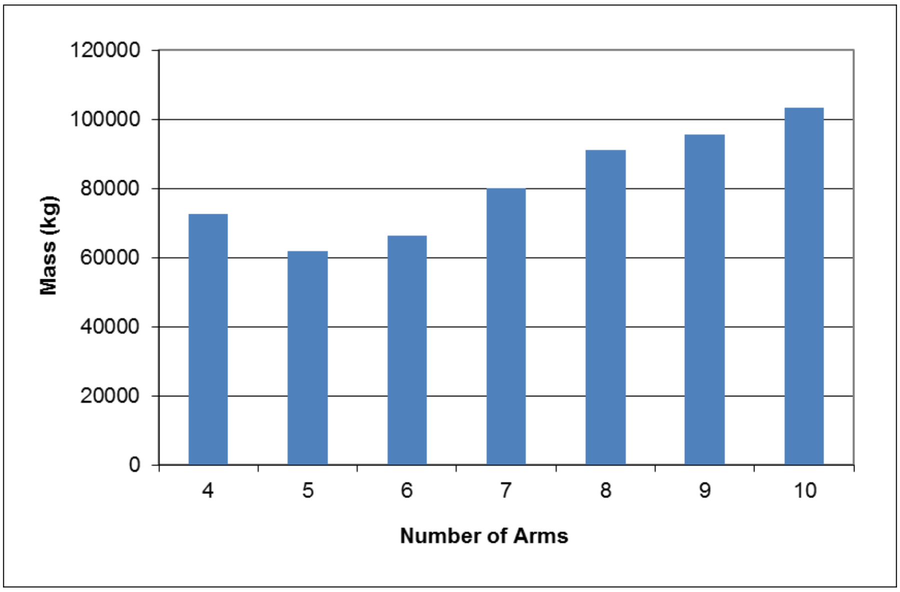

Figure 6.24 - Mass comparison of FEA optimised TF-1 stator structures

The results indicate a similar structural behaviour with the RF stator structure with arms. The structural mass of the TF-1 stator increases along with the number of arms that are employed. Due to the large structural forces that apply on this machine, the portion of mass that can be removed from each arm decreases as their number increases. Thus, the most lightweight structure in this case was the optimised 5-armed stator.

The TF-1 stator with hollow arms (Figure 6.25) proved to be much lighter than the suggested designs that came as a result of the optimisation process. The final dimensions of the stator's arms were d=300 mm and t_{ws}=75 mm. The mass of the structure was 60.0 tons, 5 tons lighter than the original TF-1 stator.

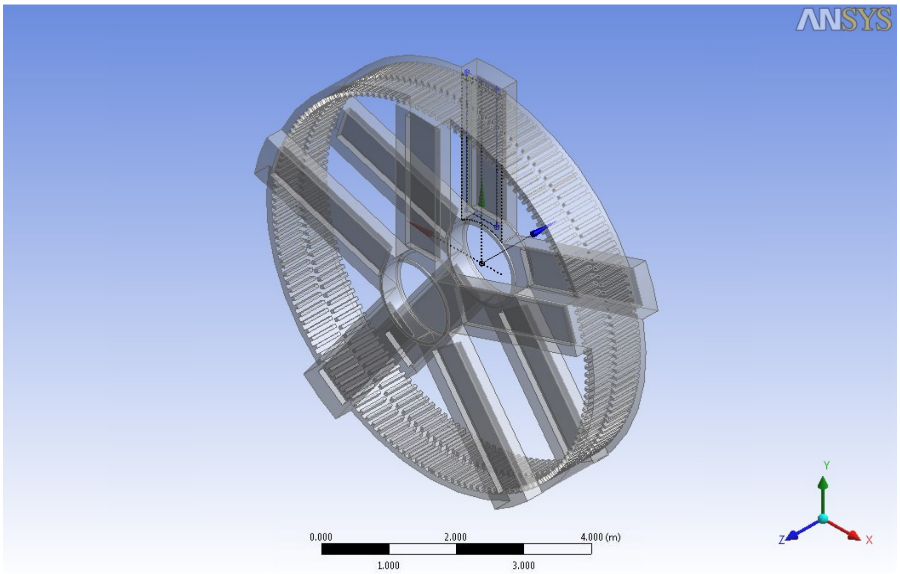

Figure 6.25 - Lightweight 5-armed TF-1 stator with hollow arms

The most lightweight combination of optimised TF-1 structures with arms was a rotor with four pattern repetitions and stator with hollow arms. The total generator mass was reduced from 105 to 96 tons, offering a total mass reduction of 8.6%.

6.3.2 Optimised TF-2 structures

6.3.2.1 Rotor

An attempt to optimise the rotor of the TF-2 machine was made. However, the results of the shape finder tool did not reveal any portions of mass on the rotor's disc that could be removed without compromising its stiffness. This can be attributed to the rotor's small axial length (l=80.8 mm) which makes it impossible for it to be further optimised. Therefore only the stator was structurally optimised in this machine. Figure 6.26 depicts the output of the shape finder tool for a number of different inputs.

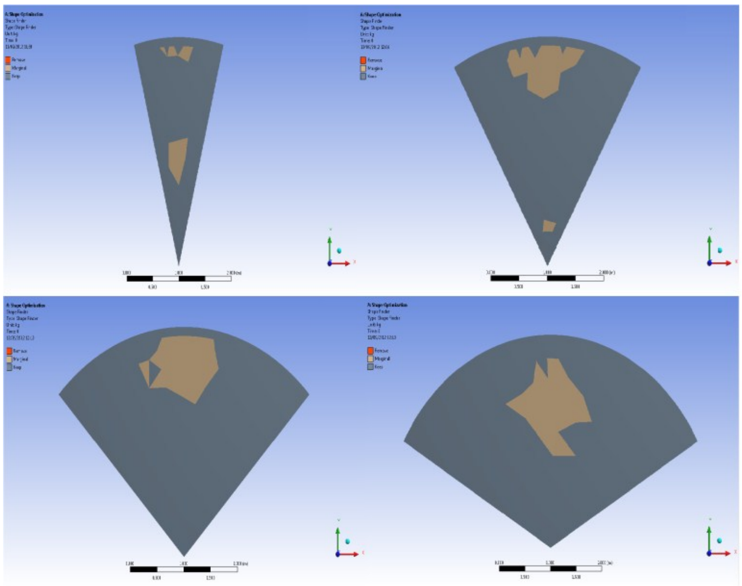

Figure 6.26 - The shape finder outputs for the TF-2 rotor. From top to bottom and from left to right: 12, 6, 4 and 3pattern repetitions.

6.3.2.2 Stator

Figure 6.27 depicts the output of the FEA optimisation tool along with the resulting lightweight stator structures. The model of a TF-2 stator with hollow arms was also created. The resulting masses are gathered in Table 6.7 and are illustrated in Figure 6.28.

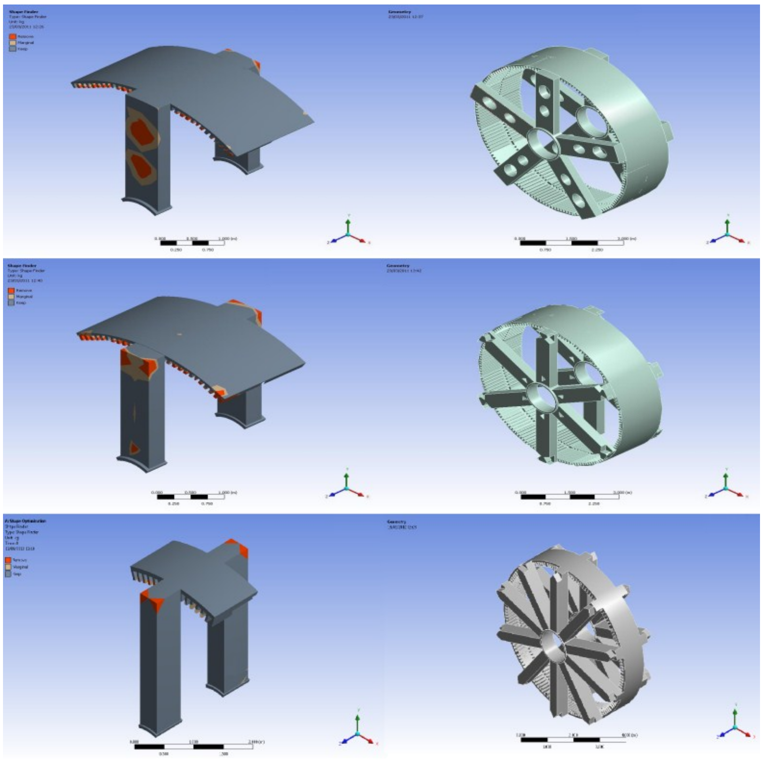

Figure 6.27 - The shape finder outputs (left) along with the resulting lightweight TF-2 stator structures (right). From top: 5-armed, 6-armed and 10-armed stators.

Number of arms	Original Mass (tons)	Final Mass (tons)
4	77.3	75.7
5	68.0	62.0
6	80.3	74.0
7	93.8	84.6
8	107.8	94.5
9	115.5	106.8
10	122.2	114.6

Table 6.7 - Resulting masses of FEA optimised TF-2 stator structures

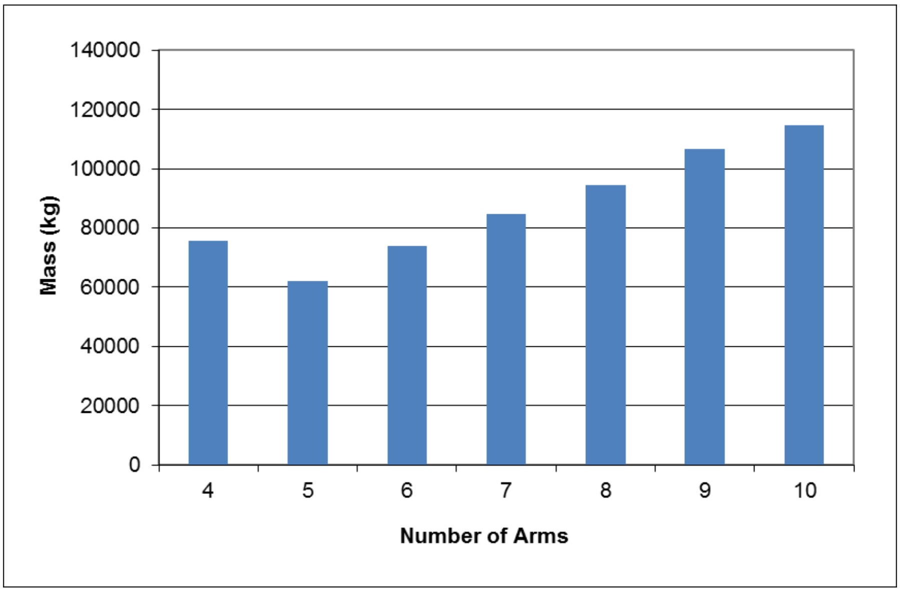

Figure 6.28 - Mass comparison of FEA optimised TF-2 stator structures

The structural mass of the TF-1 stator increases along with the number of arms that are employed for the same reasoning explained in sections 6.2.2 and 6.3.1. The most lightweight structure that came as a result of the shape optimisation process was the optimised 5-armed stator.

The TF-1 stator with hollow arms (Figure 6.29) proved to be much lighter than the suggested shape optimised designs. The final dimensions of the stator's arms were d=450 mm and t_{ws}=45 mm. The mass of the structure was 48.8 tons, 19.2 tons lighter than the original TF-2 stator.

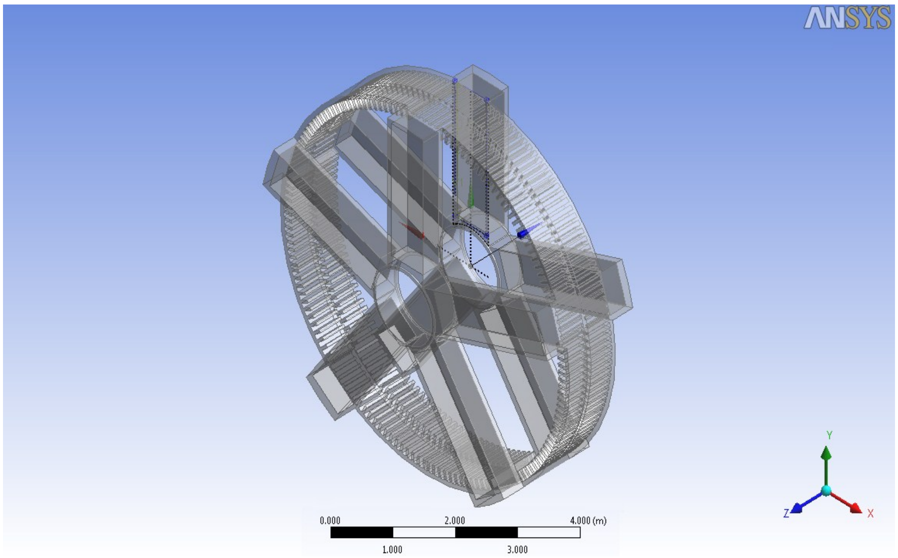

Figure 6.29 - Lightweight 5-armed TF-2 stator with hollow arms

Despite the fact that only the stator of the TF-2 machine could be optimised, the total mass of the TF-2 generator was reduced from 95 to 75.8 tons, offering a total mass reduction of 20.2%.

6.4 AF structural FEA optimisation

An attempt to optimise the rotor and stator of the AF machine was made. However, the results of the shape finder tool did not reveal any portions of mass that could be removed from both structures without compromising their stiffness. This can be attributed to the relatively small total mass of this topology which makes it impossible for the optimisation program to reduce it any further. Figures 6.30 and 6.31 depict the output of the shape finder tool for a number of different inputs for the AF aircored rotor and the stator accordingly.

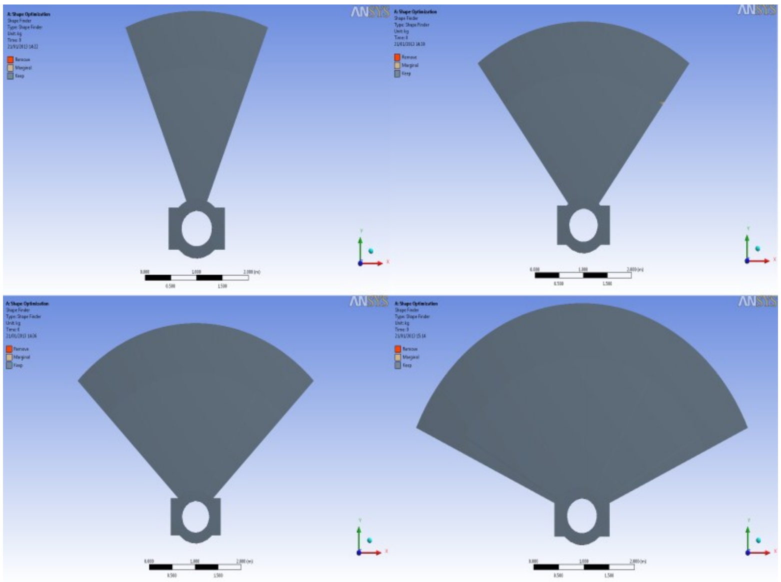

Figure 6.30 - The shape finder outputs for the AF rotor. From top to bottom and from left to right: 9, 6, 4 and 3 pattern repetitions.

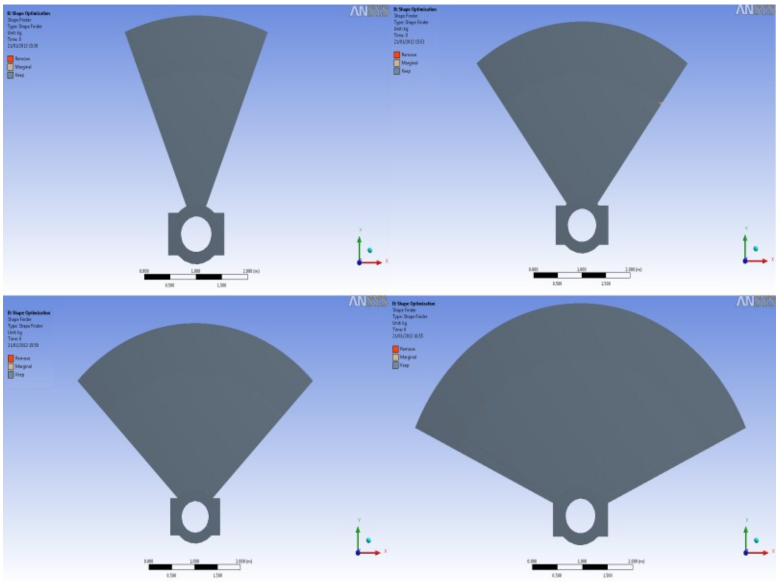

Figure 6.31 - The shape finder outputs for the AF stator. From top to bottom and from left to right: 12, 6, 4 and 3pattern repetitions.

6.5 Conclusions

The masses of the most lightweight optimised structures that occurred during the shape optimisation process are listed in Table 6.8 along with the original PMDD structures that were presented in chapter 5.

Generator Structure	Original Structural Mass (tons)	Optimised Structural Mass (tons)
RF Disc Rotor	51	46
RF Disc Stator	52	46
RF Armed Rotor	60	51
RF Armed Stator	64	48
TF-1 Rotor	40	36
TF-1 Stator	65	60
TF-2 Rotor	27	27
TF-2 Stator	68	49
AF Rotor	48	-
AF Stator	25	-

Table 6.8 - Comparison of the resulting masses of the PMDD generator structural models

The results of the FEA optimisation tool show that the structural mass of a PMDD generator can be effectively decreased without compromising its stiffness. Regarding the RF PMDD machines, the disc structures seem to have the advantage over the armed structures as far as stiffness is concerned. However, machining the suggested designs of the steel disc of the rotor and the stator of a machine would increase its initial manufacturing cost. This gives the advantage to armed structures with hollow arms, despite the fact that they are slightly heavier, as they are more likely to keep the manufacturing cost to a minimum. A RF generator with a disc rotor and an armed stator with hollow arms seems to be the ideal combination in terms of structural mass and total cost.

Regarding the TF machines, TF-1 proved to have the heaviest structural mass of all tested topologies. This is due to the great Maxwell stress that this specific generator has to overcome that did not allow any further mass to be removed from its structure. TF-2 on the other hand was the lightest structure of the tested topologies even though its rotor could not be optimised at all. The great mass reduction of the stator's structural mass, compared to the other optimised stator structures, can be attributed to the c-core design of the machine where the Maxwell attraction force acts on the axial direction.

In a final structural comparison, the AF aircored machine with C-cores on the rotor proved to be lighter compared to the structurally optimised RF and TF generators despite the fact that it was not further optimised.

This FEA tool was entirely based on static deflections. Further work needs to include a fatigue analysis as well as dynamic forces or modal analysis into the optimisation process. Although this method should be an efficient way to reduce mass, sophisticated patterns on the steel disc or arms of a rotor would decrease a machine's resistance to fatigue and increase the manufacturing cost at the same time.

In order for such process to be cost effective, the Initial Capital Cost (ICC) of the machine should be considered against the net Annual Energy Production (AEP). Further research needs to include a detailed cost analysis in order to determine the point at which the proposed improvements would start to have a negative outcome. However, the results of this work provide an indication of the design solutions that could help decrease the mass of both radial and transverse flux machines.

Chapter 7

Structural Optimisation with Analytical Tools

7.1 Introduction

A different approach to calculate and optimise the structural parameters of a PMDD machine is with the help of an analytical model. In analytical approaches, a detailed mathematical model of the generator's structure is made in an attempt to calculate useful parameters such as the generator's cost, mass, maximum operating temperature or deflection. The outcome of an analytical model is always based on predefined input parameters such as the nominal power or required torque level of the tested generator. In this chapter an analytical tool that minimises the total mass or cost of different PMDD generators will be presented. The optimisation tool was adjusted for generators with nominal power output of 5MW.

In chapter 6 it was shown that the most lightweight and easily manufactured structure for the conventional RF PMDD generator utilised a disc structure for the rotor and an armed structure with hollow arms for the stator. The same structures could be used to create a lightweight TF-1 or TF-2 machine. Thus, only such generator structures will be considered in this chapter for the tested machines, allowing all three generator designs to be described with similar mathematical models. For the creation of these models the MATLAB language environment was used [178]. The AF aircored machine was not included in this optimisation process as it has no further structural mass to spare according to the results of chapter 6.

The basic dimensions that were used to create the PMDD generator analytical models were the machine's radius R (m), the structure's axial length l (m), the rotor's disc thickness t_d (m) and back height h_{yr} (m), the number of the stator's arms N, the stator's arms width b (m) and depth d (m) and thickness t_w (m) and the stator's back height h_{ys} (m) (Figure 7.1).

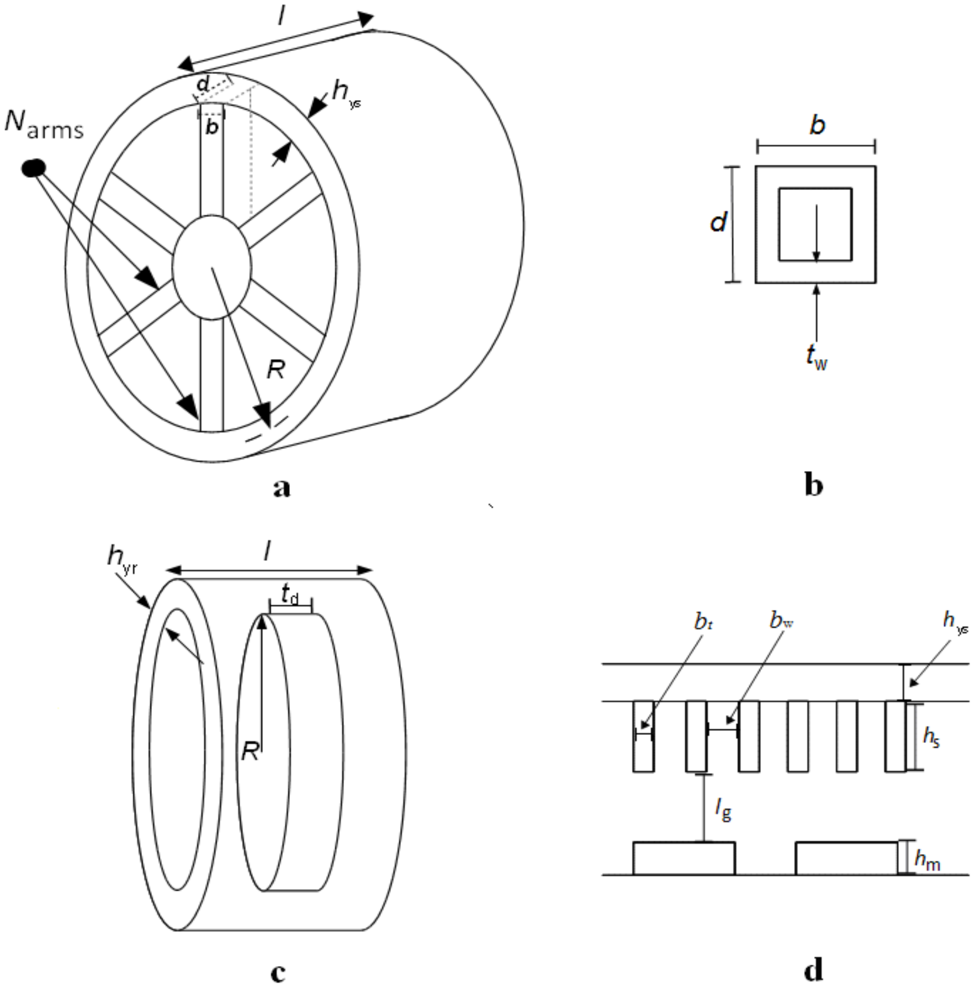

Figure 7.1 - Depiction of the variable dimensions that were used for the modelling of the generator structures: (a) The variables that describe the stator with arms (b) The variables that describe the stator's hollow arms (c) The variables that describe the rotor with disc (d) The variables that describe the electromagnetic model

Table 7.1 lists the remaining structural parameters, as calculated by Bang in [89] for the given shear stress that applies on the tested machines.

Generator Topology	**RF**	**TF-1**	**TF-2**
Airgap length, l_g (m)	$l_g = R/500$	$l_g = R/500$	$l_g = R/500$
Magnet width, b_m (m)	$0.8\tau_p$	τ_p-h_m	τ_p-h_m
Number of phase, m	3	3	3
Pole pitch, τ_p (m)	$\tau_p = 0.033m$	$\tau_p = 10l_g$	$\tau_p = 10l_g$
Winding space width, b_w (m)	0.015	0.0808	0.0808
Winding space height, h_s (m)	$h_s = 5.3b_w$	$h_s = b_w$	$h_s = b_w$
Stator tooth width, b_t (m)	$b_t = \tau_p$-b_w	$b_t = 0.8\tau_p$	$b_t = 0.8\tau_p$
Stator tooth axial length, l_{sp} (m)	$l_{sp} = l$	$l_{sp} = (l$-$b_w)/2$	$l_{sp} = (l$-$b_w)/2$
Remanent flux density, B_r (T)	1.2	1.2	1.2
Peak flux density in the Airgap, B_g (T)	1.1	1.6	0.76

Table 7.1 - Parameters and dimensions of the 5MW PMDD generator structures [89]

Analytical optimisation models that seek to minimise the structural mass of a PMDD generator have been suggested in the literature by Grauers in [30] and McDonald in [31]. Grauers created an analytical cost-optimisation function to calculate the optimal dimensions of a RF PMDD generator. The cost of the active parts, the cost of average losses and the cost of the structure were included in order to optimise a direct drive stator. McDonald *et al* used a genetic algorithm (GA) toolbox [179] to minimise the structural mass of a RF PMDD rotor. Neither researcher considered coupling the electromagnetic design with the structural in the optimisation process.

The optimisation tool that was created for the purpose of this research takes into consideration both the electromagnetic and structural design of the tested machine at the same time. The optimisation process seeks to minimise the structural mass or the total cost of the given PMDD machine while keeping a set of structural deflections within limitations. The structural models that describe these deflections vary for different generator topologies.

In the following sections, the structural and electromagnetic models of each tested machine will be described followed by the optimisation process that takes place in each case. Once the optimisation results are retrieved, a comparison is made to draw valuable conclusions.

7.2 Structural modelling

For the structural modelling of the PMDD generator topologies, only the loads that could lead to a reduction of the airgap clearance were taken into consideration. These loads as described in chapter 5 are the radial deflection that is caused due to the normal component of the Maxwell stress q, the vertital deflection due to gravity and the torsional deflection due to the centripetal force. q mainly acts on the rotor and stator active surface, which will have most impact on the back height of these structures, h_{ys} and h_{yr} respectively. Gravity acts radially during operation, therefore the arms and discs of the structure are most vulnerable. The tangential deflection due to torsional stress acts on the support of the structure.

7.2.1 Analytical models of the RF structures

The analytical expressions that describe the radial deflection due to Maxwell stress q (u_{A}) and due to gravitational pull (u_{G}) of the disc structure of a RF rotor have been described by McDonald in [180] and are presented in (7.1) and (7.2). An analytical model for the tangential deflection of a disc structure does not exist. This means that the analytical models for the disc structures lack the tangential deflection criterion, thus all results should be verified with the FEA tool to ensure their stiffness in the tangential direction.

$$u_{\mathrm{A}} = \frac{qR^2}{E(R_{\mathrm{a}} - R)} + \frac{f}{2D\lambda^3}\left[\frac{-F_1(x=0)}{C_{11}}\left(C_3C_{\mathrm{a2}} - C_4C_{\mathrm{a1}}\right) + \frac{F_2(x=0)}{2C_{11}}\left(C_2C_{\mathrm{a2}} - 2C_3C_{\mathrm{a1}}\right) - \frac{F_{\mathrm{a4}}(x=0)}{2}\right] \quad (7.1)$$

where E the Young's modulus and R_{a} the rotor's outer radius (m) with $R_{\mathrm{a}} = R + h_{\mathrm{yr}}$. f is the uniform outward radial force per unit length (N/m) and is defined as $f = f_{\mathrm{d}}t_{\mathrm{d}}$. The equation that describes f_{d} along with the constants C_2, C_3, C_4, C_{a1}, C_{a2}, C_{11}, and functions λ, D, F_1, F_2 and F_{a4} are given in Appendix A.

$$u_{\mathrm{G}} = \frac{-WR^3}{R_{\mathrm{o}}D_{\mathrm{ax}}}\left[\frac{C_2C_6}{C_5} - C_3\right] + M_{\mathrm{rb}}\frac{R_{\mathrm{a}}^2}{D_{\mathrm{ax}}}C_2 + Q_{\mathrm{b}}\frac{R_{\mathrm{a}}^3}{D_{\mathrm{ax}}}C_3 - \frac{wR_{\mathrm{a}}^4}{D_{\mathrm{ax}}}L_{11} \tag{7.2}$$

where R_{o} the radius of the generator's shaft with $R_{\mathrm{o}} = 0.5\mathrm{m}$. Constants C_5, C_6, L_{11} and functions W, w, D_{ax}, M_{rb} and Q_{b} are given in Appendix A.

The analytical expressions that describe the radial deflection due to Maxwell stress q (u_{A}), the axial deflection due to gravitational pull (u_{G}) and the tangential deflection (u_{T}) of the armed structure of a RF stator have been described by McDonald in [180] and are presented in (7.3), (7.4) and (7.5).

$$u_{\mathrm{A}} = \frac{qR^2}{Eh_{\mathrm{ys}}}\left(1 + \frac{R^3\left[\dfrac{\sin\theta - \theta\cos\theta}{4\sin^2\theta} - \dfrac{1}{2\sin\theta} + \dfrac{1}{2\theta}\right]}{I\left[\left(\dfrac{\theta}{\sin\theta} + \dfrac{1}{\tan\theta}\right)\left(\dfrac{R}{4A} + \dfrac{R^3}{4I}\right) - \dfrac{R^3}{2I\theta}\left(\dfrac{1}{m+1}\right) + \dfrac{R - R_o}{2a}\right]}\right) \tag{7.3}$$

where θ the half angle between arms (rad), I the second moment of area of the stator's cylinder (m^4), A the cross area of the stator's cylinder (m^2) and a the cross area of the stator's arm (m^2). The functions of θ, I, A, m and a are given in Appendix A.

$$u_{\mathrm{G}} = \frac{W'(R - R_o)^3}{12EI_{\text{arm-axi}}} + \frac{w_i(R - R_o)^4}{24EI_{\text{arm-axi}}} + \frac{w'(R - R_o)^4}{24EI_{\text{arm-axi}}} \tag{7.4}$$

where $I_{\text{arm-axi}}$ the second moment of the area of the stator arm (m^4). Functions $I_{\text{arm-axi}}$, W', w' and w_{i} are given in Appendix A.

$$u_{\mathrm{T}} = \left(\frac{2\pi Rl}{2N_{arms}}\right)\sigma l^3 \Big/ 3EI_{\text{arm-tor}} \tag{7.5}$$

where σ the shear stress that gives rise to torque (kPa) and $I_{\text{arm-tor}}$ the second moment of area of the stator arm (m^4). The equation that describes $I_{\text{arm-tor}}$ is given in Appendix A.

7.2.2 Analytical models of the TF-1 structures

The analysis of the disc structure of the TF-1 rotor is the same as that of the RF generator described in section 7.2.1. However, the impact of the forces acting on the armed structure in the TF-1 stator are different to that of the iron-cored PM generator, thus only analysis of the stator structure is considered for the TF-1 machine.

The axial deflection due to gravitational pull and the tangential deflection of the TF-1 stator were the same with those described for the RF machine in equations (7.4) and (7.5). In the case of the RF machine, pressure q due to the Maxwell stress was uniform and applied to the whole cylindrical shell of the stator. In the TF-1 machine though, the attraction force applies only beneath the active parts of the C-core as depicted in Figure 7.2. Thus, equation (7.3) had to be altered accordingly in order to describe accurately the deflection of the stator's cylindrical shell.

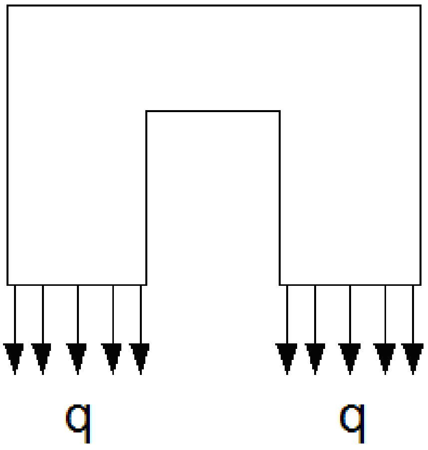

Figure 7.2 - Maxwell stress applied on C-core on TF-1 stator

In terms of simplification, it was assumed that the C-cores of the structure do not have space between them in the circumferential direction. Thus it can be assumed that both sides of the C-core create a cylindrical shell with a gap in the middle as depicted in Figure 7.3. This assumption was made for both TF machine topologies for comparison purposes. The neglected space between the cores is expected to give extra stiffness to the stator's structure resulting in deflections slightly smaller compared to the actual ones.

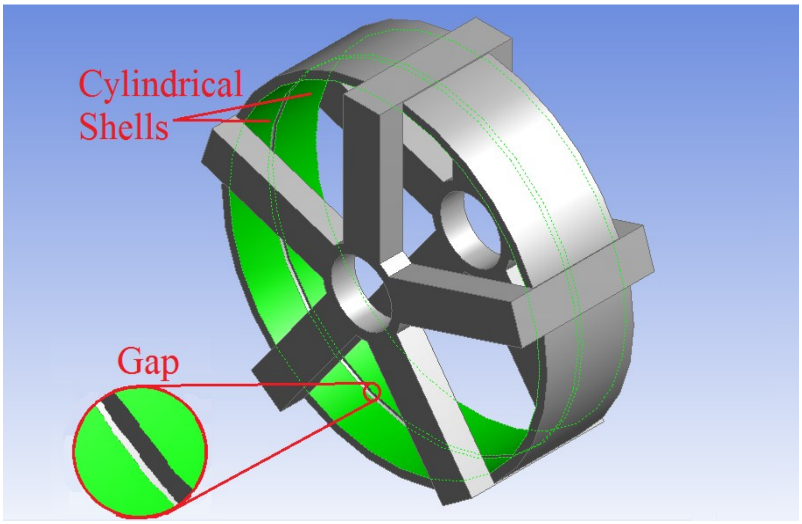

Figure 7.3 - The TF-1 stator structural model

According to Roark's formulas [181] for thin walled cylindrical shells under uniform radial pressure from a to l the force applied on the right end of the shell will cause a radial deflection on both sides of the shell as depicted in Figure 7.4. In this case $a = (l + b_w)/2$, where l is the axial length of the machine from End1 to End2.

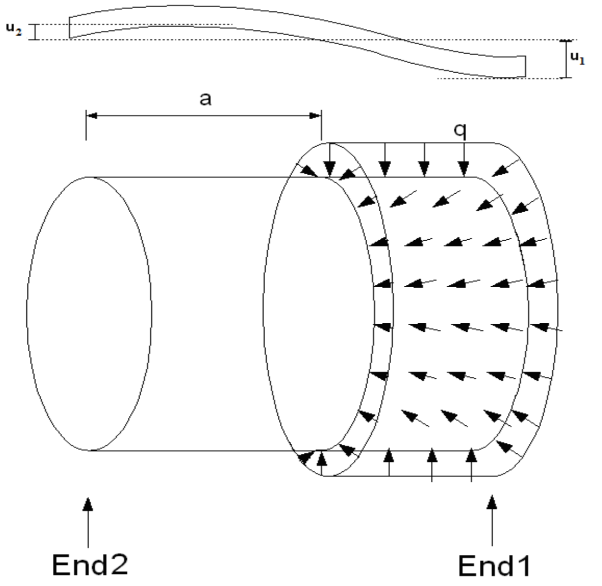

Figure 7.4 - Radial deflection of shell due to load, *q*

The equations that describe these deflections are given in (7.6) and (7.7).

$$
\begin{aligned}
u_1 &= \left(-\frac{q}{4D\lambda^4}\frac{2C_3C_{a3}-C_4C_{a2}}{C_{11}}C_1+\frac{q}{4D\lambda^4}\frac{C_2C_{a3}-C_3C_{a2}}{C_{11}}C_2-\frac{q}{4D\lambda^4}C_{a5}\right)F_{1(x=l)}+\\
&+\left(\frac{q}{4D\lambda^4}\frac{C_2C_{a3}-C_3C_{a2}}{C_{11}}C_1-\frac{q}{4D\lambda^4}\frac{C_3C_{a3}-C_4C_{a2}}{C_{11}}C_4-\frac{q}{4D\lambda^4}C_{a4}\right)F_{2(x=l)}-\frac{q}{4D\lambda^4}F_{a5(x=l)}=\\
&=\frac{q}{4D\lambda^4}\left[\begin{array}{l}\left(-\frac{2C_3C_{a3}-C_4C_{a2}}{C_{11}}C_1+\frac{C_2C_{a3}-C_3C_{a2}}{C_{11}}C_2-C_{a5}\right)F_{1(x=l)}+\\ +\left(\frac{C_2C_{a3}-C_3C_{a2}}{C_{11}}C_1-\frac{C_3C_{a3}-C_4C_{a2}}{C_{11}}C_4-C_{a4}\right)F_{2(x=l)}-F_{a5(x=l)}\end{array}\right]
\end{aligned}
\tag{7.6}
$$

$$
\begin{aligned}
u_2 &= -\frac{q}{4D\lambda^4}\frac{2C_3C_{a3}-C_4C_{a2}}{C_{11}}F_{1(x=0)}+\frac{q}{4D\lambda^4}\frac{C_2C_{a3}-C_3C_{a2}}{C_{11}}F_{2(x=0)}-\frac{q}{4D\lambda^4}F_{a5(x=0)}=\\
&=\frac{q}{4D\lambda^4}\left(-\frac{2C_3C_{a3}-C_4C_{a2}}{C_{11}}F_{1(x=0)}+\frac{C_2C_{a3}-C_3C_{a2}}{C_{11}}F_{2(x=0)}-F_{a5(x=0)}\right)
\end{aligned}
\tag{7.7}
$$

Constants λ, D, C_1, C_2, C_3, C_4, C_{a2}, C_{a3}, Ca_4, Ca_5, C_{11}, and functions F_1, F_2 and F_{a5} are given in Appendix A.

In order to verify the analytical model the structure was modelled using the suggested FEA tool [175]. As can be seen in Figure 7.5, the deflections on each end of the shell due to the Maxwell stress applied on End1 only have opposing directions. Since there is going to be an equal stress with the same direction on the other end of the shell causing the same radial deflections u_1 and u_2, and assuming that the structural material is linear, the resulting deformations can be superposed. It can be derived that the total radial deflection on each end is equal to $u_2 - u_1$.

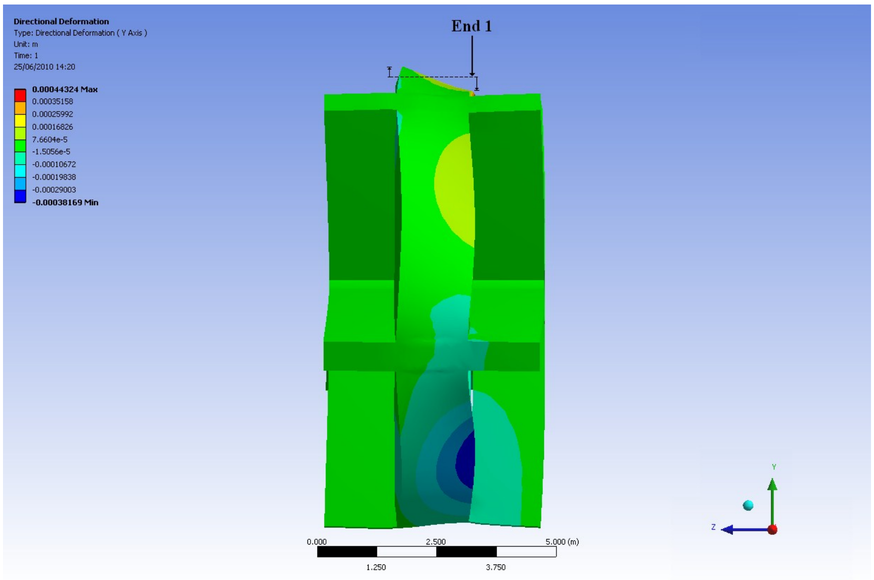

Figure 7.5 - Radial deflection of stator due to uniform load on the right side of the C-core

$$
\begin{aligned}
&u = u_2 - u_1 = \\
&= \frac{q}{4D\lambda^4}\left[\begin{aligned}&\left(-\frac{2C_3C_{a3}-C_4C_{a2}}{C_{11}}F_{1(x=0)}+\frac{C_2C_{a3}-C_3C_{a2}}{C_{11}}F_{2(x=0)}-F_{a5(x=0)}\right)- \\ &-\left(-\frac{2C_3C_{a3}-C_4C_{a2}}{C_{11}}C_1+\frac{C_2C_{a3}-C_3C_{a2}}{C_{11}}C_2-C_{a5}\right)F_{1(x=l)}-\left(\frac{C_2C_{a3}-C_3C_{a2}}{C_{11}}C_1-\frac{C_3C_{a3}-C_4C_{a2}}{C_{11}}C_4-C_{a4}\right)F_{2(x=l)}+F_{a5(x=l)}\end{aligned}\right]
\end{aligned}
\tag{7.8}
$$

The combination of (7.3) and (7.8) can be used to provide the total radial deflection of a stator with arms for this type of transverse-flux machine (7.9)

$$u_{TF-1} = \frac{q}{4D\lambda^4}\left[\begin{aligned}&\left(-\frac{2C_3C_{a3}-C_4C_{a2}}{C_{11}}F_{1(x=0)}+\frac{C_2C_{a3}-C_3C_{a2}}{C_{11}}F_{2(x=0)}-F_{a5(x=0)}\right)+\\&+\left(\frac{2C_3C_{a3}-C_4C_{a2}}{C_{11}}C_1-\frac{C_2C_{a3}-C_3C_{a2}}{C_{11}}C_2+C_{a5}\right)F_{1(x=l)}-\left(\frac{C_2C_{a3}-C_3C_{a2}}{C_{11}}C_1-\frac{C_3C_{a3}-C_4C_{a2}}{C_{11}}C_4-C_{a4}\right)F_{2(x=l)}+F_{a5(x=l)}\end{aligned}\right]*$$

$$*\left(1+\frac{R^3\left[\dfrac{\sin\theta-\theta\cos\theta}{4\sin^2\theta}-\dfrac{1}{2\sin\theta}+\dfrac{1}{2\theta}\right]}{I\left[\left(\dfrac{\theta}{\sin\theta}+\dfrac{1}{\tan\theta}\right)\left(\dfrac{R}{4A}+\dfrac{R^3}{4I}\right)-\dfrac{R^3}{2I\theta}\left(\dfrac{1}{m+1}\right)+\dfrac{R-R_o}{2a}\right]}\right) \tag{7.9}$$

The accuracy of the analytical model for the radial deflection was verified with the help of the FEA tool for a variety of different aspect ratios (K_{rad}).

As can be seen in Figure 7.6, for the majority of the tested cases the radial deflection obtained by the structural model was slightly smaller compared to the radial deflection returned by the analytical model. For all cases tested the difference between the two models was less than 20%, with a 10.2% average error. The results are presented for different values of aspect ratios.

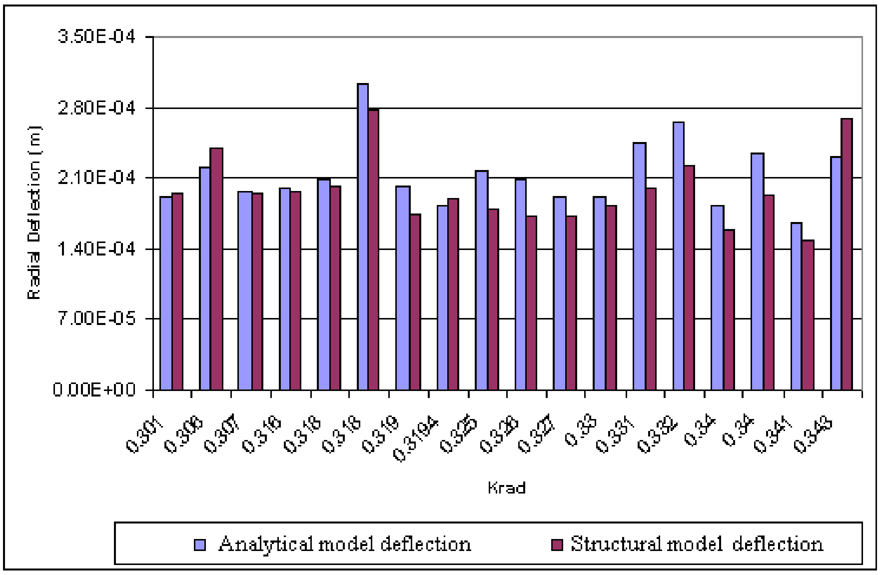

Figure 7.6 - Comparison between analytical and structural models for the 5MW TF-1 machine

7.2.3 Analytical models of the TF-2 structures

Both the electromagnetic attraction force and the gravitational pull act on the axial direction of the TF-2 rotor. The analytical expressions that describe the axial deflection of a disc rotor structure due to Maxwell stress and due to gravitational attraction have been described by McDonald and Mueller in [86] and [180]. The axial deflection of the armed stator structure due to gravitational attraction when it is lifted or transported and the circumferential deflection have been described in [180] and are the same as (7.4) and (7.5) described in Section 7.2.1.

The attraction force however applies only inside the winding space of the C-core of the TF-2 stator (Figure 7.7).

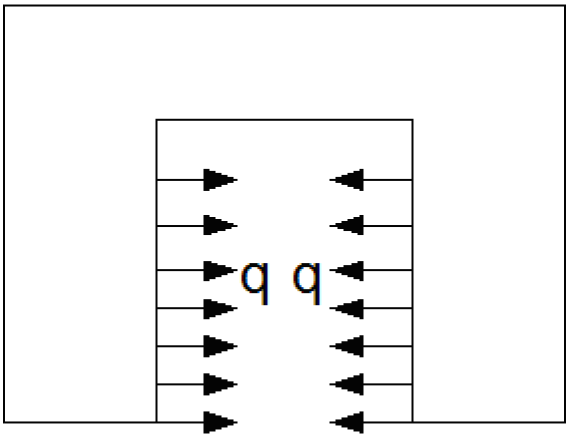

Figure 7.7 - Maxwell stress applied on C-core on TF-2 stator

In terms of simplification, it was assumed that the C-cores of the structure do not have gaps between them in the circumferential direction. Thus it can be assumed that both sides of the C-core create a cylindrical shell with a gap in the middle as depicted in Figure 7.8.

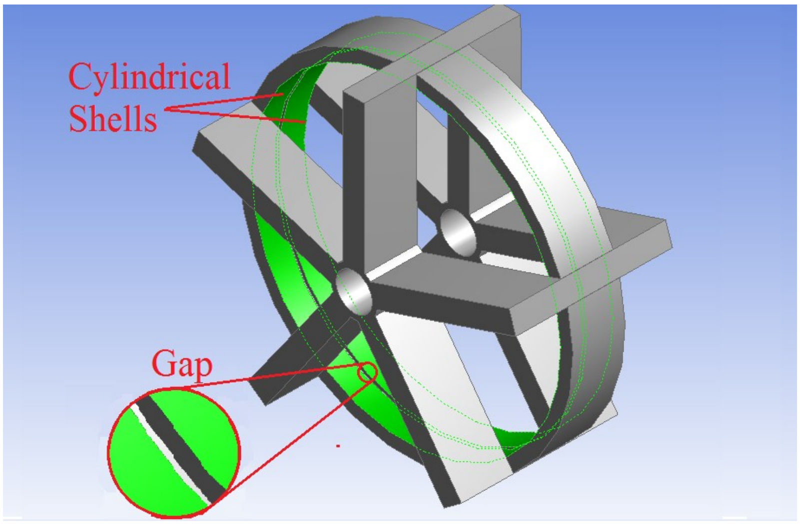

Figure 7.8 - The TF-2 stator structural model

For the description of the radial deflection of this structure, it was assumed that the normal stress applied on the inside of the C-core of the TF-2 machine creates a moment on each side of the stator core that tries to bend the cylindrical shell of the stator as depicted in Figure 7.9.

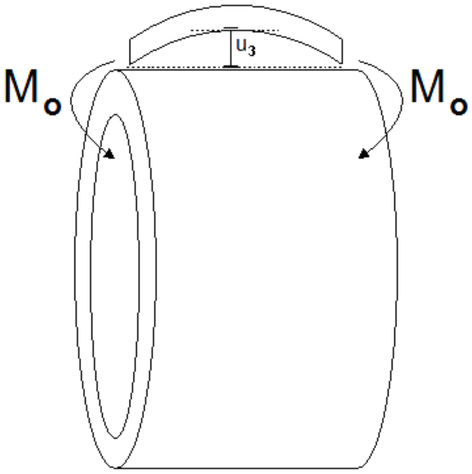

Figure 7.9 - Radial deflection of shell due to moment M_o

According to Roark's formulas for thin walled cylindrical shells under a moment M_o [181], where

$$M_o = \frac{2\pi(R+h_{ys})M_{ra}}{N_s} \quad (7.10) \qquad \text{and} \qquad M_{ra} = -qh_{ys}^{\ 2}\left(L_{17} - \frac{C_7}{C_4}L_{14}\right) \quad (7.11)$$

The force applied on each end of the shell is going to cause a radial deflection as given in (7.12):

$$u_3 = \frac{M_o}{2D\lambda^2}\frac{C_{14}}{C_{11}}F_{1(x=0)} - \frac{M_o}{2D\lambda^2}\frac{C_{12}}{C_{11}}F_{2(x=0)} + \frac{M_o}{2D\lambda^2}F_{3(x=0)} = \frac{M_o}{2D\lambda^2}\left(\frac{C_{14}}{C_{11}}F_{1(x=0)} - \frac{C_{12}}{C_{11}}F_{2(x=0)} + F_{3(x=0)}\right) \quad (7.12)$$

Constants λ, D, C_{11}, C_{12}, C_{14}, and functions F_1, F_2 and F_3 are given in Appendix A. Since there is an equal moment applied on the other side of the stator's shell, the total radial deflection of the structure is $2u_3$. The combination of (7.3) and (7.12) can be used to provide the total radial deflection of a stator with arms for the TF-2 stator:

$$u_{TF-2} = \frac{M_o}{D\lambda^2}\left(\frac{C_{14}}{C_{11}}F_{1(x=0)} - \frac{C_{12}}{C_{11}}F_{2(x=0)} + F_{3(x=0)}\right)\left(1 + \frac{R^3\left[\frac{\sin\theta - \theta\cos\theta}{4\sin^2\theta} - \frac{1}{2\sin\theta} + \frac{1}{2\theta}\right]}{I\left[\left(\frac{\theta}{\sin\theta} + \frac{1}{\tan\theta}\right)\left(\frac{R}{4A} + \frac{R^3}{4I}\right) - \frac{R^3}{2I\theta}\left(\frac{1}{m+1}\right) + \frac{R - R_o}{2a}\right]}\right) \quad (7.13)$$

Apart from the radial deflection, the moment M_o that tries to bend the cylindrical shell of the stator core also gives rise to an axial deflection δ1 as depicted in Figure 7.10.

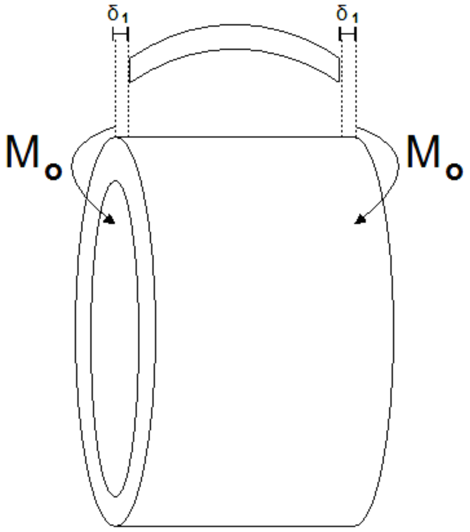

Figure 7.10 - Axial deflection of shell due to moment M_o

This axial deflection can be calculated with the help of the meridional slope ψ_1 that is caused due to the moment M_o (Figure 7.11).

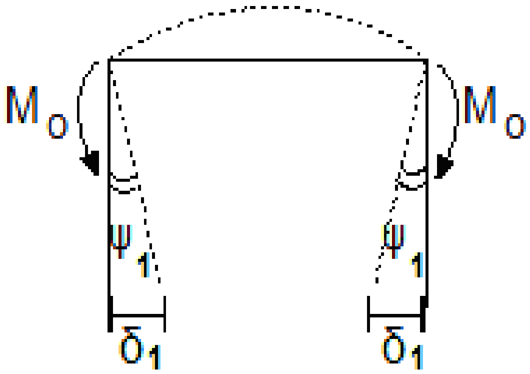

Figure 7.11 - Meridian slope of shell due to moment M_o

According to Roark's formulas for thin walled cylindrical shells under a moment M_o [181], this slope can be calculated with the use of (7.14):

$$\psi_1 = -\frac{M_o}{D\lambda}\frac{C_{12}}{C_{11}}F_{1(x=0)} - \frac{M_o}{2D\lambda}\frac{C_{14}}{C_{11}}F_{4(x=0)} + \frac{M_o}{2D\lambda}F_{2(x=0)} = \frac{M_o}{2D\lambda}\left(-2\frac{C_{12}}{C_{11}}F_{1(x=0)} - \frac{C_{14}}{C_{11}}F_{4(x=0)} + F_{2(x=0)}\right) \quad (7.14)$$

The axial deflection δ_1 due to the moment M_o is given in (7.15).

$$\delta_1 = h_{ys}\sin(\psi_1) \quad (7.15)$$

Constants λ, D, C_{11}, C_{12}, C_{14}, and functions F_1, F_2 and F_4 for cylindrical shells are given in Appendix A.

Apart from δ_1 there is also going to be another axial deflection δ_2 due to the stress q applied on the inside of the C-core (Figure 7.12).

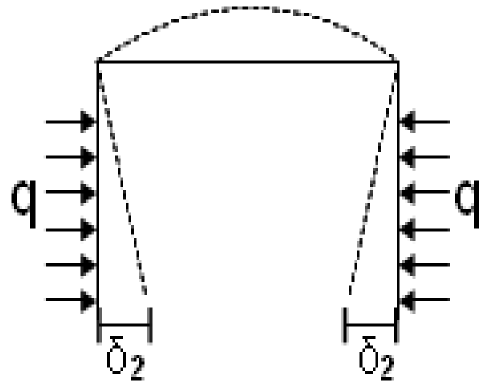

Figure 7.12 - Axial deflection of shell due to normal component of Maxwell stress

Since it was assumed that there is no gap between the C-cores of the stator, a circular plate is formed. According to circular plate theory described in [181], the axial deflection δ_2 can be calculated from (7.16).

$$\delta_2 = -\frac{qR^4}{D}\left(\frac{C_1 L_{14}}{C_4} - L_{11}\right) \tag{7.16}$$

Constants D, C_1, C_4, C_7, L_{11}, L_{17}, and L_{14}, for circular plates are given in Appendix A.

The total axial deflection $\delta_{\text{TFPM-2}}$ is the sum of (7.15) and (7.16):

$$\delta_{TFPM-2} = \delta_1 + \delta_2 \tag{7.17}$$

The accuracy of the analytical model for the radial and axial deflection of the stator was verified with the FEA tool. Various values of aspect ratio (K_{rad}) were used in the comparison.

As can be seen in Figure 7.13, for the majority of the tested cases the radial deflection obtained by the analytical model was slightly smaller for the 5MW machine compared to the radial deflection returned by the structural model. The analytical model was more accurate for greater aspect ratios. For all cases tested the difference between the two models was less than 20%, with an 11.3% average error.

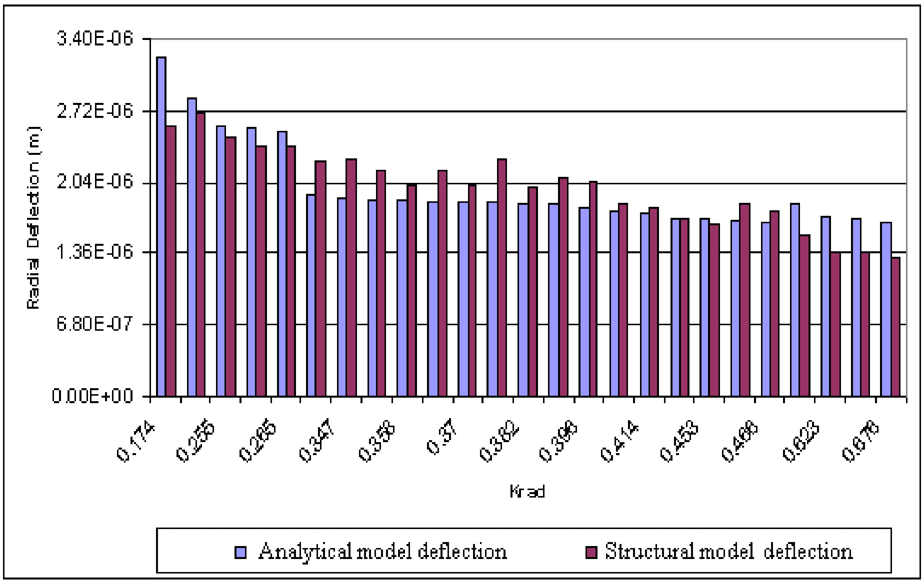

Figure 7.13 - Comparison between analytical and structural models for radial deflection of stator for the 5MW TF-2 machine

Figure 7.14 depicts the comparison between the structural and analytical models for the axial deformation of the structure for the 5MW TF-2 machine. Again the axial deflection obtained by the analytical model was slightly smaller compared to the axial deflection returned by the structural model in most cases. In all tested cases the difference between the two models was less than 20%, with a 15.3% mean error.

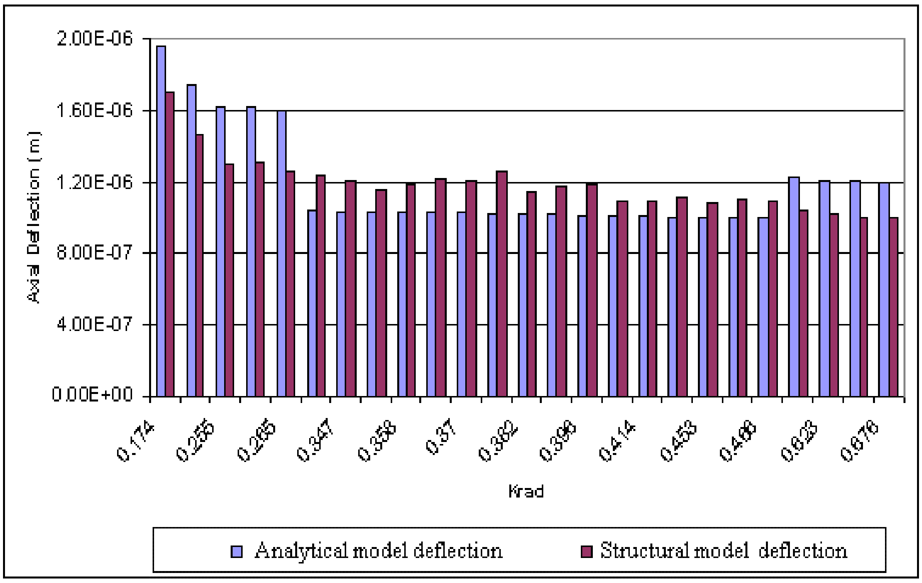

Figure 7.14 - Comparison between analytical and structural models for axial deflection of stator for the 5MW TF-2 machine

7.3 Electromagnetic modelling

The electromagnetically active material of a PMDD generator consists of the permanent magnets mounted on the surface of the rotor, the copper windings on the stator and the steel laminations placed on the stator's teeth and back. Within the air gap it was assumed that all flux crosses it normal to the stator surface and the leakage flux paths were ignored.

Regarding the stator, it was assumed that the amount of copper per unit of air gap surface area was constant and the iron is infinitely permeable so that only the air gap region was modelled.

Given the above assumptions, permanent magnet mass on the rotor of the machine was calculated as shown in (7.18).

$$mass_{\mathrm{PM}} = 2\pi Rl(b_{\mathrm{m}}/\tau_{\rho})h_{\mathrm{m}}\rho_{\mathrm{PM}} \tag{7.18}$$

where $b_{\mathrm{m}}/\tau_{\mathrm{p}} = 0.8$ and ρ_{PM} the permanent magnet's density with $\rho_{\mathrm{PM}} = 7500$ kg/m³.

Equation (7.19) gives the mathematical model that was used for the calculation of the height of the permanent magnet on a conventional RF rotor, as described by McDonald and Mueller in [31]. Equation (7.20) gives the same relationship for a TF machine according to Bang [89].

$$h_{\mathrm{m}} = l_{\mathrm{g}}/ [B_{\mathrm{r}} 4sin(b_{\mathrm{m}}\pi/2\tau_{\rho})/\pi]/ \{(1/ B_{\mathrm{g}})-(1/[B_{\mathrm{r}} 4sin(b_{\mathrm{m}}\pi/2\tau_{\rho})/\pi])\} \tag{7.19}$$

$$h_{\mathrm{m}} = 10l_{\mathrm{g}}b_{\mathrm{m}}/2\tau_{\rho} \tag{7.20}$$

The mathematical model that describes the mass of the copper windings that are wound around the slots of the stator is described in (7.21).

$$mass_{\mathrm{copper}} = sh_{\mathrm{s}}b_{\mathrm{w}}(l+2\ \tau_{\rho})\rho_{\mathrm{copper}}K_{\mathrm{fill}} \tag{7.21}$$

where s the number of the stator's slots with $s = 2\pi R/(b_w+b_t)$, ρ_{copper} the copper's density with $\rho_{copper} = 8940$ kg/m³ and K_{fill} the slot's fill factor with $K_{fill} = 0.6$.

Steel can be found on the stator's teeth and on the yoke of the stator. The equation that describes the mass of the steel placed on the stator is given in (7.22)

$$mass_{steel} = sh_sb_wl\rho_{steel} + \pi l[(R+h_{ys}/2)^2-(R-h_{ys}/2)^2] \tag{7.22}$$

The mass of the permanent magnets was included in the final mass of the rotor and the mass of the copper windings and the steel on the stator was included in the stator's final mass.

For direct drive machines with slotted stators, the flux per pole is reduced due to the slotted armature. This effect can be accounted for by introducing the Carter coefficient K_c into the calculation of the field produced by the magnets. K_c is calculated as given by Zhu in [182] according to (7.23).

$$K_c = \tau_t / (\tau_t - 4\{b_w\tan^{-1}(b_w/2l_g')/2l_g'-\ln\sqrt{[1+(b_w/2\,l_g')^2]}\}/\pi\, l_g') \tag{7.23}$$

where τ_t the armature slot pitch (m) calculated as $\tau_t = 2\pi R/s$ and $l_g' = l_g + h_m/\mu_r$, with μ_r the relative permeability of the permanent magnet material ($\mu_r = 1.06$).

Therefore, the effective air gap l_{ge} for an internal rotor machine is given by (7.24).

$$l_{ge} = l_g + (K_c-1)l_g' \tag{7.24}$$

However, for small slot openings such as the tested cases with $b_w/2R \approx 3.7\%$, the effect of the stator slotting on the calculation of flux per pole can be neglected. Thus, the effective air gap was not included into the calculations.

7.4 The optimisation process

The GAs [179] seek the best possible outcome through simulated evolution. The given parameters are randomly changing in order to create "generations" of the object under examination. Each generation is evaluated according to the given objective function that returns a rating for each one of them. At the end, the parameters of the one that scored the highest are returned to the user. During this research, two different objective functions were created: one that rates the structures according to their mass and seeks the most lightweight one and one that rates them according to their cost seeking the cheapest one. The objective function that was created for the purposes of this research gives a high score to structures that can comply with the set criteria but have the smallest weight or price among the ones created in each run.

The GA toolbox does not guarantee though that the lightest or cheapest possible structure is found at the end of every optimisation run. It only returns the dimensions of the structure that gathered the highest rating among the rest during that specific run. Thus, a large number of optimisation runs had to be made for each generator type in order to come up with the best possible combination of structural variables.

The deflections calculated by the structural models described in section 7.2 were used as criteria, along with the structural total mass or cost, to optimise the generator whilst ensuring a robust design. The allowable values were 10% of the air gap clearance for the deflection due to Maxwell stress, 2% of the axial length for the gravitational deflection and a relative twist of 0.01° for torsional deflection. Thus, the best possible dimensions for a structure that can produce the necessary torque for a 5MW machine were acquired while making sure the structure is robust enough to withstand the given loads. The results of the optimisation process are presented in comparison to the structure's aspect ratio, in order to understand how the structural mass changes for different structural dimensions.

The structural variables that were used as inputs to create the different structure generations were the radius of the structure R that was allowed to vary from 1m to 5m, the axial length of the structure l that could vary from 0.5m to 6m, the thickness of the structures' back iron h_{yr} and h_{ys} that could vary from 0.06m to 0.5m, the stator's arm depth d which could vary from 0.1m to 0.5m, the stator's arm thickness t_{w} that could vary from 0.01m to 0.5m and the rotor's disc thickness t_{d} which was allowed to vary from 0.1m to 1m. The number of arms for the stator structures was kept at $N_{\mathrm{arms}} = 5$. Since an analytical model for the calculation of the tangential deflection of a rotating disc structure does not exist, the minimum disc thickness that is adequate to withstand the given torque was acquired for each machine according to the results of the FEA tool in chapter 5.

Figure 7.15 shows the trend of the total mass of the three different structural topologies for an increasing K_{rad} according to the results of the structural optimisation tool. The optimal dimensions along with the masses of the most lightweight structures that occurred during the mass optimisation process are listed in Table 7.2. Electromagnetically active material is described as "Active Mass", while the structural steel is described as "Inactive Mass". The mass of the copper windings and the permanent magnet (PM) material of the lightweight structures are listed in Table 7.3.

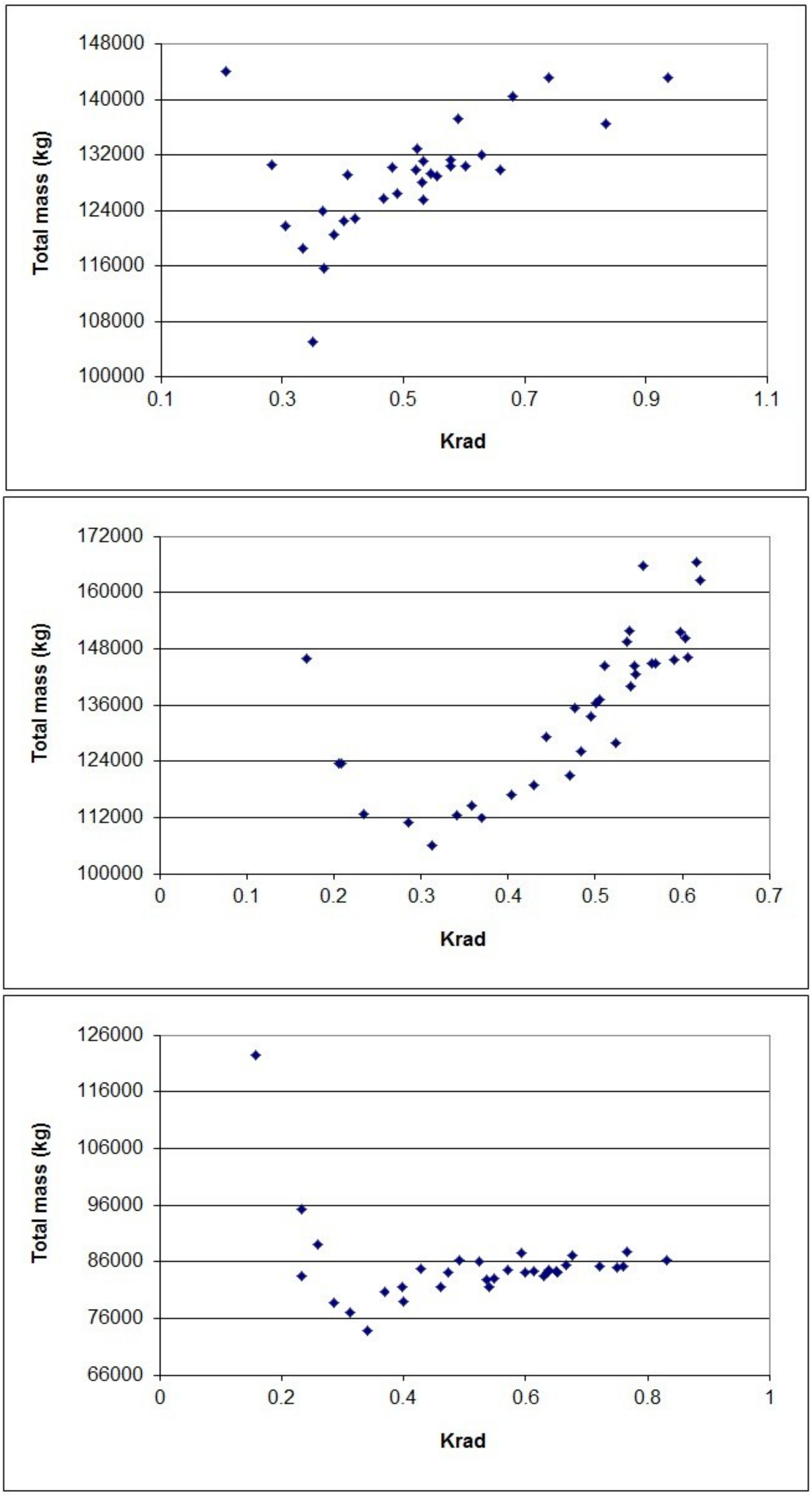

Figure 7.15 - Total mass of a 5MW generator for a range of aspect ratios. RF machine (top) TF-1 machine (centre) TF-2 machine (bottom)

Generator Topology	**RF**	**TF-1**	**TF-2**
K_{rad}	0.35	0.31	0.34
R (m)	2.57	2.72	2.64
l (m)	1.91	1.70	1.78
t_{d} (m)	0.13	0.14	0.11
h_{yr} (m)	0.09	0.08	0.28
d (m)	0.36	0.41	0.35
t_{w} (m)	0.01	0.03	0.04
h_{ys} (m)	0.05	0.19	0.25
Rotor mass (kg)	47000	50000	27000
Stator mass (kg)	58000	56000	47000
Active mass (kg)	16000	10000	5000
Inactive mass (kg)	89000	96000	69000
Total mass (kg)	105000	106000	74000

Table 7.2 - Optimal dimensions and masses of 5MW PMDD generator structures

Generator Topology	**RF**	**TF-1**	**TF-2**
Copper (kg)	11000	3000	4000
PM (kg)	5000	7000	1000
Active Mass (kg)	16000	10000	5000

Table 7.3 - Optimal masses for copper and PM material of 5MW PMDD generators

It can be derived from the results that small aspect ratios can lead to lighter generator structures for PMDD generator topologies up to a minimum point until the total mass of the structure starts to increase again. The comparison among the resulting masses shows that the TF-2 machine had the lightest optimised structure. TF-1 and the conventional RF machine had similar optimised masses with the RF structure being slightly heavier, despite the fact that the TF-1 machine had a heavier inactive mass than that of the RF topology.

The difference in the resulting active and inactive masses can be attributed to the different structural topologies and flux densities in the airgap of the tested machines. TF-1 has the highest airgap flux density, leading to a significantly greater Maxwell stress force compared to its TF-2 counterpart and the conventional RF generator. Thus TF-1 requires a stiffer structure with much more inactive mass than the other two machines. In TF-2 the Maxwell stress acts in the axial direction. Thus, the c-core structure is of benefit in this machine, as it provides structural support against the attraction forces. The demand on the support structure is therefore less for this topology.

The comparison of the active mass confirms that the TF machine topologies have the highest power density, thus require less active material compared to the RF machine. It is also clear that TF topologies drastically reduce copper mass since they offer a simpler copper winding with less non-active material.

The same mathematical models and procedure were used for the cost optimisation of the tested structures. This was achieved by introducing costs for the structural materials and changing the objective function into seeking to minimise the total cost instead of the mass of the structure. Structural steel and steel laminations had the same price for simplification. Manufacturing costs were not included in the cost analysis. The given costs were:

- Cost of steel = €3/kg [89]
- Cost of copper = €15/kg [89]
- Cost of PM material = €115/kg [183]

Figure 7.16 shows the trend of the total cost of the three different structures as their K_{rad} increased during the cost optimisation process. The optimal dimensions, costs and masses of the cheapest structures that occurred during the cost optimisation process are listed in Table 7.4. The cost of the electromagnetically active material is described as “Active Cost”, while the cost of the structural steel is described as “Inactive Cost”. The cost and the mass of the electromagnetically active material of the cheapest structures are listed in Table 7.5.

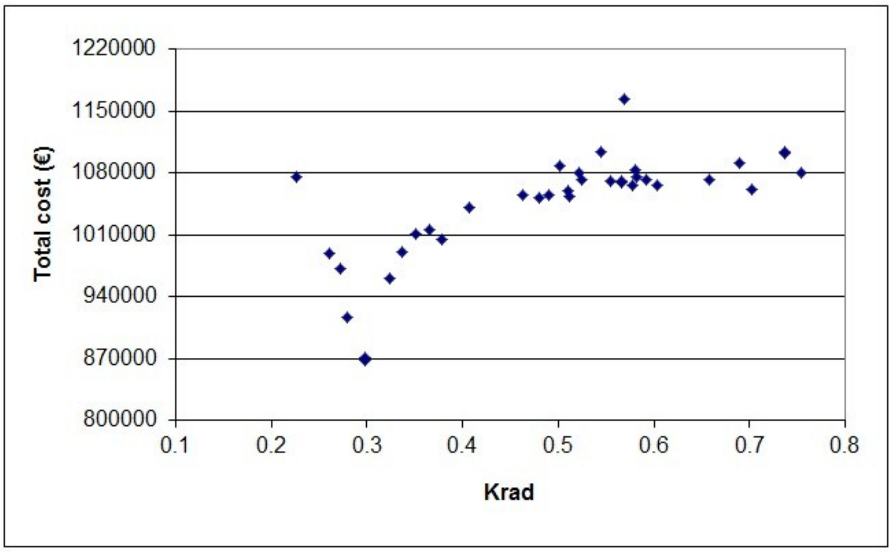

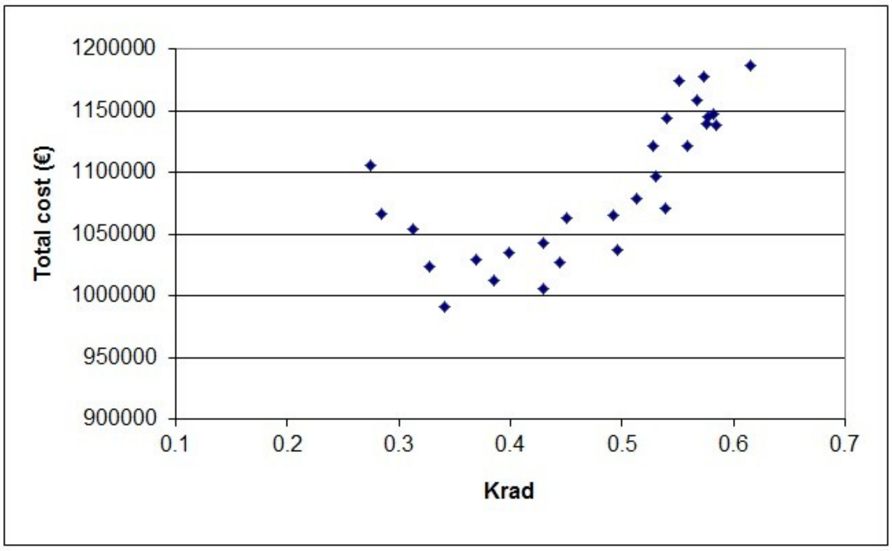

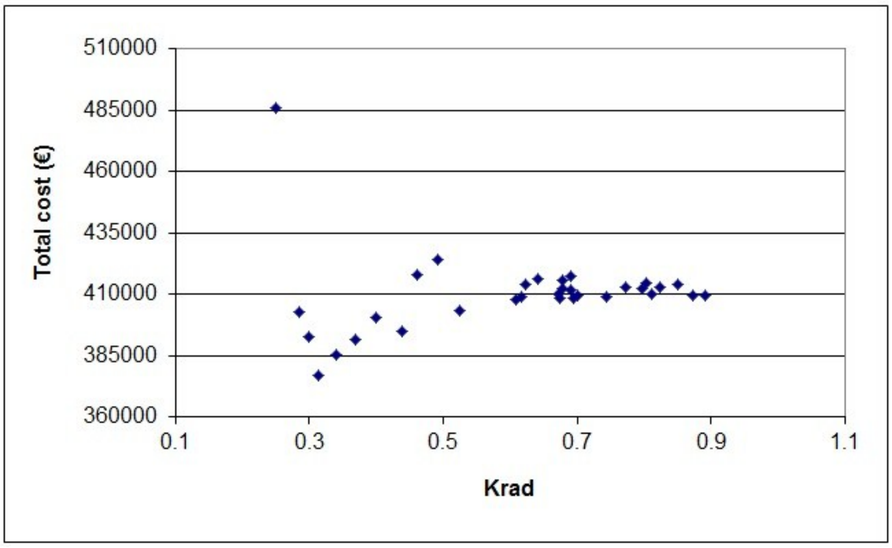

Figure 7.16 - Total cost of a 5MW generator for a range of aspect ratios. RF machine (top) TF-1 machine (centre) TF-2 machine (bottom)

Generator Topology	**RF**	**TF-1**	**TF-2**
K_{rad}	0.30	0.34	0.31
R (m)	2.72	2.64	2.72
l (m)	1.71	1.78	1.69
t_{d} (m)	0.14	0.14	0.11
h_{yr} (m)	0.13	0.09	0.28
d (m)	0.25	0.41	0.38
t_{w} (m)	0.09	0.02	0.04
h_{ys} (m)	0.05	0.19	0.25
Active Cost (€)	503000	711000	164000
Inactive Cost (€)	368000	276000	213000
Total Cost (€)	871000	987000	377000
Total Mass (kg)	137000	110000	76000

Table 7.4 - Optimal dimensions, costs and masses of 5MW PMDD generator structures

Generator Topology	**RF**	**TF-1**	**TF-2**
Copper (€)	166000	41000	49000
PM (€)	337000	670000	115000
Active Cost (€)	503000	711000	164000
Active Mass (kg)	14000	9000	5000

Table 7.5 - Optimal cost & mass of copper and PM material of 5MW PMDD generator structures

It can be derived from the results that small aspect ratios can lead to PMDD generator structures with decreased cost of raw materials. In all tested cases the resulting aspect ratios are smaller compared to the ones that came as a result during the mass optimisation process. The resulting K_{rad}s increase the cheap structural mass of the PMDD generators while decreasing the demand in the expensive active mass. This optimisation process reaches its minimum value when the inactive mass becomes too expensive as the structural mass of the tested machine starts to increase rapidly after a certain point. The comparison among the resulting costs shows that the TF-1 machine was the most expensive while the TF-2 machine was the cheapest in terms of raw materials. This can be attributed to the higher demands of the TF-1 machine in permanent magnet material.

However these results do not give a complete cost analysis, only an indication of the minimum cost of the materials needed for each tested machine. For a more accurate cost analysis, the manufacturing cost of each machine should be included in the optimisation process. However, the manufacturing cost differs for each machine type thus a simplifying estimation should be avoided.

7.5 Comparison with geared technologies

The combined mass of a DFIG or a brushless generator and a three-stage gearbox that drives it were calculated in order to compare such geared topologies with the resulting masses of the PMDD generators.

The equations that were used to calculate the masses of a three-stage gearbox, an air-cooled DFIG and a brushless generator are given in (7.25), (7.26) and (7.27) according to [184] and [185]. All masses are calculated in kg, torque ratings in kNm and machine ratings in MW.

$$\text{3-stage gearbox mass} = 10.5 \times \text{high-speed shaft torque} + 3800 \tag{7.25}$$

$$\text{DFIG mass} = 3910 \times \text{machine rating}^{0.69} \tag{7.26}$$

$$\text{Brushless generator mass} = 3 \times \text{high-speed shaft torque} + 1464 \tag{7.27}$$

The resulting masses that correspond to generators with nominal power output 5MW are gathered in Table 7.6.

	Gearbox Mass (tons)	**Generator Mass (tons)**	**Total Mass (tons)**
DFIG	56	13	69
Brushless Generator	56	17	73

Table 7.6 - Collective masses of 5MW DFIG and brushless generator and their gearboxes

Results show that the AF and the TF-2 machine can be in pair with a 5MW brushless generator that is driven by a 3-stage gearbox. The DFIG system with a 3-stage gearbox was calculated to be only four tons lighter compared to the AF PMDD machine.

7.6 Conclusions

Table 7.7 summarises the optimal structural masses of the different PMDD generator structures. For the original cases a disc rotor structure and an armed stator structure with hollow arms were assumed according to chapters 5 and 6. For the optimised cases, only the inactive mass of the structures is presented.

Generator Structure	**Original Structural Mass (tons)**	**Optimised Structural Mass (tons)**
RF Disc Rotor	51	47
RF Armed Stator	48	47
TF-1 Rotor	39	43
TF-1 Stator	60	53
TF-2 Rotor	27	27
TF-2 Stator	49	47
AF Rotor	48	-
AF Stator	25	-

Table 7.7 - Mass comparison of the original and the resulting structural masses of the analytical structural optimisation process

The structural mass of the RF machine was reduced by five tons, the TF-1 machine was six tons lighter compared to its original value and the structural mass of TF-2 machine was decreased by two tons. The results of the optimisation process confirm that the TF topology offers greater torque/mass and torque/cost ratios for a machine such as TF-2. The small diameter of the TF-2 rotor leads to a minimum demand in permanent magnet material, an attribute that drastically reduces both the mass and cost of the machine.

In all cases the resulting structural masses of the machines were slightly smaller compared to the original ones. The accuracy of these results and the stiffness of the resulting structures were verified with the help of the FEA tool. However none of the resulting generator structures was lighter than the AF aircored machine presented in chapters 4 and 5. Final results indicate that the structural mass of a 5MW PMDD generator can be effectively reduced to be comparable with geared topologies of the same power output.

In all tested cases smaller aspect ratios were preferred by the analytical tool. These results contradict previous publications in the literature that favoured higher aspect ratios for the RF machines [186][187]. This difference can be attributed to the minimum values applied for the back height of the rotor and stator structures which was set to 5mm. In the original work described in [186] and [187], the GA toolbox tried to decrease the RF rotor's structural weight by decreasing its back iron height to the minimum value allowed, leading to structures with very thin rings. In an attempt to compensate for the very thin surfaces, the toolbox increased the axial length of the RF machine in order to reduce the radial deflection in the airgap due to the calculated Maxwell stress, which explains the high K_{rad} values. Clearly a 5mm ring thickness (h_{yr}) is unrealistic for a PMDD machine. Under the structural limitations that were introduced to the optimisation process after the structural analysis described in chapter 5, the minimum allowable value of the back height of a RF machine increased from 5mm to 40mm for the rotor (h_{yr}) and 70mm for the stator (h_{ys}). The RF structures had now enough back height to resist the electromagnetic attraction without having to increase their axial length, leading the optimisation process to more realistic results. The results regarding the TF machines were not affected that much due to the different orientation of their flux path which alters the structural forces that act on their structures. This outlines the importance of the analytical models to be verified with the use of FEA models.

Chapter 8

Discussion & Conclusions

8.1 Chapter summaries

This thesis addresses the structural analysis and mass optimisation of low speed, high torque permanent magnet direct drive generators for wind energy converters with a nominal power output of 5MW. In this chapter, a summary of each chapter is presented.

In chapter 2 an introduction to wind energy converters and the parts that compose a wind turbine were presented. The chapter focused on the two different drive trains that currently compete in the market, namely the geared and the direct drive. Direct drive generators seem to offer a number of advantages compared to their geared counterparts in terms of drive train simplicity, reduced maintenance issues, annual energy yield and ancillary services. These characteristics are essential for the development of wind farms, especially when considering offshore sites where large power outputs are required and maintenance is difficult to provide.

Chapter 3 reviewed the different direct drive generator technologies that have been suggested for wind power generation. The PMDD machine was favoured compared to its EEDD and SRG counterparts for offering higher annual energy yield. The different PMDD generator topologies that have been proposed in the literature were presented. A representative of each major topology was selected from the overview to be tested and compared for their structural stiffness and to be structurally optimised in the following chapters of the thesis. The three selected PMDD machines were the conventional iron-cored RF machine, the iron-cored TF machine with an inner rotor and a C-cored shaped stator as described in [89] and the aircored AF generator with C-cored shaped modules on its rotor described in [148].

The potential lightweight topologies that were chosen from literature were modelled with the help of an FEA tool in chapter 4. All support structures were made of structural steel while the magnet poles are made of NdFeB material. The stator models were simulated without the necessary copper windings in an attempt to simplify the models and reduce hardware requirements. These structural models were created in chapters 5 and 6 of this thesis for comparison purposes and for validation of the analytical structural models presented in chapter 7.

In chapter 5, analytical models for calculating the acting forces on the different modelled structures were presented. Mechanical finite element analysis was used to complete a structural comparison among the suggested direct drive generator topologies for 5MW wind turbines. The structural analysis included prediction of the static structural deflections such as Maxwell stress, gravitational pull and centripetal force due to rotation, modal analysis and dynamic analysis. The results demonstrated the highest potential of the AF aircored machine with C-cored modules for offshore wind development. In order to bring the structural mass of the other suggested topologies closer to the aircored topology, structural optimisation techniques were developed and presented in chapters 6 and 7.

Chapter 6 presented a FEA tool that can optimise the structural mass of a 5MW PMDD generator under a set of selected structural loads. Results showed that the structural mass of a PMDD generator can be effectively decreased without compromising its stiffness. Regarding the RF PMDD machines, a disc rotor and an armed stator with hollow arms structure seems to be the ideal combination in terms of structural mass and total cost. Regarding TF machines, the TF-2 generator with the same topology selected for the RF machine was the most lightweight option. Comparing the resulting lightweight topologies, the resulting TF-2 machine was the most lightweight. However it was not as lightweight as the AF aircored machine from chapter 5.

An analytical optimisation tool was presented in chapter 7 that can optimise both active and inactive material on a permanent magnet direct drive machine simultaneously while keeping a set of selected structural criteria under necessary limitations. The analytical models that can accurately calculate the deflections due to the electromagnetic attraction between rotor and stator, the gravitational pull and rotational velocity were presented in this chapter. The optimisation tool was used to further minimise the total mass or the total cost of the lightweight RF and TF machines presented in chapter 6. All tested generators employed a disc rotor structure and an armed stator structure with hollow arms. The GA toolbox embedded in this analytical tool sought the best combination of structural parameters that would lead to a lightweight or cheap structure. Results indicated that structures with smaller aspect ratios could lead to the desired results up to a minimum point. Once again, the optimised TF-2 machine had the smaller structural mass but it was not as lightweight as the AF aircored machine described in chapter 5.

8.2 Discussion & conclusions

8.2.1 The approach of the problem

The broad approach of this thesis towards the problem of the large structural mass of different PMDD generator topologies includes the following main steps:

1. Use simple structures that can represent the mass characteristics of suggested PMDD generator topology designs.

2. Use these models to calculate deflection and fatigue levels due to structural forces acting on such wind turbine generators. This would demonstrate which generator design is best suitable to withstand the given stresses.

3. Use the developed structural optimisation tools to decrease the structural mass of the generator without compromising its stiffness against the structural loads. An alternative way to minimise the generator's mass can be achieved with the help of the analytical tool for faster results.

4. Verify the stiffness of the resulting lightweight structures with the help of the finite element tool.

Generator material that is needed for other roles such as coil, cooling equipment, bearings, bolts and manufacturing requirements have been ignored in this thesis. Thus, it can be said that every model presented is by its nature an approximation and the expected resulting mass of the modelled PMDD generators would be slightly greater. More detailed models would give a better perspective of the estimated mass of the generator. Nevertheless, since the structural mass of a PMDD generator dominates its total mass, it can be assumed that the presented models are realistic and good enough for the first stage of design.

The author believes that this should be the strategy of any design team trying to produce a lightweight PMDD generator for wind turbines. These tools can easily be adopted to any generator design and effectively provide structural solutions to reduce the structural mass of tested machine regardless its power output

8.2.2 Revisiting the thesis statement

In chapter 1 the thesis is stated as:

"If there are ways to efficiently decrease both the active and inactive mass of multi MW permanent magnet direct drive generator systems to a minimum, then their resulting total mass could be comparable with commercial DFIG or geared brushless machines".

In chapter 5, the AF aircored machine had a total structural mass of 73 tons. According to the results from chapters 6 and 7 the structural mass of the TF-2 machine was reduced to 74 tons. In chapter 7 a comparison was made with geared topologies that employ induction and brushless generators. Results indicated that the 5MW AF machine and the optimised TF-2 machine had similar mass with the combined mass of a three-stage gearbox and a brushless generator of the same power output. The combined mass of a 5MW DFIG and a gearbox was only 5.5% lighter than the AF machine and 6.8% lighter than the TF-2 one.

8.2.3 Contribution to knowledge

This thesis has contributed to knowledge in a number of ways. Structural design tools for large RF, TF and AF aircored PMDD machines have been introduced and verified. These have then been used to carry out an extended structural comparison among them to identify the most lightweight solution for onshore and offshore development. Structural and analytical tools that can perform an optimisation of the total mass of such machine structures were developed based on the knowledge gained from the structural analysis. These tools could contribute to the early stages of generator design. The resulting lightweight structures indicate that the suggested PMDD machines can be made lighter and cheaper by identifying the critical point at which the structural and electromagnetically active masses minimise.

The work in this thesis has contributed to a number of other publications:
The structural comparison among the suggested PMDD topologies in chapter 5 in [188]; The FEA structural optimisation tool presented in chapter 6 in [187] and [189]; The analytical calculation of the deflection due to Maxwell stress for different C-cored TF machines in chapter 7 in [189] and [190]; The analytical structural and cost optimisation tool presented in chapter 7 in [186], [187] and [190]. All publications are gathered in chronological order in Appendix B.

8.2.4 Further work

In chapters 5 and 6 it was assumed that the resulting deflections due to the static structural stresses were the maximum resulting ones for the given structures. This is not a completely valid assumption though for the stress due to electromagnetic attraction which changes along with the airgap clearance. A decrease in the airgap due to deformation of the rotor or the stator surface would lead to a greater Maxwell stress which has to be recalculated. In order to further investigate the elastic stability of the resulting structures, the development of an iterative tool is required. The suggested tool should extract the resulting deflection around surface of the tested machine structures in each iteration and use them to recalculate the resulting Maxwell stress. The inability to maintain a constant airgap clearance after a given number of iterations would indicate a poor design and the necessity to increase its stiffness and the resulting structural mass.

The modal analysis described in chapter 5 can be further extended to include torque pulsations, cogging torque for the iron-cored machines and short circuit transient.

The forces acting on the tested generators are not the only ones acting on the structures as it was pointed out in chapter 5. Further work should investigate the effect that the stress due to thermal expansion or the forces and moments from the rotor blades have on the airgap of a PMDD generator. Analytical models able to calculate these resulting deflections could also be created. The addition of these deflection criteria to the optimisation process might lead to different results regarding the final structural dimensions and masses of the machines.

The structural optimisation process described in chapter 6 should be expanded to include a fatigue analysis that validates the life expectancy of the resulting models. This should be followed by cost analysis that would compare the ICC of the resulting machine against its net AEP to determine the point at which the proposed improvements are beneficial to the manufacturer.

An attempt was made in chapter 7 to calculate the cost of different PMDD generators. However the resulting costs are incomplete without manufacturing cost data. Since each generator topology has different manufacturing process and cost a fair comparison would not be possible with a straightforward equation such as those presented in [184]. Further work should investigate into the manufacturing costs of different PMDD machines and include them to the optimisation process.

References

[1] O. Edenhofer, R. Pichs-Madruga, Y. Sokona, K. Seyboth, P. Matschoss, S. Kadner, T. Zwickel, P. Eickemeier, G. Hansen, S. Schlomer and C. von Stechow, “IPCC, 2011: Summary for policymakers. In: IPCC special report on renewable rnergy sources and climate change mitigation”, Cambridge University Press, Cambridge, United Kingdom and New York, NY, USA, 2011.

[2] International Energy Agency, “World energy outlook 2011”, October 2011.

[3] M.G. Salameh, “Can renewable and unconventional energy sources bridge the global energy gap in the 21st century?”, Applied Energy Journal, No. 75, pp. 33–42, 2003.

[4] J.J. McCarthy, O.F Canziani, N.A. Leary, D.J. Dokken and K.S. White, “Intergovernmental panel on climate change third assessment report climate change 2001: Impacts, adaptation, and vulnerability”, Cambridge University Press, Cambridge, 2001.

[5] D.R. Easterling, G.A. Meehl, C. Parmesan, S.A. Changnon, T.R. Karl and L.O. Mearns, “Climate extremes: observations, modeling, and impacts”, Science Journal 22, Volume 289, No. 5487, pp. 2068–74, September 2000.

[6] C. Parmesan, T.L. Root and M. Willig, “Impacts of extreme weather and climate on terrestrial biota”, Bulletin of American Meteorologic Society, Volume 81, No. 3, pp. 443–50, 2000.

[7] J.A. Pounds, “Climate and amphibian declines” Nature Journal, Volume 410, pp. 639-40, April 2001.

[8] G. Otterson, B. Planque, A. Belgrano, E. Post, P.C. Reid and N.C. Stenseth, “Ecological effects of the North Atlantic Oscillation”. Oecologia Journal, Volume 128, No. 1, pp. 1–14, June 2001.

[9] G.R. Walther, E. Post, P. Convey, A. Menzel, C. Parmesan, T. J. C. Beebee, J.M. Fromentin, O. Hoegh-Guldberg and F. Bairlein, “Ecological responses to recent climate change”, Nature Journal, Volume 416, pp. 389–95, March 2002.

[10] J. Penuelas and I. Filella, “Responses to a warming world”, Science Journal, Volume 294, No. 5543, pp. 793-5, October 2001.

[11] R.C. Smith, D. Ainley, K. Baker, E. Domack, S. Emslie, B. Fraser, J. Kennett, A. Leventer, E. Mosley-Thompson, S. Stammerjohn and M. Vernet, “Marine ecosystem sensitivity to climate change”, Bioscience Journal, Volume 49, No. 5, pp. 393-404, May 1999.

[12] O. Hoegh-Guldberg, “Climate change, coral bleaching and the future of the world’s coral reefs”, Marine & Freshwater Research Journal, Volume 50, No. 8, pp. 839–66, 1999.

[13] J. Hansen, R. Ruedy, M. Sato, M. Imhoff, W. Lawrence, D. Easterling, T. Peterson and T. Karl, “A closer look at United States and global surface temperature change”, Geophysical Research Journal, Volume 106, No. 20, pp. 23,947-64, 2001.

[14] T.B. Johansson, ‘Renewable energy: sources for fuels and electricity’, Washington, DC, 1993

[15] J. Florence, “Global wind power expands in 2006”, June 28, 2006.

[16] Z. Chen and F. Blaabjerg, “Wind Energy - The world's fastest growing energy source”, IEEE Power Electronics Society Newsletter, Volume18, No. 3, pp. 15-9, 2006.

[17] J. Wilkes, “Wind in power, 2009 European statistics”, The European Wind Energy Association, February 2010.

[18] A.D. Hansen and L.H. Hansen, “Wind turbine concept market penetration over 10 years (1995-2004)”, Wind Energy Journal, Volume 10, No. 1, pp. 81-97, 2007.

[19] Vestas, http://www.vestas.com, last accessed 4th July 2012.

[20] Enercon, http://www.enercon.de/en-en/, last accessed 12th July 2012.

[21] L. H. Hansen and L. Helle, “Conceptual survey of generators and power electronics for wind turbines”, Risø-R-1205(EN), 2001.

[22] P.J. Tavner, F. Spinato, G.J.W. van Bussel and E. Koutoulakos, “Reliability of different wind turbine concepts with relevance to offshore application”, Proceedings of the European Wind Energy Conference, Brussels, 31 March - 3 April, 2008.

[23] E. de Vries, “Trouble spots - Gearbox failures and design solutions”, Renewable Energy World Journal, Volume 9, No. 2, pp. 37-47, March 2006.

[24] J. Wallace, M. Jackson, S. Rogers, “The problem with O&M”, Renewable Energy Focus Journal, Volume 9, No. 7, pp. 22-7, January-February 2009.

[25] P. Lampola, “Directly driven, low-speed permanent-magnet generators for wind power applications”, Ph.D. Thesis, Helsinki University of Technology, Finland, 2000.

[26] D. Bang, H. Polinder, G. Shrestha and J. A. Ferreira, “Comparative design of radial and transverse flux PM generators for direct-drive wind turbines”, Electrical Power Processing / DUWIND, Delft University of Technology, International Conference on Electrical Machines, pp. 1-6, Vilamoura, September 2008.

[27] H. Polinder, F.F.A. van der Pijl, G.J. de Vilder and P. Tavner, “Comparison of direct-drive and geared generator concepts for wind turbines”, IEEE Transactions on Energy Conversion, Volume 21, pp. 725-33, September 2006.

[28] S. Widyan, “Design, optimization, construction and test of rare-earth permanent-magnet electrical machines with new topology for wind energy applications”, Ph.D. thesis Technische Universität Berlin, Berlin, Germany, 2006.

[29] J.R Bumby and R. Martin, “Axial-flux permanent-magnet air-cored generator for small-scale wind turbines”, Electric Power Applications, IEE Proceedings Volume 152, No. 5, pp. 1065-75, September 2005.

[30] A. Grauers, “Design of direct-driven permanent-magnet generators for wind turbines”, Ph.D. thesis, Chalmers University of Technology, Göteborg, Sweden, 1996.

[31] A.S. McDonald and M.A. Mueller, “Development of analytical tools for estimating inactive mass”, University of Edinburgh, Scotland, UPWIND report, 2008.

[32] J.H. Brown, W.R. Burnside, A.D. Davidsson, J.P. DeLong, W.C. Dunn, M.J. Hamilton, N. Mercado-Silva, J.C. Nekola, J.G. Okie, W.H. Woodruff and W. Zuo “Energetic limits to economic growth”, Bioscience Journal, Volume 61, No. 1, pp. 19-26, 2010.

[33] B.S. Warr and R.U. Ayres, “Evidence of causality between the quantity and quality of energy consumption and economic growth”, Energy Journal, Volume 35, No. 4, pp. 1688–93, 2010.

[34] C. J. Campbell and J. H. Laherrere, “The end of cheap oil: Forecasts about the abundance of oil are usually warped by inconsistent definitions of "reserves"”, Scientific American Journal, Volume 278, No. 3, pp. 78-83, 1998.

[35] P. E. Steinberg, “The Deepwater Horizon, the Mavi Marmara, and the dynamic zonation of ocean space”, The Geographical Journal, Volume 177, No. 1, pages 12-6, March 2011.

[36] G.E. Boyle, “Renewable energy: Power for a sustainable future”, Oxford University Press, Oxford, 2003.

[37] DTI: “Our energy future: creating a low carbon economy”, Energy White Paper, February 2003.

[38] Global Wind Energy Council, “Global Wind report - Annual market update”, 2011.

[39] www.c2es.org/energy/source/renewables, last accessed January 2013.

[40] Emerging Energy Research, “Global offshore wind energy markets and strategies: 2009-2020”, 2009.

[41] S. Heier, “Grid integration of wind energy conversion systems”, Chichester, England, 2006.

[42] J.G. Slootweg, H. Polinder and W.L. Kling, “Dynamic modelling of a wind turbine with direct drive synchronous generator and back to back voltage source converter and its controls”, Proceedings of European Wind Energy Conference and Exhibition, Copenhagen, Denmark, pp. 1014-7, July 2001.

[43] T. Burton, N. Jenkins, D. Sharpe and E. Bossanyi, “Wind energy handbook - Second edition”, May 2011.

[44] http://thenextplanet.wordpress.com/wind-turbines/, last accessed May 2012.

[45] http://www.wind-energie.de/infocenter/technik/funktionsweise/auftriebslaeufer, last accessed May 2013

[46] R Stewart, “Wind turbine blade production - new products keep pace as scale increases”, Reinforced Plastics Journal, Volume 56, No. 1, pp. 18-25, February 2012.

[47] C. Varrone, “Generation innovation: Despite tricky times of late, innovations in aerodynamics, drive train and intelligent operation should help drive the cost of wind energy back down again”, Renewable Energy Focus Journal, Volume 12, No. 1, pp. 26-30, January 2011.

[48] UpWind, “Design limits and solutions for very large wind turbines - EU 6th Frame Project”, 2011.

[49] www.wwindea.org/technology/ch01/en/1_2_1_2.html, last accessed June 2011.

[50] A.J.G. Westlake, J.R. Bumby and E. Spooner, "Damping the power-angle oscillations of a permanent-magnet synchronous generator with particular reference to wind turbine applications", Proceedings of IEE - Electrical Power Applications, Volume 143, No. 3, pp. 269-80, May 1996.

[51] www.coemiwindturbines.co.uk/coemi-wind-turbines-general-information/wind-turbine-design, last accessed June 2012.

[52] S. Yagi and N. Ninoyu, "Technical trends in wind turbine bearings", Technical Report Review No. 76, NTN Corporation, Osaka, Japan, 2008.

[53] J. Peeters, "Simulation of dynamic drive train loads in a wind turbine", Ph.D. thesis, Catholic University of Leuven, Leuven, Belgium, 2006.

[54] J. Puigcorbe, A. De-Beaumont, "Wind turbine gearbox reliability: The impact of rotor support", Renewable Energy World, June 2010.

[55] R. Harrison, E. Hau and S. Herman, "Large wind turbines: Design and economics", Wiley, 2000.

[56] www.windpowerengineering.com/design/mechanical/understanding-costs-for-large-wind-turbine-drivetrains, last accessed July 2012.

[57] www.alstom.com/power/renewables/wind/turbines, last accessed July 2012.

[58] J. Varley, "Eco 100: Talking the torque and getting into good shape for O&M", Modern Power Systems, pp. 52-5, September 2008.

[59] Alstom brochures, www.alstom.com/Global/Power/Resources/Documents/Brochures/wind-power-solutions.pdf.

[60] SKF Brochure, "Nautilus bearing arrangement solution from SKF." 2010.

[61] A. Ragheb and M. Ragheb, "Wind turbine gearbox technologies", Proceedings of the 1st International Nuclear and Renewable Energy Conference (INREC'10), Amman, Jordan, March 2010.

[62] J. Cotrell, "A preliminary evaluation of a multiple-generator drivetrain configuration for wind turbines preprint," American Society of Mechanical Engineers (ASME) Wind Energy Symposium, January 2002.

[63] www.ge-energy.com/products_and_services/products/wind_turbines/index.jsp, last accessed July 2012.

[64] J. Ribrant and L. M. Bertling, “Survey of failures in wind power systems with focus on Swedish wind power plants during 1997-2005”, IEEE Transactions on Energy Conversion EC, Volume 22, No. 1, pp. 167-73, 2007.

[65] S. Faulstich, B. Hahn and P. J. Tavner, “Wind turbine downtime and its importance for offshore deployment,” Wind Energy Journal, Volume 14, No. 3, pp. 327-37, April 2011.

[66] Z. Hameeda, Y. S. Honga, Y. M. Choa, S. H. Ahnb and C. K. Song, “Condition monitoring and fault detection of wind turbines and related algorithms: A review”, Renewable and Sustainable Energy Reviews Journal, Volume 13, No. 1, pp. 1-39, January 2009.

[67] H. Polinder, “Overview of and trends in wind turbine generator systems”, Proceedings of IEEE Power and Energy Society General Meeting, pp. 1-8, July 2011.

[68] A.D. Hansen, F. Iov, F. Blaabjerg and L. H. Hansen, “Review of contemporary wind turbine concepts and their market penetration,” Wind Engineering Journal, Volume 28, No. 3, pp. 247-63, 2004.

[69] J.G. Slootweg and E. de Vries, “Inside wind turbines - Fixed vs. variable speed”, Renewable Energy World Journal, pp. 30-40, 2003.

[70] Siemens, www.siemens.com/wind, last accessed July 2012.

[71] GoldWind, www.goldwindglobal.com, last accessed July 2012.

[72] GE, www.gereports.com/ges-offshore-technology-expands-with-scanwind-buy/, last accessed July 2012.

[73] Emergya Wind Technologies, www.ewtinternational.com/products/product-single/dw-9096-20-mw.html, last accessed July 2012.

[74] Leitwind, en.leitwind.com/Products-Services/Product-Overview2, last accessed July 2012.

[75] AMSC, www.amsc.com/windtec/index.html, last accessed July 2012.

[76] STX, www.stxwind.com/nl/products/7-products, last accessed July 2012.

[77] S. K. Chaudhary, R. Teodorescu and P. Rodriguez, “Wind farm grid integration using VSC based HVDC transmission - An overview”, Proceedings of the IEEE Energy 2030 Conference, pp. 1-7, November 2008.

[78] S. Haier, "Grid integration of wind energy conversions systems", John Wiley and Sons Ltd., England, 2006.

[79] "Grid Connection Regulations for High and Extra High Voltage", E.ON Netz GmbH, Bayreuth, April 2006.

[80] Z. Chen, "Issues of connecting wind farms into power systems", Conference publications of the IEE/PES Transmission and Distribution Conference & Exhibition: Asia and Pacific Dalian, China, 2005.

[81] J.G. Slootweg, S.W.H. de Haan, H. Polinder and W.L. Kling, "Voltage control methods with grid connected wind turbines: a tutorial review", Wind Engineering Journal, Volume 25, No. 6, pp. 353-65, 2001.

[82] M. Liserre and M. Molinas, "Overview of multi-MW wind turbines and wind parks", IEEE Transactions on Industrial Electronics, Volume 58, No. 4, pp. 1081-95, April 2011.

[83] J.M. Carrasco, L.G. Franquelo, J.T. Bialasiewicz, E. Galvan, R.C.P. Guisado, Ma.A.M. Prats, J.I. Leon and N. Moreno-Alfonso, "Power-electronic systems for the grid integration of renewable energy sources: A survey", IEEE Transactions on Industrial Electronics, Volume 53, No. 4, pp. 1002-16, June 2006.

[84] 7-MW-WEC-by-11, www.7mw-wec-by-11.eu, last accessed June 2012.

[85] A. Beekmann, J. Marques, E. Quitmann and S. Wachtel, "Wind energy converters with FACTS Capabilities for optimized integration of wind power into transmission and distribution systems", Proceedings of CIGRE/IEEE Integration of Wide-Scale Renewable Resources Into the Power Delivery System Joint Symposium, July 2009.

[86] M.A. Mueller, A.S. McDonald and D.E. Macpherson, "Structural analysis of low-speed axial-flux permanent-magnet machines", IEE Proceedings of Electric Power Applications, Volume 152, No 6, pp. 1417-26, November 2005.

[87] A.S. McDonald, M.A Mueller and H. Polinder, "Structural mass in direct drive permanent magnet electrical generator", IET Renewable Power Generation Special Issue - selected papers from EWEC 2007, Volume 2, No. 1, pp 3-15, March 2008.

[88] G. Bywaters, V. John, J. Lynch, P. Mattila, G. Norton, J. Stowell, M. Salata, O. Labath, A. Chertok and D. Hablanian, "Northern Power Systems WindPACT drive train alternative design study report", report NREL/SR-500-35524, 2004.

[89] D. Bang, "Design of Transverse Flux Permanent Magnet Machines for Large Direct-Drive Wind Turbines", Ph.D. thesis, Delft University of Technology, Delft, The Netherlands, 2010.

[90] J. Soens, "Impact of wind energy in a future power grid", Ph.D. thesis, Katholieke Universiteit Leuven, Leuven, Belgium 2005.

[91] www.mtoi.es/en/productos-y-servicios/aerogeneradores-twt.aspx, last accessed July 2012.

[92] S. Jöckel, "Gearless wind energy converters with permanent magnet generators - an option for the future?", Proceedings of European Union Wind Energy Conference, pp. 414-7, 1996.

[93] E. Spooner and B.J. Chalmers, 'TORUS: A slotless, toroidal-stator, permanent magnet generator', International Conference on Electrical Machines, Cambridge, pp. 1053-8, 1990.

[94] N. Vilsbøll, A. Pinegin, D. Goussarov and J. Bugge, "The experience of designing and testing a 20kW multi pole permanent magnet generator for wind turbines", DEWI Magazine, No. 9, pp. 74-83, August 1996.

[95] P.J. Tavner, J. Xiang and F. Spinato, "Reliability Analysis for Wind Turbines," Wind Energy Journal, Volume 10, pp. 1-18, 2007.

[96] www.vensys.de/energy-en/produkte-und-service/produkte-und-service.php, last accessed July 2012.

[97] xemc-darwind.com/index.php/solutions.html, last accessed July 2012.

[98] D.A. Torrey, "Variable Reluctance Generators in Wind Energy Systems", Proceedings of IEEE Power Electronics Specialists Conference, pp. 561-77, 1993.

[99] E. Darie, C. Cepisca and E. Darie, "The use of switched reluctance generator in wind energy applications", Proceedings of Power Electronics and Motion Control Conference, pp. 1963-6, September 2008.

[100] M.A. Mueller, "Design of Low Speed Reluctance Machines for Wind Energy Converters", Proceedings of IEE Electrical Machines and Drives Conference, Conference Publications No. 468, pp. 60-4, 1999.

[101] D.A. Torrey, "Switched reluctance generators and their control", IEEE Transactions on Industrial Electronics, Volume 49, No. 1, pp. 3-14, February 2002.

[102] S.W.H. De Haan, A.T. Veltman, J. Janousek, Z. Cerovsky, J. Mericka, J. Pavelka, J. Perina and F. Petrasek, “A high efficiency electrical conversion system with variable reluctance generator for variable speed wind turbine”, ECN report no. ECN-C--95-033, 1995.

[103] E. Spooner, P. Gordon, J.R. Bumby and C.D. French, “Lightweight, ironless-stator, PM generators for direct-drive wind turbines”, IEE Proceedings of Electrical Power Applications, Volume 152, No. 1, pp. 17-26, January 2005.

[104] http://www.flintbox.com/public/project/5358/, last accessed February 2013.

[105] E. Spooner and A.C. Williamson, “Direct coupled, permanent magnet generators for wind turbine applications”, IEE Proceedings of Electrical Power Applications, Volume 143, No. 1, pp. 1-8, January 1996.

[106] E. Spooner and A.C. Williamson, “Modular, permanent magnet wind turbine generators”, Proceedings of IEEE Industry Applications Conference, Volume 1, pp. 497-502, 1996.

[107] E. Spooner, A.C. Williamson and G. Catto, “Modular design of permanent-magnet generators for wind turbines”, IEE Proccedings of Electrical Power Applications, Volume 143, No. 5, pp. 388-95, September 1996.

[108] M.R. Dubois, H. Polinder and J.A. Ferreira, “Comparison of Generator Topologies for Direct-Drive for Wind Turbines”, Nordic Countries Power Industrial Electronics Conference Proceedings, Aalborg, Denmark, pp.22-6, June 2000.

[109] E. Spooner and A.C. Williamson, “Permanent-magnet generators for wind turbine applications”, Proceedings of IEEE Electrical Power Applications, Volume 143, No. 1, pp. 1-8, 1996.

[110] J. Chen, C.V. Nayar and L. Xu, “Design and finite-element analysis of an outer-rotor permanent-magnet generator for directly coupled wind turbines”, IEEE Transactions on Magnetics, Vol. 36, No. 5, pp. 3802-9, September 2000.

[111] F. Libert and J. Soulard, “Design study of different direct-driven permanent-magnet motors for a low speed application”, in Proceedings of the Nordic Workshop on Power and Industrial Electronics (NORpie), Trondheim, Norway, June 2004.

[112] F. Libert and J. Soulard, “Design study of low-speed direct-driven permanent magnet motors with concentrated windings”, Proceedings of 6th International

Symposium on Advanced Electromechanical Motion Systems (Electromotion), September 2005.

[113] W. Wu, V.S. Ramsden, T. Crawford and G. Hill, “A low-speed, high-torque, direct drive permanent magnet generator for wind turbine”, Proceedings of IEEE Industrial Applications Conference, Volume 1, pp. 147-54, 2000.

[114] G. Korouji, “Design, construction and test study of a wind energy generator with dual permanent magnet excitation”, Ph.D. thesis, Berlin University of Technology, Berlin, Germany, 2004.

[115] M.S. Widyan, “Design, optimization, construction and test of rare-earth permanent-magnet electrical machines with new topology for wind energy applications”, Ph.D. thesis, Berlin University of Technology, Berlin, Germany, 2006.

[116] H. Polinder, M.J. Hoeijmakers and M. Scuotto, ‘Eddy-current losses in the solid back-iron of permanent-magnet machines with different concentrated fractional pitch windings’. Proceedings of IEEE International Electrical Machines and Drives Conference (IEMDC07), Antalya, pp. 652-7, 3-5 May 2007

[117] E. Spooner, P. Gordon, J.R. Bumby and C.D. French, “Lightweight, ironless-stator, PM generators for direct-drive wind turbines”, IEE Proceedings of Electrical Power Applications, Volume 152, No. 1, pp. 17-26, January 2005.

[118] C.J.A. Versteegh, “Desig of Zephyros Z72 wind turbine with emphasis on the direct drive PM generator”, Proceedings of Nordic Workshop Power Industrial Electronics (NORPIE), Paper No. 68, Trondheim, Norway, 14-16 June 2004.

[119] S. Engstrom and S. Lindgren: “Design of NewGen direct drive generator for demonstration in a 3.5 MW Wind Turbine”, EWEC, Milan, Italy, 2007.

[120] G. Shrestha, H. Polinder, D.J. Bang and J.A. Ferreira, “Structural flexibility: A solution for mass reduction of large direct-drive wind-turbine generators”, IEEE Energy Conversion Journal, Volume 25, No. 3, pp. 732-40, September 2010.

[121] G. Shrestha, H. Polinder, D.J. Bang and J.A. Ferreira, “Direct drive wind turbine generator with magnetic bearing”, Proceedings of the European Offshore Wind conference, paper No. 194, pp. 1-10, Berlin, Germany, 2007.

[122] J.N. Stander, G. Venter and M.J Kamper, “Review of direct-drive radial flux wind turbine generator mechanical design”, Wind Energy Journal, Volume 15, No. 3, pp. 459-72, April 2012.

[123] P. Campbell, “Principles of a permanent-magnet axial-field DC machine”, Proceedings of IEE, Volume 121, No. 12, pp. 1489-94, December 1974.

[124] P. Campbell, “The magnetic circuit of an axial-field DC electrical machine”, IEEE Transactions on Magnetics, Volume 11, No. 5, pp. 1541-3, September 1975.

[125] G. Henneberger, H. Harer, S. Schustek and L. Verstege, “A new range of DC and AC pancake motors”, Proceedings of International Conference on Electrical Machines (ICEM), pp. 916-9, 1986.

[126] H. Weh, “High power synchronous machines with permanent magnet excitation”, Proceedings of International Conference on Electrical Machines (ICEM), pp.295-303, 1980.

[127] C. C. Chan, “Axial-field electrical machines-design and applications”, IEEE Transactions on Energy Conversion, Volume EC-2, No.2, pp. 294-300, 1987.

[128] G. B. Kliman, “Permanent magnet AC disc motor electric vehicle drive”, SAE Technical Paper Series, International Congress and Exposition, Detroit, Michigan, 1983.

[129] M. Aydin, S. Huang and T.A. Lipo, “Axial Flux Permanent Magnet Disc Machines: A Review”, Symposium on Power Electronics, Research report, 2004.

[130] Z. Zhang, F. Profumo and A. Tenconi, “Axial-flux versus radialflux PM motors”, SPEEDAM, Italy, pp. A4-19, 1996.

[131] J. Rizk and M. Nagrial, “Performance of axial type coupling”, Proceedings of International Conference on Electrical Machines (ICEM), 1998.

[132] S. Huang, M. Aydin and T.A. Lipo, “Torque quality assessment and sizing optimization for surface mounted PM machines”, IEEE Industry Applications Society Annual Meeting, pp. 1603-10, Chicago, September 2001.

[133] A. Cavagnino, M. Lazzari, F. Profumo and A. Tenconi, “A comparison between the axial flux and the radial flux structures for PM synchronous motors”, IEEE Transactions on Industry Applications, Volume 38, No.6, pp. 1517-24, November/December 2002.

[134] K. Sitapati and R. Krishnan, “Performance comparison of radial and axial field permanent magnet brushless machines”, IEEE Transactions on Industry Applications, Volume 37, No.5, pp. 1219-26, September/October 2001.

[135] Y. Chen, P. Pillay and A. Khan, “PM wind generator topologies”, IEEE Transactions on Industrial Applications, Volume 41, No. 6, pp. 1619-26, 2005.

[136] E. Spooner and B.J. Chalmers, “TORUS, a slotless, toroidal stator, permanent magnet generator”, Proceedings of IEE, Part-B, Volume 139, No. 6, pp. 497-506, November 1992.

[137] E. Spooner and B.J. Chalmers, “Toroidally-wound, slotless, axial-flux, permanent-magnet, brushless-DC motors”, Proceedings of International Conference on Electrical Machines (ICEM), pp. 81-6, 1988.

[138] B.J. Chalmers, A.M. Green, A.B.J. Reece and A.H. Al-Badi, “Modeling and simulation of the TORUS generator”, IEE Proceedings on Electric Power Applications, Volume 144, No. 6, pp. 446-52, November 1997

[139] B.J. Chalmers, W. Wu and E. Spooner, “An axial flux permanent-magnet generator for a gearless wind energy system”, IEEE Transactions on Energy Conversion, Volume 14, No.2, pp. 251-7, 1999.

[140] R.J. Wang, M.J. Kamper, K. VanderWesthuizen and J.F. Gieras, “Optimal design of a coreless stator axial flux permanent-magnet generator”, IEEE Transactions on Magnetics, Volume 141, No. 1, pp. 55-64, 2005.

[141] N.F. Lombard and M.J. Kamper, “Analysis and performance of an ironless stator axial flux PM machine”, IEEE Transactions on Energy Conversion, Volume 14, No. 4, pp. 1051-6, 1999.

[142] F. Caricchi, F. Crescimbini, F. Mezzetti and E. Santini, “Multi stage axial flux PM machine for wheel direct drive”, IEEE Industry Applications Society Annual Meeting, pp. 679-84, October 1995.

[143] F. Caricchi, F. Crescimbini, F. Mezzetti and E Santini, “Multistage axial-flux PM machine for wheel direct drive”, IEEE Transactions on Industry Applications, Volume 34, No. 4, pp.882-8, July/August 1996.

[144] E. Spooner and A. C. Williamson, “Direct coupled, permanent magnet generators for wind turbine applications”, Proceedings of IEE Electric Power Application, Volume 143, No. 1, pp.1-8, January 1996.

[145] R. J. Hill-Cottingham, P. C. Coles, J. F. Eastham, F. Profumo, A. Tenconi and G. Gianolio, “Multi-disc axial flux stratospheric aircraft propeller drive”, IEEE Industry Applications Society Annual Meeting, 2001.

[146] J. Braid, A. van Zyl and C. Landy, “Design, analysis and development of a multistage axial-flux permanent magnet synchronous machine”, Proceedings of 6th IEEE Africon Conference, Africa, Volume 2, pp. 675-80, October 2002.

[147] J. Braid, A. van Zyl and C. Landy, “Unbalanced load sharing in a prototype multistage axial-flux permanent magnet synchronous machine”, IEEE International Conference on Electric Machines and Drives 2003 (IEMDC'03), Volume 3, pp. 1935- 40, 1-4 June 2003.

[148] M.A. Mueller and A.S. McDonald, “A Lightweight Lowspeed Permanent Magnet Electrical Generator for Direct drive Wind Turbines”, Journal of Wind Energy, Volume 12, No. 8, pp. 768-80, November 2009.

[149] A.S. McDonald, N. Al-Khayat, D. Belshaw, M. Ravilious, A. Kumaraperumal, M. Benatmane, M. Galbraith, D. Staton, K. Benoit and M. Mueller, “1MW Multi-stage air-cored permanent magnet generator for wind turbines”, IET Power Electronics Machines and Drives Conference (PEMD), Bristol, 27-29 March 2012.

[150] NGenTec, www.ngentec.com/, last accessed July 2012.

[151] H. Weh, H. Hoffmann, J. Landrath, H. Mosebach and J. Poschadel, “Directly driven permanent magnet excited synchronous generator for variable speed operation”, European Community Wind Energy Conference, pp. 566-72, 1988.

[152] M.R. Harris, G.H. Pajooman and S.M. Abu Sharkh, “The problem of power factor in VRPM (transverse-flux) machines”. Eighth International Conference on Electrical Machines and Drives, Conference Publications No. 444, pp. 386-90, 1997.

[153] J. Schüttler, H. Groke, M. Siatkowski, J. Adler and B. Orlik, “Power optimized symmetrizing current control with a 8.7 kNm transverse flux generator”, Proceedings of 12th International Conference on Optimization of Electrical and Electronic Equipment (OPTIM), pp. 352-7, 2010.

[154] S. Hosseini, J.S. Moghani, N.F. Ershad and B.B. Jensen, “Design, Prototyping, and Analysis of a Novel Modular Permanent-Magnet Transverse Flux Disk Generator”, IEEE Transactions on Magnetics, Volume 47, No. 4, pp. 772-80, April 2011.

[155] M.R. Dubois and H. Polinder, “Study of TFPM machines with the toothed rotor applied to direct-drive generators for wind turbines”, Proceedings of Nordic Workshop on Power and Industrial Electronics, Trondheim, Norway, June 2004.

[156] M. Vinogradski, U. Werner and B. Orlik, “Genetic Algorithms Used for Geometrical Structure Design of Transverse Flux Permanent Magnet Motors to Optimize the Torque Wave Form”, PCIM Nürnberg, Germany, 2004.

[157] K.Y. Lu, E. Ritchie, P.O. Rasmussen and P. Sandholdt, “Modelling a single phase surface-mounted permanent magnet transverse flux machine based on Fourier Series Method”, Proceedings of IEEE Conference on Electric Machines and Drives, Volume 1, pp. 340-5, 2003.

[158] Y.G. Guo, J.G. Zhu, P.A. Watterson and W. Wu, “Development of a PM transverse flux motor with soft magnetic composite core”, IEEE Transactions on Energy Conversion, Volume 21, No. 2, pp. 426-34, June 2006.

[159] W.M. Arshad, T. Bäckström and C. Sadarangani, “Investigating a transverse flux machine with intermediate poles”, Proceedings of IEE Conference on Power Electronics, Machines and Drives (PEMD), pp. 325-8, 2002.

[160] P. Anpalaham, “Design of transverse flux machines using analytical calculations and finite element analysis”, Tech. Licentiate Thesis, Royal Institute of Technology, Stockholm, 2001.

[161] D. Svechkarenko, J. Soulard and C. Sadarangani, “A Novel Transverse Flux Generator in Direct-Driven Wind Turbines”, Proceedings of Nordic Workshop on Power and Industrial Electronics, June 2006.

[162] G. Henneberger and M. Bork, “Development of a new transverse flux motor”, in Proceedings of IEE Colloquium on New Topologies for PM Machines, Volume 1, pp. 1-6, 1997.

[163] G. Kastinger and A. Schumacher, “Reducing torque ripple of transverse flux machines by structural designs”, Proceedings of IEE Conference on Power Electronics, Machines and Drives (PEMD), pp. 320-4, 2002.

[164] J.F. Gieras, “Performance characteristics of a permanent magnet transverse flux generator”, Proceedings of IEEE Conference on Electric Machines and Drives, pp. 1293-9, 2005.

[165] P. Dickinson, A.G. Jack and B.C. Mecrow, “Improved permanent magnet machines with claw pole armatures”, Proceedings of International Conference on Electric Machines, paper 245, 2002.

[166] M.R. Harris, G.H.Pajooman, S.M.A. Sharkh and B.C. Mecrow, "Comparison of Flux-Concentrated and Surface-Magnet Configurations of the VRPM (Transverse-Flux) machine", Proceedings of the International Conference on Electrical Machines, p. 1119, 1998.

[167] H. Weh, "Transverse-flux machines in drive and generator application", Proceedings of the IEEE Symposium on Electric Power Engineering (Stockholm Power Tech), Strockholm, Sweden, Volume Invited speaker' session, pp. 75-80, 1995.

[168] E. Schmidt, "3-D finite element analysis of the cogging torque of a transverse flux machine", IEEE Transactions on Magnetics, Volume 41, No. 5, pp. 1836-9, May 2005.

[169] B.E. Hasubek and E.P. Nowicki, "Design limitations of reduced magnet material passive rotor transverse flux motors investigated using 3D finite element analysis", Proceedings of IEEE Canadian Conference on Electrical and Computer Engineering, Volume 1, pp. 365-9, March 2000.

[170] C. P. Maddison, "Transverse flux machines for high torque applications", Ph.D. thesis, University of Newcastle upon Tyne, UK, 1999.

[171] A.J. Mitcham, "Transverse flux motors for electric propulsion of ships", Proceedings of IEE Colloquium on New Topologies for PM Machines, Volume 3, pp. 1-6, 1997.

[172] Y. Rang, Chenglin Gu and H. Li, "Analytical design and modeling of a transverse flux permanent magnet machine", Proceedings of Power System Technology Conference, Volume 4, pp. 2164-7, 2002.

[173] A. Masmoudi, A. Njeh, A. Mansouri, H. Trabelsi and A. Elantably, "Optimizing the overlap between the stator teeth of a claw pole transverse-flux permanent-magnet machine", IEEE Transactions on Magnetics, Volume 40, No. 3, pp. 1573-8, May 2004.

[174] M. Dubois, "Optimized permanent magnet generator topologies for direct drive wind turbines", Ph.D. thesis, Delft University of Technology, Delft, The Netherlands, 2004.

[175] ANSYS Workbench, www.ansys.com, last accessed July 2012.

[176] Material Properties Database and Estimation Tools, www.matdat.com, last accessed August 2012.

[177] A.S. McDonald, M.A. Mueller and H. Polinder, “Comparison of generator topologies for direct-drive wind turbines including structural mass”, Proceedings of the International Conference on Electrical Machines (ICEM), Volume 360, pp. 1-7, September 2006.

[178] MATLAB, www.mathworks.co.uk/products/matlab, last accessed September 2012.

[179] A.J. Chipperfield and P.J. Fleming, “The MATLAB® Genetic Algorithm Toolbox”, IEEE Colloquium on Applied Control Techniques Using MATLAB, Volume 14, No. 10, pp. 1-4, London, UK, January 1995.

[180] A.S. McDonald, “Structural Analysis of Low Speed, High Torque Electrical Generators for Direct Drive Renewable Energy Converters”, PhD thesis, Edinburgh University, UK, 2008.

[181] R.J. Roark and W.C. Young, “Roark's Formulas for Stress and Strain”, McGraw-Hill International Editions, Singapore, 1989, 6th edition.

[182] Z.Q. Zhu and D.Howe, “Instantaneous Magnetic Field Distribution in Brushless Permanent Magnet dc Motors, Part III: Effect of Stator Slotting”, IEEE Transactions on Magnetics, Volume 29, no. 1, pages 143 -51, January 1993.

[183] J.J. Pyrhönen, Y. Alexandrova, R.S. Semken and H. Hämäläinen, “Wind Power Electrical Drives for Permanent Magnet Generators – Development in Finland”, Proceedings of the 9th ELEKTRO International Conference, pp. 9-16, May 2012.

[184] L. Fingersh, M. Hand and A. Laxson, “Wind Turbine Design Cost and Scaling Model Wind Turbine Design Cost and Scaling Model”, National Renewable Energy Laboratory (NREL) Technical Report, U.S., December 2006.

[185] O. Keysan and M. Mueller, “An Open Source Tool to Estimate Mass and Efficiency of Wind Turbine Power Take-off Systems”, accepted for publication in the IET conference on Renewable Power Generation (RPG), Beijing, China, September 2013.

[186] A. Zavvos, A.S. McDonald and M. Mueller, “Electromagnetic and Mechanical Optimisation of Direct-Drive Generators for Large Wind Turbines”, IET Conference on Power Electronics Machines and Drives (PEMD), Brighton, UK, April 2010.

[187] A. Zavvos, A.S. McDonald and M. Mueller, "Structural Optimisation Tools for Iron Cored Permanent Magnet Generators for Large Direct Drive Wind Turbines", IET conference on Renewable Power Generation (RPG), Edinburgh, UK, September 2011.

[188] A. Zavvos, A.S. McDonald, M. Mueller, D.J. Bang and H. Polinder, "Structural Comparison of Permanent Magnet Direct Drive Generator Topologies for 5MW Wind Turbines", IET Conference on Power Electronics Machines and Drives (PEMD), Bristol, UK, March 2012.

[189] A. Zavvos, A.S. McDonald, M. Mueller, "Optimisation Tools for Large Permanent Magnet Generators for Direct Drive Wind Turbines", Journal of Renewable Power Generation, Volume 7, No. 2, pages 163-171, March 2013.

[190] A. Zavvos, D.J. Bang, A.S. McDonald, H. Polinder and M. Mueller, "Structural Analysis & Optimisation of Transverse Flux Permanent Magnet Machines for 5MW and 10 MW Direct Drive Wind Turbines" , Journal of Wind Energy: The UpWind Special Issue, Volume 15, No. 1, pages 19-43, January 2012.

Appendix A

Disc rotor functions

$$f_{\mathrm{d}} = \frac{qR^2}{E(R_{\mathrm{a}} - R)\left[\frac{R}{E\left(R^2 - R_{\mathrm{o}}^2\right)}\left[(1-v)R^2 + (1+v)R_{\mathrm{o}}^2\right] - t_{\mathrm{d}}\left[\frac{1}{4D\lambda^3}\frac{\left(C_2C_{a2} - 2C_3C_{a1}\right)}{2C_{11}}F_2\left(x = l/2\right) - \frac{1}{2D\lambda^3}\frac{\left(C_3C_{a2} - C_4C_{a1}\right)}{C_{11}}F_1\left(x = l/2\right) - \frac{1}{4D\lambda^3}F_{\mathrm{a4}}\left(x = l/2\right)\right]\right]}$$

$\lambda = \left(\frac{3\left(1 - v^2\right)}{R^2 h_{\mathrm{yr}}^2}\right)^{1/4}$, where v the Poisson's ratio, 0.3

$D = Eh_{\mathrm{yr}}^3 / 12(1 - v^2)$, where $E = 200$ GPa

$D_{\mathrm{ax}} = Et_{\mathrm{d}}^3 / 12(1 - v^2)$

$W = \frac{1}{2}\rho_{steel} g \sin(\varphi)(l_{\mathrm{s}} - t_{\mathrm{d}})h_{\mathrm{ys}}$, where ρ_{steel} the steel density, $\rho_{\mathrm{steel}} = 7850\ \mathrm{kg/m^3}$

and $\varphi = 90°$

$w = \rho g \sin(\varphi) t_{\mathrm{d}}$

$$M_{\mathrm{rb}} = \frac{-wR_a^2}{C_5}\left[\frac{C_6}{2R_{\mathrm{a}}R_{\mathrm{o}}}\left((R_a^2 - R_{\mathrm{o}}^2\right) - L_{14}\right]$$

$$Q_{\mathrm{b}} = \frac{w}{2R_{\mathrm{o}}}\left(R_{\mathrm{a}}^2 - R_{\mathrm{o}}^2\right)$$

Armed stator functions

$$\lambda = \left(\frac{3\left(1 - v^2\right)}{R^2 h_{\mathrm{ys}}^2}\right)^{1/4}$$

$\theta = \pi / N_{\mathrm{arms}}$

$I = lh_{\mathrm{ys}}^3 / 12$

$A = lh_{\mathrm{ys}}$

$m = \left(\sqrt{I/A}/R\right)^2$

$a = bd - (b - 2t_{\mathrm{w}})(d - 2t_{\mathrm{w}})$

$W' = 0.5\rho g \sin(\phi) l d^2$

$$w' = \rho g \sin(\phi) A$$

$$w_i = \frac{\rho g \sin(\phi) l h_{\mathrm{ys}} \pi R}{N_{arms}}$$

$$I_{\mathrm{arm\text{-}axi}} = [bd^3 - (b-2t_{\mathrm{w}})(d-2t_{\mathrm{w}})^3]/12$$

$$I_{\mathrm{arm\text{-}tor}} = [db^3 - (d-2t_{\mathrm{w}})(b-2t_{\mathrm{w}})^3]/12$$

Cylindrical shell functions

$$F_1 = \cosh(\lambda x)\cos(\lambda x)$$

$$F_2 = \cosh(\lambda x)\sin(\lambda x) + \sinh(\lambda x)\cos(\lambda x)$$

$$F_3 = \sinh(\lambda x)\sin(\lambda x)$$

$$F_4 = \cosh(\lambda x)\sin(\lambda x) - \sinh(\lambda x)\cos(\lambda x)$$

$$F_{a1} = \langle x-a \rangle^0 \cosh\lambda\langle x-a \rangle \cos\lambda\langle x-a \rangle$$

$$F_{a5} = \langle x-a \rangle^0 - F_{a1}$$

where the use of the angle brackets is defined as follows: If x<a, $\langle x-a \rangle = 0$; if x>a, $\langle x-a \rangle = 1$.

Cylindrical shell constants

$$C_1 = \cosh(\lambda l)\cos(\lambda l)$$

$$C_2 = \cosh(\lambda l)\sin(\lambda l) + \sinh(\lambda l)\cos(\lambda l)$$

$$C_3 = \sinh(\lambda l)\sin(\lambda l)$$

$$C_4 = \cosh(\lambda l)\sin(\lambda l) - \sinh(\lambda l)\cos(\lambda l)$$

$$C_5 = \tfrac{1}{2}\left[1 - (R_{\mathrm{o}}/R_{\mathrm{a}})^2\right]$$

$$C_6 = \frac{R_{\mathrm{o}}}{4R_{\mathrm{a}}}\left[(R_{\mathrm{o}}/R_{\mathrm{a}})^2 - 1 + 2\ln(R_{\mathrm{a}}/R_{\mathrm{o}})\right]$$

$$C_{11} = \sinh^2(\lambda l) - \sin^2(\lambda l)$$

$$C_{12} = \cosh(\lambda l)\sinh(\lambda l) + \cos(\lambda l)\sin(\lambda l)$$

$$C_{14} = \sinh^2(\lambda l) + \sin^2(\lambda l)$$

$$C_{a1} = \cosh\lambda(l-a)\cos\lambda(l-a)$$

$$C_{a2} = \cosh\lambda(l-a)\sin\lambda(l-a) + \sinh\lambda(l-a)\cos\lambda(l-a)$$

$$C_{a3} = \sinh\lambda(l-a)\sin\lambda(l-a)$$

$$C_{a4} = \cosh\lambda(l-a)\sin\lambda(l-a) - \sinh\lambda(l-a)\cos\lambda(l-a)$$

$$C_{a5} = 1 - C_{a1}$$

Flat circular plate loading constants

$$L_{14} = \frac{1}{16}\left\{1 - \left(\frac{R_{\mathrm{o}}}{R}\right)^4 - 4\left(\frac{R_{\mathrm{o}}}{R}\right)^2 \ln\left(\frac{R_{\mathrm{a}}}{R}\right)^2\right\}$$

$$L_{17} = \frac{1}{4}\left\{1 - \frac{1-v}{4}\left[1 - \left(\frac{R_{\mathrm{o}}}{R}\right)^4\right] - \left(\frac{R_{\mathrm{o}}}{R}\right)^2\left[1 + 1(1+v)\ln\left(\frac{R}{R_{\mathrm{o}}}\right)\right]\right\}$$

Appendix B

List of publications

[1] A. Zavvos, A.S. McDonald and M. Mueller, "Electromagnetic and Mechanical Optimisation of Direct-Drive Generators for Large Wind Turbines", IET Conference on Power Electronics Machines and Drives (PEMD), Brighton, UK, April 2010.

[2] A. Zavvos, A.S. McDonald and M. Mueller, "Structural Optimisation Tools for Iron Cored Permanent Magnet Generators for Large Direct Drive Wind Turbines", IET conference on Renewable Power Generation (RPG), Edinburgh, UK, September 2011.

[3] A. Zavvos, D.J. Bang, A.S. McDonald, H. Polinder and M. Mueller, "Structural Analysis & Optimisation of Transverse Flux Permanent Magnet Machines for 5MW and 10 MW Direct Drive Wind Turbines" , Journal of Wind Energy: The UpWind Special Issue, Volume 15, No. 1, pages 19-43, January 2012.

[4] A. Zavvos, A.S. McDonald, M. Mueller, D.J. Bang and H. Polinder, "Structural Comparison of Permanent Magnet Direct Drive Generator Topologies for 5MW Wind Turbines", IET Conference on Power Electronics Machines and Drives (PEMD), Bristol, UK, March 2012.

[5] A. Zavvos, A.S. McDonald, M. Mueller, "Optimisation Tools for Large Permanent Magnet Generators for Direct Drive Wind Turbines", Journal of Renewable Power Generation, Volume 7, No. 2, pages 163-171, March 2013.